OPTIMIZATION OF MARINE CLAY STABILITY TREATED BY ENVIRONMENTALLY FRIENDLY MATERIALS USING MACHINE LEARNING TECHNIQUES

By

AHMED HASSAN SAAD ABDELRAHMAN MOUSA

Thesis Submitted to the School of Graduate Studies, Universiti Putra Malaysia, in Fulfilment of the Requirements for the Degree of Doctor of Philosophy

November 2023

DEDICATIONS

To my parents
To my grandparents
To my siblings
To my fiancé
To my supervisors
To my teachers
To my friends
…

Abstract of thesis presented to the Senate of Universiti Putra Malaysia in fulfilment of the requirement for the degree of Doctor of Philosophy

OPTIMIZATION OF MARINE CLAY STABILITY TREATED BY ENVIRONMENTALLY FRIENDLY MATERIALS USING MACHINE LEARNING TECHNIQUES

By

AHMED HASSAN SAAD ABDELRAHMAN MOUSA

November 2023

Chair : Haslinda binti Nahazanan, PhD
Faculty : Engineering

Marine clay is instable soil under loading due to its limited shear strength, leading to significant settlements. Such weakness poses a risk to structures, often causing collapses and disasters, especially on long–term of loading, impacting economy, society, and ecology. Consequently, geotechnical strategies for soil stabilization become crucial. However, conventional methods employing calcium–based binders exacerbate environmental degradation and contribute to climate change concerns such as cement which accounts for 30% of all CO_2 emissions worldwide. Besides, controlling the ratio of used materials in reinforcing and stabilizing marine clay from the strengthening perspective is challenging. Therefore, this study focuses on reinforcing marine clay to resist short–term and long–term loading using ecofriendly materials such as natural or green pozzolanic materials, using machine learning algorithms. The used ecofriendly materials were palm oil fly ash (POFA) and calcined shale (CS) as supplementary materials for lime (L). The treated marine clay specimens were investigated using ratios of 1%, 3%, and 5% for lime, 1%, 5%, 10%, 15%, and 20% for POFA, and 5%, 10%, 15%, and 20% for CS. Various L–POFA–CS treated specimens were tested under various curing durations: 7, 14, 21, 28, 56, and 90 days. Promising enhancements in soil properties were observed, particularly in sample SL5P5C10, comprising 5% lime, 5% POFA, and 10% CS, where c_u increased by 4 times, $Ø_u$ increased by 50%, c' increased by 6 times, and Ø' increased by 90% compared to the control specimen. The Atterberg enhanced significantly after 7 curing days from 75.20 to 34.50 for liquid limit W_{LL}, from 48.95 to 32.01 for plastic limit W_{PL}, and treated specimens resisted compressibility under loading, with compression index C_v reduced significantly from 147.5 to 3.15 m^2/yr and permeability k from 3.25E–08 to 6.30E–09 cm/sec after 7 curing days for SL5P5C10 treated specimens. 90 finite element model (FEM) simulations of consolidated undrained (CU) triaxial tests were executed using PLAXIS 2D to compare and indicate the relation between the experimental and simulation results. The FEMs produced stress–strain relationships that were consistent with the experimental data, although the FEMs trended towards normal consolidated behavior, while the experimental results were more over consolidated. To enhance the accuracy of the results for final work without experimental work, machine learning techniques were utilized. Machine learning algorithms, including LR, PR, ANN, GBoost, xGBoost, and RF, were used in optimizing eight manual selected feature models of a total 48 models and hybrid algorithms incorporating genetic feature selection, forward feature selection, and backward feature elimination yielded a total of 52 models. Machine learning helped in generation 102 models and optimizing the ratios of used materials in limited time compared to the traditional analyzing methods using cross–validation process. The machine learning models could be used as a guideline and estimation and prediction for shear strength after treatment using mixture of lime, CS, and POFA for future research. Eventually, a further investigation was then made on the natural and optimum mixture (SL5P5C10) through FEM to indicate its deformation behavior using PLAXIS 2D program for both short–term and long and long term of loading of Serdang Landslide. The simulation shows a substantial increase in soil resistance to horizontal stresses post–treatment, with stress levels decreasing from 20 kN/m^2 in natural soil to 2 kN/m^2 in SL5P5C10 treated soil fill. This signifies a tenfold enhancement in soil's ability to withstand horizontal stresses compared to untreated soil under similar loading conditions. Utilizing SL5P5C10 treated soil as fill behind retaining walls holds potential for engineering, geotechnical, and economic advantages, facilitating taller building constructions and accommodating heavier traffic loads in adjacent parking areas.

Keywords: Ecofriendly materials, Long-term strength, Machine learning, Marine clay, Soil stabilization

SDG: GOAL 6: Clean Water and Sanitation, GOAL 9: Innovation, and Infrastructure, GOAL 13: Climate Action.

Abstrak tesis yang dikemukakan kepada Senat Universiti Putra Malaysia sebagai memenuhi keperluan untuk ijazah Doktor Falsafah

OPTIMASI KESTABILAN TANAH LIAT MARIN YANG DIRAWAT DENGAN BAHAN MESRA ALAM MENGGUNAKAN TEKNIK PEMBELAJARAN MESIN

Oleh

AHMED HASSAN SAAD ABDELRAHMAN MOUSA

November 2023

Pengerusi : Haslinda binti Nahazanan, PhD
Fakulti : Kejuruteraan

Tanah liat marin adalah tanah yang tidak stabil di bawah beban disebabkan oleh kekuatan ricih yang terhad, menyebabkan enapan yang signifikan. Kelemahan sedemikian membawa risiko kepada struktur, sering menyebabkan runtuhan dan bencana, terutamanya pada jangka masa panjang, memberi impak kepada ekonomi, masyarakat, dan ekologi. Oleh itu, strategi geoteknik untuk penstabilan tanah menjadi penting. Walau bagaimanapun, kaedah konvensional yang menggunakan bahan pengikat berbasis kalsium memperburuk degradasi alam sekitar dan menyumbang kepada kebimbangan perubahan iklim seperti simen yang menyumbang 30% dari semua pelepasan CO_2 di seluruh dunia. Selain itu, mengawal nisbah bahan yang digunakan dalam memperkuat dan menstabilkan liat marin dari perspektif penguatan adalah mencabar. Oleh itu, kajian ini memberi tumpuan kepada memperkuat liat marin untuk menentang beban jangka pendek dan jangka panjang menggunakan bahan mesra alam seperti bahan pozzolan semulajadi atau hijau, dengan menggunakan algoritma pembelajaran mesin. Bahan mesra alam yang digunakan adalah abu terbang kelapa sawit (POFA) dan shale tercalcined (CS) sebagai bahan tambahan untuk kapur (L). Sampel liat marin yang dirawat dengan campuran L–POFA–CS disiasat menggunakan nisbah 1%, 3%, dan 5% untuk kapur, 1%, 5%, 10%, 15%, dan 20% untuk POFA, dan 5%, 10%, 15%, dan 20% untuk CS. Berbagai spesimen yang dirawat L–POFA–CS diuji di bawah pelbagai tempoh penyembuhan: 7, 14, 21, 28, 56, dan 90 hari. Peningkatan yang menjanjikan dalam sifat tanah diperhatikan, terutamanya dalam sampel SL5P5C10, yang mengandungi 5% kapur, 5% POFA, dan 10% CS, di mana c_u meningkat 4 kali ganda, $Ø_u$ meningkat 50%, c' meningkat 6 kali ganda, dan Ø' meningkat 90% berbanding dengan sampel kawalan. Atterberg ditingkatkan secara signifikan selepas 7 hari penyembuhan dari 75.20 kepada 34.50 untuk had cecair W_{LL}, dari 48.95 kepada 32.01 untuk had plastik W_{PL}, dan spesimen yang dirawat menolak pemampatan di bawah beban, dengan indeks pemampatan C_v berkurang secara signifikan dari 147.5 kepada 3.15 m^2/yr dan kebolehtelapan k dari 3.25E–08 kepada 6.30E–09 cm/s selepas 7 hari penyembuhan untuk sampel SL5P5C10 yang dirawat. Simulasi model elemen terhad (FEM) sebanyak 90 ujian triaksial terkonsolidasi tanpa terkonsolidasi (CU) dilakukan menggunakan PLAXIS 2D untuk membandingkan dan menunjukkan hubungan antara data eksperimen dan simulasi. FEM menghasilkan hubungan regangan–tekanan yang konsisten dengan data eksperimen, walaupun FEM cenderung ke arah perilaku terkonsolidasi normal, sementara hasil eksperimen lebih terkonsolidasi. Untuk meningkatkan ketepatan hasil bagi kerja akhir tanpa kerja eksperimental, teknik pembelajaran mesin digunakan. Algoritma pembelajaran mesin, termasuk LR, PR, ANN, GBoost, xGBoost, dan RF, digunakan dalam mengoptimumkan lapan model ciri manual yang dipilih daripada jumlah 48 model dan algoritma hibrid yang menggabungkan pemilihan ciri genetik, pemilihan ciri ke hadapan, dan penyingkiran ciri ke belakang menghasilkan jumlah 52 model. Pembelajaran mesin membantu dalam menghasilkan 102 model dan mengoptimumkan nisbah bahan yang digunakan dalam masa yang terhad berbanding dengan kaedah analisis tradisional menggunakan proses validasi silang. Model pembelajaran mesin boleh digunakan sebagai panduan dan ramalan untuk kekuatan ricih selepas rawatan menggunakan campuran kapur, CS, dan POFA untuk penyelidikan masa depan. Akhirnya, penyelidikan lanjut dilakukan pada campuran semulajadi dan optimum (SL5P5C10) melalui FEM untuk menunjukkan tingkah laku pembentukan menggunakan program PLAXIS 2D untuk jangka masa pendek dan panjang dan jangka masa panjang penimpaan tanah tanah runtuh Serdang. Simulasi menunjukkan peningkatan yang ketara dalam rintangan tanah terhadap tekanan mendatar selepas rawatan, dengan tahap tekanan yang menurun dari 20 kN/m^2 dalam tanah asli kepada 2 kN/m^2 dalam bahan tanah yang dirawat SL5P5C10. Ini menandakan peningkatan sepuluh kali ganda dalam keupayaan tanah untuk menahan tekanan mendatar berbanding dengan tanah yang tidak dirawat dalam keadaan beban yang serupa. Penggunaan tanah yang dirawat SL5P5C10 sebagai bahan tanah di belakang dinding penahan mempunyai potensi kelebihan kejuruteraan, geoteknik, dan ekonomi, memudahkan pembinaan bangunan yang lebih tinggi dan menampung beban kenderaan yang lebih berat di kawasan tempat letak kereta yang berdekatan.

Kata Kunci: Bahan mesra alam, Kekuatan jangka panjang, Pembelajaran mesin, Tanah liat marin, Penstabilan tanah

SDG: MATLAMAT 6: Air Bersih dan Sanitasi, MATLAMAT 9: Inovasi dan Infrastruktur, MATLAMAT 13: Tindakan Iklim.

ACKNOWLEDGEMENTS

قُلْ بِفَضْلِ اللَّهِ وَبِرَحْمَتِهِ فَبِذَٰلِكَ فَلْيَفْرَحُوا هُوَ خَيْرٌ مِّمَّا يَجْمَعُونَ

For my father, **Engr**. **Hassan Mousa** and my mother **Dr**. **Shadia Nagy**, both who supported me along this journey spiritually, morally and financially,

For my siblings **Mohammed**, **Kareem** and **Nada** who supported me for finishing this work,

For my supervisor, **Dr**. **Haslinda Nahazanan** who supported me along this journey and she spared no effort in completing the work and the thesis by their final format,

For my co-supervisor **Dr**. **Badronnisa**, for her technical support during this journey,

For my co-supervisor **Prof. Fauziah** who without her help in the machine learning part of this project, it was not done and was no project, for her technically support.

For all my friends in UPM, especially my colleague **Dr. Angham Ali** for sharing her research data, **Dr. Mahmoud Abdelrehim, Dr. Mhammed Ibrahim** and all members of the **Egyptian Association in UPM**,

For **Mr**. **Hafizan** the laboratory officers for his support,

Thanks to you all, for support, without you all the work has not existed.

At the beginning and at the end, I thank the only one without him there was nothing, I thank **Allah** "Alhamdulillah".

وَقَالُوا الْحَمْدُ لِلَّهِ الَّذِي صَدَقَنَا وَعْدَهُ وَأَوْرَثَنَا الْأَرْضَ نَتَبَوَّأُ
مِنَ الْجَنَّةِ حَيْثُ نَشَاءُ ۖ فَنِعْمَ أَجْرُ الْعَامِلِينَ

الْحَمْدُ لِلَّهِ الَّذِي بِنِعْمَتِهِ تَتِمُّ الصَّالِحَاتُ

This thesis was submitted to the Senate of Universiti Putra Malaysia and has been accepted as fulfilment of the requirement for the degree of Doctoral of Philosophy. The members of the Supervisory Committee were as follows:

Haslinda binti Nahazanan, PhD
Associate Professor
Faculty of Engineering
Universiti Putra Malaysia
(Chairman)

Badronnisa binti Yusuf, PhD
Associate Professor
Faculty of Engineering
Universiti Putra Malaysia
(Member)

Siti Fauziah binti Toha, PhD
Professor, Ir.
Kulliyyah of Engineering
International Islamic University Malaysia
(Member)

____

ZALILAH MOHD SHARIFF, PhD
Professor and Dean
School of Graduate Studies
Universiti Putra Malaysia

Date: 13 June 2024

TABLE OF CONTENTS

LIST OF TABLES

LIST OF FIGURES

LIST OF ABBREVIATIONS

1–D	One dimensional consolidation test
AI	Artificial intelligence
ASTM	American society for testing and materials
ANOVA	Analysis of variation test
ANN	Artificial neural network
BS	Backward feature selection
BS	British standards
BSI	British standards institution
CEC	Cation exchange capacity
CU	consolidated undrained triaxial test
CS	Calcined shale
FEM	Finite element model
FLX	Flexural strength
FS	forward feature selection
GBoost	Gradient boost algorithm
GS	Genetic feature selection
L	lime
LL	Liquid limit
LR	linear regression
LOI	Loss on Ignition
MANOVA	Multivariant analysis of variation test
MDD	Maximum dry density
ML	Machine learning

MLR	Multi–layer regression
OLS	Ordinary Least Squares
OMC	Optimum moisture content
PL	Plastic limit
POFA	Palm oil fly ash
PR	Polynomial regression
UCS	Unconfined compressive strength test
UPM	Universiti Putra Malaysia
USCS	Unified soil classification system
UU	Undrained unconfined test
RF	Random forest regression
SEM	Scanning electron microscope analyzer
SL	Shrinkage limit
SSA	Specific surface area
STR	Simple regressing tree
VPM	Virtual programming module
xGBoost	Extreme gradient boost algorithm
XRD	X–ray powder diffraction

LIST OF SYMBOLS

Al_2O_3	Aluminium oxide
a_v	Coefficient of compressibility
Ca	Calcium atom
Ca^{2+}	Calcium ion
$CaCO_3$	Calcium carbonates
$CaCl_2$	Calcium chloride
C_C	Compression index
CI	Consistency index
CO_3^{2-}	Carbonates ion
CaO	Calcium oxide
C_V	Coefficient of consolidation
C_R	Recompression index
C_S	Swelling index
c_u	Undrained cohesion
c'	Drained cohesion
E	Modulus of elasticity (Young's Modulus)
e	Void ratio
E_{er}	Error
$F_{m-1}(x)$	Prediction of the $(m-1)^{th}$ model
Fe_2O_3	Iron oxide
G_s	Specific gravity
$h_m(x)$	The m^{th} weak learner
H_2O	Water

k	permeability
MAE	Mean absolute error
Mg	Magnesium atom
Mg^{2+}	Magnesium ion
$MgCO_3$	Magnesium carbonates
$MgCl_2$	Magnesium chloride
MgO	Magnesium oxide
MSE	Mean square error
m_v	Coefficient of volume compressibility
n	Porosity
N	Number of samples
P_c’	Yield (pre–consolidation) stress
pH	Acidity scale factor
PI	Plasticity index
RMSE	Root mean square error
R^2	Coefficient of determination
SI	Scatter index
SiO_2	Silicon oxide
SO_3	Sulfate
S_u	Undrained shear strength
w_{LL}	Liquid limit
w_n	Natural water content
w_{PL}	Plastic limit
Y	Observed output (experimental value)

$\hat{Y}$	Predicted output
y_p.	Dependent variable
y	Imputed target
$\hat{y}$	Mean of targeted values
x_p.	Independent variable
x	Input data
x_i	Features
β_p.	Coefficients to be estimated
ϵ	Error term
γ_{bulk}	Bulk soil density
γ_{dry}	Dry soil density
σ_1	Vertical stress
σ_1	Confining stress
$\Delta\sigma$	Deviatoric stress
ϕ_u	Undrained internal angle of friction
ϕ'	Drained internal angle of friction
^{o}C	Degree Celsius

CHAPTER 1

INTRODUCTION

1.1 General

Marine clay has an instability problem under applied load due to the absence or the limitation of its shear strength. The weak nature of marine clay results in the formation of enormous settlements when subjected to loads, which causes structures to collapse and lose their capacity to perform their intended functions. This occurs in the areas around riverbanks and beaches. The town's size is a direct result of the vast quantities of water deposited there, and significant breakdowns threaten both the inhabitants and the structures erected. marine clay tends to extend quite a bit below the surface of the earth, which makes it difficult to be removed and makes it rather costly to construct appropriate foundations for structures. Thus, treatment is required to be applied to marine clay. Technical calcium–based blinders such as lime and cement, which contributes to climate change (Damineli et al., 2010; Mohammed et al., 2023).

Some forms of industrial waste are hazardous and cannot be recycled. Industrial waste poses a hazard to the environment and contributes to the acceleration of climate change. Their huge production pace pertains to the biological sciences. POFA is a byproduct substance that should be recycled to overcome its hazardous effect. The high concentration of silica in it gives it pozzolanic qualities, which means that it might be used in lieu of cement (Tangchirapat et al., 2003).

The stability of soil can be improved by adding metakaolin and other extra cementitious chemicals. However, it is important to note that such improvements come with associated costs of used materials. Calcined shale is a natural pozzolanic material that helps in strengthening concrete and soil economically and effectively. However, it is important to ensure that the calcined shale used is of high quality and meets any applicable standards and regulations. Pozzolan obtained from natural sources is a soil treatment that is resistant to sulfate corrosion. However, it is difficult to use conventional analysis to determine how best to use these components in order to enhance marine clay.

Machine learning has become an increasingly popular application for the analysis and forecasting of massive amounts of data. Machine learning algorithms are used and taught by data (input and target variables) to build models that are widely applied for predicting accurate target values. Accordingly, machine learning will be an extremely useful tool in the prediction and evaluation of the optimized amounts of cementitious materials (calcined shale), calcium–based binders (lime), and palm oil fuel ash (POFA) as a green material mixture for sustainable treatment for marine clay.

This study attempted to forecast and evaluate both the strength and deformation of marine clay treated with lime, calcined shale, and POFA. Its applicability in real–world settings and locations, in particular, the reduction of differential settlement and the improvement of shear strength was also environmental friendly and sustainable materials, calcined shale, lime, and palm oil fuel ash can be used in the construction of future projects and side slopes that will be constructed on treated marine clay. However, the study limited to treating marine clay specimens from the Kuala Langat area using calcined shale, lime, and palm oil fuel ash. In addition, the specimen quantity and experimental data imposed in the experimental study were limited in machine learning application, besides the meshing and controlling inputs in finite element modeling in specifying certain analysis points, especially beneath the structures' midpoints.

1.2 Problem Statement

Marine clay is a challenging soil to work with because of its unstable nature, which results in differential settlement. Marine clay near the sea in particular is very difficult to work with because of its high void ratio that is filled with water. Both the removal of surplus water and the compression of the soil are processes that are time–consuming. This characteristic of marine clay results in non–uniform deformation, which worsens when subjected to cyclic stresses, as can be seen in the case of metro tunnels of Shanghai (Shen et al., 2014) causing the deformation of the tunnel's concrete rings. Moreover, large deformations have led to enormous disasters such as in Serdang, Selangor, where retaining walls collapsed twice within five years (Aziz, 2022; Faris, 2022) and landslide in Cameron Highland, Perak (Alagesh, 2021). The repercussions extend across economic, societal, and ecological issues.

Although cement and lime are commonly used materials for improving soil strength, it has a notable negative impact on climate change (Farooq et al., 2021). In order to improve the performance of marine clay’s capacity to resist sulphate corrosion in cement and lime, it will be helpful to make use of a resource that is both inexpensive and environmental friendly. Alternatively, soil improvement that employs calcium based green materials which are eco-friendly and cost–effective materials such as palm oil fly ash (POFA) and calcined shale (CS) seem to be useful and effective in short-term of load resistance (Mohamed et al., 2023; Nik et al., 2021). However, the materials were not investigated in treating marine clay under long-term of loading which is the main issue for the resulted deformations of the marine clay under loading. Besides, the green materials’ optimal and/or engineering ratios were not identified for consolidated undrained (CU) and consolidated drained (CD) strengths to indicate the enhancement in load and deformation resistance on the long-run.

Accordingly, expensive and time-consuming experiments of geotechnical investigation are required such as; triaxial test, X–ray fluorescence (XRF), X–ray diffraction (XRD) diffraction characteristics, scanning electron microscope (SEM) and others (Saad et al., 2021). Therefore, the application of finite element modeling for the experiments and comparing the results to experimental outputs could help in reducing the time and cost consuming for the future geotechnical research and work (Raja & Shukla, 2021).

However, the concerns of the wide range of geotechnical parameters make it difficult to control only through FEM. Besides, conventional analytical methodologies encounter limitations in accommodating numerous factors, thereby diminishing their applicability. In addition, the simulation of the geotechnical investigation and/or loading cases consumes time and is costly activity compared to the accuracy of the model. Besides, the geotechnical uncertainties are difficult to be incorporated into the models. Therefore, incorporating artificial intelligence (AI) and machine learning (ML) models offers a potential solution to this conundrum.

Hence, the goal of this research is to develop a machine learning model that can assess various proportions of calcined shale (CS), lime (L), and palm oil fuel ash (POFA) in order to create a novel treatment combination that is optimal for marine clay. The intelligent model that was proposed is believed to be helpful in predicting shear strength and deformation of the treatment. On that account, the outcome of the study will be very useful for future construction on marine clay. Therefore, its potential use in future research, it might also be used to improve the stability of marine clay, construct foundations and tunnels, and construct roadways. Besides, FEM and ML application will help in reduction of cost and time of the geotechnical investigation directly and/or indirectly of the future research and work for geotechnical engineers.

1.3 Objectives of The Study

The research aims to assess and predict the short–term and the long–term loading effect on marine clay treated by calcined shale, lime and palm oil fuel ash using machine learning algorithms. To achieve the aim, four objectives have been set as below:

1. To investigate the deformation and strength behaviour of an optimum treated marine clay mixture under both short–term and long–term loading conditions using triaxial compressive strength test
2. To investigate the deformation and strength behaviour of an optimum treated marine clay mixture under both short–term and long–term loading conditions using FEM by PLAXIS 2D program
3. To optimize the prediction of shear strength and deformation limits for the treated Kuala Langat marine clay using machine learning algorithms
4. To validate the machine learning model of the new soil matrix of Kuala Langat treated marine clay in civil engineering construction applications.

1.4 Research Questions

Marine clay is a common geological formation of the seashore and riverbank in Malaysia. The engineering use of these materials is problematic due to the tendency of marine clay to undergo a settlement resulting in breakdown of road pavement structures, damages to buildings built on it and instability of embankments. The research is aimed to predict the long–term behaviour of marine clay treated with calcined shale, lime and palm oil fuel ash. The critical questions about this research are as follows:

1. What are the chemical and mineral compositions of marine clay?

2. What is the optimum amount of POFA to enhance the shear strength of marine clay?

3. What is the optimum amount of lime to enhance the shear strength of marine clay?

4. What is the optimum amount of calcined shale (CS) to enhance the shear strength of marine clay?

5. What is the optimum mixture of lime–CS–POFA to enhance the shear strength of marine clay?

6. What are the effects of loading time on shear strength and deformations of the treated marine clay using lime–CS–POFA?

7. How sustainable is the lime–CS–POFA treated marine clay?

8. What algorithm is applicable in the prediction of shear strength for treated marine clay?

9. What is the relationship between finite element model and ML models?

1.5 Significance of The Study

Marine clay is a problematic soil that is spreading all over South–East Asia generally and Malaysia specifically. This type of soil usually locates at regions around seashores, around lakes and riverbanks. All those areas usually have structures and roads established above or within their layers as in Kuala Lumpur, Bangkok, and Singapore. All these structures are subjected to significant values of differential settlements that lead to their failure. With no doubt, this will cause a negative impacts on country's economy and people.

Costly solutions such as replacing soil layers or constructing special deep foundations would be difficult to be applied specially with the usually huge depths of marine clay soils. Hence, treating marine clay through replacing water in voids with cementation matter to guarantee prevention or reduction of large deformation occurrence can be a solution to this problem.

It is believed that the cementitious treating mix of calcined shale, lime and palm oil fuel ash would help in strengthening marine clay. The cementation matter helps in improving the engineering properties of the soil and enhancing its deformation resistance under short-term and long-term loading conditions. Besides, finite element modeling for short-term and long-term loading conditions will assess the relation between FEM and experimental results, which can reduce the time and cost consuming of the experimental investigation. Improving the treatment process technically and scientifically in laboratory would help in making the method of the treatment applicable in construction and more related to real construction cases.

In this study, the treatment method proposed would help in reduction of differential settlement effect on constructions. Besides, it is an environmentally friendly method of treatment that utilise industrial waste materials. Thus, it also helps in reducing the climate changes due to the over emitting of CO_2 all over the world caused by production of traditional calcium–based binders, lime, and cement.

The main purpose of this study will be the generation of a precise and effective machine learning model for the development and utilization of supplementary cementitious materials and binders; calcined shale, and palm oil fuel ash, in order to meet the demand for green materials to reduce the use of calcium–based binders in soil stabilization methods. In addition, this green material aids to reduce CO_2 emissions and is particularly beneficial for subterranean construction owing to its capacity to prevent foundation damage caused by sulphate affect. That meets the goals of the Malaysian Economic Planning Unit for sustainable developments.

The purpose of this work is to predict, develop and validate a new machine learning model for a revolutionary soil mix matrix of Kuala Langat treated marine clay that has not yet been defined in the geotechnical engineering field. Once this material's aptitude for enhancing soil strength and load-bearing capacity is established. By predicting and controlling settlement and shear strength, it may be used in civil engineering applications such as soil stabilization, foundation and tunnel building, and road construction, besides future research.

1.6 Study Limitations

This investigation was constrained to the treatment of marine clay specimens obtained from the Kuala Langat area. It is essential to acknowledge that each marine clay sample exhibits distinctive properties, thereby necessitating individualized examination irrespective of the overarching behavioral traits inherent to marine clay as a category. Given the experimental nature of this study, constraints were imposed on both the quantity of specimens and the volume of experimental data utilized for training the machine learning models aimed at predicting outcomes.

The finite element modelling aspect of the research was executed through the utilization of the PLAXIS 2D software. It is imperative to note that the finite element mesh, a critical component of the modelling process, was automatically generated. Despite the auto–mesh refining near special elements, it is limited to specify certain points to study in the models, such as points under the middle of the structures.

For the machine learning, the study was limited to the used algorithms which are (1) Linear regression (LR), (2) Polynomial regression (PR) (3) Random Forest regression (RF), (4) Multilayer regression MLR (ANN) (5) Gradient boost tree regression (GBoost), and (6) eXtreme Gradient Boost (xGBoost) for the manual feature selection, and hybrid feature selection using (1) GBoost, (2) RF, and (3) XGBoost by the backword, froward and Genetic algorithm (GA). Where in future studies different algorithms could be used to compare with the used algorithms and models accuracy in this research and to cover this gap.

1.7 Thesis Structure

There are 5 chapters in this thesis. According to the Thesis Preparation April 2009, School of Graduate Studies, Universiti Putra Malaysia guidelines, chapters should be organised in accordance with style 2. The introduction is designated as Chapter 1, whereas the literature review is designated as Chapter 2. Chapters deal with the study's research are Chapters 3, and 4 which presents the methodology, findings, summary, whereas Chapter 5 represents conclusions, and suggestions. Introduction, goals, study scope, and organisation are all included in Chapter 1. While Chapter 2 contains earlier studies and background, the topic in that chapter will focus on marine clays properties, green materials characteristics, soil treatment techniques, treated soil characteristics, and data analysis and prediction by machine learning algorithms.

Chapter 3 aimed to drive the methodology of marine clays treatment using green materials and application of machine learning algorithms for data analysis and prediction. Also, it aimed to the methodology of improvement of data prediction for long–term behaviour of marine clays treatment using green materials for overall soil stabilisation. Chapter 4 presents the results of marine clays treatment using green materials, and the results of machine learning algorithms application for data analysis and prediction of marine clays long–term behaviour after treatment using green materials. Finally, Chapter 5 highlights the conclusions from this research and represent the recommendations as per this research for future studies and further research.

CHAPTER 2

LITERATURE REVIEW

2.1 Introduction

Problematic soil is identified as the soil that is not capable to sustain applied loads with compliance of significant deformations. Accordingly, the safety and the efficiency of the structures constructed above it are questionable. Marine clay is one of the soils identified as a problematic soil as per the perspectives of geotechnical engineering. The weakness is caused by a high natural water content and the lack of or low shear resistance values. Additionally, weak soils, such as soft marine clay, can be found in riverbanks and coastal areas at large depths, making it impossible or extremely expensive to rebuild or install a suitable foundation system for buildings.

Marine clay is very sensitive to application of loads resulting with significant deformations. Thus, the prediction of the soil deformations and pore water pressure during loading is challenging to be achieved (Balasubramaniam et al., 2010; Bo et al., 2019; Saad et al., 2021). As a consequence, marine clay becomes a problematic soil, affecting the safety, stability, and sustainability of existing and new structures, as well as resulting in ambiguous behaviour (Bo et al., 2019; Saad et al., 2021; Shen et al., 2014).

Marine clays are typically found in coastal regions, lakeshores, and riverbanks, which reflects a significant high natural water content. Accordingly, significant big values of void ratio are reflected in a crucially high level of soil compressibility, which in turn causes unstable deformations when subjected to nonuniform loads. Furthermore, the bulk density in zones of the high groundwater table is larger than its dry density. Therefore, it will have an effect on the stresses that are placed on the soil utilities, especially those that are exposed to uplift force and recurrent loading and unloading. In this hypothetical situation, the utilities and the soil collapse either together or separately, depending on which occurs first. Marine clay found near the ocean tend to have these characteristics, and the Marine clay found in Southeast Asia follow the same trend (Chompoorat et al., 2022; Gao et al., 2020; Gouw, 2020; Hassan et al., 2019; Md Zain et al., 2020; Sapar et al., 2020; Zainorabidin et al., 2019).

Soil treatment using calcium–based binders is a popular solution for weak soils such as marine clay. However, the environmental challenges such as climate change, CO_2 emissions and waste management presses for using green or/and green materials instead of the traditional calcium–based binders such as cement and lime (Al–Bared et al., 2018; Emmanuel et al., 2019; Kee, 2016; Latifi et al., 2016). Therefore, research on using alternative materials is required to be covered. Furthermore, the method of controlling the amounts of green materials usage should be explored in engineering wise for resulting an efficient soil treatment (Aamir et al., 2019; Kannan et al., 2021;

Lal et al., 2018; Mohajerani et al., 2019; Naveed et al., 2020; Rezazadeh Eidgahee et al., 2020; Shah et al., 2020; Shariatmadari et al., 2021).

Problematic soils, exemplified by marine clay, pose significant challenges in geotechnical engineering due to their inability to sustain applied loads while experiencing substantial deformations. The high natural water content and low shear resistance values inherent in marine clay contribute to its weakness, making it a troublesome substrate for construction. Structures built on such soils face safety, stability, and sustainability concerns, often resulting in ambiguous behavior and potential structural failure. Marine clays, prevalent in coastal regions, exhibit notable compressibility due to their high void ratios, leading to unstable deformations under nonuniform loads. Moreover, areas with high groundwater tables exacerbate soil stress, particularly impacting soil utilities exposed to uplift forces and recurrent loading and unloading cycles. Despite the common use of calcium–based binders for soil treatment, environmental imperatives, including climate change and waste management, necessitate the exploration of green materials as alternatives. However, effective strategies for controlling the use of these materials in soil treatment processes remain a critical gap in engineering knowledge. Addressing this gap is essential for developing efficient and sustainable solutions to mitigate the challenges posed by problematic soils like marine clay.

2.2 Engineering Properties of Southeast Asian Marine Clay

Soil formation in South–East Asia has developed along a predetermined range of physical and mechanical properties as a result of the region's consistent climate and consistent presence of water. This environment created the weak soil formation known as marine clay covers significant portion of Southeast Asia region. In general, South–East Asian cities are growing at a rapid rate due to the construction and improvement of infrastructure. According to population, tourism and various industries growth, there is a high demand for construction in this region. However, the cities in this area are situated on soft marine clay, which poses significant challenges for building and infrastructure construction. Moreover, the complicated geotechnical solutions required for new construction projects make it difficult to propose new initiatives in the city. Soil formation in western region of Peninsular Malaysia is characterised by soft peats, organic soils, marine clay, and silt as shown in Figure 2.1 (Tate et al., 2008).

The development of that region was significantly hampered by the presence of marine clay soils. During construction and operation time, significant soil deformations can be seen occurred. Because of the diversity in the distribution of the loads, the deformations are severe and non–uniform. These problems can be seen in cities such as Seri Iskandar (Yusof et al., 2018), Muar (Baral et al., 2019), Alor Pudak (Rendana et al., 2021), Malacca (Saad et al., 2021), Johor (Al–Bared et al., 2018), Batu Pahat (Tajudin et al., 2016), Serdang (Tate et al., 2008), and others (Anggraini et al., 2015; Azhar et al., 2018; Lat et al., 2018).

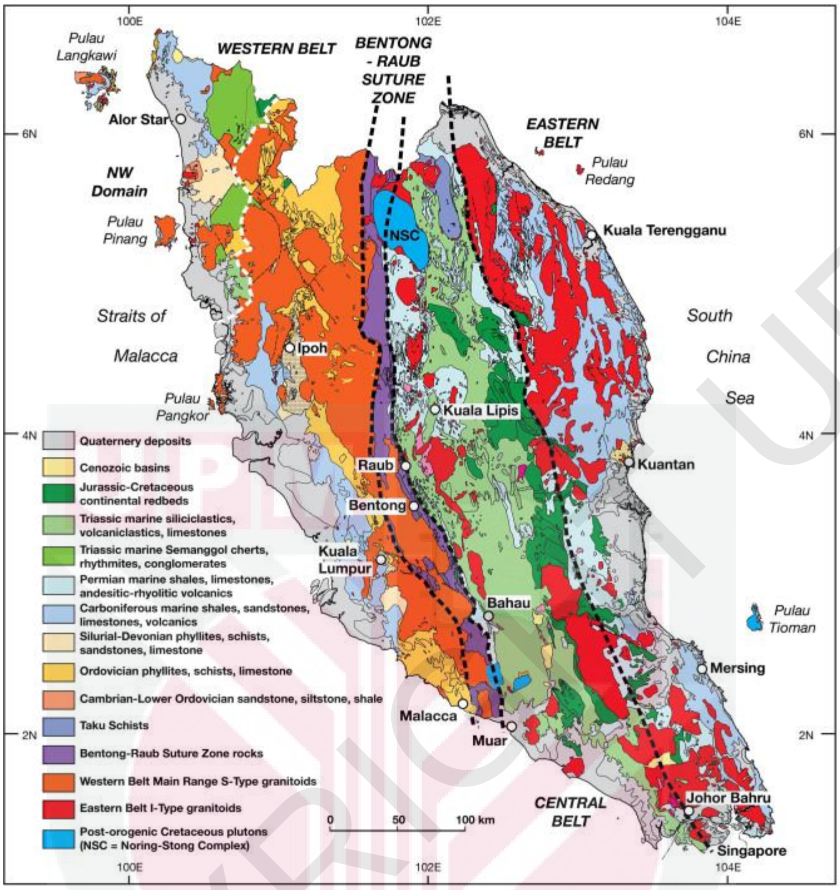

Figure 2.1: Geological map of Malaysian Peninsular (Tate et al., 2008)

For instance, some major disaster occurred in Malaysia such as large deformations due to landslides in Serdang, Selangor, where retaining walls twice within five years (Aziz, 2022; Faris, 2022) and Cameron Highland, Perak (Alagesh, 2021). The last landslide shows that soil replacement or soil treatment were not applied during construction process, eventhough the site is known to be sitted on marine clay. As a result, differential settlements occurred and led to the collapse of road besides riverbank, as was the case in Serdang landslides. In addition, the weakness of the natural soil in the area around Serdang area makes it impossible or/and significantly expensive to make soil replacement using traditional soil filling materials. Hence new treatment method for existing soil is essential to overcome or reduce such disasters. New green treatment material mixture is believed to be useful to strengthen the existing soil. It is also believed to be efficient, eco–friendly and low–cost without any side impact to the environment. In addition, settlements which costed 3.6 billion MYR in 2014 occurred at KLIA2 terminal Kuala Lumpur International Airport. The significant deformations were detected in the runway due to uplift and subsidence presumably in parallel with the loads of landing and taking off aircrafts due to difference in structure foundations and fill work constructed above marine clay (Marshall et al., 2018) as shown in Figure 2.2. That critically influences the economy, society, and the environment.

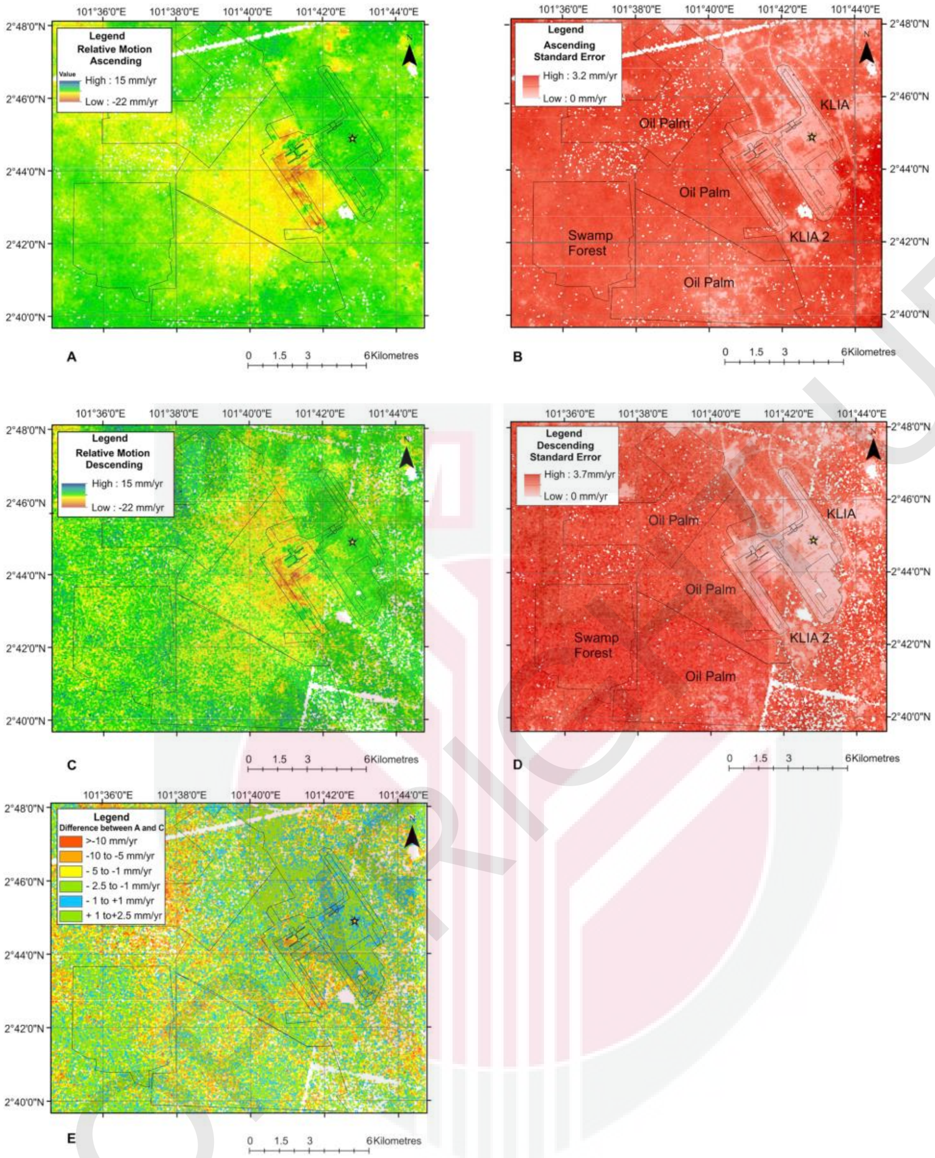

Figure 2.1: InSAR map shows at KLIA; (A) Ascending vertical ground motion, (B) Ascending Standard Error, (C) Descending vertical ground motion, (D) Descending Standard Error, and (E) Difference between Ascending and Descending tracks for the three years (Marshall et al., 2018)

Previous studies investigated marine clay samples from South–East Asia (Afnan Ahmad et al., 2021; Bergado et al., 2022; Chompoorat et al., 2022; Hoy et al., 2022; Moe et al., 2021; Ngo et al., 2021; X Wang, 2021; Yu et al., 2021) and examined their behaviour and engineering characteristics physically and mechanically. It has been observed that there have been significant changes in geotechnical characteristics in the same area, if not in the same borehole. Different conditions of partial deposition throughout the process of soil layer growth are the reason of this variation.

In spite of these variances, results demonstrated that there is a similar tendency in the behaviour of the marine clay; a high void ratio e_o. In addition, certain parameters, such as the natural water content w_n, the liquid limit w_{LL}, the plastic limit w_{PL}, the plasticity index PI, the coefficient of consolidation C_v, the coefficient of compressibility C_c, the coefficient of reloading C_r, small values of permeability k, specific gravity G_s, and bulk density γ_{bulk}, all exhibit the same general trend. The behaviour of the marine clay was very weak to resist loading specially for long term of loading, where the deformation was always significant and significantly variable (Saad et al., 2021). In addition, the strength was significant weak due to the high content of water that exceeds or equals to the liquid limit tending to get the instability of marine clay. Although, there are several conclusions that do not match up with general characteristics of some Malaysian marine clay (Amuda et al., 2019; Dehghanbanadaki et al., 2019; Kamaruidzaman et al., 2019; Noridah Mohamad et al., 2019; Mohamed Jais et al., 2019; Mohd Zambri et al., 2018; Rahmat et al., 2018; Razali et al., 2018; Sapar et al., 2020; Zainorabidin et al., 2019), marine clay in general is challenging soil that traditional treatment or/and special foundation systems are expensive and non–friendly to the environment (Saad et al., 2021).

2.2.1 Physical Properties of Southeast Asian Marine Clay

The detected value of liquid limit, w_{LL} was not less than an average of 60%; although the plastic limit, w_{PL} was with an average of below 30%. Correspondingly, the natural water content, w_n was within the liquid limit range but sometimes higher such as reported by Hassan et al. (2019), Jang (2018), Lam et al. (2018), Ngo et al. (Ngo et al., 2020), Wang et al. (H Wang et al., 2021), and Yu et al. (2021). The Atterberg limits of the marine clay fall with in the range between 10 – 200% and at average of 74.15% for natural water content, whereas a range between 30 – 128% and average 75.3% for liquid limit, while a range between 15 – 68% and average 35% for plastic limit, and plasticity index is between 2 – 55% and its average is 30%. The findings are based on the data that were collected and can be found as summarised in Table 2.1. Accordingly, the high water content controls marine clays to be loaded over the liquid and plastic limits, which results in crucial unstable behaviour that occurs as tremendous deformations and differential settlements due to loading and consolidation time (Marshall et al., 2018; Poulos et al., 1989).

Specific gravity G_s was ranging between 2.62 ~ 2.86 and averaged at 2.74 as shown in Table 2.2. Additionally, the bulk density, γ_{bulk} varied from 12.00 to 19.60 kN/m^3 with an average of 15.80 kN/m^3. Marine clays, regardless of their specific gravities, have low dry densities based on data conducted and water content by previous research (Dehghanbanadaki et al., 2019; Kamaruidzaman et al., 2019; Ngo et al., 2020, 2021; Saad et al., 2021). That is a reflect for the high void ratio e of the marine clay regardless the mineralogy formation and directly indicates the limited strength that make loading resistance a critical challenge.

Table 2.1: Previous research conducted values for natural water content and Atterberg limits

City	Country	w_n (%)	w_{LL} (%)	w_{PL} (%)	PI (%)	Author
Jakarta	Indonesia	–	116~122	–	–	(Adi Tirta et al., 2018)
Pontain	Malaysia	495	260	–	–	(Dehghanbanadaki et al., 2019)
Pontain	Malaysia	533	189	–	–	(Kamaruidzaman et al., 2019)
Parit Nipah	Malaysia	635	252	–	–	(Zainorabidin et al., 2019)
Parit Nipah	Malaysia	593	243	–	–	(Mohamad et al., 2020)
Lumadan	Malaysia	455	211	–	–	(Mohamad et al., 2020)
Parit Nipah	Malaysia	605	203	–	–	(Razali et al., 2018)
Perlis	Malaysia	327	–	–	–	(Mohd Zambri et al., 2018)
Mukah	Malaysia	130	128.85	–	–	(Hassan et al., 2019)
Klang	Malaysia	606.8	–	–	–	(Md Zain et al., 2020)
Klang	Malaysia	599.2	–	–	–	(Mohamed Jais et al., 2019)
Seri Iskandar	Malaysia	141.5	–	–	–	(Yusof et al., 2018)
Klias, Sabah	Malaysia	673.99	–	–	–	(Sapar et al., 2020)
Lumada, Sabah	Malaysia	630.35	–	–	–	(Sapar et al., 2020)
Kampung Endap	Malaysia	378~620	540~602	–	–	(Amuda et al., 2019)
Kampung Endap	Malaysia	540	–	–	–	(Amuda et al., 2019)
Kampung Meranek	Malaysia	1210	–	–	–	(Rahmi et al., 2018)
Muar Clay	Malaysia	15~110	50~112	30~68	18~40	(Baral et al., 2019)
–	Australia	–	55.8	27.4	28.4	(Basack et al., 2018)
Bangkok	Thailand	40~155	–	–	–	(Bergado et al., 2022)
Bangkok	Thailand	62.24	77.8	35.78	42.02	(Chompoorat et al., 2022)
Lvliang	China	15.2	27.4	15.1	12.3	(Gao et al., 2020)
Bandung	Indonesia	100~200	–	–	–	(Gouw, 2020)

Table 2.1: Continued

City	Country	w_n (%)	w_{LL} (%)	w_{PL} (%)	PI (%)	Author
Nava Nakorn	Thailand	40~155	–	–	–	(Hoy et al., 2022)
–	Taiwan				2~23	(Hsieh et al., 2018)
Haiphong	Vietnam	30~58	32~56	18~28	5~29	(Jang, 2018)
Shanghai	China	41.89~42.25	36.6~45.5	19.66~24.15	16.94~21.35	(Khalid et al., 2019)
–	Singapore	92	88	36	52	(Lam et al., 2018)
Kallang	Singapore	65~80	70~85	24~28	45~55	(Lam et al., 2020)
Changi East	Singapore	70~88	80~95	20~28	–	(Moe et al., 2021)
Changi East	Singapore	40~60	65~90	20~30	–	(Moe et al., 2021)
–	Singapore	–	73	39	34	(Ng et al., 2020)
Mae Moh	Thailand	114~180	57	26	31	(Ngo et al., 2020)
Mae Moh	Thailand	163	57	26	31	(Ngo et al., 2021)
Cai Mep	Vietnam	53~123	57~128	–	–	(Wang et al., 2021)
Hiep Phuoc	Vietnam	53~93	56~65	–	–	(Wang et al., 2021)
Hai Phong	Vietnam	30~71	45~77	–	–	(Wang et al., 2021)
Ca Mau	Vietnam	58~80	62~90	–	–	(Wang et al., 2021)
Alor Pudak	Malaysia	48.02	–	–	–	(Rendana et al., 2021)
–	Singapore	70	88	38	50	(Wang et al., 2021)
–	Singapore	10~91	30~97	18~31	–	(Wang et al., 2021)
Bukit Tunku	Malaysia	–	50.1	21.8	28.3	(Yong et al., 2019)
–	Singapore	50~70	59	25	34	(Yu et al., 2021)

Table 2.2: Previous research conducted values for bulk soil density and specific gravity

City	Country	γ_{bulk} (kN/m^3)	γ_{dry} (kN/m^3)	G_s	Author
Jakarta	Indonesia	13.6–14	–	–	(Adi Tirta et al., 2018)
Pontain	Malaysia	–	10.19	1.38	(Dehghanbanadaki et al., 2019)
Pontain	Malaysia	–	9.56	1.66	(Kamaruidzaman et al., 2019)
Parit Nipah	Malaysia	–	10.4	1.34	(Zainorabidin et al., 2019)
Parit Nipah	Malaysia			1.3	(Mohamad et al., 2020)
Lumadan	Malaysia			1.37	(Mohamad et al., 2020)
Mukah	Malaysia			1.6	(Hassan et al., 2019)
Klang	Malaysia			1.57	(Md Zain et al., 2020)
Klang	Malaysia			1.38	(Mohamed Jais et al., 2019)
Seri Iskandar	Malaysia			1.45	(Yusof et al., 2018)
Klias, Sabah	Malaysia			1.22	(Sapar et al., 2020)
Lumada, Sabah	Malaysia			1.57	(Sapar et al., 2020)
Kampung Endap	Malaysia	–	–	1.69–1.71	(Amuda et al., 2019)
Kampung Endap	Malaysia	–	–	1.7	(Amuda et al., 2019)
Kampung Meranek	Malaysia	–	–	1.408	(Rahmi et al., 2018)
Muar Clay	Malaysia	12~18	–	2.74~2.86	(Baral et al., 2019)
–	Australia	18	–	2.68	(Basack et al., 2018)
Bangkok	Thailand	13.2~16.6	–	–	(Bergado et al., 2022)
Bangkok	Thailand	16.81	–	2.64	(Chompoorat et al., 2022)

Table 2.2: Continued

City	Country	γ_{bulk} (kN/m^3)	γ_{dry} (kN/m^3)	G_s	Author
Lvliang	China	16.7	14.5	2.74	(Gao et al., 2020)
Nava Nakorn	Thailand	17	–	–	(Hoy et al., 2022)
–	Taiwan	18~18.74	–	–	(Hsieh et al., 2018)
Haiphong	Vietnam	16~17.8	–	2.62~2.7	(Jang, 2018)
Shanghai	China	18.1~18.4	–	2.70~2.72	(Khalid et al., 2019)
–	Singapore	15.5	–	2.65	(Lam et al., 2018)
Shanghai	China	16~18.8	–	–	(Ying Liu et al., 2019)
Changi East	Singapore	1.56~16.8	–	–	(Moe et al., 2021)
Changi East	Singapore	16.5~17	–	–	(Moe et al., 2021)
–	Singapore			2.7	(Ng et al., 2020)
Mae Moh	Thailand	18	16	2.5	(Ngo et al., 2020)
Mae Moh	Thailand	–	13	2.5	(Ngo et al., 2021)
Semarang	Indonesia	15.0–18.3	–	–	(Sarah et al., 2018)
Jakarta	Indonesia	15.0–17.6	–	–	(Sarah et al., 2018)
Surabaya	Indonesia	14.9–19.0	–	–	(Sarah et al., 2018)
–	Singapore	15–16	–	–	(Wang et al., 2021)
–	Singapore	14.2–19.6	–	2.60–2.76	(Wang et al., 2021)

2.2.2 Mechanical Properties of Southeast Asian Marine Clay

Table 2.3 shows the results of a comparison of the various marine clay values collected for compression indices. Consolidation coefficient C_v varied from 0.20 to 4.0 m^2/year with average 1.90 m^2/year, compression index C_c varied from 0.08 to 7.48 with an average of 3.70, the swelling index varied from C_r 0.020 to 0.4 with an average of 0.19, and yield (preconsolidation) stress P_C' ranged from 26.0 to 318 with an average of 172 kPa, as conducted by (Kamaruidzaman et al., 2019; Ngo et al., 2021; Nguyen et al., 2020; Sarah et al., 2018; Wang et al., 2021; Zainorabidin et al., 2019) This demonstrates the limited permeability and great compressibility of marine clay soils regardless the mineralogy formation and directly indicates the limited strength that make loading resistance a critical challenge, which makes the traditional soil reinforcement questionable (Saad et al., 2021).

Table 2.3: Previous research conducted values for compression index, swelling index and preconsolidation stress

City	Country	P_C' (kPa)	C_c	C_r	C_α	C_v (m^2/yr)	Author
Jakarta	Indonesia	–	5	0.25~0.26	–	0.63~2.52	(Adi Tirta et al., 2018)
Pontain	Malaysia	–	3	0.01028	0.0608	–	(Dehghanbanadaki et al., 2019)
Pontain	Malaysia	–	3.76	–	–	–	(Kamaruidzaman et al., 2019)
Parit Nipah	Malaysia	–	1.48	–	–	–	(Zainorabidin et al., 2019)
Kampung Endap	Malaysia	–	5.45	0.08073	0.24	–	(Amuda et al., 2019)
Muar Clay	Malaysia	46~67	1.248~1.440	0.078~0.234	–	–	(Baral et al., 2019)
Bangkok	Thailand	–	1.5~3.2	0.2~0.4	–	–	(Bergado et al., 2022)
Nava Nakorn	Thailand	–	0.1	0.02	–	–	(Hoy et al., 2022)
–	Taiwan	–	0.3~0.4	0.03~0.04	–	–	(Hsieh et al., 2018)
Haiphong	Vietnam	30~80	0.08~0.62	–	–	–	(Jang, 2018)
Shanghai	China	48~50	0.27~0.325	–	–	–	(Khalid et al., 2019)
Changi East	Singapore	50~160	–	–	–	0.47~0.6	(Moe et al., 2021)
Changi East	Singapore	280~460	–	–	–	0.8~1.5	(Moe et al., 2021)
Mae Moh	Thailand	–	1.1	–	–	–	(Ngo et al., 2021)
Cai Mep	Vietnam	29~300	0.85~1.80	0.20~0.40	–	–	(Nguyen et al., 2020)
Hiep Phuoc	Vietnam	65~264	0.65~2.70	0.12~0.3	–	–	(Nguyen et al., 2020)
Hai Phong	Vietnam	53~318	0.48~0.91	0.12~0.30	–	–	(Nguyen et al., 2020)
Ca Mau	Vietnam	26~125	0.42~1.10	0.050~0.075	–	–	(Nguyen et al., 2020)
Semarang	Indonesia	–	0.2~0.6	–	–	0.2~1.1	(Sarah et al., 2018)
Jakarta	Indonesia	–	0.2~ 0.5	–	–	3.0~4.0	(Sarah et al., 2018)
Surabaya	Indonesia	–	–	–	–	1.8~ 2.0	(Sarah et al., 2018)
–	Singapore	–	0.7~1.3	–	–	–	(Wang et al., 2021)
–	Singapore	–	0.20~1.50	0.02~0.20	–	–	(Wang et al., 2021)

2.2.3 Mineralogy of Southeast Asian Marine Clay

Marine clay found along the coasts of South–East Asia composed of smectite, vermiculite, kaolinite, halloysite, and mica (Abbas et al., 2020; Afnan Ahmad et al., 2021; Chompoorat et al., 2022; Chua et al., 2020; Estabragh et al., 2022; Nayak et al., 2021; Rendana et al., 2021; Tyagi et al., 2019; Yong et al., 2019). The coastal clay in different regions has different mineral makeups, which causes it to behave differently. The high–water content of coastal clays is clarified by the presence of smectite, which is a common and sensitive mineral. It was challenging to develop construct structures of the immersed tunnel of the Hong Kong–Zhuhai–Macao Bridge (HZMB) (Hongtao He et al., 2018) and the Shanghai metro station (Guolin Xu et al., 2018) or to maintain those structures once they have failed, regardless of the minerals that are responsible for forming the marine clay (Shen et al., 2014).

2.3 Methods and Challenges of Soil Treatment

2.3.1 Method of Soil Treatment

Due to the impacts of soil consolidation and yielding under loading, it is challenging to consistently provide an accurate calculation of settlements and deformations. Additionally, even within the same location, the marine clay's geotechnical properties varied, making each project an unique situation itself and making it more difficult to predict how it would behave under stress. As a result, the following treatment strategies are suggested based on the kind of soil and its behaviour:

1. Physically: Vacuum preloading (Zhu et al., 2018), heat treatment (Abuel–Naga et al., 2009), and EK stabilisation (Azhar et al., 2018; Eng Choy Lee, 2015)

2. Chemically (that is, using chemical additives): cement mixing (Anggraini et al., 2017; Tran–Nguyen et al., 2014), halloysite nanotubes (Emmanuel et al., 2019), nanomaterial additions (Anggraini et al., 2016), Biomass Silica (Marto et al., 2014), and cementation process utilising various chemical materials infusion (Yoobanpot et al., 2017)

3. Biomineralization employing bacteria and fungi (Amini Kiasari et al., 2018; Chittoori et al., 2018; DeJong et al., 2006; Fiore et al., 2011; Whiffin et al., 2007) is a biological (i.e., microorganism–based) method (Kavazanjian et al., 2017; Pasquale et al., 2019)

4. Combination of two or more of the mentioned procedures previously: mechanical mixing with chemical additives (i.e., material removal or addition): using recycled blended tiles (RBT) (Al–Bared, Marto, Harahap, et al., 2018; Al–Bared et al., 2019), treated coir fibres (Anggraini et al., 2015; Ayininuola et al., 2016), adding nanomaterials (Gao et al., 2020; Haeri et al., 2021; Jafari et al., 2021; Yong et al., 2019), electroosmotic chemical treatment utilising $CaCl_2$ solution (Lei Zhang et al., 2018), and electroosmotic chemical

treatment (EOC) electroosmotic treatment with heating (Xue et al., 2017), compacted piles of sand (Baral et al., 2019; Hongtao He et al., 2018), geopolymers mixing (Teerawattanasuk et al., 2019; Yaghoubi et al., 2019), biocementation via mechanical pressure (Van Paassen et al., 2009, 2010), recycled cured rubber treating (Zhongnian Yang et al., 2020) and biomineralization using bacteria under the EK method (Keykha et al., 2014, 2015; Saad et al., 2021).

The advantages and disadvantages of each treatment method have been summarised in Table 2.4. Depending on the scope of the project, the needed level of application, the budget, the available time, and the environmental constraints, each is constrained by certain limitations that may fit the case study. Nevertheless, each technique improves the qualities of the treated soil, leading to a variety of results while concentrating on various influencing elements. In this research the focus will be on the marine clay strengthening alternative cementation materials and binders.

Table 2.4: Different methods of marine clay treatment

Treatment method	Advantages	Disadvantages	Source
Electrokinetic stabilization	▪ Strength enhanced significantly specially in the vicinity of the cathode ▪ Strength enhances via electroosmosis process through increasing soil pore water pressure	▪ Limited ranges for curing ▪ Energy consuming as zones area increases ▪ More investigation required as it is a treatment method ▪ Disturbance occurs by the force migration due to electric potential effect in pH, mineralogy, and minerals inside soil texture	(Azhar et al., 2018; Micic et al., 2001)
Nanomaterial addition	▪ Significant reduction in Atterberg limits ▪ Compressive strength enhancement	▪ Unapplicable for massive treatment as the limitation of mixing process ▪ Hard to control amounts and sizes of nanomaterial additions for required strength	(Jafari et al., 2021; Majeed et al., 2012; Yong et al., 2019)
Electroosmotic Chemical Treatment Using $CaCl_2$ Solution	▪ Rapid and efficient dewatering ▪ Efficient in improvement of bearing capacity	▪ Energy consuming as zones area increases, especially with the increase of $CaCl_2$ solution concentration ▪ For more efficient dewatering more $CaCl_2$ consumed ▪ Disturbance occurs by the force migration due to electric potential effect in pH, mineralogy, and minerals inside soil texture	(Lei Zhang et al., 2018)
Vacuum preloading	▪ Ten times improvement in bearing capacity at least ▪ Three times reduction in water content	▪ Consumes time for getting the targeted strength; a year is required for rising strength from 4 kPa to 50 kPa	(Bergado et al., 2022; Zhu et al., 2018)
Cement mixing	▪ Increment of undrained consolidated strength with increment of cement content amount	▪ Underestimated stiffness using external strain measurements	(Bouazza et al., 2004)

Table 2.4: Continued

Treatment method	Advantages	Disadvantages	Source
Thermal treatment	▪ Enhancement in soil's consolidation ▪ In a period of 105 days consolidation can be completed	▪ Waste energy ▪ Limited applications as per various surrounding conditions at each location; temperature, moisture content, soil conductivity, etc.	(Abuel–Naga et al., 2009)
RBT (recycled blended tiles)	▪ Significant reduction in Atterberg limits ▪ Significantly increment in MMD and reduction in OMC	▪ Unapplicable for massive treatment as the limitation of mixing process	(Al–Bared et al., 2018)
Treated coir fibres	▪ Enhances strength and mechanical behaviour, depending on fibre content and curing time ▪ Significant increment in tensile strength by fibre inclusion	▪ Unapplicable for massive treatment as the limitation of mixing process ▪ Uncertainties in shear strength results through uncertainties in the preparation of the mix	(Anggraini et al., 2015; Ayininuola et al., 2016)
Sand compacted piles	▪ Significant improvement in soil strength wit settlements reduction ▪ Major settlements occur during the construction period	▪ Upheaval soil obviously removed with massive ratio of replaced area during installation	(Baral et al., 2019; Hongtao He et al., 2018),
Biomass Silica	▪ Decrement in liquid limit via Biomass Silica increment ▪ Biomass Silica is stabilizing agent	▪ Plastic limits increment with Biomass Silica increment	(Marto et al., 2014)
Cement mixing	▪ Increment of undrained consolidated strength with increment of cement content amount	▪ Underestimated stiffness using external strain measurements	(Bouazza et al., 2004)

2.3.2 Stabilized Soil Strength Controlling Factors

There are some factors the affect on the treatment and consequently the soil strength after treatment. These factors are; organic matter content in the soil, presence of sulphates and their content, compaction rate, moisture content, and temperature required for curing treating material (Afrin, 2017), and factors are specified in the following in detail as shown in Table 5.

Table 2.5: Factors Controlling Stabilized Soil Strength

Factor	Influence on Stabilized Soil Strength	Source
Organic matters	▪ High organic content in topsoil layers may result in low pH values, hindering hydration and complicating compaction.	(Afrin, 2017)
Sulfate	▪ Calcium–based stabilizers react with excess moisture, producing expansive compounds. ▪ Adequate water is crucial for the reaction to commence.	(Afrin, 2017; Hicks, 2002; Sherwood, 1993)
Sulphides	▪ Oxidation of iron pyrites generates sulfuric acid, leading to gypsum formation. ▪ Hydrated sulfate, when excessive, can weaken the stabilized material.	(Al–Tabbaa et al., 2006; Sherwood, 1993)
Compaction	▪ Stabilized mixtures exhibit lower maximum dry density than unstabilized soil. ▪ Optimal moisture content increases with higher binder concentrations.	(Sherwood, 1993)
Moisture Content	▪ Adequate moisture is essential for effective compaction and hydration. ▪ Insufficient moisture can impede the hydration process and weaken the final strength.	(Afrin, 2017; Hebib et al., 2017; Sherwood, 1993)
Temperature	▪ Temperature fluctuations impact pozzolanic reactions. ▪ Lower temperatures slow down these interactions, potentially reducing the strength of the stabilized mass.	(Sherwood, 1993)

2.4 Green and Non–Green Treatment Materials

Due to their impulsive deformation and shriveling characteristics, marine clay is considered to be the most precarious and vulnerable in the global building industry. If structures are to be constructed in wet environments, the consolidation phenomenon has an adverse effect on their performance. Due to their high moisture content, soil particles lose contact under loading and become loose, which causes soil shear failure. For structures erected on expansive soil as depicted in Figure 2.3, innumerable building damages have already been seen during unexpected soil deformation and shrinkage (Parthiban et al., 2022).

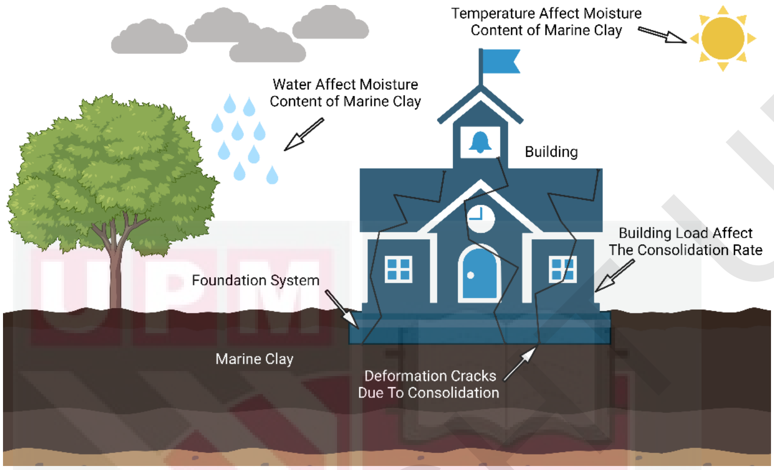

Figure 2.3: Structural failure as a result of the marine clay soil properties

2.4.1 Cement Impact on Environment As A Traditional Soil Stabilizer

Cement is the most consumed building material in the world after water, where the countries of production and the construction industries involved in are shown in Figure 2.4. It is also the most traditional strengthening material used in soil treatment. However, its production had caused an increasing climate change worldwide (Farooq et al., 2021).

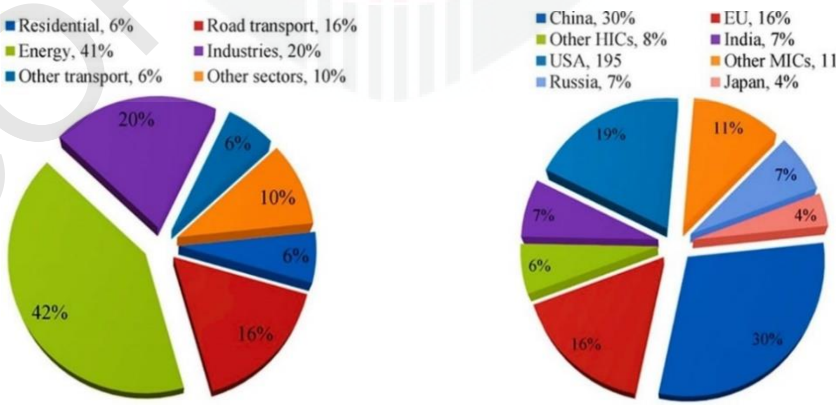

Figure 2.4: Emissions of CO_2 as per (a) involved industry and as per (b) countries (Farooq et al., 2021)

Construction industries use 2.6 billion tonnes of cement (Chu et al., 2021) and could increase by 25% in the upcoming ten years (Aleem et al., 2012) where the greenhouse impact is strongly influenced by concrete industry. Cement manufacture uses 4 Giga Joule of energy and emits an equivalent amount of CO_2 into the atmosphere, which accounts for 30% of all CO_2 emissions worldwide as per the environmental perceptive (Li et al., 2019). The cement industry released about 5% of the global CO_2 emissions (Dao, Trinh, et al., 2019; Hendriks et al., 1999; Mo et al., 2016), where Figure 2.5 shows the emissions of CO_2 due to cement. Additionally, limestone is an essential to the production of cement, and a severe shortage of it may develop over the course of the next five years (Sumanth Kumar et al., 2020). As a result of the burning of raw materials, fossils, and minerals in the kiln chamber, CO_2 emissions are produced, which have a detrimental impact on the environment (Farooq et al., 2021; Hendriks et al., 1999), where an overview of CO_2 emissions for cement in grade 40 concrete mixtures (Turner et al., 2013). Accordingly, utilization of alternative materials such as waste industrial materials. Byproduct materials are essential to reduce the cement industry severe impacts to environment and at the same time helps to recycle those industrial waste materials.

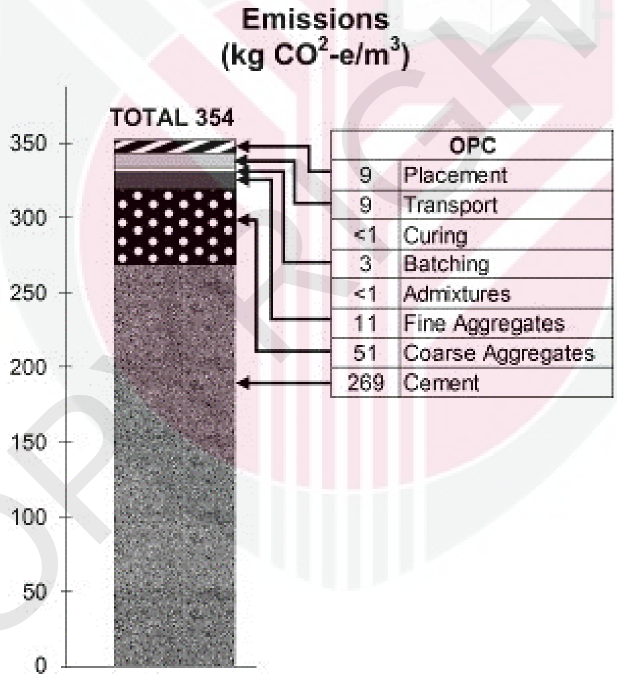

Figure 2.5: An overview of CO_2 –e/m^3 emission because of creating grade 40 concrete mixture showing that cement has the maximum emission of CO_2 (Turner et al., 2013)

2.4.2 Palm Oil Fly Ash As A Soil Stabilizer

In coal–burning power plants, fly ash is created during the energy production process (Woolard et al., 2003). Fly ash is collected using an electrostatic or mechanical precipitator (Aprianti S, 2017; Ibrahim et al., 2016; Muhammad Nazrin Akmal et al., 2017; Rafieizonooz et al., 2016). Although landfilling is a common method of disposing of fly ash, rises disposal costs and significant environmental concerns regarding the leaching of latent toxic substances from the ash to soil, surface water, and groundwater (Carlson et al., 1993; Davidson et al., 1993; Jianmin Wang et al., 2006) had caused utilisation of fly ash to be an appealing alternative to direct landfilling (Adeboje et al., 2021; Cao et al., 2007).

As China has the most electricity generation plants that are consuming coal as the main fuel, China was expected to produce about 200 million ton of fly ash in 2010 (Jianmin Wang et al., 2006) while around 375 million tons of fly ash are produced annually by the thermal coal sector globally which simply deposited into landfills (Chu et al., 2021). Accordingly, that amount of produced fly ash would require a space of 1.33 million square meters to occupy (Jianmin Wang et al., 2006). Additionally, fly ash disposal cost per ton reaches to 40 (Chu et al., 2021). Countries like Japan has successfully reused fly ash by 100% (Yan et al., 2012). However, it is still less than 50% reused in countries such as China (Xia et al., 2000). Therefore, it is important to look into innovative strategies to increase the ratio (Cao et al., 2007). In addition, the fly ash is produced by several industries, which increases the need for recycling this material in geotechnical and construction industries.

Fly ash is a useful commercial component used in the creation of blended cements and concrete mixtures because of its advantageous pozzolanic qualities (Cao et al., 2007). Additionally, a significant amount of fly ash is used as a soil amendment in agriculture and as a raw material in the chemical sector. Palm oil fly ash as solid wastes from different industries, although their content are reach with Si, Al, and/or Ca and used as treating materials and replacement for cement in geotechnical and construction applications (Alabduljabbar et al., 2020; Huseien et al., 2016; Ranjbar et al., 2014; Salih et al., 2015).

A by–product of the combustion process used to obtain palm oil is palm oil fuel ash POFA (Yuriz et al., 2020). For production of 1 kg of palm oil, a 4 kg of palm oil fuel ash were produced (Blessen Skariah Thomas et al., 2017). The pozzolanic characteristics of POFA allow the interaction with calcium hydroxide $Ca(OH)_2$ generated by Portland cement hydration to provide binding qualities (Ishak et al., 2015). Therefore, in an effort to create more sustainable cementitious materials, the use of POFA as a raw material in the production of cement and as a partial replacement for cement in concrete has attracted a lot of attention (Atiş, 2003; Korpa et al., 2012; Ondova et al., 2012). However, the maximum used amounts of POFA is 30% as a cement replacement materials, despite the fact that fly ash production is rising globally (Ishak et al., 2015; Montes–Hernandez et al., 2009). When considering how fly ash interacts with the mixture, soil enhancement involves changes to the texture of soil brought on by cationic exchange and the adhesion of particles caused by the pozzolanic reaction (Khajeh et al., 2020; McCarthy et al., 2012).

2.4.2.1 Physical and Chemical Properties of POFA Used in Soil Stabilisation

The chemical properties of the fly ash identified through the X–ray diffraction XRD test. The results for various sources of fly ash have shown that the major minerals amount was for SiO_2, Al_2O_3, and Fe_2O_3 while there are other minerals CaO, MgO and SO_3 are in significant amounts but less compared to SiO_2, Al_2O_3, and Fe_2O_3. The amount of SiO_2 ranged from 0.68% to 66.39%, Al_2O_3 amount ranged from 1.25 to 55.00%, and Fe_2O_3 amount ranged from 0.37% to 25.50% (Alabduljabbar et al., 2020; Aravind et al., 2021; Ardhira et al., 2022; Bhavani Chowdary et al., 2022; Binal, 2016; Blissett et al., 2012; Borhan et al., 2010; Cao et al., 2007; Chen et al., 2020; Dao, Trinh, et al., 2019; Faridmehr, Nehdi, Nikoo, et al., 2021; Yu–Ke Ke Wang et al., 2016). These minerals control the pozzolanic activity, the zeta potential and the strength of the fly ash products (Kroehong et al., 2011).

The physical properties of fly ash were identified for values of; pH, average particle size, specific gravity G_s, specific surface area SSA, cation exchange capacity CEC, and passing ratio from sieve number 200 as shown in Table 2.6. The pH of fly ash solution ranged from 6.4 to 8.3, average partice size ranged from 0.002 to 0.3 mm, G_s ranged from 1.60 to 3.10, SSA ranged from 0.094 to 18.10 m^2/g, CEC ranged from 1.00 to 17.44, and passing from sieve no. 200 ranged from 67.72% to 98.09% (Aravind et al., 2021; Ardhira et al., 2022; Binal, 2016; John et al., 2021).

Table 2.6: Previous research conducted values for pH, specific gravity, CEC, size of fly ash

City	Country	FA Source	pH	Size (mm)	G_s	SSA (m^2/g)	CEC	Passing No. 200 (%)	Source
Shandong	China	Coal–consuming	6.4						(Cao et al., 2007)
Denizli	Turkey			0.002 – 0.2	2.35	0.334	2.61	67.72	(Binal et al., 2020)
Zonguldak	Turkey			0.002 – 0.3	2.1	0.139	1	80.27	(Binal et al., 2020)
Kütahya	Turkey			0.002 – 0.2	2.1	0.115	2.21	75.39	(Binal et al., 2020)
Bursa	Turkey			0.002 – 0.18	2.4	0.303	5.01	83.02	(Binal et al., 2020)
Manisa	Turkey			0.002 – 0.1	1.98	0.207	17.44	98.09	(Binal et al., 2020)
Kütahya	Turkey			0.002 – 0.18	1.97	0.094	1.4	84.6	(Binal et al., 2020)
					1.6–3.1				Pandian et al. (1998)
		Pulp & Paper Mill		0.001–0.4	2.4–2.8				(Cherian et al., 2019)
Delta Electricity	Australia	coal ash	8.3						(Ebrahimi et al., 2017)
Tuticorin	India	coal ash			2.97	0.382			(John et al., 2021)
Johor	Malaysia				2.2	18.1			(Alabduljabbar et al., 2020; Faridmehr, Nehdi, Huseien, et al., 2021; Lei Wang et al., 2016)
Farakka	India	coal ash				0.3			(Mozumder et al., 2015)
Tamil Nadu	India				2.15				(Ardhira et al., 2022)
Hai Duong	Vietnam			0.005–0.03					(Dao, Ly, et al., 2019; Dao, Trinh, et al., 2019)
Chennai	India				2.13				(Aravind et al., 2021)
	Malaysia	Palm Oil Fly Ash			2.22				(Borhan et al., 2010)
	Malaysia	Palm Oil Fly Ash			2.35				(Mujah et al., 2015)

2.4.2.2 Pozzolanic Activity of POFA Used in Soil Stabilisation

Pozzolanic activity of fly ash affects the mechanical characteristics of both concrete (Zhen Shuang Wang, 2011) and soil (Binal et al., 2020). Chemical analysis to identify the amount of silica or monitoring the heat generated during the hydration process can both be used to quantify the pozzolanic reactivity of fly ash. The amount of silica utilised in the gel formation must be taken into account, though, as the silicate forms a gel at a pH higher than 10 (Bumrongjaroen et al., 2007; Hassett et al., 1997). X–Ray diffraction (XRD) or thermal analysis can be used to determine the consumption of C–H through a pozzolanic reaction of fly ash after 28 days of curing (Kurda et al., 2017). Marly limestones are calcined and then slaked to produce natural hydraulic lime (limestones with clay impurities, which after calcination become reactive silicates and aluminates). Thus, it solidifies through the processes of hydration and carbonation, resulting in the creation of hydraulic compounds and calcite, respectively (Abdalla et al., 2022). In general, adding fly ash decreases dilatation and increases strength. Unconfined compression tests on specimens of raw fly ash–soil with a three percent cement addition have demonstrated that the resulting UCS value is significantly higher than the strength of the corresponding mixes made with only cement (Kaniraj et al., 2001).

A source of geopolymer precursor species and a material that is conducive to polymerization is a pozzolanic substance with a source of silica and alumina that is easily dissolved in solution (Mozumder et al., 2015; Hua Xu et al., 2000). Additionally, roughness in the dispersed clay can be promoted by the divalent and trivalent cations that fly ash particles can offer under ionised circumstances. Accordingly, the fly ash was classified into three classes; Class N, Class F, and Class C as per ASTM C618 – 03 (2003a). The classification was applied as per the chemical and physical requirements.

As per the chemical requirements, the pozzolanic activity is controlled by the total amount of the three minerals silicon dioxide SiO_2, aluminum oxide Al_2O_3, and iron oxide Fe_2O_3; for both classes NFA and FFA should be not less than 70%, while for class CFA should be not less than 50%. In parallel, sulfur trioxide SO_3 should not exceed 4% of the total weight for NFA, while 5% for FFA and CFA. For moisture content, the maximum ratio for the three classes was 3%, while loss on ignition LOI maximum percentage is 10% for NFA, and 6% for CFA and FFA. However, in some circumstances it LOI could be accepted to reach 12% for FFA as per ASTM C618 – 03 (2003a). The summary is shown in Table 2.7.

Table 2.7: ASTM C618 – 03 (2003a) **fly ash chemical requirements**

Requirement	**Limit**	**NFA**	**FFA**	**CFA**
$SiO_2+Al_2O_3+Fe_2O_3$ (%)	Min	70	70	50
SO_3 (%)	Max	4	5	5
MC (%)	Max	3	3	3
LOI (%)	Max	10	6 (up to 12)	6

According to ASTM C618 – 03 (2003a) specifications, the physical requirements are related to wet–sieved retained amount on sieve No. 325, strength activity index, and autoclave expansion or contraction. Strength activity index is related to the strength of the samples for fly ash mixed with Portland cement at 7 days SAI07 and 28 days SAI28 from the control sample. Besides, the water required for the mixing process compared to the required water amount control sample mixture. The requirements are shown in Table 2.8.

Table 2.8: ASTM C618 – 03 (2003a) **fly ash physical requirements**

Requirement	**Limit**	**NFA**	**FFA**	**CFA**
Retained wet–sieved on 45 µm (No. 325) (%)	Max	34	34	34
Strength activity index SAI07 (%)	Min	75	75	75
Strength activity index SAI28 (%)	Min	75	75	75
Water requirement (%)	Max	115	105	105
Autoclave expansion or contraction (%)	Max	0.8	0.8	0.8
Variation in density from average (%)	Max	5	5	5
Variation in retained on 45 µm from average (%)	Max	5	5	5

The primary and most crucial reaction of cementitious materials is tricalcium silicate ($3CaO.SiO_2$, also known as C_3S), which significantly affects how hard and how quickly cementitious sets. The reaction occurs as show in chemical Equation 2.1 (Hewlett et al., 2019). Calcium hydroxide $Ca(OH)_2$ is an amorphous calcium–silicate–hydrate phase with a CaO/SiO_2 molar ratio of less than 3.0 which is defined by 'C–S–H phase' and calcium hydroxide (Hewlett et al., 2019) as shown in Figure 2.6. That defines the valuable cementitious properties and benefits of fly ash.

$$3CaO.SiO_2 + (3+m-n)H_2O = nCaO.SiO_2 + mH_2O + (3+n)Ca(OH)_2 \quad (2.1)$$

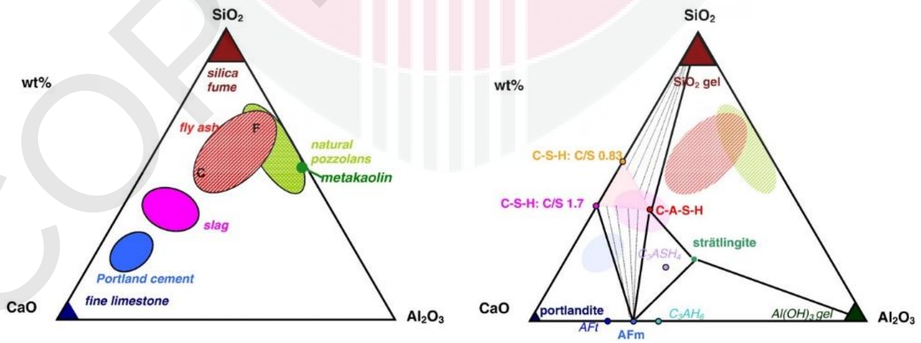

(a) (b)

Figure 2.6: C–A–S diagrams for (a) cementitious materials and (b) hydrate phase (Lothenbach et al., 2011)

2.4.2.3 Soil Treatment Using POFA

Industrial waste is frequently utilised as a stabiliser to lessen the negative effects on engineering properties of weak soils through reactions with soil particles that improve the engineering qualities of the soils (Al–Taie, 2020). Accordingly, palm oil fly ash behaviour was covered by previous research. The addition of fly ash to the soft soils such as marine clay and soft clay soils has changed the micro–mechanical and macro–mechanical properties after treatment (Al–Taie, 2020).

2.4.2.3.1 Shear Strength Behaviour of Treated Soil Using POFA

The unconfined shear strength gradually increased by improvement using fly ash content up to 30% (Turan et al., 2019). The shear strength of palm oil fly ash POFA treated soil shear strength has significantly increased compared to the non–treated soil as shown in Figure 2.7. The minimum increase was 10 kPa after treatment using POFA. Furthermore, both cohesion and internal fiction angle increase significantly at least by 50%. Besides, both values increased as the vertical pressure increased by 10%, which could be related to matric suction caused by the effect of the vertical pressure as shown in Figure 2.8 (Mujah et al., 2015).

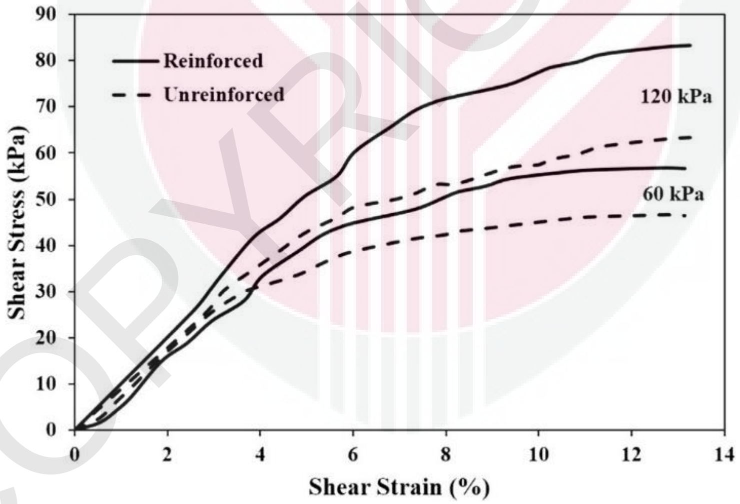

Figure 2.7: Treated and untreated samples shear stress–strain Behaviour (Mujah et al., 2015)

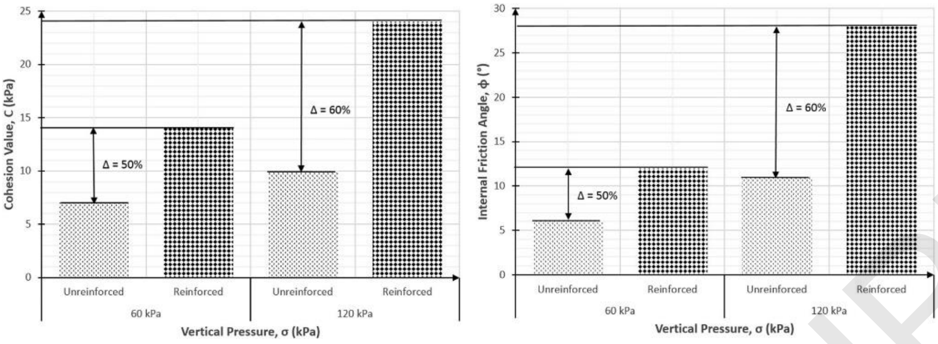

(a) (b)

Figure 2.8: Improvement of (a) Cohesion and (b) internal friction angle after treatment using POFA (Mujah et al., 2015)

2.4.2.3.2 Settlement Behaviour of Treated Soil Using POFA

Soft soils such as soft clay shown improvement in the resistance for deformation after using palm oil fly ash POFA as shown in Figure 2.9. Both saturation degrees 100% and 50% have shown a decreasing in deformation values and rates by the increase of POFA ratio. Furthermore, the maximum decrement in deformation was by 50% for 20% POFA sample. That illustrates the benefit using POFA in deformation reduction for geotechnical and construction applications. This is explained by the fact that the water molecules in the inter–particle gaps in the soft soil were only partially filled up at the time of partial saturation, allowing the soil POFA composite to contract before the loading was applied. This indicates that a larger POFA percent is needed to fill up these voids in order to strengthen the soil POFA composite matrix (Mujah et al., 2015).

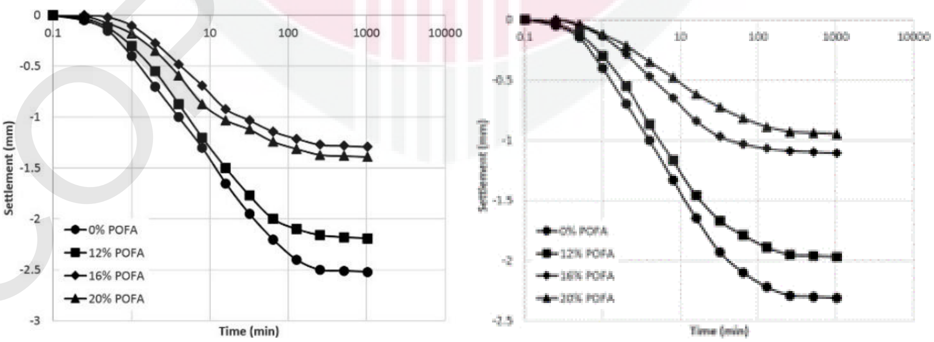

(a) (b)

Figure 2.9: Deformation for (a) 100% saturated and (b) 50% saturated samples with different fly ash ratio (Mujah et al., 2015)

2.4.2.3.3 Atterberg Limits of Treated Soil Using POFA

Plasticity index of soft clay soil depends on the particles surface charge and the fines activity (Saad et al., 2021). Calcium content in fly ash increases clay flocculation and decreases plasticity. The fluctuation in the plasticity index caused by the addition of fly ash as shown in Figure 2.10. Furthermore, high plasticity clay CH showed a faster reduction in plasticity compared low clay CL after treatment (Zimar et al., 2022).

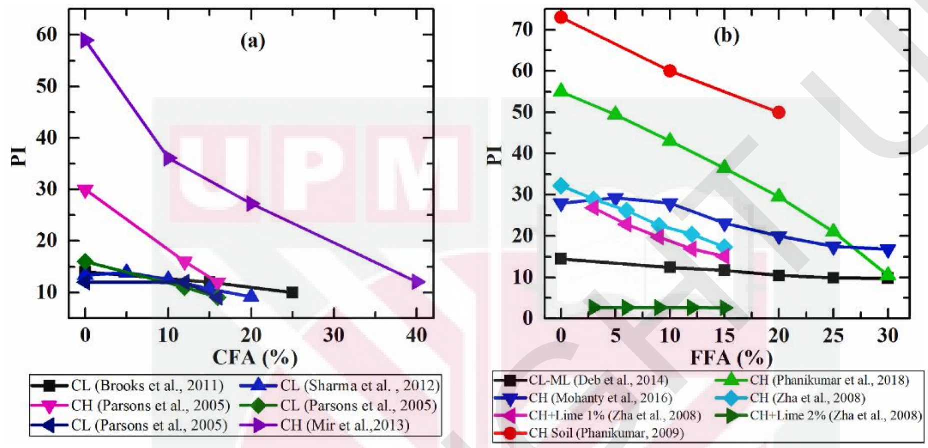

Figure 2.10: Plasticity index values as per previous research for CFA and FFA ratios treating additions (Zimar et al., 2022)

2.4.2.3.4 California Bearing Strength of Treated Soil Using POFA

After soft soil treatment, fly ash reduced the plasticity index, swelling index, and compressibility index while increased compressive strength which impacts the consistency, swelling and strength characteristics of the improved clayey soils (Al–Taie, 2020) as shown in Figure 11. In addition, the heave decreased as fly ash content increased (Han–bing Liu et al., 2009), where California bearing ratio CBR also increased (Sabat et al., 2015).

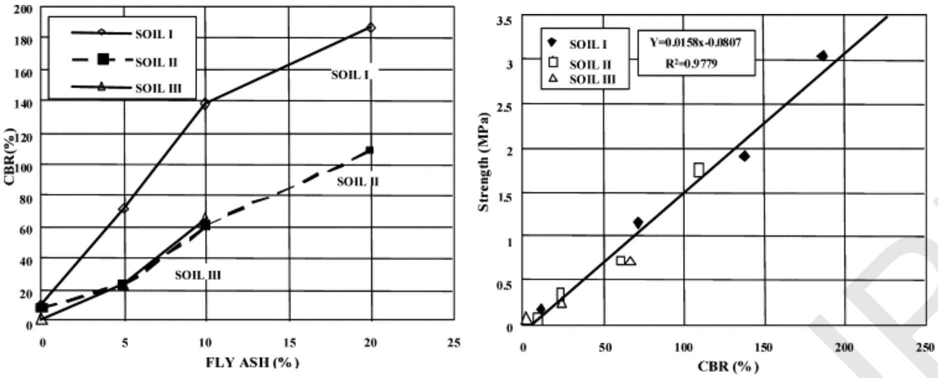

(a) (b)

Figure 2.11: Relationship between (a) California bearing ratio and fly ash content, and (b) California bearing ratio and strength (Kolias et al., 2005)

2.4.2.3.5 Maximum Dry Density of Treated Soil Using POFA

Soil improvement using different ratios of palm oil fly ash POFA has shown significant changes in optimum moisture content and maximum dry density after treatment (Azim et al., 2021). By increment of fly ash content, the optimum moisture content increased and maximum dry density decreased (Sabat et al., 2015; Senol et al., 2011). The maximum improvement was for 15% of POFA for both modified and standard proctor compaction methods as shown in Figure 2.12 and 2.13. For standard proctor test, optimum change was for 10% POFA while for modified proctor test was for 15% POFA (Nik Daud et al., 2017). However fly ash content beyond 30%, the trend has reversed for both of MDD and OMC (Turan et al., 2019). Additionally, the use of POFA in a soft soil, such as peat soil, was dependable in the road construction sector (Yuriz et al., 2020).

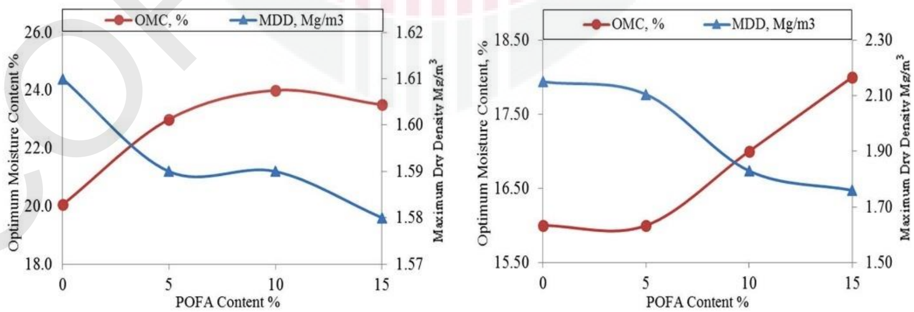

(a) (b)

Figure 2.12: OMC and MDD Variation as per POFA ratio for (a) standard proctor and (b) modified proctor compaction efforts (Nik Daud et al., 2017)

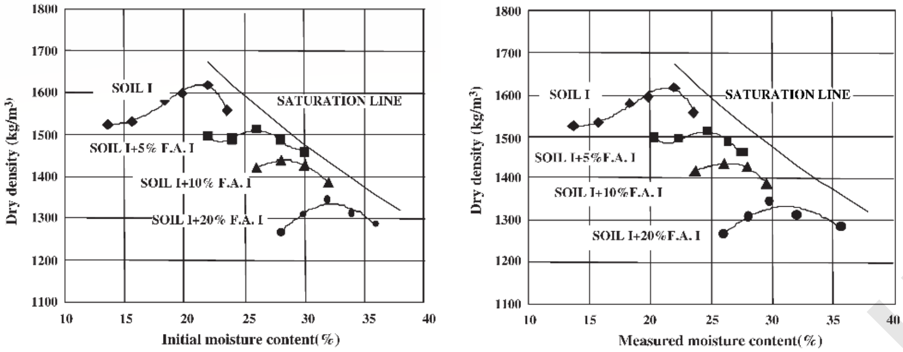

(a) (b)

Figure 2.13: Improved soil after treatment using fly ash (a) initial moisture and (b) measured moisture content (Kolias et al., 2005)

2.4.2.3.6 Creep Stiffness and Deformation Behaviour of Treated Soil Using POFA

Creep stiffness deformation resistance were significantly enhanced after soil improvement using palm oil fly ash POFA as shown in both Figures 2.14 and 2.15 for both static and dynamic loading behavior (Borhan et al., 2010). The optimum ratio was found to be 5% of POFA. In general, the palm oil fly ash POFA has enhanced the behaviour of the soft soil in creep stiffness which reflected in the decline of deformation rate.

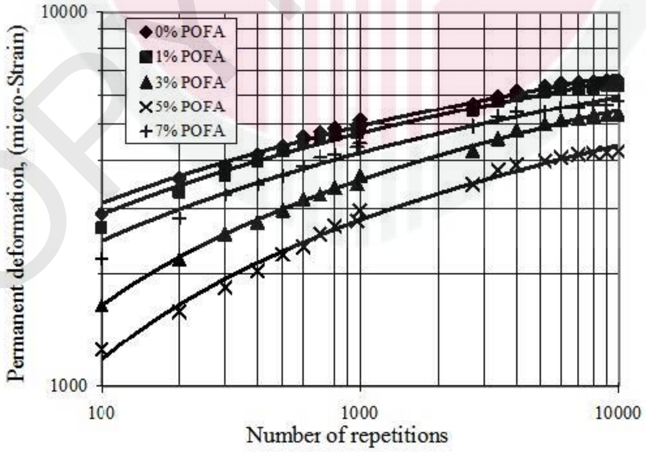

Figure 2.14: Behaviour of dynamic creep related to POFA ratio at $40^{o}C$ (Borhan et al., 2010)

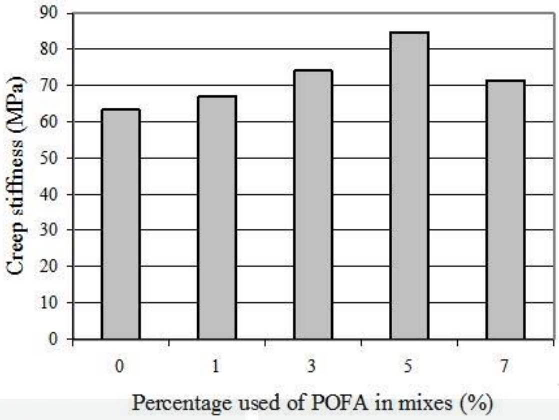

Figure 2.15: Creep stiffness behaviour related to POFA ratio (Borhan et al., 2010)

2.4.2.3.7 Volume Change Behaviour of Treated Soil Using POFA

The treated soil acted as dense soil having some contraction at the beginning then dilation which means the palm oil fly ash has filled the pore gaps. That shows that the treated soil can resist significant stresses compared to none treated soil regardless the vertical pressure as shown in Figure 2.16 (Mujah et al., 2015).

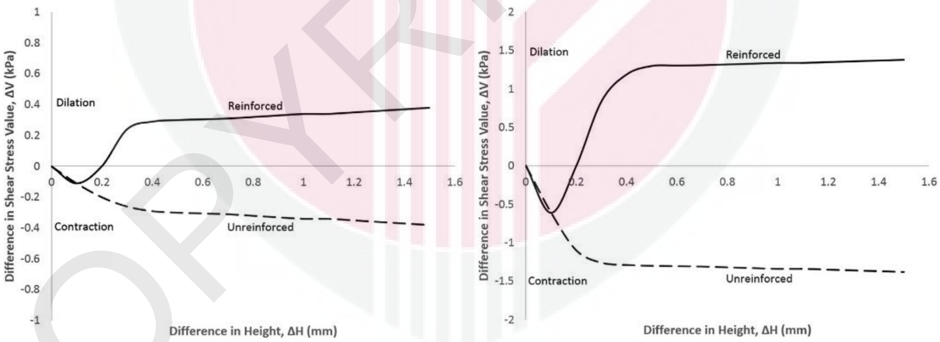

Figure 2.16: Change in volume under (a) 60 kPa and (b) 120 kPa vertical pressure (Mujah et al., 2015)

2.4.2.4 Hazardous Environmental Climate Change of POFA

The traditional cementitious materials such as cement have bad impact on the environment and enhance the climate change risks. Therefore, a variety of waste powders were employed to partially substitute cement in order to reduce the cement usage, or additional ingredients to improve the mechanical behaviour of soil or/and concrete (Fasihihour et al., 2022). Various studies have been conducted on the impact of palm oil fly ash (POFA) on the mechanical properties and durability of concrete in the field of raw materials. Accordingly, its encouraged for totally or partially replacement cement by green byproduct such as fly ash, where fly ash is an ideal option as an additional cementitious material while making green concrete (Chu et al., 2021).

Fly ash is a byproduct of several industries, where it is a product of direct burn to raw materials which make it as industrial waste material. However, fly ash has valuable content of SiO_2, Al_2O_3, Fe_2O_3, and CaO minerals that give fly ash its pozzolanic activity (Lingyu et al., 2021). Thus, fly ash is a cheap cementitious material consists of an amorphous alumina–silicate framework (Al–Zboon et al., 2011), which used to produce materials with low permeability, high temperature resistance, minimal shrinkage, and high mechanical strength (Niklioć et al., 2016; Zeng et al., 2016; Mo Zhang et al., 2016). Fly ash–based materials are prospective replacement materials for Portland cement due to their decreased CO_2 emissions and reduced manufacturing energy requirements (Al–Zboon et al., 2011; Duan et al., 2016; Y Zhang et al., 2013), where the emissions of carbon dioxide CO_2 for both fly ash and cement is shown in Figure 2.17.

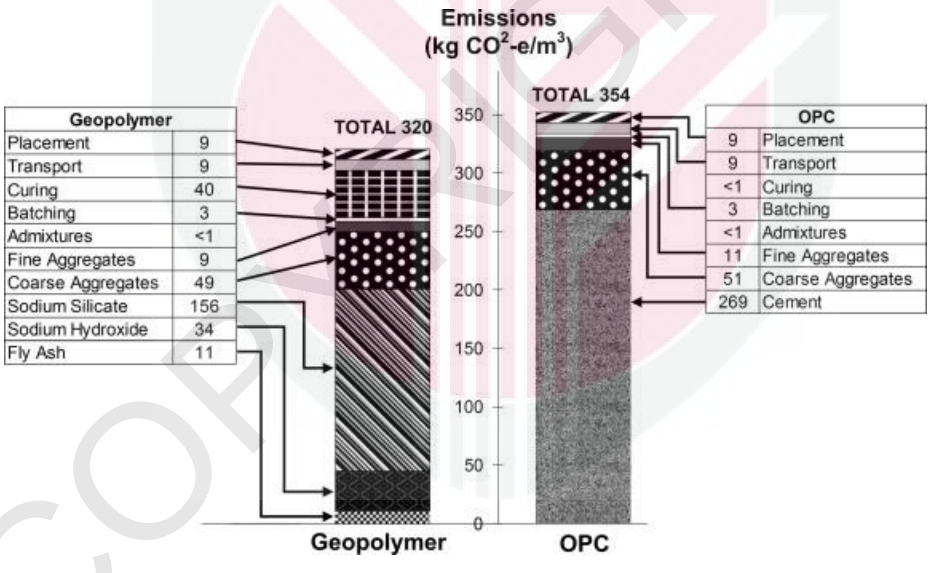

Figure 2.17: Summary of CO_2 $-e/m^2$ for Grade 40 concrete mixtures with OPC and geopolymer binders (Turner et al., 2013)

2.4.2.5 Curing Time Effect on Treated Soil Using POFA

Curing time is a critical factor for both treating materials and soil samples after treatment. Achievement of the engineering curing time for fly ash allows enhanced polymerization for fly ash minerals. Besides, assessment on the curing time for samples

allows researchers and engineers to target the required strength of treated soil. The strength increased with longer curing times after fly ash addition (Jie Zhang et al., 2008).
Curing time for specimens is crucial factor for unconfined compressive strength UCS as cementitious hardens over time. Critically, the strength growth was non–linear as shown in Figure 2.18 (Stegemann et al., 2003). Furthermore, the hydration requires time fo reaction of water with minerals for cementitious materials creation, where the cementitious increases by time leading to increase in strength significantly (Neville, 1995).

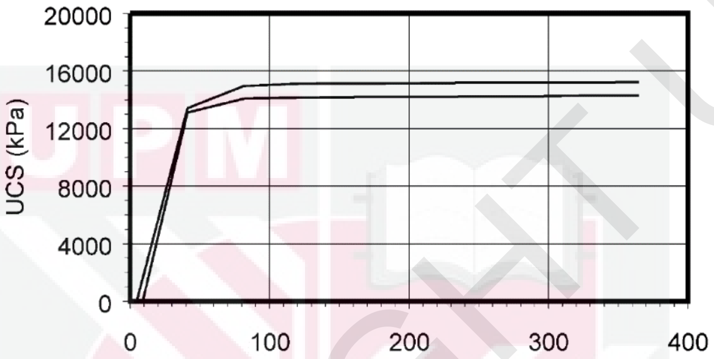

Figure 2.18: Compressive strength relationship with curing time (Stegemann et al., 2003)

Concrete cylinders were created using fly ash and were examined for compressive strength. For fixed curing temperature, the curing time was increased. As a result, higher compressive strength exhibited due to enhanced polymerization caused by longer curing times. Up to 24 hours of curing, the rate of strength rise was quick as shown in Figure 2.19 (Hardjito et al., 2005). Although, it is important to understand the behaviour of clayey soil in log–term of loading, it was not covered by previous research.

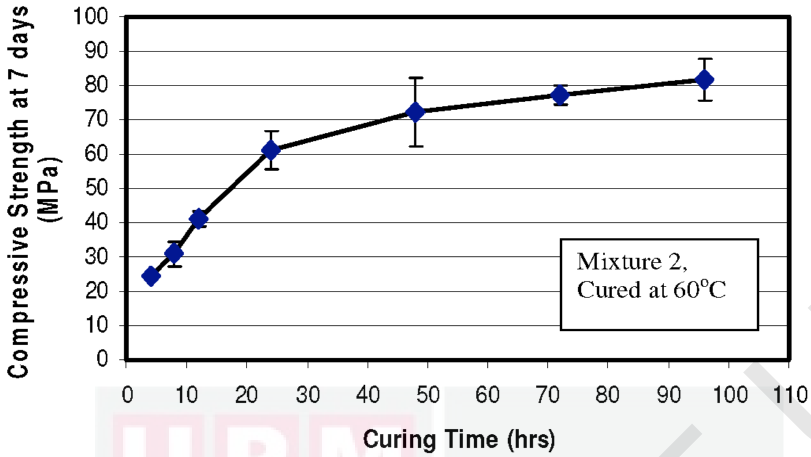

Figure 2.19: Compressive strength relationship with curing time (Hardjito et al., 2005)

2.4.3 Lime Properties As A Soil Stabilizer

Lime is one of the traditional cementitious materials that is commonly used in geo–technical and construction industries. It has a pozzolanic activity that caused treatment using lime to be significant in soil improvement as shown in Figure 2.6. However, stabilisation with lime results in an unfavourable expansion in the presence of sulphate (Behnood, 2018).

2.4.3.1 Source of Lime Used in Soil Stabilisation

Lime is a low cost and effective method of stabilising soil. Lime stabilisation is a technique for enhancing soil wherein lime is given to the soil to enhance its qualities. Hydrated high calcium lime, monohydrated dolomite lime, calcite fast lime, and dolomite lime are several types of lime that are applied to the soil (Afrin, 2017). Lime is created from burning lime stone $CaCO_3$ and can be found in both forms hydrated lime $Ca(OH)_2$ and non–hydrated lime CaO. This widespread use of lime is primarily because of its general affordability and ease of building, together with the simplicity of this technology, which attracts engineers further. Numerous studies have emphasised the usefulness of lime in enhancing soil functionality (Dash et al., 2012).

2.4.3.2 Physical and Chemical Properties of Lime Used in Soil Stabilisation

Chemical properties of lime were identified through X–ray diffraction XRD test. Results for various sources of lime have shown that the major minerals amount was for CaO, where the others are impurities and usually negligible as shown in Table 2.9. The usually used lime are both quick lime CaO and the hydrated lime $Ca(OH)_2$ where the molecular weight of both are 56 and 78 respectively (Mudgal et al., 2014). These minerals control the pozzolanic activity, the zeta potential and the strength of the calcined shale products (Hou et al., 2021). The most important physical property of lime is its specific gravity, where the specific gravity of lime differs as per the chemical condition of the lime that the quick lime is 3.3 while the hydrated lime is 2.2 (Deng Fong Lin et al., 2007; Mudgal et al., 2014).

Table 2.9: Previous research conducted values form XRF test results of lime

SiO_2 (%)	Al_2O_3 (%)	Fe_2O_3 (%)	CaO (%)	MgO (%)	SO_3 (%)	Other (%)	LOI	Source
2.54	0.00	0.03	67.08	1.26	1.09	28.00	28.5	(Akbulut et al., 2010)
0.00	0.00	0.47	93.70	0.53	1.20	4.10	3.90	(Al–Swaidani et al., 2016)
–	–	–	94.00	–	–	6.00	–	(Al–Mukhtar et al., 2010a)
1.4	0.3	0.20	93.50	0.40	0.50	3.70	–	(Anggraini et al., 2016)
–	–	–	89–100	–	–	0–11	–	(Deng Fong Lin et al., 2007)

2.4.3.3 Pozzolanic Activity of Lime Used in Soil Stabilisation

Instead of cementing effect brought on by pozzolanic reaction, lime modification describes an improvement in strength brought on by cation exchange capacity (Sherwood, 1993). In the process of altering soil, clay particles that are typically shaped like plates become interconnecting metallize structures that resemble needles as they flocculate. The aridification of clay soils makes them less sensitive to variations in water concentration (Afrin, 2017). The change in the mineralogical phases of soil is the outcome of the pozzolanic reaction between the soil and the admixtures. As a result, the treated soil's mineralogical analysis becomes crucial. The mineral ettringite is created when sulphate, which is prevalent in the soil, combines with calcium (from lime). This ettringite mineral strengthens the soil and lessens its propensity to swell as illustrated in the chemical Equation 2.2 (Hunter, 1988).

$$6Ca + 2Al(OH)^{-}_{4} + (OH)^{-} + 3(SO_4)^{2-} + 26H_2O \rightarrow Ca_6[(Al(OH)_6)]_2(SO_4)_3.26H_2O \quad (2.2)$$

Lime stabilisation can also refer to the pozzolanic reaction, in which water containing pozzolana minerals combine with lime to create cement–like compounds (Sherwood, 1993; White et al., 2005). Both quicklime CaO and hydrated lime $Ca(OH)_2$ can have the desired effect. Slurry lime can also be used to dry soils where water may be needed to ensure adequate compaction (Rogers et al., 1993). The most often used lime is quicklime, which has the following advantages over hydrated lime. Equation 2.3 states that higher accessible free lime content per unit mass is denser than hydrated lime (less storage space is needed), and less dust produces heat that accelerates strength gain and substantial moisture content reduction (Afrin, 2017).

$$CaO + H_2O \rightarrow Ca(OH)_2 + \text{Heat } (65\text{kJ/mol}) \quad (2.3)$$

2.4.3.4 Soil Treatment Using Lime

To obtain the MDD and OMC values, light compaction tests were done on the untreated and treated soil in the inquiry (Mudgal et al., 2014). The fluctuation of MDD with lime ratio is illustrated in Figure 2.20. When no lime is supplied or 9% lime is added, the MDD value is found to climb from 16.1 kN/m^3 to 16.6 kN/m^3, respectively, and then drop. The soil particles coagulate, agglomerate, or flocculate when exposed to lime. As a result, soil is easier to deal with and gains strength and stiffness up to a certain point. The MDD values for the soil combined with 3%, 6%, 9%, and 12% lime are 16.2 kN/m^3, 16.4 kN/m^3, 16.6 kN/m^3, and 16.5 kN/m^3, respectively (Mudgal et al., 2014).

Lime addition has incased the CBR values significantly (Osinubi et al., 2006). The sample was then compressed and placed in water for 72 hours together with the mould. The fluctuation in CBR with ratio of lime is shown in Figure 2.21. CBR increased up to 12.8 at lime ratio of 9% then gradually decreased (Mudgal et al., 2014). That indicate that the optimum ratio for lime treatment is 9% for the optimum value of CBR.

Figure 2.20: MDD Variation with lime percentage (Mudgal et al., 2014)

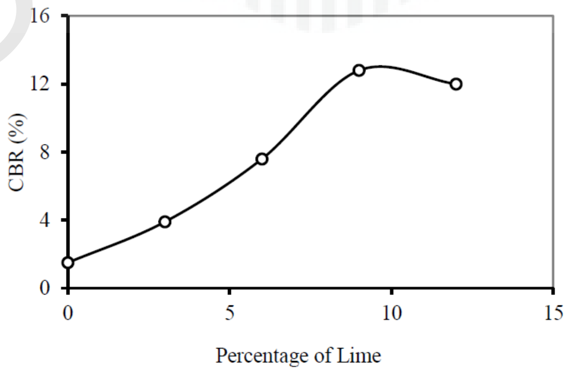

Figure 2.21: CBR Variation with lime percentage (Mudgal et al., 2014)

Most soil stabilisers used between 5 and 10 percent of lime in their formulations (Afrin, 2017; Mohd Yunus et al., 2015). It has been noted that the UCS value increases up to a lime addition of 9% before declining. When no lime is added to the soil, the UCS value is 154 kN/m^2. The UCS values for soil combined with 3, 6, 9, and 12% of lime are 159 kN/m^2, 164 kN/m^2, 169 kN/m^2, and 166 kN/m^2, respectively as shown in Figure 2.22. At a lime input of 9%, the soil's MDD value reached its peak. However, Dash and Hussain (2012) indicated that compressive strength behaviour was at the peak for curing lime ratio of 5%. In addition, the effective strength was generated in both 21 and 28 days of curing. However, lime ratio of 13% did not enhance the strength of treated soil as shown in Figures 2.23 and 2.24. Accordingly, the optimum ratio of lime is between 5% and 9% (Dash et al., 2012; Mudgal et al., 2014; Osinubi et al., 2006).

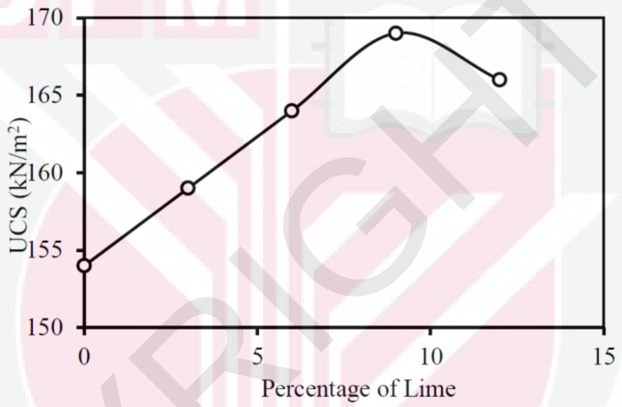

Figure 2.22: UCS Variation with lime percentage (Mudgal et al., 2014)

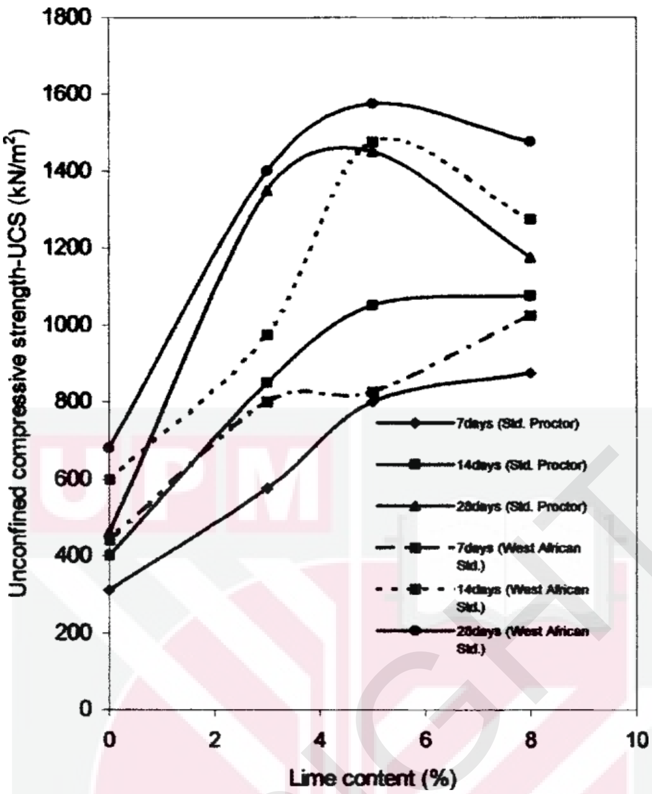

Figure 2.23: Compressive strength variation for residual soil with lime content (Osinubi et al., 2006)

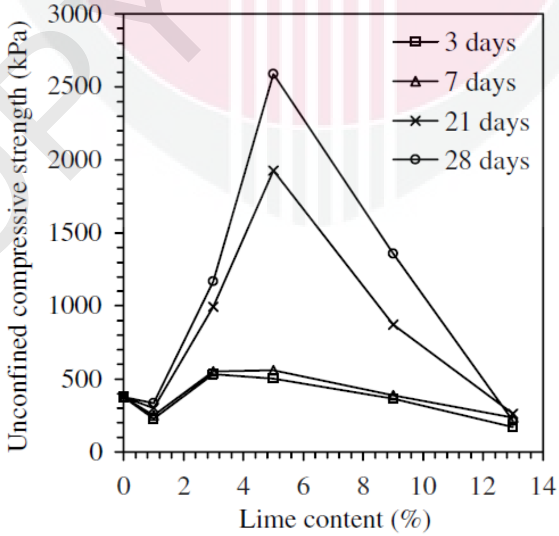

Figure 2.24: Compressive strength variation for residual soil with lime content (Dash et al., 2012)**.**

2.4.3.5 Curing Time of Treated Soil Using Lime

Curing period has a significant impact on shear strength results of the treated specimens (Dash et al., 2012; Osinubi et al., 2006). Regardless the lime content, the strength increased with the increase of the curing duration as shown in Figures 2.23 and 2.24. However, the difference was negligible for both 1% and 13% of lime addition (Dash et al., 2012). Although the importance of clayey soils behaviour in long–term of loading, it was not covered by previous research.

2.4.4 Calcined Shale As A Soil Stabiliser

2.4.4.1 Source of Calcined Shale Used in Soil Stabilisation

Calcined shales were included in concrete mixtures to help calcium hydroxide (CH) transformation into calcium silicate hydrate. As stated in ASTM C–618 (ASTM, 2003a), class N is made of raw or calcined shales. However, manufactured materials are used more frequently than raw pozzolans in typical dispensation such as calcined clay, calcined shale, and metakaolin (Seraj et al., 2015). Although calcined shale also has some cementing or hydraulic properties, it is used in general construction with other pozzolans (Ramli et al., 2016). Meanwhile, most of kaolin clay content is calcined at a low temperature, followed by grinded to an average particle size of between 1 and 2 μ_m, to create metakaolin. Comparing it to silica fume, it is roughly ten times coarser in diameter but about ten times finer than cement (Mindess, 2019). While the incorporation of cementation materials in conjunction with calcium–based binders has demonstrated a significant improvement, the incorporation of treatment materials such as palm oil fuel ash (POFA) has been shown to increase overall soil strength by promoting the transition from brittle to ductile post–peak behaviour. As palm oil fuel ash is produced in large quantities, approximately 70% of the raw materials used in palm oil production end up as solid wastes. Supplementary cementation materials such as calcined shale with high silica and alumina content will be used in this study in conjunction with palm oil fuel ash to promote new low–cost material for enhancing the behaviour of marine clay matrix. However, controlling this mixture matrix requires complicated methods and/or tools for analysis and prediction.

2.4.4.2 Physical and Chemical Properties of Calcined Shale Used in Soil Stabilisation

Results from various sources of calcined shale have shown that the major minerals were SiO_2, Al_2O_3, and Fe_2O_3 while there are other minerals CaO, MgO and SO_3 are in significant amounts but less compared to SiO_2, Al_2O_3, and Fe_2O_3 as shown in Table 2.10. The amount of SiO_2 ranged from 45.82% to 74.80%, Al_2O_3 amount ranged from 12.67% to 47.30%, and Fe_2O_3 amount ranged from 0.17% to 10.80% (Cordoba et al., 2021; El–Habaak et al., 2018; Gmür et al., 2016; Hou et al., 2021; Koňáková et al., 2022; Said–Mansour et al., 2011; Seraj et al., 2015; Tironi et al., 2012, 2013, 2014; Trümer et al., 2019; Vejmelková et al., 2018). These minerals control the pozzolanic activity, the zeta potential and the strength of the calcined shale products (Hou et al., 2021).

The physical properties of calcined shale were identified for values of; pH, particle size, dry density γ_d, and specific surface is SSA as shown in Table 2.11. The pH of fly ash solution ranged from 5.0 to 6.5, ranged from to, γ_d ranged from 2.17 to 2.69, SSA ranged from 4.70 to 2287 m^2/g, and particles size ranged from 0.1 to 131.4 μ_m (Aravind et al., 2021; Ardhira et al., 2022; Binal et al., 2020; John et al., 2021).

Table 2.10: Previous research conducted values form XRF test results of calcined shale

City	Country	SiO_2 (%)	Al_2O_3 (%)	Fe_2O_3 (%)	CaO (%)	MgO (%)	SO_3 (%)	Other (%)	LOI	Source
Abu–Tartur	Egypt	45.82	12.67	0.17	4.5	1.62	0.47	34.75	25.2	(El–Habaak et al., 2018)
Abu–Tartur	Egypt	50.32	13.43	1.11	16.24	4.41	1.21	13.28	8.1	(El–Habaak et al., 2018)
Bohemia	Czech	49.1	47.3	0.9	0.2	0.1	0.1	2.3	–	(Vejmelková et al., 2018)
–	Argentina	64.2	16.3	7.7	0.5	1.4	0.01	9.89	0.58	(Cordoba et al., 2021)
–	Argentina	61.2	17.4	7.5	1.2	2.6	0.07	10.03	0.81	(Cordoba et al., 2021)
–	–	49.1	47.3	0.9	0.2	0.1	–	2.4	–	(Koňáková et al., 2022)
El–Milia	Algeria	50.08	34.03	1.62	0.08	0.41	–	13.78	10.67	(Said–Mansour et al., 2011)
La Rioja	Argentina	45.9	37	0.77	0.08	0.12	–	16.13	13.3	(Tironi et al., 2012, 2013)
Río Negro	Argentina	51.4	31.03	0.92	0.4	0.19	–	16.06	12.15	(Tironi et al., 2012, 2013)
Chubut	Argentina	59.4	27.1	0.76	0.15	0.12	–	12.47	9.65	(Tironi et al., 2012, 2013)
Santa Cruz	Argentina	65.7	21.1	0.85	0.26	0.22	–	11.87	7.77	(Tironi et al., 2012, 2013)
–	Argentina	74.8	14.8	1.1	0.3	0.26	–	8.74	3.44	(Tironi et al., 2012, 2013)
–	–	45.82	12.67	0.17	4.5	1.62	0.47	34.75	25.2	(El–Habaak et al., 2018)
La Rioja	Argentina	45.9	37	0.77	0.08	0.12	–	16.13	13.3	(Tironi et al., 2014)
Río Negro	Argentina	51.4	31.3	0.92	0.4	0.19	–	15.79	12.1	(Tironi et al., 2014)
Franconia	Germany	52	21	8	3	2	1	13	–	(Gmür et al., 2016)
Franconia	Germany	52	21	8	3	2	1	13	–	(Gmür et al., 2016)
Westerwald	Germany	53.2	18.5	10.8	3.1	1.9	–	12.5	7.8	(Trümer et al., 2019)
Texas	USA	65.43	14.55	5.72	2.44	2.3	0.39	9.17	0.36	(Seraj et al., 2015)
–	China	51.27	44.13	1.1	0.45	0.49	0.08	2.48	0.03	(Hou et al., 2021)

Table 2.11: Previous research conducted values for pH, dry density, and size of calcined shale

City	Country	CS Source	pH	Temperature (°C)	Size (µm)	Density (kN/m^3)	SSA (m^2/g)	Source
Abu–Tartur	Egypt	Black shale	–	–	0.1–100	–	–	(El–Habaak et al., 2018)
Abu–Tartur	Egypt	Dakhla shale	–	–	0.1–100	–	–	(El–Habaak et al., 2018)
Bohemia	Czech	Czech claystone	–	–	–	–	–	(Vejmelková et al., 2018)
–	Argentina	CRIS	–	–	1.62–33.65	2.63	552	(Cordoba et al., 2021)
–	Argentina	COIS	–	–	1.29–36.95	2.65	724	(Cordoba et al., 2021)
–	–	–	–	–	–	2.475	–	(Koňáková et al., 2022)
El–Milia	Algeria	Calcined Kaolin	–	850	–	–	–	(Said–Mansour et al., 2011)
La Rioja	Argentina	K1	6.5	700	–	2.38	1461	(Tironi et al., 2012, 2013)
Río Negro	Argentina	K2	5.2	700	–	2.41	2287	(Tironi et al., 2012, 2013)
Chubut	Argentina	K3	5.0	700	–	2.17	1865	(Tironi et al., 2012, 2013)
Santa Cruz	Argentina	K4	5.2	700	–	2.54	981	(Tironi et al., 2012, 2013)
	Argentina	K5	5.4	700	–	2.49	1339	(Tironi et al., 2012, 2013)
La Rioja	Argentina	A1	–	700	1.3–131.4	–	997	(Tironi et al., 2014)
Río Negro	Argentina	A2	–	750	2.1–47.0	–	1365	(Tironi et al., 2014)
Franconia	Germany	CT1	–	850	1.0–50.0	2.65	5.07	(Gmür et al., 2016)
Franconia	Germany	CT2	–	750	1.0–80.0	2.61	4.7	(Gmür et al., 2016)
Westerwald	Germany	–	–	900	–		5.5	(Trümer et al., 2019)
Texas	USA	Shale–T	–	–	–	2.69	573	(Seraj et al., 2015)
–	China	–	–	–	0.2–10.0	–	–	(Hou et al., 2021)

2.4.4.3 Pozzolanic Activity of Calcined Shale Used in Soil Stabilisation

Elimbi, Tchakoute, and Njopwouo (2011) discovered that the thermal activation of clays with a kaolinite dominance at $700^{o}C$ produced an excellent strength behaviour with a peak at 36.4 MPa. The goal of the current study is to clarify the relationship between mineral transformations during the calcination process of shale deposits and the pozzolanicity, alkali activation, and geopolymerization of clay minerals, specifically, chlorite–montmorillonite mixed layer, kaolinite, illite, and spiolite (El–Habaak et al., 2018) as their microstructure is shown in Figure 2.25. The absence of montmorillonite above this calcination temperature indicates that the mineral has completely collapsed structurally and has been replaced by a more reactive pozzolanic phase. This is evident from the strength behaviour at $750^{o}C$ and is quite compatible with the recommended dehydroxylation temperature from published studies (Garg et al., 2015).

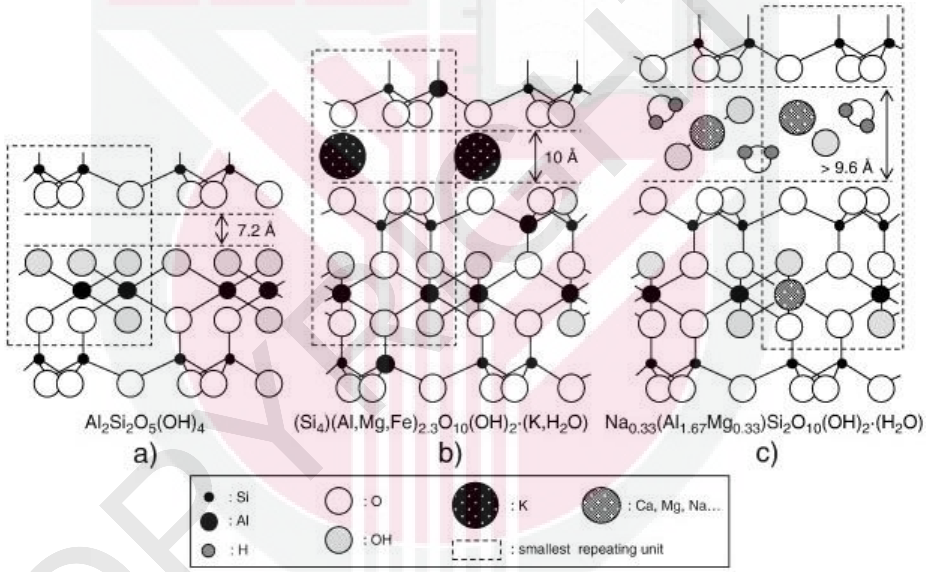

Figure 2.25: Microstructure of (a) kaolinite, (b) illite, and (c) montmorillonite (Grim et al., 1962)

The maximum pozzolanic activity was conducted to be at 28 days for 15 to 30% of calcined shale with values that were nearly identical as shown in Figure 2.26. The results of this test show that both samples of calcined shale have good pozzolanic activity, however the higher specific area has higher pozzolanic activity (Tironi et al., 2014).

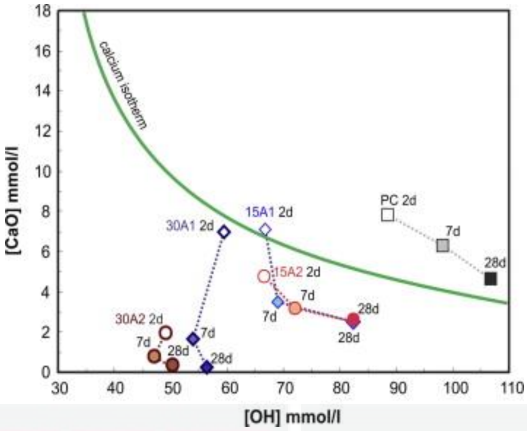

Figure 2.26: Pozzolanic activity of two different calcined shale samples (Tironi et al., 2014)

2.4.4.4 Soil Treatment Using Calcined Shale

Compressive strengths developed by time and the increment of added calcined shale ratio for concrete samples (Tironi et al., 2012). Results showed some fluctuation in compressive strength as shown in Figures 2.27 and 2.28. However, the compressive strength increased significantly for the treated samples compared to the control samples (Seraj et al., 2015; Tironi et al., 2012). Furthermore, the strength increased as the pozzolanic activity increased by time and as a result the pores size inside the concrete samples decreases as shown in Figure 2.29 (Tironi et al., 2012).

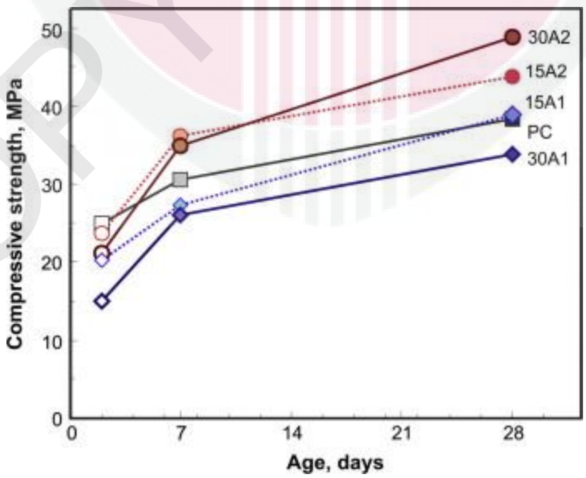

Figure 2.27: Compressive strength of samples treated with calcined shale at 2, 7 and 28 days (Tironi et al., 2014)

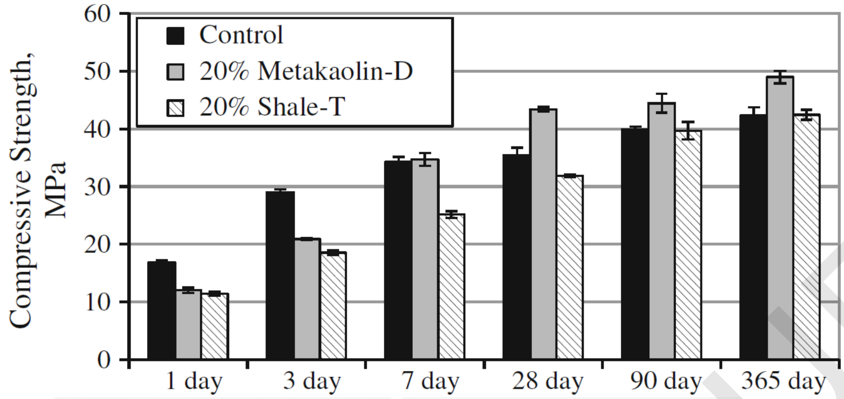

Figure 2.28: Mortar cubes compressive strength (Seraj et al., 2015)

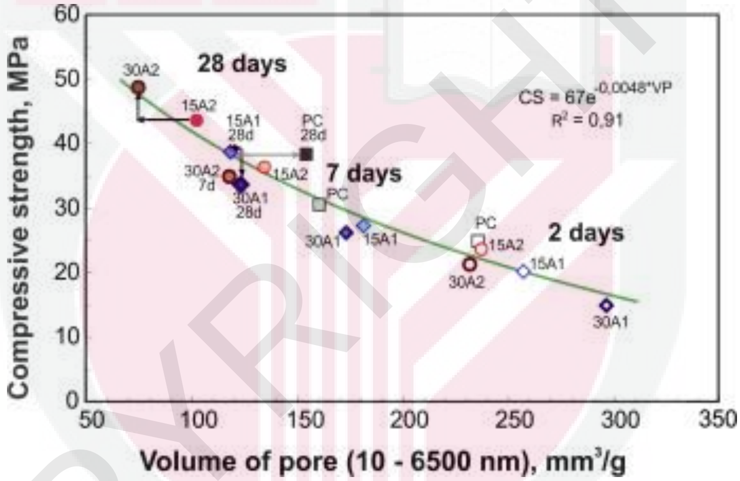

Figure 2.29: Volume of pores effect on compressive strength (Tironi et al., 2014)

2.4.4.5 Curing Time of Treated Materials Using Calcined Shale

Curing time has a significant effect on the mechanical and physical properties of the calcined shale replacement in concrete industry. Throughout the whole one–year testing period, the amount of Portland cement replacement at 30% was obtained with the highest compressive and bending strengths (Vejmelková et al., 2018) as shown in Figure 2.30. The findings showed that as specimens aged, their densities rise as shown in Figure 2.31. Due to the curing regime adopted in this research, which is a water and sea water curing regime, this may be the result of the continuous hydration process of cement in the presence of a continual water supply (Ramli et al., 2016).

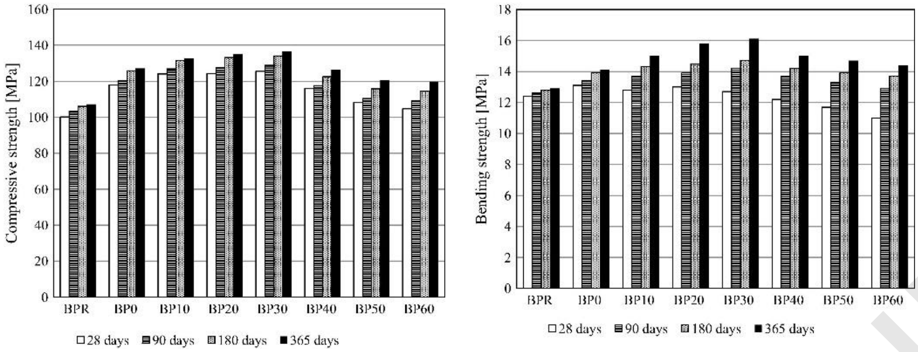

(a) (b)

Figure 2.30: Time effect on (a) compressive strength and (b) flexural strength, where BPR is specimen with Protland cemient only, BP0, cement with silica fume, BP10 to BP60 are speimens with 10 to 60% of calcined Czech claystone (Vejmelková et al., 2018)

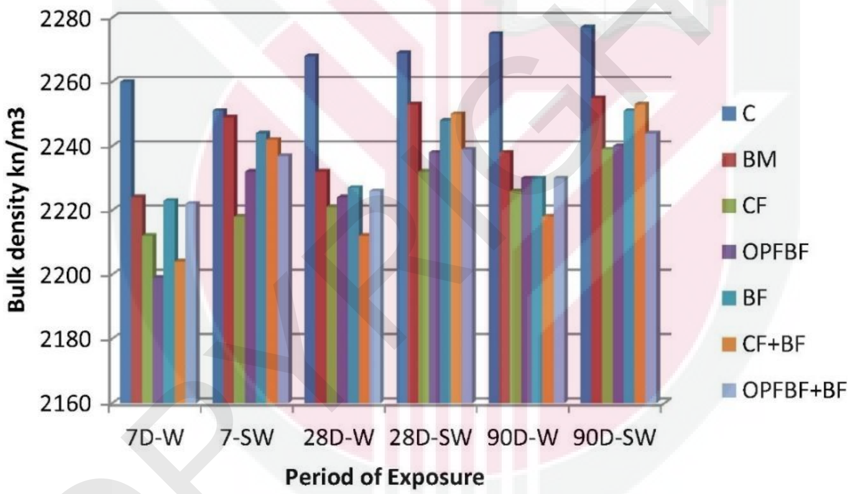

Figure 2.31: Evolution of bulk density with time, where C cement, BM calcined shale base mixture, CF coconut fiber, BF barchip fiber, OPFBF Oil palm waste fruit bunch fiber (Ramli et al., 2016)**.**

2.5 Artificial Intelligence

Recently, artificial intelligence has been used to analyse the mechanical characteristics of soil and concrete, including their micromechanical and macromechanical properties (Mohamad Ali Ridho et al., 2021). In addition, the prediction of the treated soil and concrete behaviour became essential as new materials are involving into construction and geotechnical industries. With the presence of the massive data, it was essential to use artificial intelligence to help in overcoming the problems of time consumption and accuracy of the models. Artificial intelligence algorithms show a wide variety as supervised, unsupervised, semi– supervised, and treatment learning algorithms. As per the purpose of usage artificial intelligence techniques are one approach that has been utilised in recent years for resolving engineering issues and identifying structural and material qualities. Artificial intelligence models include Radial Basis Function (RBF), Artificial Neural Network (ANN), Neuro–Fuzzy Inference System (ANFIS), Genetic Programming (GP), Support Vector Machine (SVM), and others (Pazouki et al., 2021). Moreover, the algorithms are also classified as shown in Table 2.12.

Table 2.12: Classification of Algorithms

Classification	Algorithm	Abbreviation
Classification Algorithms	Naive Bayes	NB
	Decision Tree	DT
	Random Forest	RF
	Support Vector Machines	SVM
	K Nearest Neighbours	KNN
Regression Algorithms	Linear regression	LR
	Lasso Regression	LAR
	Logistic Regression	LOR
	Multivariate Regression	MR
	Multiple Regression Algorithm	MRA
Clustering Algorithms	K–Means Clustering	KMC
	Fuzzy C–means Algorithm	F
	Expectation–Maximisation Algorithm	EMA
	Hierarchical Clustering Algorithm	HCA

In addition, numerous hybrid AI models have been applied to resolve engineering issues, where the compressive strength and other mechanical properties of soil are part of the significant concerns that could examined by various hybrid artificial Intelligence methods (Pazouki et al., 2021). Compressive strength is a crucial factor that is considered while assessing the effectiveness of both soil and concrete treatment. Therefore, it was targeted to predict the compressive strength using novel hybrid AI approaches, specifically a particle swarm optimization PSO based adaptive network–based fuzzy inference system PSOANFIS and a genetic algorithm GA based adaptive network–based fuzzy inference system GAANFIS, which had already been successfully used to resolve other real–world problems, like energy consumption prediction (Barak et al., 2016) and landslide spatial prediction (Pazouki et al., 2021). With these advancement tactics, a variety of adjustable segments are included, such as pressure with the robot layer, determining cross–stream speed, feed temperature, feed, and high productivity (Radhakrishnan et al., 2020; Tang et al., 2021).

2.5.1 Algorithms Used in Engineering Applications

The data prediction and regression using artificial intelligence differs as accuracy of the used model algorithm. The algorithms differ based on the statistical base model used by each algorithm, where this variation in algorithms helps the researchers to use the best algorithm meet the input data and output data as per the required accuracy (Radhakrishnan et al., 2020; Tang et al., 2021; Qing Yang et al., 2018; Yaseen et al., 2018; Yong et al., 2019).

2.5.1.1 Multi Linear Regression

Linear Regression is a powerful and widely used statistical technique in geotechnical engineering for modeling the linear relationship between a dependent variable, y, and one or more independent variables, $x_1, x_2, \dots, x_p$. This method is used to fit a line (known as the regression line) that best approximates the relationship between the variables such that the difference between the observed values and the values predicted by the regression line are minimized, where the equation of the regression line is shown in Equation 2.4.

$$y = \beta_0 + \beta_1 x_1 + \beta_2 x_2 + \dots + \beta_p x_p + \epsilon \qquad (2.4)$$

where $\beta_0, \beta_1, \beta_2, \dots, \beta_p$ are the coefficients to be estimated and ϵ is the error term. The coefficients are estimated using a optimization technique, such as Ordinary Least Squares (OLS), to minimize the difference between the observed values of the dependent variable and the values predicted by the regression line (Dal et al., 2019; Iravanian, Kassem, & Gokcekus, 2022).

Multi–Linear Regression is an extension of Simple Linear Regression, where multiple independent variables are used to predict the dependent variable. This method is commonly used in geotechnical engineering for analyzing the relationship between multiple factors and a dependent variable of interest, where the equation of the regression line in Multi–Linear Regression is shown in Equation 2.5.

$$y = \beta_0 + \beta_1 x_1 + \beta_2 x_2 + \dots + \beta_p x_p + \epsilon \qquad (2.5)$$

where $\beta_0, \beta_1, \beta_2, \dots, \beta_p$ are the coefficients to be estimated and ϵ is the error term. These coefficients are estimated using a optimization technique, such as Ordinary Least Squares (OLS), to minimize the difference between the observed values of the dependent variable and the values predicted by the regression model (Dal et al., 2019; Iravanian, Kassem, & Gokcekus, 2022). Multi–Linear Regression is generally used in various geotechnical engineering applications to analyze the relationship between multiple factors and various geotechnical parameters such as strength, deformation, and settlement of soil (Dal et al., 2019; Iravanian, Kassem, & Gokcekus, 2022).

2.5.1.2 Artificial Neural Network

Artificial neural network ANN is a collection of linked data structures, or neurons for statistical models that is used to attempt and determine the correlations between input and output data (Hagan et al., 1997; Kuhn et al., 2013), where ANN taxonomy is shown in Figure 2.32. Each neuron in a layer has a functional connection to every neuron in the layer below it. The mathematical link between each hidden neuron and the input variables can be described as illustrated in Equation 2.06 (Kuhn et al., 2013). The vector of p input variables is $x = [x_1, \dots, x_p]^T$, the weights vector corresponding to each input variable is $w_i = [w_i, 1, \dots, w_i, p]^T$, and σ is a nonlinear activation function. For regression problems, a sigmoidal function is most commonly used as the activation function (John Lu, 2010), as shown in Equation 2.07. The hidden neurons h are connected to the expected output Ŷ in a same manner as shown in Equation 2.08 (John Lu, 2010), where the hidden neuron vector $h = [h_1, \dots, h_k]^T$ and set of weight vectors $\beta = [\beta_1, \dots, \beta_k]^T$. Although g can be a nonlinear function in this situation as well, it is frequently assumed to be the identity matrix as shown in Equation 2.09.

$$h_i = \sigma.(w_i{}^T x) \tag{2.06}$$

$$\sigma(w_i^T x) = 1/\left(1 + e^{(w_i^T x)}\right) \tag{2.07}$$

$$\hat{Y} = g(\beta^T h) \tag{2.08}$$

$$\hat{Y} = \beta^T h \tag{2.09}$$

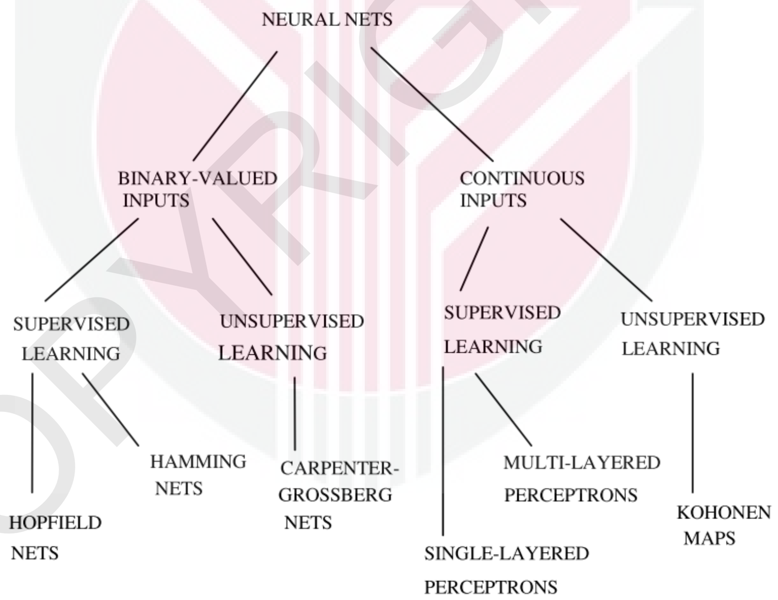

Figure 2.32: Neural networks taxonomy (Tyugu et al., 2007)

In order to minimise a measure of prediction error for a specific training data set, the weight factors w and β must have the proper values for training neural networks. Regularly, the root–mean–squared error (RMSE), where Y_i is the output that was observed or measured for observation i, $\hat{Y}_i$ are the output that was predicted, and N is the number of observations or data points in the training set, gives an adequate measure of error. To find the necessary weight factors, one can use well used numerical techniques as the Levenberg–Marquardt algorithm (Hagan et al., 1997). Neural network models have a large number of fitting parameters, which makes it simple to find nonlinear interactions between input variables, producing a potent forecasting tool. However, if employed carelessly, neural networks with a lot of hidden layers and/or hidden neurons in each layer are vulnerable to over–fitting data, which can result in generalisation mistakes (John Lu, 2010; Kuhn et al., 2013). A neural network's size should be carefully set based on cross–validation (Young et al., 2019).

2.5.1.3 Gradient Boost Regression

Gradient Boost Regression (GBR) is a powerful machine learning technique that is increasingly being used in geotechnical applications. The method involves combining multiple weak learners, such as decision trees, to form a strong predictor. In geotechnical engineering, GBR can be used to model complex relationships between soil properties and geotechnical parameters, such as soil liquefaction, settlement, and slope stability (Divesh Ranjan Kumar et al., 2022; Shan Lin et al., 2021).

GBR has several advantages over traditional statistical methods, including its ability to handle non–linear relationships and its flexibility in dealing with noisy and missing data. Additionally, GBR can automatically determine the most important input variables, making it well–suited for dealing with large datasets with many variables (Shan Lin et al., 2021).

One important application of GBR in geotechnical engineering is the prediction of soil liquefaction potential. Soil liquefaction is a phenomenon where soil loses its strength and stiffness during earthquakes, leading to significant damage to structures. GBR models can be trained using soil properties such as SPT blow count, grain size distribution, and effective stress, along with ground motion parameters, to predict the liquefaction potential of soil (Divesh Ranjan Kumar et al., 2022).

Another application of GBR in geotechnical engineering is slope stability analysis. Slope stability is the ability of a slope to remain in its original position without sliding or collapsing. GBR models can be trained using soil and rock properties, such as unit weight, shear strength, and cohesion, along with slope geometry, to predict the stability of slopes and slopes subjected to various loads and environmental conditions (Divesh Ranjan Kumar et al., 2022; Shan Lin et al., 2021). The prediction of rock strength is another example where GBR has shown promising results. GBR can be used to predict the unconfined compressive strength of siltstone using input variables such as porosity, bulk density, and grain size distribution (Divesh Ranjan Kumar et al., 2022; Shan Lin et al., 2021).

The mathematical representation of GBR can be represented as shown in Equation 2.10, where $F_{m-1}(x)$ is the prediction of the $(m-1)^{th}$ model and $h_m(x)$ is the m^{th}

weak learner, typically a decision tree. The final prediction is given by the sum of all the models as shown in Equation 2.11.

$$F_m(x) = F_{m-1}(x) + h_m(x) \quad (2.10)$$

$$F(x) = \sum_{m=1}^{M} F_m(x) \quad (2.11)$$

In GBR, the residuals are minimized using gradient descent, and new trees are added until a stopping criterion is met. The loss function used in GBR is typically mean squared error (MSE), which can be represented as shown in Equation 2.12, where N is the number of samples. The residuals are then computed as shown in Equation 2.13 and the m^{th} tree is fit to the negative gradient of the loss function with respect to the residual as in Equation 2.14.

$$L = \frac{1}{N}\sum_{i=1}^{N}\left(y_i - F(x_i)\right)^2 \quad (2.12)$$

$$r_i = y_i - F(x_i) \quad (2.13)$$

$$h_m(x) = -\partial L/\partial r_i \quad (2.14)$$

The process of adding trees and fitting to the negative gradient is repeated until a stopping criterion is met, such as a maximum number of trees, a minimum improvement in the loss function, or a combination of both.

2.5.2 Accuracy and Performance Evaluation for Models

The three most popular statistical indices, namely root mean squared error (RMSE), coefficient determination (R^2), and variance account for, were used to evaluate numerous artificial Intelligence models. Based on the simulation results and the values of the computed indices for training and test sets, it can be seen that the accuracy of proposed models. Therefore, proposed models with the best statistical indices values for can be used to develop a new, useful equation that can accurately forecast the targeted factors such as shear strength. The mean square error MSE, root mean square error RMSE, mean absolute error MAE, normalised root mean square error nRMSE, and normalised mean absolute error nMAE were calculated, along with the coefficient of determination of mean square error R^2 value. Many studies in the literature (Yaseen et al., 2018; Young et al., 2019) employed comparable metrics to evaluate the efficacy of the model's predictive capabilities. Equations from 2.15 and 2.16, where m is the number of observations in the dataset, Y is the observed output (experimental value), and Ŷ is the predicted output, are used to express these metrics.

$$MSE = \frac{1}{n}\sum_{i=1}^{n}(y_i - \hat{y}_i)^2 \quad (2.15)$$

$$RMSE = \sqrt{\frac{1}{n}\sum_{i=1}^{n}(y_i - \hat{y}_i)^2} \quad (2.16)$$

$$MAE = \frac{1}{n}\sum_{i=1}^{n}|y_i - \hat{y}_i| \quad (2.17)$$

$$nRMSE = \frac{\sqrt{\frac{1}{n}\sum_{i=1}^{n}(y_i - \hat{Y}_i)^2}}{max(y) - min(y)} \tag{2.18}$$

$$nMAE = \frac{\frac{1}{n}\sum_{i=1}^{n}|y_i - \hat{y}_i|)}{max(y) - min(y)} \tag{2.19}$$

Scatter index SI and coefficient of determination R^2 are also methods of models evaluation, where the Equations 2.20 and 2.21 are for R^2 and SI respectively. Also, the range of scatter index for models evaluation is shown in Figure 2.33, where the lesser value the better model (Abdalla et al., 2022; Ahmed et al., 2022). In addition, T–statistics T_{stat} and expanded uncertainty $U95$ are also used for model evaluation as shown in Equations 2.22 and 2.23 (Kim et al., 2018).

$$R^2 = 1 - \frac{\sum_{i=1}^{n}(y_i - \hat{Y}_i)^2}{\sum_{i=1}^{n}(y_i - \bar{y})^2} \tag{2.20}$$

$$SI = \frac{\sum_{i=1}^{n}|y_i - \hat{Y}_i|}{\sum_{i=1}^{n} y_i} \tag{2.21}$$

$$U95 = 1.96 \cdot \sqrt{\frac{\sum_{i=1}^{n}(y_i - \hat{Y}_i)^2}{n}} \tag{2.22}$$

$$MBE = \frac{1}{n}\sum_{i=1}^{n}(y_i - \hat{Y}_i) \tag{2.23}$$

$$SD = \sqrt{\frac{1}{n-1}\sum_{i=1}^{n}(y_i - \bar{y})^2} \tag{2.24}$$

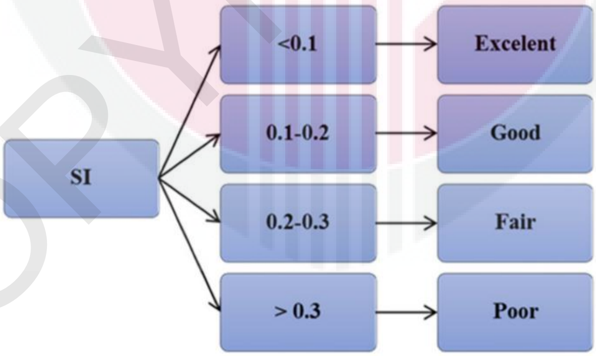

Figure 2.33: The ranges of scatter index SI for models evaluation (Ahmed et al., 2022)

2.5.3 Applications

Previous research showed several algorithms used for data regression and data prediction for soil models as shown in Table 2.13 and soil treatment applications as shown in Table 2.14. The models' accuracy was significantly high, but ANN models were the most accurate. The models were assessed for predicting settlements, deformations, shear strength, consolidation, bearing capacity, tensile strength, geotechnical proprieties, and others. That shows that the machine learning models promises huge functional accurate applications for geotechnical engineering.

However, the artificial intelligence was not applied for both data regression and data prediction of soil treatment using the combinations of lime, fly ash, and calcined shale. In addition, all previous research were focused on short term of clay loading although the long–term loading is crucial for clayey soils. Accordingly, this gap will be assessed through this research.

The used artificial intelligent models showed accuracies according to coefficient of determination R^2 that ranged between 0.8 and 1.0. Mainly, most of researchers applied the Artificial Neural Network ANN as data prediction algorithm and compared with other several algorithms such as LR, GBoost, xGBoost, SVR, SVM, DT, M5P–Tree, and MLR, where the other algorithms were less accurate compared to ANN models. In this research, a group of artificial intelligence algorithms was assess as explained in Chapter 3 and a comparison was settled between them.

Table 2.13: Previous data prediction research using different artificial intelligence algorithms for soil modelling

Treated Material	Treating Material	Curing Duration	Samples	AI Model	Error	Test	Reference
Soil	▪ Geogrid	–	▪ 2030	▪ MLR ▪ ANN	0.27 0.99	▪ Settlements	(Dal et al., 2019)
Base	▪ Quarry waste			ANN	0.9996	▪ BC ▪ Deformation	(Sheikh et al., 2022)
Strip Footing	▪ ferrochrome slag	–	–	▪ ELM ▪ ANN	0.992397 0.999786	–	(Ghani et al., 2021)
Sand	▪ PET	–	–	▪ MARS ▪ ANN	0.99–0.91 0.99	▪ UCS	(Ghorbani et al., 2021)
Sand (Raft)	▪ Planar ▪ Geocell	–	–	▪ GRNN ▪ BPNN	0.99–1.0 0.99–0.99	▪ Settlement	(V Kumar et al., 2018)
SM	▪ GRS	–	166	▪ ANN ▪ GSANN ▪ BPNN ▪ PSONN	0.87–0.93 0.981 0.943 0.973	▪ Deformation	(Momeni et al., 2021)
Geogrid	▪ Imperial Smelting Furnace slag	–	64	▪ ANN	0.97–0.99	▪ SS ▪ ECH ▪ Phy ▪ TS	(Prasad et al., 2016)
Treated Soil Foundations	▪	–	–	▪ MARS ▪ ELM ▪ SVR ▪ GPR ▪ SGBT	– – – – –	▪ Strength ▪ Settlement	(MNA Raja et al., 2021)
Sand	▪ Geogrid	▪	▪ 80	▪ ANN LM	0.99–0.99	▪ Deformation	(Sahu et al., 2018)

Table 2.13: Continued

Treated Material	Treating Material	Curing Duration	Samples	AI Model	Error	Test	Reference
Geosynthetic–Treated Soil Foundations	▪	▪	▪ 475	▪ ANN–GWO	0.96–0.98 0.94–0.97	▪ Settlement	(Nouman Amjad Raja et al., 2021)
Subgrade	▪ Coal ash ▪ Bagasse ash ▪ Groundnut shell ash	▪	▪ 210	▪ ANN ▪ MRA	0.94317 0.68	–	(Rajakumar et al., 2021)
Sand	▪ Coir	▪	▪	▪ ANN	0.97	–	(Lal et al., 2018)
Various Soils	▪ Alum sludge	▪	▪	▪ ANN	0.97–0.99	▪ MDD ▪ USCS ▪ OMC ▪ SG ▪ PI ▪ CBR	(Shah et al., 2020)
Granular Soil	▪	▪ –	▪	▪ BPNN	–	▪ Settlement	(Soleimanbeigi et al., 2006)

Table 2.14: Previous prediction models and soil treatment research for various soil applications

Treated Material	Treating Material	Curing Time	AI Model	Error	Result	Gaps	Reference
SM, ML, CH	▪ Geotextile	▪ 4 to 5	▪ EQA ▪ EQB	▪ 0.943	▪ Models were effective in data prediction	▪ Limitation of data size, included factors, & Used Algorithms	(Jotisankasa et al., 2018)
Clayey Soil	▪ Geopolymer	–	▪ ANN ▪ GMDH	▪ 0.9741 ▪ 0.9677	▪ Models were effective in data prediction	▪ Limitation of data size, & included factors	(Rezazadeh Eidgahee et al., 2020)
Sandy Soil	▪ Volcanic Ash Slag	▪ 1 to 28	▪ ANN	▪ 0.97	▪ ANN was accurate tool for UCS prediction	–	(Shariatmadari et al., 2021b)
Dry Soil (clayey soil)	▪ Aluminium	–	▪ ANN	▪ 0.9997	▪ The soil bearing was significantly improved ▪ Optimum ratio was 8% of alum sludge	▪ Limitation of used compaction properties and energy ▪ Limitation of Used Algorithms	(Aamir et al., 2019)
Clay	▪ Fly Ash ▪ Ground Granulated Blast Furnace Slag	▪ 28	▪ ANNG ▪ MRV	▪ 0.996 ▪ 0.899	▪ Because of Generalizing Data ANNG showed superiority over MVR ▪ ANNG is better than MRV in prediction of UCS	▪ Limitation of Used Algorithms	(Mozumder et al., 2015)
Soil	▪ Fly Ash	▪ 1 to 28	▪ MLR ▪ ANN ▪ TD	▪ 0.66 ▪ 0.8263 ▪ 0.84	▪ Fly ash addition improved physic–mechanical properties ▪ Ternary diagram was more effective compared to MLR and ANN	▪ Limitation of Used Algorithms	(Binal et al., 2020)

Table 2.14: Continued

Treated Material	Treating Material	Curing Time	AI Model	Error	Result	Gaps	Reference
SM ML CH,	▪ Geotextile	4 to 5	▪ EQA ▪ EQB	▪ 0.943	Models were effective in data prediction	▪ Limitation of data size ▪ Limitation included factors ▪ Limitation of Used Algorithms	(Jotisankasa et al., 2018)
Clayey Soil	▪ Geopolymer	–	▪ ANN ▪ GMDH	▪ 0.9741 ▪ 0.9677	▪ Models were effective in data prediction	▪ Limitation of data size ▪ Limitation included factors	(Rezazadeh Eidgahee et al., 2020)
Sandy Soil	▪ Alkali–Activated Volcanic Ash ▪ Blast Furnace Slag	1 to 28	▪ ANN	▪ 0.97	▪ ANN was accurate tool for UCS prediction	–	(Shariatmadari et al., 2021)
Clay	▪ NaOH	–	▪ QM ▪ MFFNN ▪ CFNN ▪ RBNN ▪ ENN ▪ MLR	▪ 0.9999 ▪ 0.9999 ▪ 0.9999 ▪ 0.9907 ▪ 0.9999 ▪ 0.9995	▪ NaOH addition improved soil's engineering properties ▪ Models effectively predicted the stress–strain behaviour of treated soil	▪ Curing time factor was not included	(Iravanian, Kassem, & Gökçekuş, 2022)
Cohesive Soils	▪ Fly Ash ▪ Blast Furnace Slag	28	▪ GMDH ▪ ANN	▪ 0.943 ▪ 0.859	▪ Models effectively predicted UCS after treatment	▪ Limitation of samples number ▪ Limitation of Used Algorithms	(Javdanian et al., 2019)
SP SW	▪ Soil–Geosynthetic	–	▪ GEP	▪ 0.977	▪ Model is effectively estimating soil–anchored geogrid interaction	▪ Limitation of Used Algorithms	(Abdi et al., 2021)

2.6 Summary

Regardless of its mineralogy, location, or formation, marine clay is a sensitive problematic soil that deforms dramatically under stress because of its high–water content, which exceeds its liquid limit. Peninsular Malaysia's soil is consisting of marine clay, which has a similar tendency to other marine clay studied in earlier study that has caused deformation issues for structures that come into touch with it. Furthermore, conventional approaches to solving the problem of general instability are ineffective and unworkable. Because of this, it is necessary to provide a new or improved method of treating marine clay, such as an improved chemical treatment using green materials; lime, calcined shale, and palm oil fly ash, in order to address the overall stability of marine clay.

Green materials such as calcined shale and palm oil fly ash have used for soil treatment. There are several factors that control green materials behaviour in treatment which are, physical properties, chemical properties, pozzolanic activity, alkaline activity, and temperature. Combination of green materials was commonly used for treatment in short loading term although the crucial behaviour of marine clay on the long–term of loading, which should be covered by research to enhance soil treatment using green materials.

Artificial intelligence applications are one of the research trending topics currently. Previous research was focusing mainly on the application of AI on prediction of green materials ratios on concrete strength and few for soils. However, the combination of lime, calcined shale and palm oil fly ash was not covered by previous research. Therefore, covering this area will help Malaysian Industrial community to recycle POFA and calcined shale in new applications for geotechnical and road construction applications. Furthermore, the optimum mixture 5% lime, 10% POFA, and 10% CS should help in achievement of the maximum strength values for soil treatment applications.

Therefore, the gap covered in this study is to create a novel eco–friendly reinforcing mixture for marine clay using green materials such as POFA and CS. In addition, investigating the treated marine clay for resisting long–term of loading and the reduction of resulted deformation as it was not covered by previous research. The evolution of eco-friendly L-POFA-CS treating mixture also attributes in reduction of CO_2 emissions caused by traditional calcium-based binders, lime, and cement used in soil stabilization methods. This green material can be used in civil engineering applications such as soil stabilization, foundation and tunnel building, and road construction. Besides, controlling and optimizing the ratio of the green materials used in the mixture for optimized strength using various machine learning algorithms and study the relationships between the experimental, FEM and machine learning results as it will help in future studies and geotechnical work, especially in reduction of the experimental work, where all the work in this study relied on the mentioned points in Chapter 2 as explained and elaborated in Chapter 3.

CHAPTER 3

METHODOLOGY

3.1 Introduction

This research progressed by identification of marine clay characteristics, and characteristics of used green materials for marine clay treatment. Then, various treatment mixtures were created from the proposed green materials. To identify the optimal ratios of green materials to treat marine clay, several mixtures were treated to evaluate the ratios for palm oil fly ash POFA, lime and calcined shale CS where the optimal engineering ratios were identified based on several factors which are: shear strength, fines activity, flexural strength, maximum dry density, California bearing ratio CBR, and consolidation rate. The samples were tested after several curing duration 7, 14, 28, 56, and 90 days for unconfined shear test UCS as for studying the short–term loading behaviour.

As for long–term loading behaviour, the optimal mixtures of treated marine clay was studied by application of consolidated undrained shear test through a triaxial test. A natural marine clay samples were also tested. As then the optimum mixture which had the the quantities for the green materials of the sample had the optimal shear strength for the long–term loading was used in creation of the finite element model for triaxial test. The finite element model used was selected to assess the long–term loading application.

Finite element modelling program was created for the triaxial test to compare the computer analysis results and relate it to the real loaded triaxial specimens. Accordingly, a relationship was identified between the triaxial results and the finite element model. Artificial intelligence modelling was applied through this study for data prediction and data analysis. Several AI algorithms were used in this study for this purpose.

Artificial intelligence modelling was applied through this study for data prediction and data analysis. Several AI algorithms were used in this study for this purpose. In addition, the detection of the optimal engineering quantities for the green materials to get the desired treatment results for marine clay, where the targeted results are based on short–term and long–term strength after treatment. Accordingly, the used algorithms were applied for data prediction and data analysis of unconsolidated undrained (UU) shear strength and consolidated undrained (CU) shear strength and other geotechnical parameters.

In this study, treatment method proposed would help in reduction of deformations effect on constructions. Also, it is an environmental friendly method of treatment that utilise the industrial waste materials. It also helps in reducing climate changes due to the over emitting of CO_2 all over the world by the traditional cementitious materials.

3.2 Research Flowchart

The summary of the research methodology shown in Figure 3.1 was followed to achieve the objectives of the research.

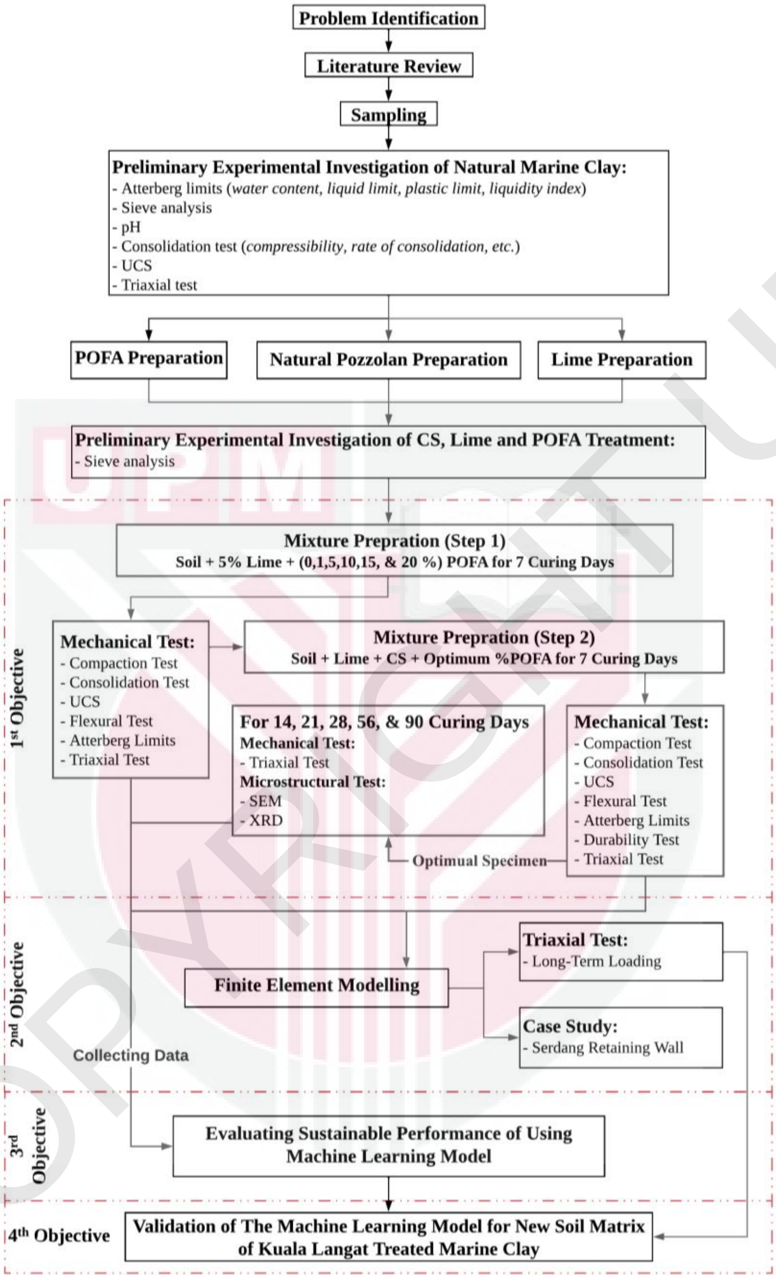

Figure 3.1: Flow Chart of Research Activities

3.3 Sampling Location

Soil samples were collected from Kuala Langat, Selangor, Malaysia. The sampling zone is located between 1.5 and 5 meters below ground level. The soil employed in this study was a typical type of soft marine clay that is extensively dispersed in Kuala Langat, Selangor, Malaysia as shown in Figure 3.2. In addition, the soil layers formation was identified into; the upper layers were consisted of sandy clay soils, and the bottom extensive layers of marine clay deposits were found at depths between 1.5 up to 30 meters following previous research results (Tan et al., 2004). Using a tractor, the representative samples were collected then were immediately transferred to polythene bags to prevent the loss of any fine particles or pore water. The polythene bags were sealed and brought to the laboratory on the same day, where the humid environment was maintained. The collection and preservation of the soil samples were following as per BS 22475–1 (2021) to prevent or to reduce the disturbance of the samples for getting accurate soil properties through process of soil investigation.

3.4 Materials

3.4.1 Investigation of Natural Soil and Determination of Properties

The soil was first air dried before it was ground to release flocculation due to the high initial water content of the samples. Following general requirements and sample preparation in accordance with BS 1377–1 (1990), the samples were dried in an oven at a temperature between $105^{o}C$ and $110^{o}C$ to prepare the necessary quantity for each experiment as shown in Figure 3.3. The soil sample was grinded using soil grinder to guarantee the soil homogeneity during mixing with water and other treating materials.

Plant roots were frequently found in soil samples made of marine clay; thus they were taken out before sieve analysis. For the investigation of the preliminary engineering properties, sieve analysis, hydrometer, Atterberg limits, specific gravity, and one–dimensional consolidation test were carried out in accordance with the ASTM standards, where ASTM D2487–00 (2000a) for sieve analysis, ASTM D422– 63R98 (1998) for hydrometer test, , ASTM D4318–05 (2019) for Atterberg limits, ASTM D854– 00R02 (2000) for specific gravity, and ASTM D2435–96 (1996) for one–dimensional consolidation test.

(a)

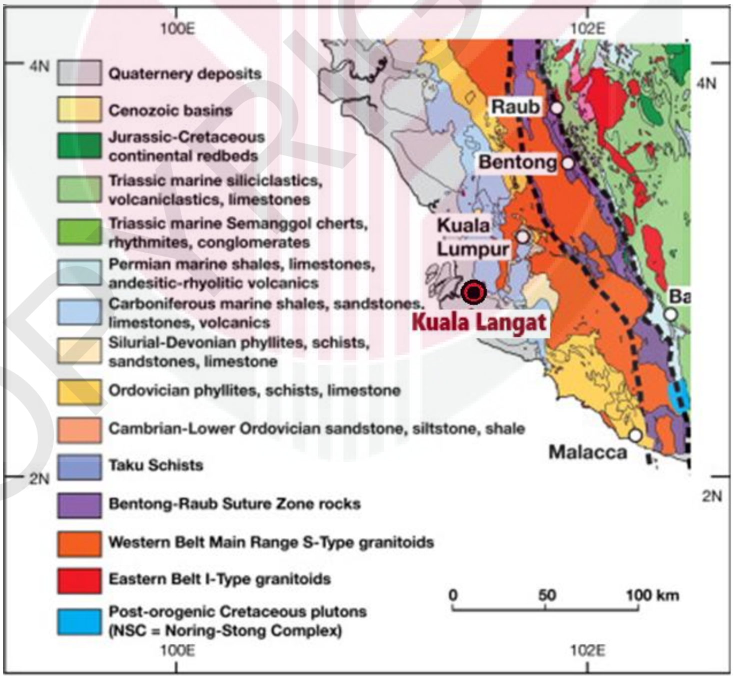

(b)

Figure 3.2: Location of (a) Kuala Langat, Selangor on map of Peninsular Malaysia and (b) its location on geological map with sampling site of GPS coordination (2°50'23.52"N, 101°31'32.28"E)


(a)


(b)

Figure 3.3: Samples (a) before and (b) after grinding process using soil grinder

3.4.1.1 Micromechanical Properties

3.4.1.1.1 SEM

A scanning electron microscope (SEM) were used to examine the soil texture of natural marine clay. Along with identifying the soil texture, that made it possible to identify the chemicals. SEM test was assessed using S34OO–N HITACHI by Volts 10Kv and Probe Current of 20 ohm, where the test was assessed in Universti Putra Malaysia, Material Characterization Laboratory.

3.4.1.1.2 XRD Analysis

Mineral identification was conducted using X–ray diffraction (XRD) diffraction characteristics that are observed when photons from X–rays are transmitted into samples as a standard technique for determining the mineral composition in sediments. To indicate the soil's initial mineral formation, this test was carried out on natural marine clay. XRD test was assessed using X–RAY DIFFRACTOMETER (XRD) SHIMADZU XRD–6000 in Universti Putra Malaysia, Material Characterization Laboratory.

3.4.1.1.3 XRF Analysis

Utilizing X–ray fluorescence (XRF), the chemical composition of dry marine clay was determined. As a result, the composition and weight percentage of the atoms and complete compounds that made up marine clay were determined. XRF test was assessed using the same machine of SEM S34OO–N HITACHI, where the test was assessed in Universti Putra Malaysia, Material Characterization Laboratory.

3.4.1.2 Macromechanical Properties

3.4.1.2.1 Soil Classification

According to ASTM D422–63R98 standards (2000b), sieve analysis and a hydrometer were used to the samples to reveal the grain size distribution of the soil samples. In accordance with ASTM D2487–00 standards (2000a), the soil was categorised using the Unified Soil Classification System USCS.

3.4.1.2.2 Fines Activity

Atterberg limits, including natural water content w_n, liquid limit w_{LL}, plastic limit w_{PL}, and plasticity index PI, were used to investigate the fines activity and the behaviour of the soil. The Unified Soil Classification System (USCS), in accordance with ASTM D2487–00 standards (2000a), is used to classify soil samples based on their fineness.

3.4.1.2.3 Soil Compressibility

According to ASTM D2435–96 standards (1996), a one–dimensional (1–D) consolidation test was performed using an oedometer device. It was carried out to determine the preconsolidation load and compressibility indices for the soil samples.

3.4.1.2.4 Density and Specific Gravity

The specific gravity, G_s, of soil samples was calculated using ASTM D854–00R02 standard's guidelines (2000). According to BS 1377–2 (1990a), the bulk density and dry density were also calculated.

3.4.2 Lime Properties

The used lime in this research is the hydrated lime $Ca(OH)_2$ which supplied by CaO Industries Sdn Bhd company, Malaysia. To prevent any changes in qualities over time due to storage, the lime bag was maintained in an airtight container. The chemical properties of the lime are shown in Table 3.1. The specific gravity of the lime is 2.2 with a molecular weight 78 and calcium oxides CaO content exceeding 93%.

Table 3.1: Chemical properties of lime

Compound	Ratio (%)
SiO_2	1.4
Al_2O_3	0.3
Fe_2O_3	0.2
CaO	93.5
MgO	0.4
SO_3	0.5
Other	3.70
LOI	3.9

3.4.3 Palm Oil Fly Ash Properties

The palm oil fly ash POFA was collected from Sime Darby East Oil Mill Factory, Carey Island, Malaysia. The samples collected in raw form from the factory. The samples were then dried using oven at a temperature of 110^oC for 24 hours. Then, it was sieved using sieve of size 300 µm and stored in plastic bags. The chemical properties of POFA is shown in Table 3.2.

Table 3.2: Chemical properties of POFA

Compound	Ratio (%)
SiO_2	55.02
Al_2O_3	8.96
Fe_2O_3	3.81
CaO	6.23
MgO	2.29
SO_3	1.11
K_2O	6.71
Other	15.87
LOI	8.91
SSA (cm^2/gm)	5720
ASTM C318–03 Classification	CFA

3.4.4 Calcined Shale Properties

The used calcined shale in this research was cured under temperature of 600^oC where the chemical composition is shown in Table 3.3. The chemical properties shows that the major content is formed by both silicate SiO_2 and Aluminate Al_2O_3. The lime grains grading is 92% passing 600 µm, 70% passing 42.5 µm, and 23% passing 3 µm.

Table 3.3: Chemical properties of calcined shale

Compound	Ratio (%)
SiO_2	63.27
Al_2O_3	25.57
Fe_2O_3	4.36
CaO	1.19
MgO	1.10
SO_3	0.29
Other	4.22
LOI	8.82

3.5 Samples Preparation

The ratio of materials; lime, palm oil fly ash (POFA), and calcined shale (CS) for marine clay treatment was based on the ratios of previous research as mentioned in Section 2.4 in Chapter 2. The general layout of material mixtures is shown in Figure 3.4. The prepared specimens were limited to 60 cases for 150 triaxial total specimens for both unconsolidated undrained and consolidated undrained conditions related to 17 different mixtures, which are limited for accurate machine learning modeling but with acceptable accuracy as the experimental work consumes time regarding to the core research objectives and.

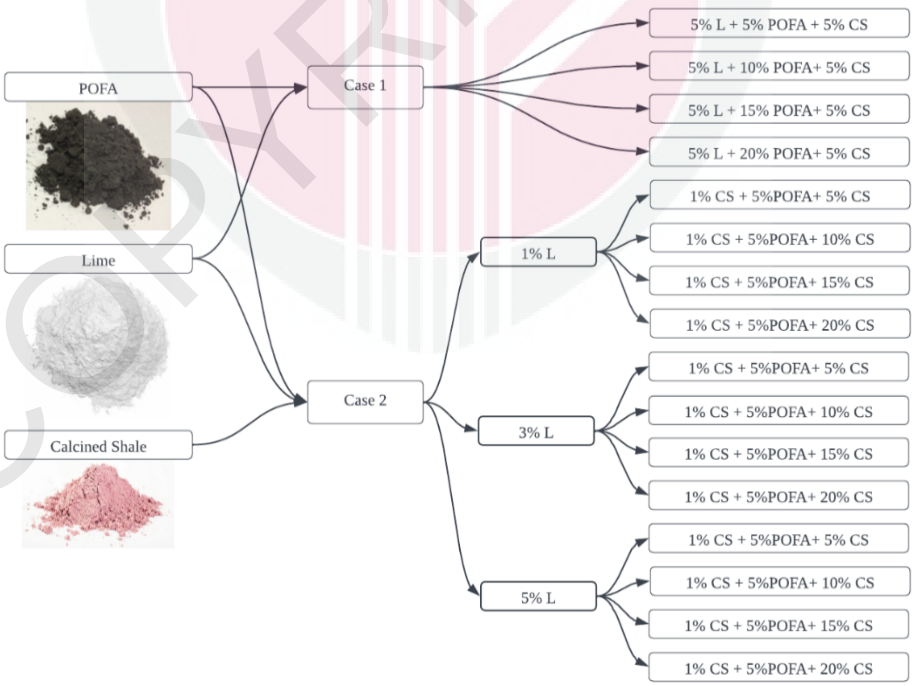

Figure 3.4: Treatment mixtures

The investigation process was divided into two groups of soil mixtures as the previous research investigation by (Mohammed, 2023). Mixtures groups are identified as follows:

1. One with fixed lime content, various ratios of POFA and without calcined shale, and,
2. Second with optimum ratio of POFA and various ratios of calcined shale,

where the mixtures were mixed thoroughly at their optimum moisture content, OMC and maximum dry density, MDD. The mixtures amounts of lime (1.0%, 3%, and 5% by dry weight of soil), POFA (5%, 10%, 15%, and 20% by dry weight of soil), and calcined shale (0.0%, 5%, 10%, 15% and 20% by dry weight of soil), which were manually added. It was found that preparing specimens with less replacing materials content was challenging as they broke when removed from the mold. mixture group one is tabulated in Table 3.4. Table 3.5 presents the second group mixtures.

Table 3.4: First mixture group

ID	Lime	POFA	Calcined Shale	OMC	MDD
	(%)	(%)	(%)	(%)	(kN/m^3)
S	0	0	0	26	14.30
SL5P0C0–7	5	0	0	32.00	13.81
SL5P1C0–7	5	1	0	32.50	13.79
SL5P5C0–7	5	5	0	33.00	13.76
SL5P10C0–7	5	10	0	34.00	13.70
SL5P15C0–7	5	15	0	34.90	13.60
SL5P20C0–7	5	20	0	35.00	13.44

Acronyms: S soil, L lime, P POFA, and C Calcined Shale

Table 3.5: Second mixture group

ID	Lime	POFA	Calcined Shale	OMC	MDD
	(%)	(%)	(%)	(%)	(kN/m^3)
SL5P5C5–7	5	5	5	31.50	14.59
SL3P5C5–7	3	5	5	31.00	14.74
SL1P5C5–7	1	5	5	30.50	14.71
SL5P5C10–7	5	5	10	31.30	14.60
SL3P5C10–7	3	5	10	30.20	14.80
SL1P5C10–7	1	5	10	29.77	14.85
SL5P5C15–7	5	5	15	34.00	13.78
SL3P5C15–7	3	5	15	33.20	13.95
SL1P5C15–7	1	5	15	29.80	14.80
SL5P5C20–7	5	5	20	35.00	13.76
SL3P5C20–7	3	5	20	34.30	13.81
SL1P5C20–7	1	5	20	30.00	14.43

Acronyms: S soil, L lime, P POFA, and C Calcined Shale

The decision to use 5% lime by dry weight of soil was based on practical experience, as it was determined that this is the point at which the maximum strength can be achieved while still maintaining a significant increase in soil workability (Dash et al., 2012; Petry et al., 2002). Additionally, it is known that a higher amount of lime is not necessary in soils with high montmorillonite clay content, typically not exceeding 8% (Bell, 1996), which supports the optimum lime requirement found in this study.

3.6 Improved Soil Investigation

The treated soil specimens were investigated both microstructurally and macrostructurally. The mechanical investigation included shear and compressive strength following below stages:

1. First stage is to investigate the behaviour of treated samples under loading on short–term
2. Second stage is to investigate the behaviour of treated samples loading on long–term

Based on results of shear and compressive strength investigation, the optimal ratios of treating materials lime, POFA and calcined shale were tested for XRD and SEM for microstructurally investigation.

3.6.1 Investigation of L–POFA–CS Ratios Impact

Through this process, the impact of the used materials in soil improvement which are lime, POFA and calcined shale were investigated based on shear strength, physical, geotechnical, and chemical properties, and to microstructure. The effect of POFA ratio was firstly investigated as per the specimen mixture defined in Table 3.4 previously. Then, the optimum ratio of POFA was used with various ratios of lime and calcined shale, as identified previously in Table 3.5, to investigate their impact on the improved soil. Each mixture was examined at 7 curing days, while the optimum treatment mixture was examined at 14, 21, 28, 56, and 90 curing days as to also assess the impact of curing time. The shear strength was assessed through series of triaxial tests as tabulated in Tables 3.6 and 3.7 for both mixture cases using automated triaxial system. The used system was GDS Automated Triaxial Unit GDSTAS with loading cell GDSFL50 of 50kN Digital Load Frame V2 with two transducers of maximum pressure 3 MPa to control pore water pressure and cell pressure automatically by GDSLAB V2.0 software through USB 8 channel data logger as shown in Figure 3.5.

Table 3.6: Triaxial experiments for Stage No.1

Code	Duration (days)												Total No. of Specimens
	UU						CU						
	7	14	21	28	56	90	7	14	21	28	56	90	
S	3	–	–	–	–	–	3	–	–	–	–	–	6
SL5P0C0	3	–	–	–	–	–	3	–	–	–	–	–	6
SL5P1C0	3	–	–	–	–	–	3	–	–	–	–	–	6
SL5P5C0	3	–	–	–	–	–	3	–	–	–	–	–	6
SL5P10C0	3	–	–	–	–	–	3	–	–	–	–	–	6
SL5P15C0	3	–	–	–	–	–	3	–	–	–	–	–	6
SL5P20C0	3	–	–	–	–	–	3	–	–	–	–	–	6

Acronyms: S soil, L lime, P POFA, and C Calcined Shale

Table 3.7: Triaxial experiments for Stage No.2

Code	Duration (days)												Total No. of Specimens
	UU						CU						
	7	14	21	28	56	90	7	14	21	28	56	90	
S	3	–	–	–	–	–	3	–	–	–	–	–	6
SL1PoC05	3	–	–	–	–	–	3	–	–	–	–	–	6
SL1PoC10	3	–	–	–	–	–	3	–	–	–	–	–	6
SL1PoC15	3	–	–	–	–	–	3	–	–	–	–	–	6
SL1PoC20	3	–	–	–	–	–	3	–	–	–	–	–	6
SL3PoC05	3	–	–	–	–	–	3	–	–	–	–	–	6
SL3PoC10	3	–	–	–	–	–	3	–	–	–	–	–	6
SL3PoC15	3	–	–	–	–	–	3	–	–	–	–	–	6
SL3PoC20	3	–	–	–	–	–	3	–	–	–	–	–	6
SL5PoC05	3	–	–	–	–	–	3	–	–	–	–	–	6
SL5PoC10	3	3	3	3	3	3	3	3	3	3	3	3	36
SL5PoC15	3	–	–	–	–	–	3	–	–	–	–	–	6
SL5PoC20	3	–	–	–	–	–	3	–	–	–	–	–	6

Acronyms: S soil, L lime, P POFA, and C Calcined Shale

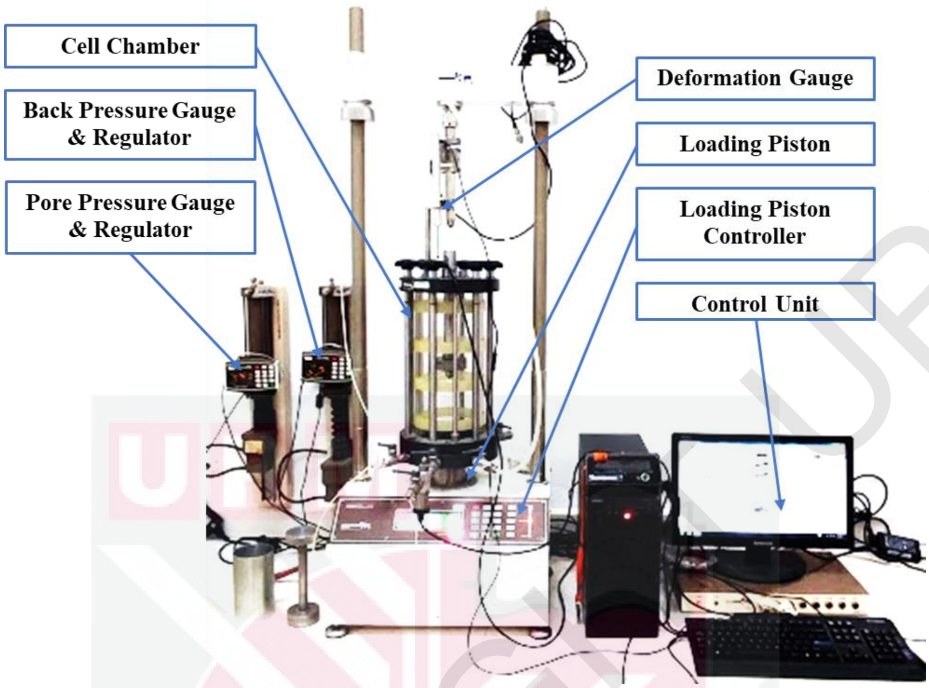

Figure 3.5: Triaxial test equipment

3.6.2 Triaxial Compression Test

The specimens preparation for triaxial test was assessed as per ASTM D4767–03 Standards (2003b) for consolidated undrained triaxial compression test CU and ASTM D2850–03R07 Standards (2007) for unconsolidated undrained triaxial compression test UU.

3.6.2.1 Specimens Preparation

To achieve the proper water content, the soil needed for compacted specimens must be thoroughly mixed with water. Before compacting the soil, it should be stored in a sealed container for a duration not less than 16 hours after water has been added to soil mixture. Compacted specimens was created by compacting material using a split circular mould with dimensions of 70 mm diameter and 180 mm height as shown in Figure 3.6, which meet the specifications limits of ASTM Standards (2003b, 2007), where the material compaction was achieved in at eight layers each 20 mm as per ASTM specifications limits (ASTM, 2003b, 2007).

Figure 3.6: Compaction mould

The materials quantities were calculated for the commutative mass of soil mixture as shown in Figure 3.7, Then, the mixture was placed to the targeted volume of the mould, as shown in Figure 3.8, by kneading or tamping each layer and was compacted to the required density. The extra 20 mm layer was added to help in specimen adjustment after achievement of specimen compaction. Before adding the material for the following layer, the top of each layer was scratched. The diameter of the tamper used to compact the material was equal to half diameter of the mould as per ASTM instructions (2003b, 2007).

Figure 3.7: Materials ratios before mixing process

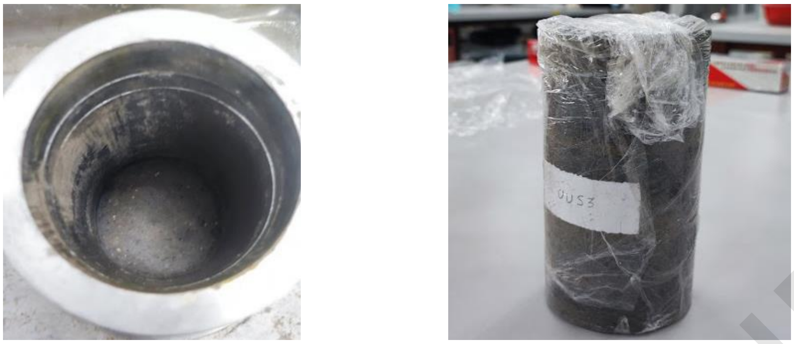

(a) (b)

Figure 3.8: Specimen (a) during preparation and (b) after adjustment

Once a specimen was compacted, the ends were adjusted perpendicular to the longitudinal axis of the mould. The detected dimensions of specimens were the average of both: (1) three diameter readings at top middle and bottom of each specimen as shown in Figure 3.9, and (2) three height readings of each specimen 120 degrees apart for each reading as shown in Figure 3.10 the extra materials resulted from specimen adjustment was used to detect the water content the specimen in line with testing method ASTM–D2216–19 (2019).

(a) (b) (c)

Figure 3.9: Specimen diameters at (a) top, (b) middle and (c) bottom

(a) (b) (c)

Figure 3.10: Specimen height at 120 degrees apart for each reading

3.6.2.2 Mounting Specimen

Triaxial system used in this research is shown in Figure 3.11, where the system is following the instructions of both ASTM D4767–03 Standards (2003b) for consolidated undrained triaxial compression test CU and ASTM D2850–03R07 Standards (2007)for unconsolidated undrained triaxial compression test UU. The method controlling of valves differs according to test type, where it was automatically controlled by the triaxial machine. For CU test, side drain filter paper was used for consolidation and saturation time reduction as shown in Figure 3.11–b. Membrane and side drain correction was automatically corrected through the triaxial user interface program.

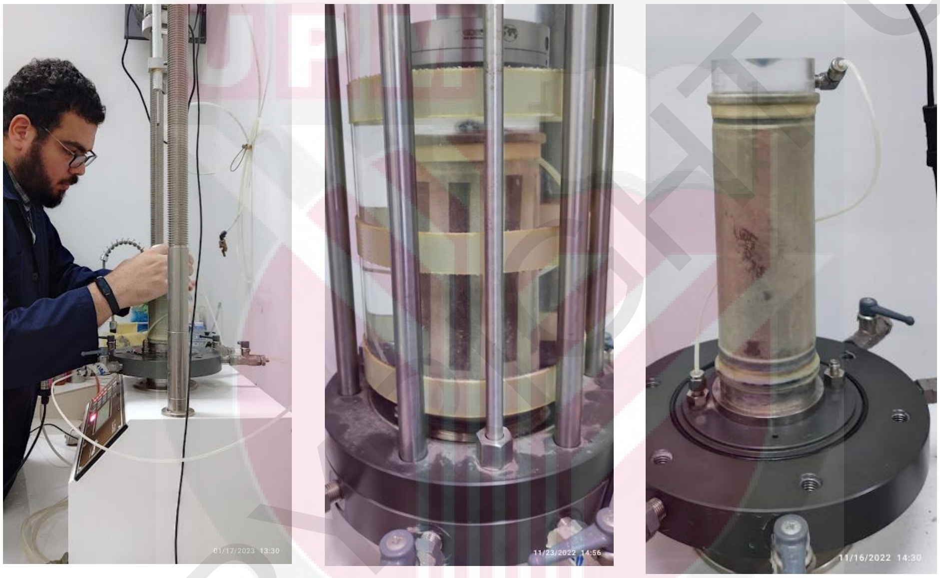

(a) (b) (c)

Figure 3.11: Mounting of triaxial specimen (a) process, for both (b) CU specimen and (c) UU specimen)

3.6.2.3 Triaxial Experiment Procedure

For short–term loading investigation, a series of unconsolidated undrained UU compression tests were conducted on the specimens listed in both Tables 3.6 and 3.7, where the axial load to produce axial strain at a rate of around 5 mm per minute was applied during the test for maximum strain rate between 18% and 20%.

For long–term loading investigation, a series of experiments were conducted using consolidated undrained triaxial tests on natural soil and treated soil specimens as listed in both Tables 3.6 and 3.7. The samples were consolidated under a set confining pressure for 24 hours. The triaxial tests were conducted at cell pressures of 50, 100 and 150 kPa and at a constant rate of axial strain. The specimens were saturated where the B–value check was always above 0.95, besides the axial load was applied at a strain rate of 0.015 mm/min to ensure equilibrium of pore water pressure during the test.

3.6.2.4 Triaxial Calculations

The system of GDS Automated Triaxial Unit GDSTAS is automatically controlling the valves and correcting the output values for the correction factors of (1) membrane, (2) side drainage, and (3) axial stress during application of the deviatoric stress. according to BS 1377–8 standards (1990b). Also B–value is calculated automatically, where the check of coefficient B was always more than 95% as shown in Equation 3.1, where $\Delta\sigma_3$ equals to 50 kPa.

$$B = \frac{\Delta u}{50} \qquad (3.1)$$

The plots and calculations were assessed from CU test for both drained and undrained conditions using Equations 3.2 to 3.4, where $\sigma_1 - \sigma_3$ is the deviatoric stress $\Delta\sigma$.

$$(\sigma_1 - \sigma_3)' = (\sigma_1 - \sigma_3) - u \qquad (3.2)$$

$$\sigma_1' = \sigma_1 - u \qquad (3.3)$$

$$\sigma_3' = \sigma_3 - u \qquad (3.4)$$

3.7 Finite Element Modelling

Finite element modelling FEM is a powerful tool that is commonly used by researchers and geotechnical engineers in studying the stresses and deformations resulted from external effects. Therefore, this study aims to link the laboratory results with FEM results to investigate the difference between both confuted results to assess a relationship that could be used as future research and geotechnical work guideline. The used FEM program is PLAXIS 2D V22. Actual properties of constitutive materials and geometry are used in the numerical model. Particular consideration was given to how the mechanical characteristics of the treated soil were affected by the effectiveness of the soil reinforcement.

3.7.1 Finite Element Modelling for CU Triaxial FEM

FEM was assessed for CU triaxial specimens as identified in Tables 3.6 and 3.7 to indicate the differences between FEM and actual triaxial results. The model was identified as axisymmetric section as shown in Figure 3.12 and the type of the test consolidated undrained CU as shown in Figure 3.13. The used parameters for model identification used was based on the conducted values of 50% of elasticity E_{50}, reloading modulus of elasticity E_{ur}, effective angle of internal friction ϕ', and effective cohesion C', as shown in Figure 3.14, where the used data is shown in Table 3.8.

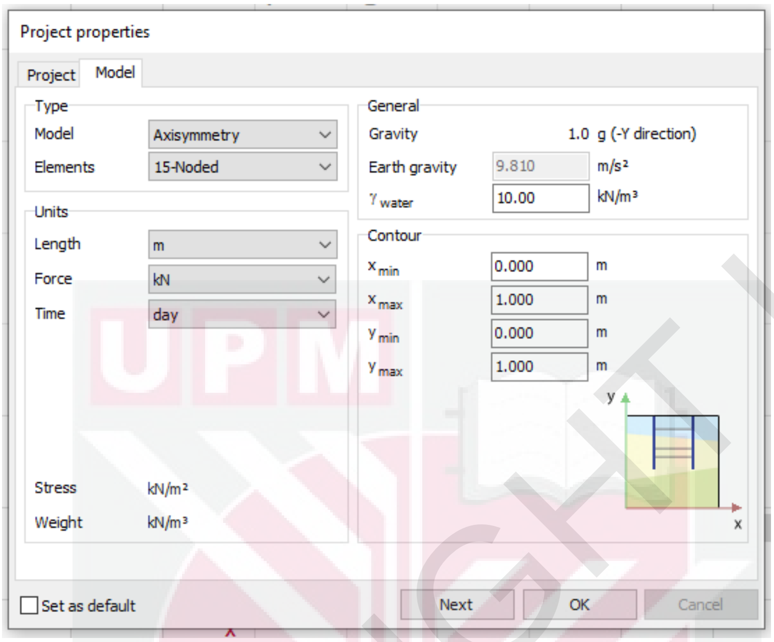

Figure 3.12: Definition of FEM in PLAXIS

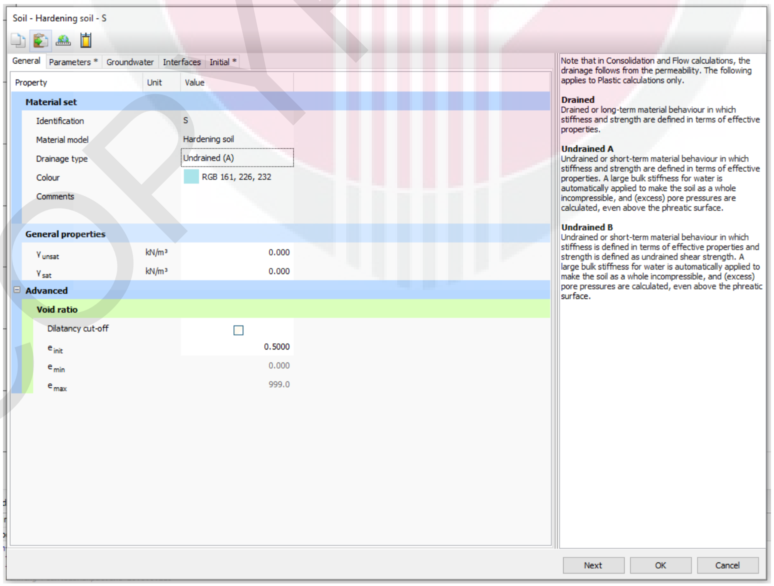

Figure 3.13: Definition of type of triaxial test and drainage condition in PLAXIS FEM.

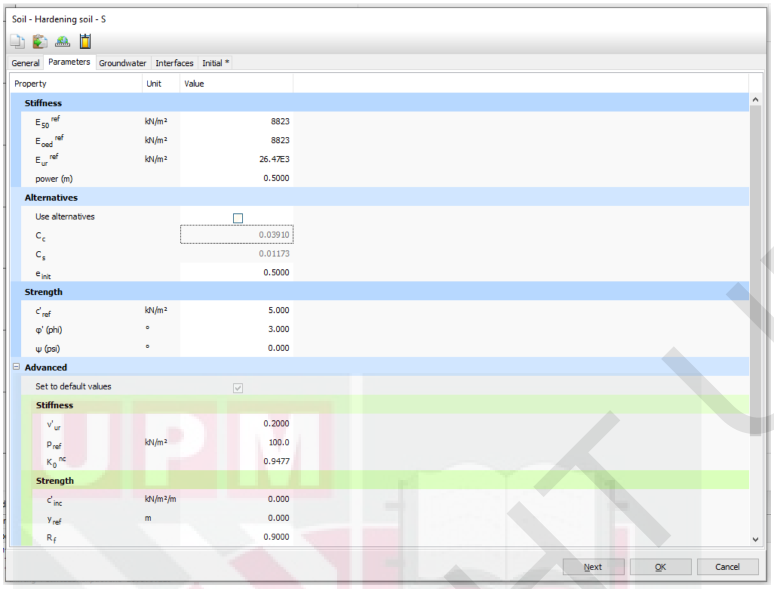

Figure 3.14: Definition of soil parameters for simulating triaxial test Using PLAXIS.

Table 3.8: Input data for modelling triaxial test using PLAXIS

Specimen	E_{oed}	$E_{ur,ref}$	C'	ϕ'
S	8823	29341	61.07	19.51
SL5P0C0–7	27806	87392	116.82	20.14
SL5P1C0–7	26370	86076	110.65	21.21
SL5P5C0–7	21789	81213	86.11	24.5
SL5P10C0–7	21369	85797	68.03	21.21
SL5P15C0–7	12366	41462	56.91	20.66
SL5P20C0–7	8750	36095	59.51	20.5
SL5P5C5–7	27380	99331	79.77	22.65
SL3P5C5–7	33627	124871	98.05	22.92
SL1P5C5–7	20415	117078	79.67	22.9
SL5P5C10–7	51414	155945	99.67	23.27
SL3P5C10–7	21254	60563	72.64	22.87
SL1P5C10–7	35536	151895	84.91	23.3
SL5P5C15–7	32313	95399	66.32	23.06
SL3P5C15–7	26680	110278	62.99	22.98
SL1P5C15–7	19101	62967	57.85	22.9
SL5P5C20–7	20128	48308	56.18	22.81
SL3P5C20–7	18070	119581	56.45	22.94
SL1P5C20–7	16813	57783	58.68	22.93
SL5P5C5–14	60447	200165	92.24	22.65
SL3P5C5–14	41275	109295	114.07	23.03
SL1P5C5–14	41804	154883	93.91	23.34
SL5P5C10–14	58336	238480	171.16	23.96
SL3P5C10–14	54578	262625	95.79	23.2
SL1P5C10–14	41598	170284	111.62	23.3
SL5P5C15–14	55554	268358	85.91	23.28

Specimen	E_{oed}	$E_{ur,ref}$	C'	ϕ'
SL3P5C15–14	25603	52072	89.7	23.42
SL1P5C15–14	14721	68026	75.65	22.9
SL5P5C20–14	41294	182316	73.99	23.14
SL3P5C20–14	34369	71727	67.13	23.38
SL1P5C20–14	11799	92768	72.92	23.15
SL5P5C5–21	76764	277090	117.16	22.76
SL3P5C5–21	71109	274410	130.1	23.47
SL1P5C5–21	38543	161666	118.84	23.45
SL5P5C10–21	64446	231794	207.03	24.55
SL3P5C10–21	51470	193507	111.81	23.64
SL1P5C10–21	46619	199766	131.2	23.52
SL5P5C15–21	61592	234135	110.83	23.61
SL3P5C15–21	38748	148922	111.06	23.97
SL1P5C15–21	18537	71535	91.68	23.12
SL5P5C20–21	37580	108681	86.45	23.36
SL3P5C20–21	18377	71489	79.59	23.38
SL1P5C20–21	15496	90943	97.85	23.59
SL5P5C5–28	15648	86986	142.09	23.53
SL3P5C5–28	58656	75264	156.81	24.56
SL1P5C5–28	43564	178431	134.86	24.22
SL5P5C10–28	87740	159987	224.78	25.12
SL3P5C10–28	16706	66353	126.06	24.52
SL1P5C10–28	42001	197868	156.13	24.5
SL5P5C15–28	15313	112399	132.2	24.16
SL3P5C15–28	45716	123752	135.99	24.52
SL1P5C15–28	20129	70939	118.39	24.22

Table 3.8: Continued

Specimen	E_{oed}	$E_{ur,ref}$	C'	ϕ'
SL5P5C20–28	49602	89947	106.04	25.01
SL3P5C20–28	22341	69465	90.28	24.48
SL1P5C20–28	12620	91805	122.78	24.69
SL5P5C5–56	18573	50247	118.94	25.5
SL3P5C5–56	11222	35709	139	26.1
SL1P5C5–56	43059	187187	109.93	27.29
SL5P5C10–56	87904	273839	201.63	28.08
SL3P5C10–56	17363	147351	110.03	25.83
SL1P5C10–56	33200	129659	147.23	25.93
SL5P5C15–56	19053	46803	109.05	25.48
SL3P5C15–56	43495	100352	114.62	26.38
SL1P5C15–56	20295	56752	107.7	26.08
SL5P5C20–56	11071	35590	82.89	26.76
SL3P5C20–56	35508	98898	77.81	26.45
SL1P5C20–56	18121	81154	112.1	26.22
SL5P5C5–90	53584	193283	92.24	26.71
SL3P5C5–90	32623	126385	115.85	27.2
SL1P5C5–90	28028	118113	92.13	28.06
SL5P5C10–90	87120	312102	46.73	30.47
SL3P5C10–90	28968	109218	92.23	27.04
SL1P5C10–90	25818	111249	124.08	27.03
SL5P5C15–90	37905	143936	96.59	26.57
SL3P5C15–90	25643	98753	98.6	27.7
SL1P5C15–90	15198	58643	95.24	27.4
SL5P5C20–90	23632	90397	70.43	28.63
SL3P5C20–90	18643	66262	56.45	27.55

3.7.2 Long–term and Short–Term Serdang Landslide Case Study Using FEM

In this section, a couple of simulation for long–term and short–term behaviours under loading were investigated relying on dimensions of open flood channel using the parameters of natural marine clay and the optimum treated marine clay using L–POFA–CS optimal ratios.

3.7.2.1 Case History of Case Study

Landslide occurred on January 25th 2022, in Lestari Perdana, Serdang, Selangor, Malaysia, see Figure 3.15. The pictures show deep squared cross–sectional open channel before the landslide, see Figure 3.16. The channel was constructed for guiding the collected water of floods from the heavy rainfall to Taman Putra Permainan Lake, Puchong, Malaysia. The channel is U–section with depth of 6 meters and width of 10 meters. The section has failed after series of heavy rainfall during the wet season in

Malaysia (heavy rainfall season form November to March). The site condition shown that the area was under construction and preparation in 2001, see Figure 3.17. By comparing the failure pictures shown in Figure 3.18, it is contoured that there is no replacement for the natural soil beneath the pavement layers. In addition, the failure shape illustrates that the soil is containing significant amount of fines (silt and clay) that makes the failure shape vertical, which is critical in failure.

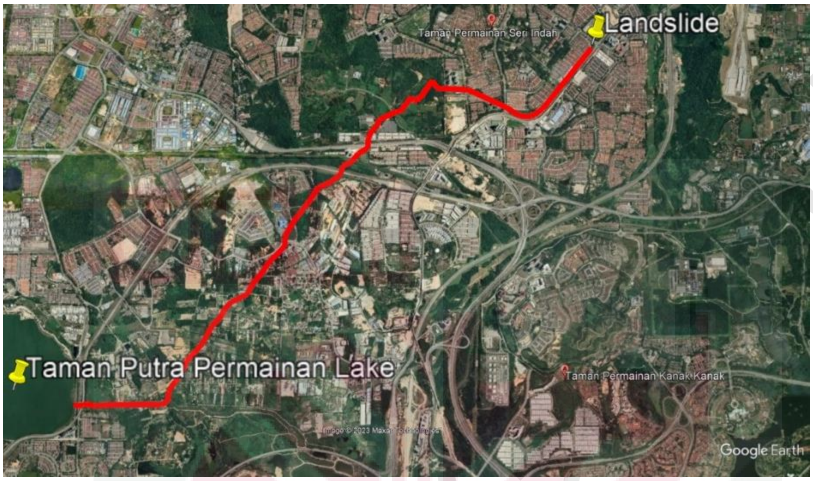

Figure 3.15: Location of landslide in Lestari Perdana (101°40'27.48"E, 2°59'33.70"N) and Taman Putra Permainan Lake (101°36'34.23"E, 2°57'12.16"N), and the red line represents the channel path

Figure 3.16: The area before landslide failure (Date of picture January 2021)

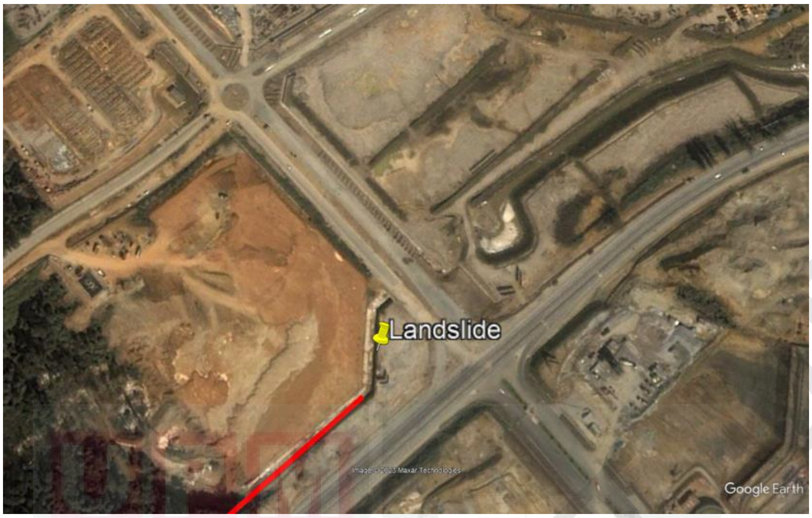

Figure 3.17: Site condition since 2001 showing the soil type in the construction area not changed

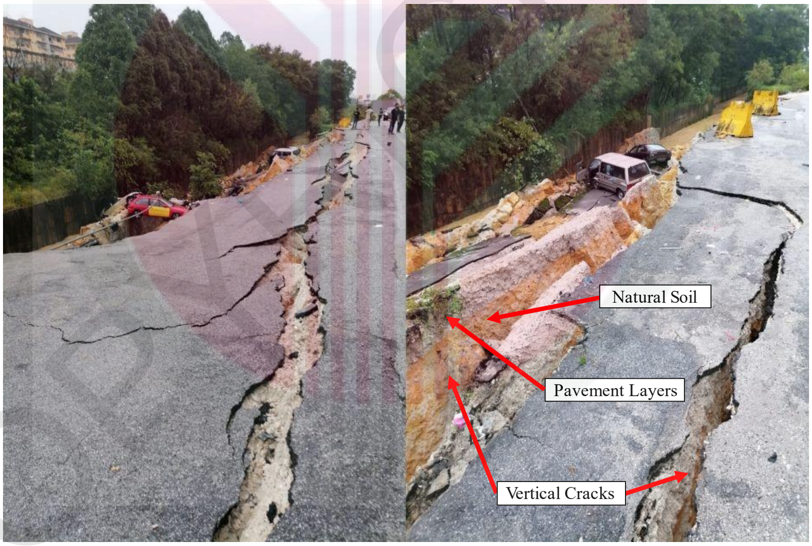

Figure 3.18: Landslide failure showing cracks condition since 2001 showing the soil type in the construction area not changed

3.7.2.2 Finite Element Modelling for Channel Section Stability

The study case is based on two models; (1) modelling of the natural soil for the structure (natural soil with no replacement), and (2) modelling of the soil replacement using the optimum ratio of L–POFA–CS based on the results conducted in Section

3.6.2. The study was based on the two loading conditions; short–term and long–term. FEM was assessed using the PLAXIS 2D V22. The model is shown in Figure 3.19. Using PLAXIS modelling is constrained for the mesh generation as the mesh is automatically generated by the program, which constrains with studding specific points, regardless the auto refining for the mesh at special elements. In addition, the soil definitions are related to natural and improved soils' properties conducted thought the laboratory investigations as shown in Table 3.9. Tables 3.10, 3.11 and 3.12 show canal section properties, retaining wall and loads respectively, where the channel was 20 m width, 6 m heigh with additional extension of 3 m wall height at the buildings side.

The used parameters shown in tables are the inputs for the PLAXIS models, where Young's modulus E, permeability k, and Poisson's ratio ν as the physical properties, drained internal angle of friction $\boldsymbol{\phi}'$, drainded cohesion $\boldsymbol{C}'$, and angle of dilation $\boldsymbol{\psi}$ for the mechanical properties, and wall thickness t, area of perimeter A and moment of inertia I for the channel section properties. The soil layer modeling was assumed to be a thickness of 25 metres and 100 m width to not restrain the deformations during the analysis and not to affect the results. The water table was assumed to be in the level of the water channel of a height 4 m, where for the construction phase modeling the water table was drained in the area of construction only. The buildings and traffic loads where assumed to be the maximum loads for the design as per BS 6399–1 building code practice (1996).

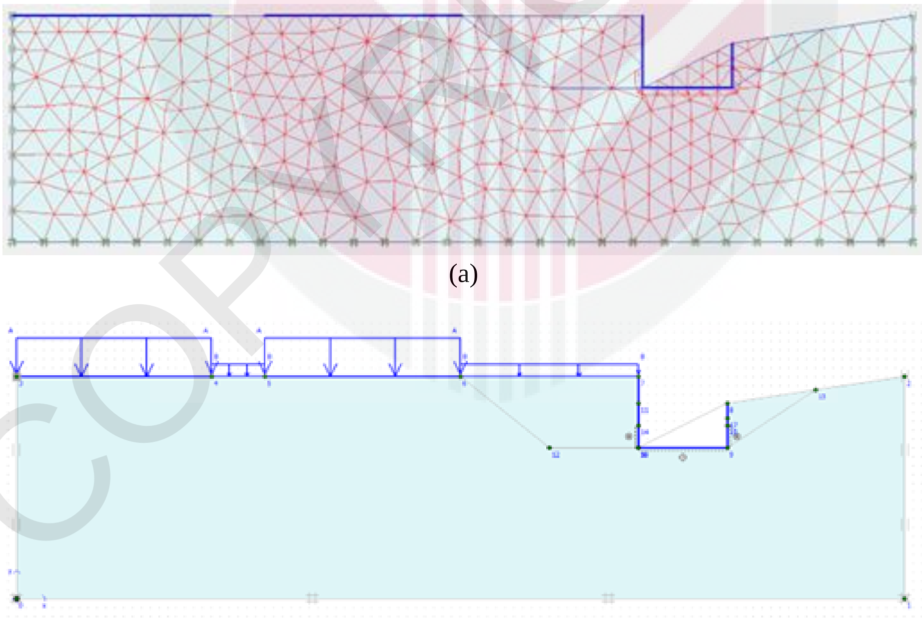

(a)

(b)

Figure 3.19: FEM model of open channel in PLAXIS showing (a) mesh and (b) loads and current section

Table 3.9: The data used in FEM using Open Channel Modelling in PLAXIS

Factor	E	ϕ'	ν	C'	ψ	k	E_{oed}	E_{ur}
(Units)	(GPa)	(o)	(kPa)		(o)	(m/yr)	(MPa)	(MPa)
S	1.22	19.51	0.2	61.07	0	1.20E–05	8823	29341
SL5P5C10–90	7.7509	30.47	0.2	46.73	0	1.30E–06	87120	312102

Table 3.10: Retaining Wall Input to PLAXIS Model

Property		Unit	Value
Young modulus	E	kN/m^2	29771100
Poisson ratio	ν		0.25
Thickness	t	m	0.3
Area of Perimeter	A	m^2	0.3
Moment of Inertia	I	m^4	0.00225
	EA	kN/m	8931330
	EI	kN.m^2	66984.98

Table 3.11: Concrete Channel/Canal Input to PLAXIS Model

Property		Unit	Value
Young modulus	E	kN/m^2	29771100
Poisson ratio	ν		0.25
Thickness	t	m	0.5
Area of Perimeter	A	m^2	0.5
Moment of Inertia	I	m^4	0.010416667
	EA	kN/m	14885550
	EI	kN.m^2	310115.625

Table 3.12: Building details input to PLAXIS Model

Level	LL	SIDL	DL	Total
Roof	2	$0.10 * 22$	$0.20 * 25$	
1st Floor	4	$0.15 * 22$	$0.20 * 25$	
Ground Floor	4	$0.25 * 22$	$0.40 * 25$	
Total	10	11	20	41

3.8 Artificial Intelligence Data Analysis

The artificial intelligence AI algorithms were used to analyze and obtain the data prediction accuracy using virtual programming module VPM called KNIME. The data prediction was applied using several AI algorithms.

3.8.1 Analysis of Collected Data

3.8.1.1 Datasets Analysis

The data was analyzed using statistical methods for data hypothesis using KNIME. The standard deviation, mean, median, skewness, kurtosis and variance were conducted as pervious research mentioned (Chai et al., 2014; Kim et al., 2018; Sprent et al., 2004). In addition, t–test, t–paired–test, kolmogorov–samirnov, and Bland–Atlman plot data hypothesis test were assessed using KNIME tools as shown in Figure 3.20.

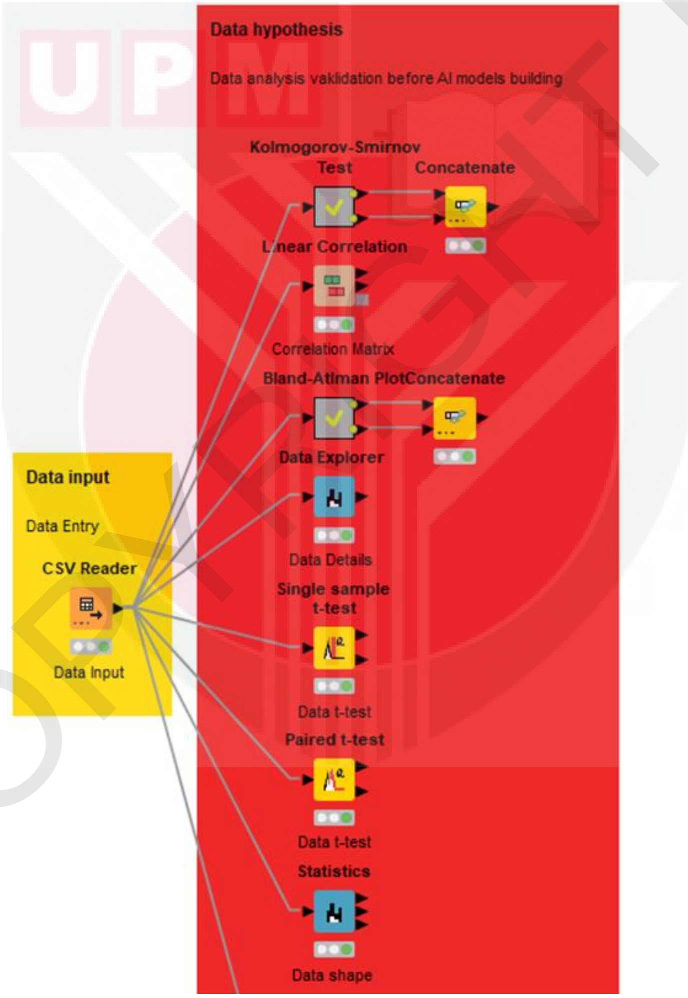

Figure 3.20: KNIME tools for data hypothesis and analysis

3.8.1.2 ANOVA Analysis

The data was analyzed using multivariant ANOVA (analysis of variation) test as a statistical analyzing method as the data was depending on four different independent variables, which are: undrained shear strength UCS, total and effective cohesion (C_u and C') and internal angle of friction (ϕ_u and ϕ') with the relation to cases of study (Case 1 and Case 2). The multivariant ANOVA test was used as the factors affecting the results are various. The data shown in Table 3.13 was analyzed using IBM SPSS Statistics 26 program.

Table 3.13: The analyzed data by IBM SPSS Statistics 26 program

ID	q_u	C'	ϕ'	C_u	ϕ_u	Case
3	0.84	134.86	24.22	73.94	19.47	S+3%L+5%P+x%C (Case 2)
3	1.55	224.78	25.12	52.97	20.83	S+1%L+5%P+x%C (Case 2)
3	1.26	126.06	24.52	34.9	20.14	S+5%L+5%P+x%C (Case 2)
3	0.88	156.13	24.5	129.8	19.18	S+3%L+5%P+x%C (Case 2)
3	1.22	132.2	24.16	44.92	20.77	S+1%L+5%P+x%C (Case 2)
3	0.72	135.99	24.52	80.39	19.17	S+5%L+5%P+x%C (Case 2)
3	0.52	118.39	24.22	102.45	17.42	S+3%L+5%P+x%C (Case 2)
3	1.02	106.04	25.01	59.04	19.41	S+1%L+5%P+x%C (Case 2)
3	0.56	90.28	24.48	49.82	17.82	S+5%L+5%P+x%C (Case 2)
3	0.45	122.78	24.69	38.5	17.69	S+3%L+5%P+x%C (Case 2)
3	1.24	118.94	25.5	33.2	19.64	S+1%L+5%P+x%C (Case 2)
3	1.09	139	26.1	46.47	20.29	S+5%L+5%P+x%C (Case 2)
3	0.84	109.93	27.29	88	19.06	S+3%L+5%P+x%C (Case 2)
3	1.66	201.63	28.08	61.76	21.02	S+1%L+5%P+x%C (Case 2)
3	1.31	110.03	25.83	52.48	19.73	S+5%L+5%P+x%C (Case 2)
3	0.89	147.23	25.93	140.35	18.76	S+3%L+5%P+x%C (Case 2)
3	1.23	109.05	25.48	62.49	20.35	S+1%L+5%P+x%C (Case 2)
3	0.75	114.62	26.38	92.7	18.75	S+5%L+5%P+x%C (Case 2)
3	0.52	107.7	26.08	116.51	17.01	S+3%L+5%P+x%C (Case 2)
3	1.09	82.89	26.76	73.1	19	S+1%L+5%P+x%C (Case 2)
3	0.64	77.81	26.45	65.63	17.4	S+5%L+5%P+x%C (Case 2)
3	0.45	112.1	26.22	54.31	17.28	S+3%L+5%P+x%C (Case 2)
3	1.21	92.24	26.71	45.5	19.22	S+1%L+5%P+x%C (Case 2)
3	1.1	115.85	27.2	60.53	19.87	S+5%L+5%P+x%C (Case 2)
3	0.84	92.13	28.06	102.06	18.64	S+3%L+5%P+x%C (Case 2)
3	1.79	46.73	30.47	177.12	20.6	S+1%L+5%P+x%C (Case 2)
3	1.1	92.23	27.04	164.81	19.31	S+5%L+5%P+x%C (Case 2)
3	0.89	124.08	27.03	152.65	18.34	S+3%L+5%P+x%C (Case 2)
3	1.24	96.59	26.57	80.07	19.93	S+1%L+5%P+x%C (Case 2)
3	0.72	98.6	27.7	106.76	18.33	S+5%L+5%P+x%C (Case 2)
3	0.52	95.24	27.4	149.9	16.59	S+3%L+5%P+x%C (Case 2)
3	0.91	70.43	28.63	87.16	18.58	S+1%L+5%P+x%C (Case 2)
3	0.61	56.45	27.55	79.69	16.98	S+5%L+5%P+x%C (Case 2)
3	0.45	87.17	28.2	73.85	16.86	S+3%L+5%P+x%C (Case 2)

Table 3.13: Continued

ID	q_u	C'	ϕ'	C_u	ϕ_u	Case
1	0.36	61.07	19.51	38.64	12.84	S (Control Sample)
2	0.89	116.82	20.14	64.28	15.89	S (Control Sample)
2	0.92	110.65	21.21	69.55	16.39	S+5%L+x%P (Case 1)
2	0.94	86.11	24.5	81.37	17.51	S+5%L+x%P (Case 1)
2	0.73	68.03	21.21	69.55	15.07	S+5%L+x%P (Case 1)
2	0.59	56.91	20.66	57.73	15.27	S+5%L+x%P (Case 1)
2	0.56	59.51	20.5	58.22	15.31	S+5%L+x%P (Case 1)
3	0.99	79.77	22.65	1.38	17.39	S+5%L+x%P (Case 1)
3	0.96	98.05	22.92	1.37	19.62	S+5%L+5%P+x%C (Case 2)
3	0.8	79.67	22.9	2	16.8	S+3%L+5%P+x%C (Case 2)
3	1.08	99.67	23.27	3.56	19.69	S+1%L+5%P+x%C (Case 2)
3	0.98	72.64	22.87	4.09	19.14	S+5%L+5%P+x%C (Case 2)
3	0.82	84.91	23.3	8.26	18.84	S+3%L+5%P+x%C (Case 2)
3	1.03	66.32	23.06	46.7	18.77	S+1%L+5%P+x%C (Case 2)
3	0.64	62.99	22.98	64.28	17.16	S+5%L+5%P+x%C (Case 2)
3	0.5	57.85	22.9	121.35	6.58	S+3%L+5%P+x%C (Case 2)
3	0.74	56.18	22.81	117.29	17.41	S+1%L+5%P+x%C (Case 2)
3	0.42	56.45	22.94	113.23	15.82	S+5%L+5%P+x%C (Case 2)
3	0.41	58.68	22.93	104.59	15.69	S+3%L+5%P+x%C (Case 2)
3	1.07	92.24	22.65	10.35	19.89	S+1%L+5%P+x%C (Case 2)
3	0.99	114.07	23.03	20.1	20.37	S+5%L+5%P+x%C (Case 2)
3	0.82	93.91	23.34	28.58	19.31	S+3%L+5%P+x%C (Case 2)
3	1.26	171.16	23.96	48.79	19.4	S+1%L+5%P+x%C (Case 2)
3	1.1	95.79	23.2	105.41	19.98	S+5%L+5%P+x%C (Case 2)
3	0.84	111.62	23.3	128.33	19.68	S+3%L+5%P+x%C (Case 2)
3	1.11	85.91	23.28	37.56	21.27	S+1%L+5%P+x%C (Case 2)
3	0.65	89.7	23.42	43.13	19.67	S+5%L+5%P+x%C (Case 2)
3	0.5	75.65	22.9	38.1	17.92	S+3%L+5%P+x%C (Case 2)
3	0.85	73.99	23.14	45.13	19.92	S+1%L+5%P+x%C (Case 2)
3	0.47	67.13	23.38	48.7	18.32	S+5%L+5%P+x%C (Case 2)
3	0.42	72.92	23.15	51.75	18.19	S+3%L+5%P+x%C (Case 2)
3	1.15	117.16	22.76	13.87	20.31	S+1%L+5%P+x%C (Case 2)
3	1.02	130.1	23.47	25.38	20.79	S+5%L+5%P+x%C (Case 2)
3	0.83	118.84	23.45	37.37	19.72	S+3%L+5%P+x%C (Case 2)
3	1.46	207.03	24.55	9.79	23.26	S+1%L+5%P+x%C (Case 2)
3	1.24	111.81	23.64	26.12	20.39	S+5%L+5%P+x%C (Case 2)
3	0.87	131.2	23.52	121.01	19.43	S+3%L+5%P+x%C (Case 2)
3	1.19	110.83	23.61	36.13	21.02	S+1%L+5%P+x%C (Case 2)
3	0.7	111.06	23.97	54.03	19.42	S+5%L+5%P+x%C (Case 2)
3	0.51	91.68	23.12	58.51	17.67	S+3%L+5%P+x%C (Case 2)
3	0.92	86.45	23.36	44.98	19.66	S+1%L+5%P+x%C (Case 2)
3	0.51	79.59	23.38	41.03	18.07	S+5%L+5%P+x%C (Case 2)
3	0.43	97.85	23.59	47.28	17.94	S+3%L+5%P+x%C (Case 2)
3	1.24	142.09	23.53	22.65	20.06	S+1%L+5%P+x%C (Case 2)
3	1.05	156.81	24.56	34.16	20.54	S+5%L+5%P+x%C (Case 2)

3.8.2 Models Definition

The models were defined based on the type of conducted data from the experiments applied. The data were classified based on the models as shown in Table 3.14. However, AI feature selection was used to select the best features based of accuracy of the predicted data as shown in Table 3.15.

Table 3.14: Models definition showing target and features

Model	**Targets Features**
Model 1	Undrained Compressive Strength, Duration & Treating Materials Ratio
Model 2	Undrained Compressive Strength & Physical Properties
Model 3	Undrained Compressive Strength & Flexural Strength
Model 4	Undrained Compressive Strength & Chemical Content
Model 5	Undrained Compressive Strength & Consolidation Parameters
Model 6	Undrained Compressive Strength & Compaction Parameters
Model 7	Undrained Compressive Strength & All Parameters
Model 8	CU stress–strain, Duration & Treating Materials Ratio

Table 3.15: Models definition showing target and features using AI

Model	**Targets Features**
Model 9	Undrained Compressive Strength Genetic Feature Selection
Model 10	Undrained Compressive Strength Forward Feature Selection
Model 11	Undrained Compressive Strength Backward Feature Elimination

3.8.3 Used Algorithms for Prediction and Optimization

The algorithms employed were both simple and hybrid algorithms. The used algorithms with the proposed feature selections based as defined in Section 3.6.1 are as follows: (1) Linear regression LR, (2) Polynomial regression PR (3) Random Forest regression RF, (4) Multilayer regression MLR (ANN) (5) Gradient boost tree regression GBoost, and (6) Simple regressing tree STR where the used method is called eXtreme Gradient Boost xGBoost.

Machine learning depends on training, validating and test sets. Training set is defined as a set of inputs and outputs which the algorithm begins to "learn" the relationships hidden in the data set by changing the weightings (Mair et al., 2000). On the other hand, test set is a set used for testing the predicted model and evaluate the algorithm prediction accuracy and efficiency, where the test set could be part of same distribution of the training data, or new data. Labelled data in test sets is typically regarded as "accurate" as long as it is chosen from the same distribution as the train set. This is untrue: ML benchmarks can become unstable as a result of flaws in machine learning test sets, which can and do exist (Northcutt et al., 2021). Furthermore, data mining is feedbacked using validation data set, where it can be data out of distribution of both training and testing data, part or, whole distribution of both training and testing data.

The models were created by the method of partitioning or splitting the data into training data and testing data. The cross–validation method was used was based of five iteration method, where the ratios are 80% for training and 20% for testing as shown in Figure 3.21. On the same hand, the user interface for cross–validation in KNIME is shown in Figure 3.22 and 3.23 showing the method of process assessment. Besides, the validation data set is the whole data.

Figure 3.21: Cross–validation idea for assessment the highest accuracy using 5 iterations.

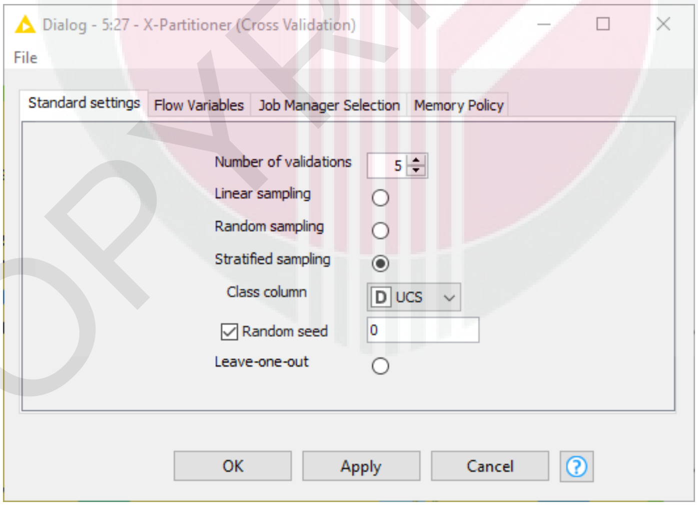

Figure 3.22: Cross–validation idea for assessment the highest accuracy using 5 iterations.

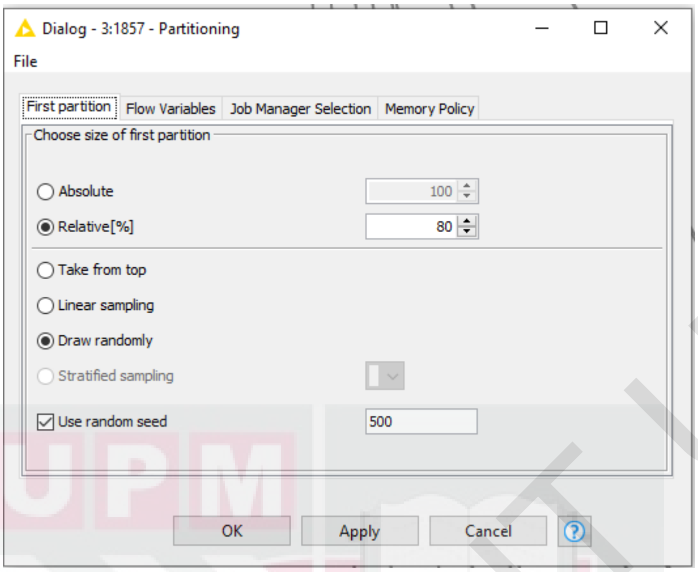

Figure 3.23: Partitioning idea for assessment the highest accuracy.

3.8.3.1 Linear Regressor Algorithm

This algorithm carries out a multiple linear regression. The response is selected as the target column in the dialog's top combo box as shown in Figure 3.24 and the program structure is shown in Figure 3.25. Accordingly, the shear strength was selected as dependent column and the other features as columns that reflect the independent variables in the two lists in the dialog's centre. Linear regression algorithms is working by the procedure as shown in Equations 3.5 to 3.9 which assumes that the relationship between the dependent and independent variables is linear.

$$y = \beta_0 + \beta_1 x_1 + \beta_2 x_2 + \cdots + \beta_p x_p \tag{3.5}$$

$$y = x\,\beta + \epsilon \tag{3.6}$$

$$y = \begin{bmatrix} y_1 \\ y_2 \\ \vdots \\ y_n \end{bmatrix} \tag{3.7}$$

$$X = \begin{bmatrix} x_{11} & x_{12} & \cdots & x_{1p} \\ x_{21} & x_{22} & \cdots & x_{2p} \\ \vdots & \vdots & \ddots & \vdots \\ x_{n1} & x_{n2} & \cdots & x_{np} \end{bmatrix} \tag{3.8}$$

$$\beta = \begin{bmatrix} \beta_1 \\ \beta_2 \\ \vdots \\ \beta_p \end{bmatrix}, \ \epsilon \ = \begin{bmatrix} \epsilon_1 \\ \epsilon_2 \\ \vdots \\ \epsilon_n \end{bmatrix} \tag{3.9}$$

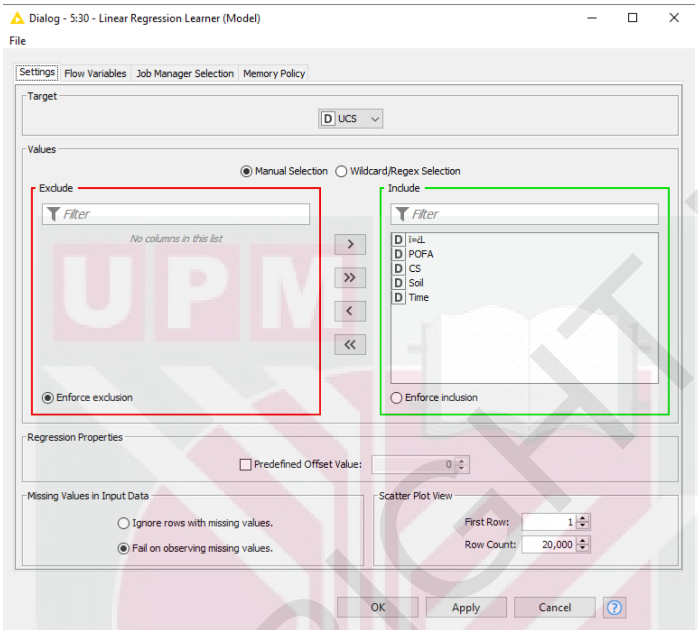

Figure 3.24: Linear regression analysis model number 1 showing the target and the independent variables in KINME

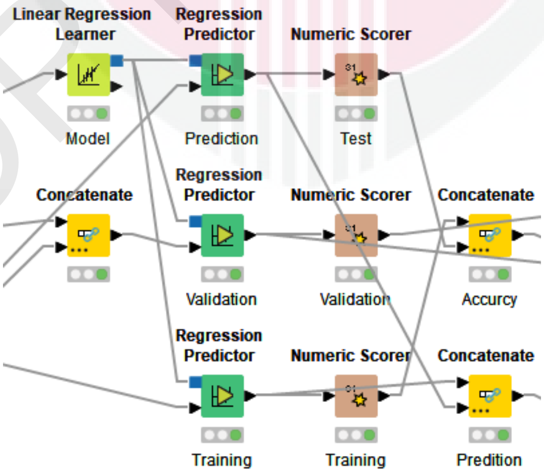

Figure 3.25: Linear regression analysis structure in KINME

3.8.3.2 Polynomial Regressor Algorithm

This algorithm computes the coefficients that minimise the squared error using polynomial regression on the supplied data as the algorithm structure in KINME as shown in Figure 3.26, where the structure is looped to get the maximum accuracy based on the ML degree selection. The independent variables, single target column as the dependent variable, and polynomials of degrees are defined as shown in Figure 3.27. The polynomial regressor algorithm is assuming that the relationship between the independent variables and the dependent variables are non–linear following the Equations 3.10 to 3.13.

$$y = \beta_0 + \beta_{1x} + \beta_{2x}^2 + \cdots + \beta_{px}^p \tag{3.10}$$

$$\begin{bmatrix} y_1 \\ y_2 \\ y_3 \\ \vdots \\ y_n \end{bmatrix} = \begin{bmatrix} 1 & x_1 & x_1^2 & \cdots & x_1^m \\ 1 & x_2 & x_2^2 & \cdots & x_2^m \\ 1 & x_3 & x_3^2 & \cdots & x_3^m \\ \vdots & \vdots & \vdots & \ddots & \vdots \\ 1 & x_n & x_n^2 & \cdots & x_n^m \end{bmatrix} \begin{bmatrix} \beta_0 \\ \beta_1 \\ \beta_2 \\ \vdots \\ \beta_p \end{bmatrix} + \begin{bmatrix} \epsilon_1 \\ \epsilon_2 \\ \epsilon_3 \\ \vdots \\ \epsilon_n \end{bmatrix} \tag{3.11}$$

$$\hat{y}_{ij} = X\,\hat{\beta} + \epsilon \tag{3.12}$$

$$\hat{\beta} = (X^T X)^{-1} X^T \hat{y} \tag{3.13}$$

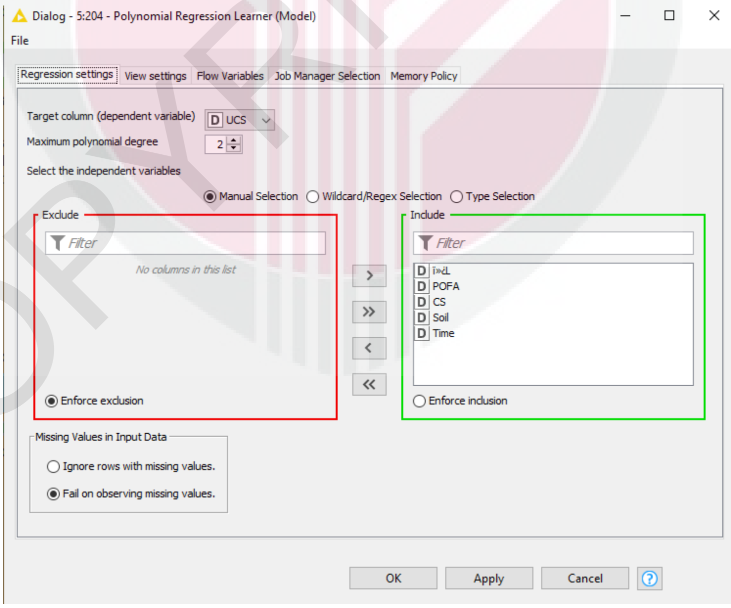

Figure 3.26: Polynomial regression analysis model number 1 showing the target, the independent variables and polynomial degrees in KINME

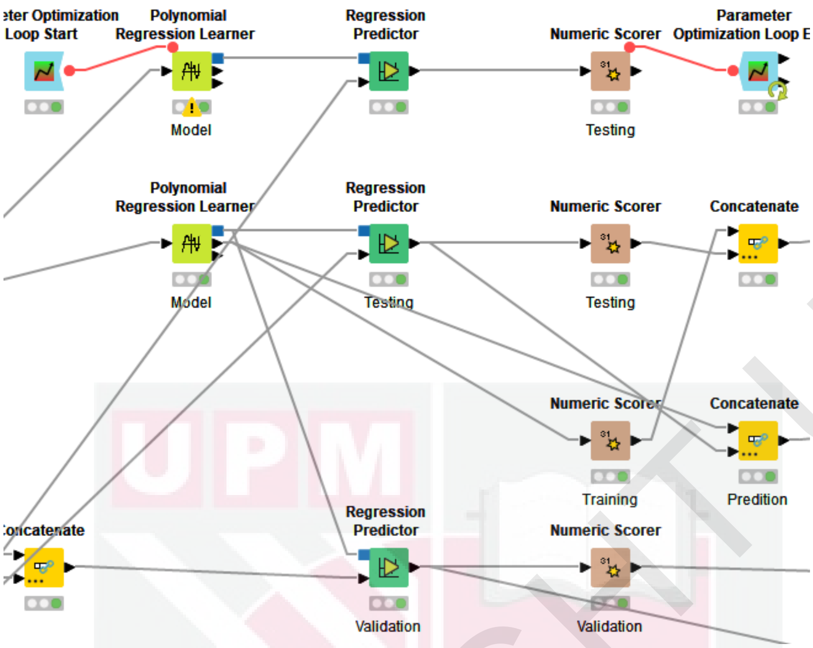

Figure 3.27: Polynomial regression structure in KINME

3.8.3.3 Multilayer Regressor Algorithm

Previous research demonstrated the advantages of local adaptation techniques over global learning algorithms by pointing out that they are more directly tied to the idea of neural learning and are more suitable for parallel implementations. Resilient propagation, or RPROP, is an effective new learning strategy that directly adapts the weight step depending on local gradient information. The effort of adaptation is in no way obscured by gradient behaviour, which is a critical distinction from previously developed adaptation strategies. To assess that, a unique weight is achieved its unique update–value Δ_{ij}, which exclusively controls the magnitude of the weight–update. The following learning rule governs how this adaptive update value changes as learning progresses depending on its local sight on the error function E as shown in Equations 3.14 and 3.15.

$$\Delta\omega_{ij}^{t} = \begin{cases} \eta^{-} * \Delta_{ij}^{t} & ,if \ \left(\frac{\partial\epsilon}{\partial\omega_{ij}}\right)^{t-1}\left(\frac{\partial\epsilon}{\partial\omega_{ij}}\right)^{t} > 0 \\ \eta^{+} * \Delta_{ij}^{t} & if \ \left(\frac{\partial\epsilon}{\partial\omega_{ij}}\right)^{t-1}\left(\frac{\partial\epsilon}{\partial\omega_{ij}}\right)^{t} < 0 \\ 0 & else \end{cases} \tag{3.14}$$

$$0 < \eta^{-} < 1 < \eta^{+} \tag{3.15}$$

The adaptation–rule is expressed as follows: The update–value Δ_{ij} is reduced by the factor η^{-} each time the partial derivative of the corresponding weight Δ_{ij} changes its sign, indicating that the most recent update was too large, and the algorithm had leaped over a local minimum. The update–value is somewhat raised to hasten convergence in shallow places if the derivative keeps its sign. After each weight's update–value has been adjusted, the weight update itself adheres to a relatively straightforward rule: if the derivative is positive (increasing error), the weight is reduced by its update–value, and if the derivative is negative, the update–value is added as shown in Equations 3.16 and 3.17 (Riedmiller et al., 1993).

$$\Delta\omega_{ij}^{(t)} = \begin{cases} -\Delta_{\mathrm{ij}}^{(\mathrm{t})} & , \text{ if } \left(\frac{\partial\epsilon}{\partial\omega_{\mathrm{ij}}}\right)^{\mathrm{t}} > 0 \\ +\Delta_{\mathrm{ij}}^{(\mathrm{t})} & , \text{ if } \left(\frac{\partial\epsilon}{\partial\omega_{\mathrm{ij}}}\right)^{\mathrm{t}} < 0 \\ 0 & , \; else \end{cases} \tag{3.16}$$

$$\omega_{ij}^{(t+1)} = \omega_{ij}^{(t)} + \Delta\omega_{ij}^{(t)} \tag{3.17}$$

The structure of the algorithm in KNIME is shown in Figure 3.28, while the independent variables, single target column as the dependent variable, number of neurons and number of layers are defined as shown in Figure 3.29.

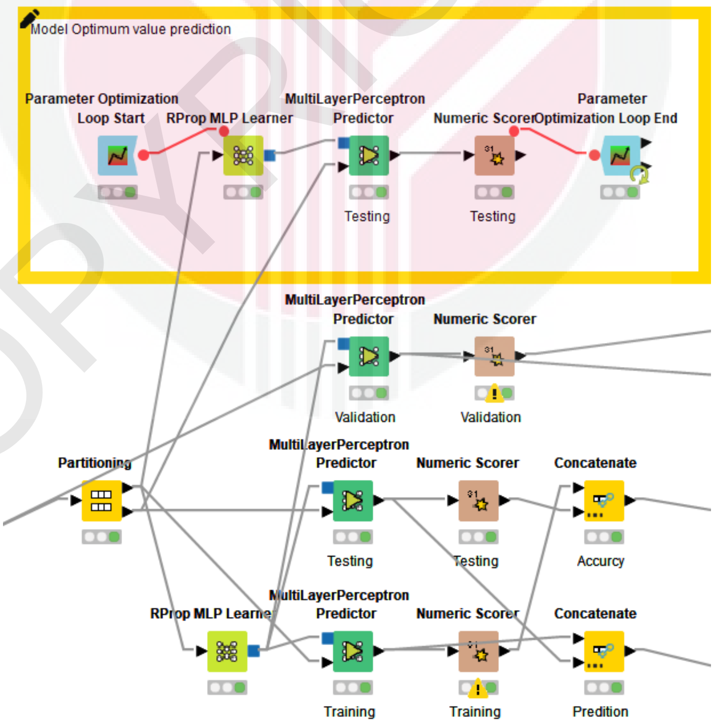

Figure 3.28: Multilayer regression analysis structure in KINME

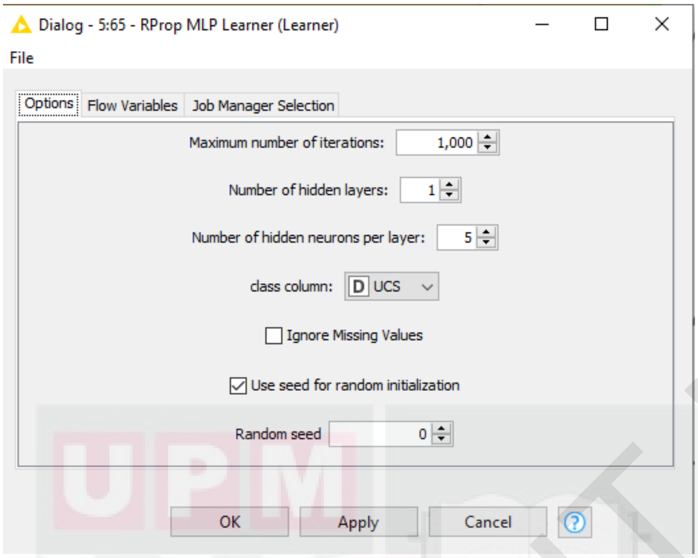

Figure 3.29: Multilayer regression analysis model number 1 showing the target, the independent variables, number of neurons and number of layers in KINME

3.8.3.4 Gradient Boost Tree Algorithm

Gradient boosted model is by definition a weighted linear combination of the base learners as shown in Equation 3.18, where $h(x; a)$ is a base learner parameterized by a. Although the basic learners are weak learners and only produce hypotheses that forecast somewhat better than random guessing, it has been demonstrated that recursive learning with weak learners can perform just as well as a powerful learning system (Zhiyuan He et al., 2019). Binary splits are used to build decision trees, and recursive splits produce a big tree that is then pruned to remove the weak branches as the optimized process as shown in Equation 3.19, where the steps of consecutive boosting are $P^* = \sum_{m=0}^{M} P_m$ and P_m. the steepest decent algorithm for creating the gradient is used in generating these steps as shown in Equations 3.20, where the boosting steps are given in Equations 3.21 and 3.22. GBoost structure in KNIME is shown in Figure 3.30, while the independent variables, and learning rater are defined as shown in Figure 3.31.

$$F(x; \beta_m, \alpha_m\}_1^M) = \sum_{m=1}^{M} \beta_m h(x : \alpha_m), \tag{3.18}$$

$$P^* = argmin\ \Phi(P)\Phi(P) = E_{y,x}L\big(y, F(x; P)\big)F^*(x) = F(x; P^*), \tag{3.19}$$

$$g_m = \{g_{jm}\} = \left\{ \frac{\delta\phi(P)}{\delta P_j} \bigg|_{P=P_{m-1}} \right\} \tag{3.20}$$

$$P_{m-1} = \sum_{i=0}^{m-1} p_i \tag{3.21}$$

$$p_m = -\rho_m g_m \tag{3.22}$$

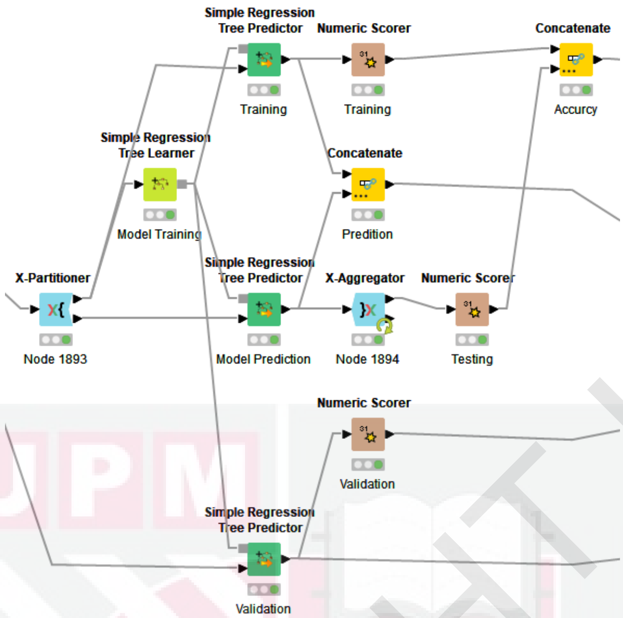

Figure 3.30: GBoost trees regression analysis structure in KINME

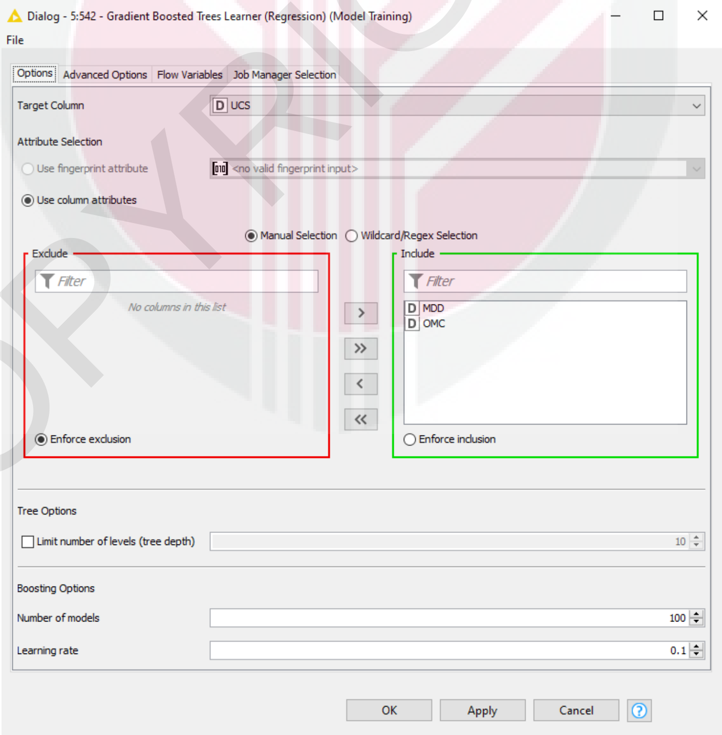

Figure 3.31: GBoost trees regression analysis model number 3 showing the target, the independent variables, and learning rate in KINME

3.8.3.5 Random Forest Tree Algorithm

Random forest is type of decision trees algorithms (Breiman, 2001). Each decision tree model is constructed using a unique collection of rows (records), and a randomly selected set of columns (describing attributes) is utilised for each split within the tree. Each decision tree's row sets are generated via bootstrapping and are the same size as the first input table. The root of attributes M are chosen at random from the available attributes, where M is the total number of learning columns, to form the attribute set for a certain split in a decision tree. Additional formats for the properties include bit, byte, and double vector. The appropriate predictor node receives the output model, which specifies an ensemble of regression tree models as shown in Figures 3.32 and 3.33 for input data and the programming structure respectively.

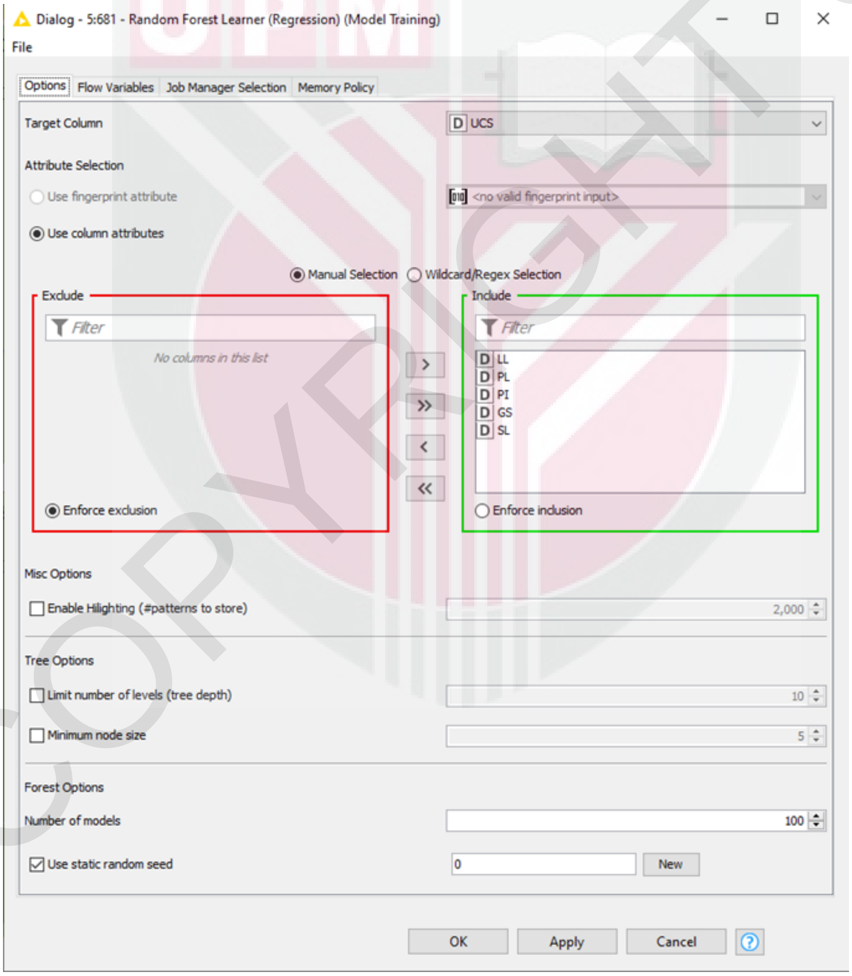

Figure 3.32: Random Forest trees regression analysis model number 1 showing the target, the independent variables, and number of models in KINME

The mean target value of the records inside a leaf node determines the predicted value for that node in a regression tree. Therefore, if there is little volatility in the target values within a leaf, the predictions will be the most accurate (in relation to the training data). Splits that reduce the sum of squared errors in their respective points are used to achieve this.

3.8.3.6 eXtreme Gradient Boost Tree Algorithm

The algorithm sends the missing values in all possible directions during each split, choosing the one that produces the best result which is the largest gain. The process, which is presented here, was modified from the well–known XGBoost algorithm (Breiman et al., 1984). Although, there have been a few simplifications made, such as not using pruning or only using binary trees in the current version. The mean target value of the records inside a leaf node determines the predicted value for that node in a regression tree. Therefore, if there is little volatility in the target values within a leaf, the predictions will be the most accurate in relation to the training data. Splits that reduce the sum of squared errors in their respective are used to achieve. The structure of the algorithm in KNIME is shown in Figure 3.34, while the input process is shown in Figure 3.35.

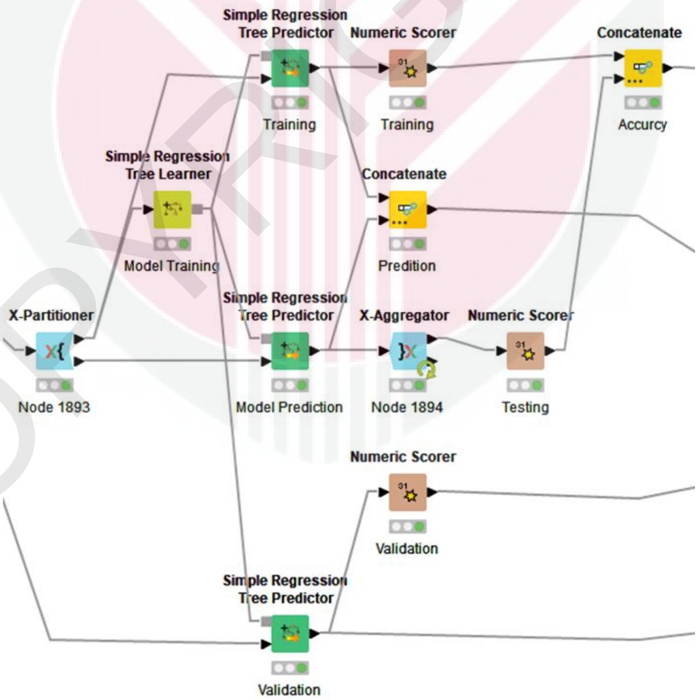

Figure 3.34: XGBoost trees regression analysis structure in KINME

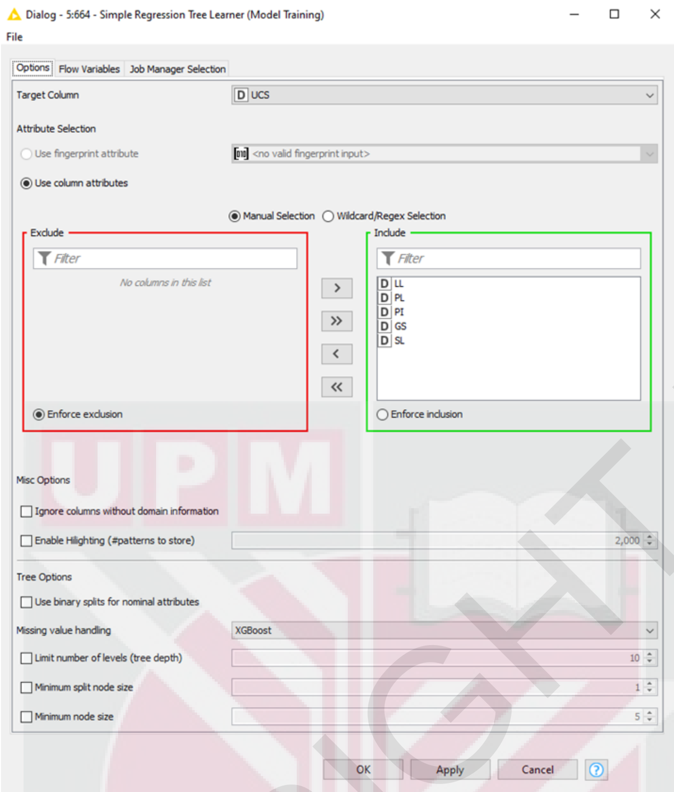

Figure 3.35: XGBoost trees regression analysis model number 1 showing the target, the independent variables, and polynomial degrees in KINME

3.8.3.7 Manual Feature Selection

Manually, the features (x_i) were based on the characteristics of the obtained and collected data as shown in Tables 3.13 and 3.14. The mentioned algorithms were applied to each model to indicate the best algorithm and the best model for predicting both drained and undrained shear strength. Accordingly, the prediction will depend on certain type of geotechnical engineering experiments and/or data used for creating the different models.

3.8.3.8 Hybrid Feature Selection

The hybrid algorithms were based on genetic feature selection, forward feature selection and backward feature elimination through AI loops depending on the accuracy of the models and the least errors as shown in Figure 3.36 and the methods of selection as shown in Figure 3.37. For the process of feature selection three algorithms were used: (1) GBoost, (2) Random Forest, and (3) XGBoost. Accordingly, all mentioned AI algorithms were repeated to detect the best accuracy after feature selection.

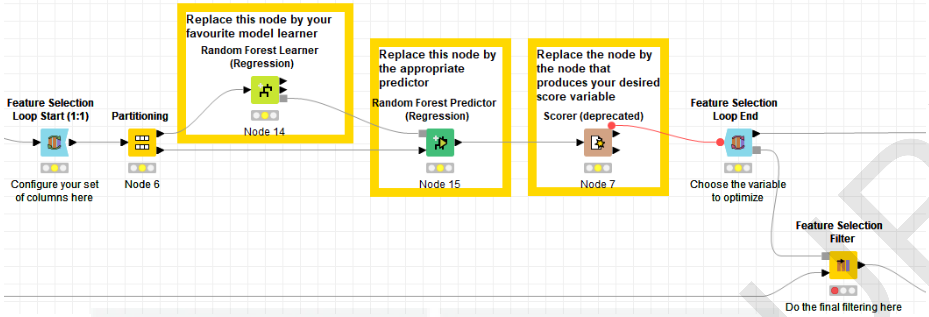

Figure 3.36: KNIME loop structure used for features selection

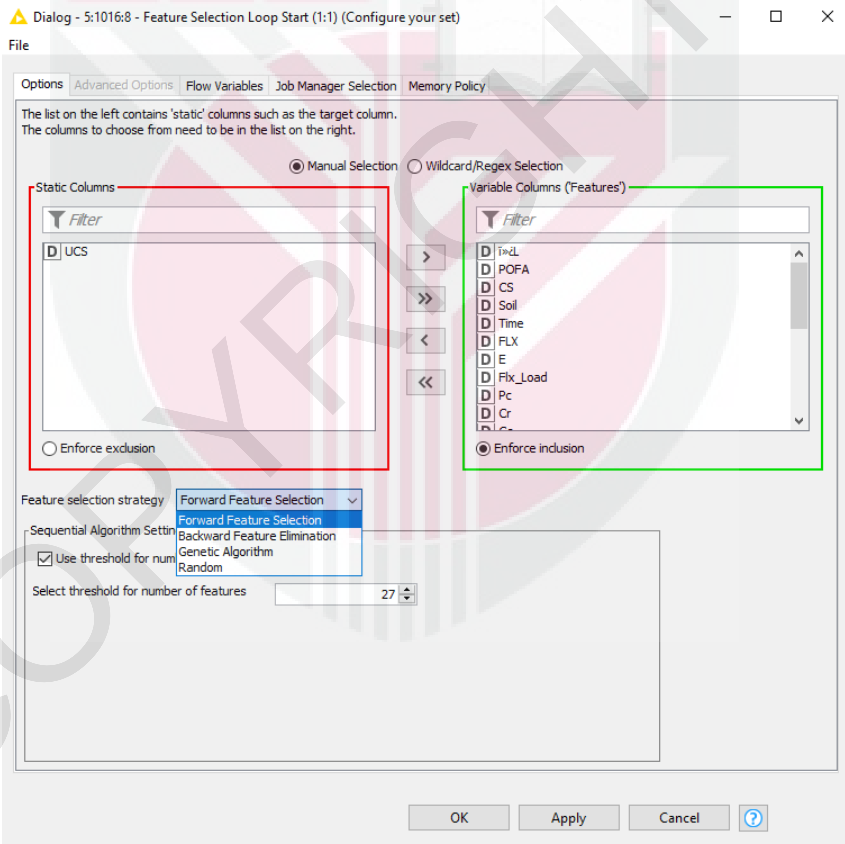

Figure 3.37: Hybrid feature selection method

3.8.4 Accuracy and Models Evaluation

The three most popular statistical indices, namely root mean squared error (RMSE), coefficient determination (R^2), and variance account for, were used to evaluate numerous artificial intelligence models. Based on the simulation results and the values of the computed indices for training and test sets, it can be compared the accuracy of both results. The mean square error MSE, root mean square error RMSE, and mean absolute error MAE were calculated, along with the coefficient of determination of mean square error R^2 value.

3.8.4.1 Evaluation Equations

Comparable metrics to evaluate the efficacy of the model's predictive capabilities were employed. Equations from 3.24 and 3.26, where m is the number of observations in the dataset, Y is the observed output (experimental value), and $\hat{Y}$ is the predicted output, are used to express these metrics.

$$\mathrm{MSE} = \frac{1}{N}\sum_{i=1}^{N}\left(Y - \hat{Y}\right)^2 \tag{3.24}$$

$$\mathrm{RMSE} = \sqrt{\frac{1}{N}\sum_{i=1}^{N}\left(Y - \hat{Y}\right)^2} \tag{3.25}$$

$$\mathrm{MAE} = \frac{1}{N}\sum_{i=1}^{N}\left|Y - \hat{Y}\right| \tag{3.26}$$

Scatter index SI and coefficient of determination R^2 are also methods of models' evaluation, where the Equations 3.27 and 3.28 are for SI and R^2 respectively, where Table 3.16 defines SI limits. In addition, mean signed error or difference MSD, mean absolute percentage error MAPE, and adjusted R^2 were conducted using Equations 3.29 to 3.31 respectively.

$$R^2 = 1 - \frac{\sum_{i=1}^{N}\left(Y_p - Y_e\right)^2}{\sum_{i=1}^{N}\left(Y_e - \widehat{Y_e}\right)^2} \tag{3.27}$$

$$\mathrm{SI} = \mathrm{RMSE}/\widehat{Y}_e \tag{3.28}$$

$$\mathrm{MSD} = \frac{\sum_{i=1}^{N}\left(Y_p - Y_e\right)}{n} \tag{3.29}$$

$$\mathrm{MAPE} = \frac{100\%}{n}\sum_{i=1}^{N}\left|\frac{Y_e - Y_p}{Y_e}\right| \tag{3.30}$$

$$\text{Adjusted } R^2 = 1 - \frac{(1-R^2)(N-1)}{N-p-1} \tag{3.31}$$

Table 3.16: Scatter index range

Range	Model Evaluation
<01	Excellent
0.1–0.2	Good
0.2–0.3	Fair
>0.3	Poor

3.8.4.2 KNIME Accuracy Tools

KNIME is providing tools for both accuracy and scattering for predicted and actual values for the whole trained and tested values. The used tools are numeric scorer tool for the trained data and tested data, and scatter plot tool, where both are shown in Figures 3.38 and 3.39 and their positions in the structure of the nodes in KNIME as shown in Figures 3.25, 3.26, 3.28, 3.30, 3.32, 3.34.

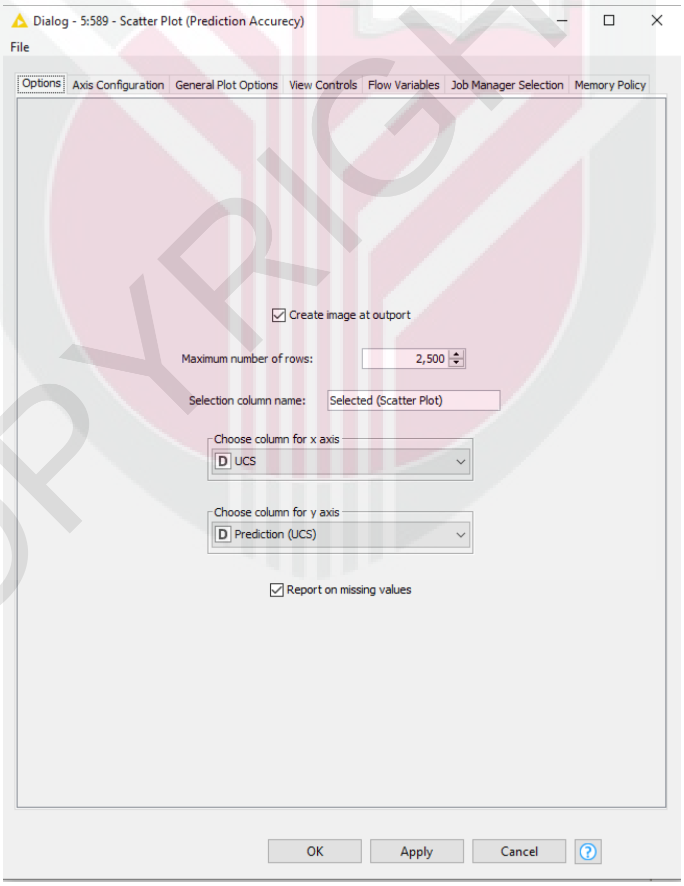

Figure 3.37: Scatter tool (node) in KNIME to visualize the actual and predicted shear strength (target) as evaluating method for the models.

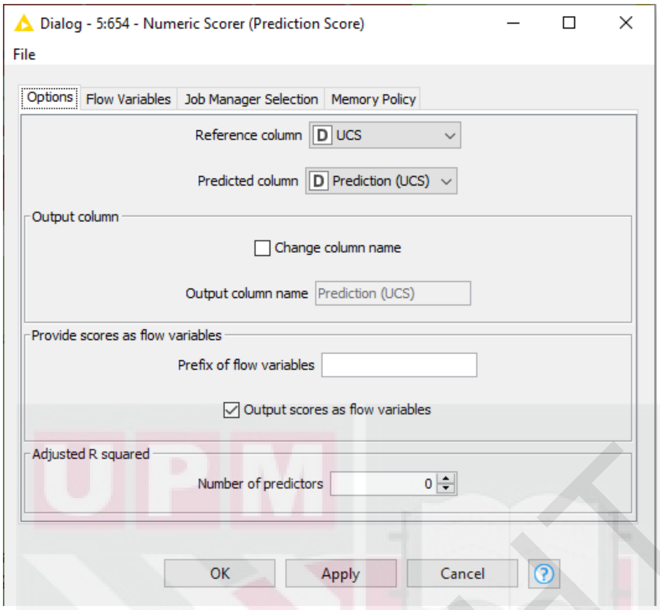

Figure 3.38: Numeric scorer tool in KINME for evaluating the models.

Finally, the best model will be the model selected with the highest score with the least error as illustrated in justification and evaluation plan through this research as shown in Figure 3.40. Accordingly, the future researchers and geotechnical engineers can use as a guide in drained and undrained shear strength of marine clay treated with green materials.

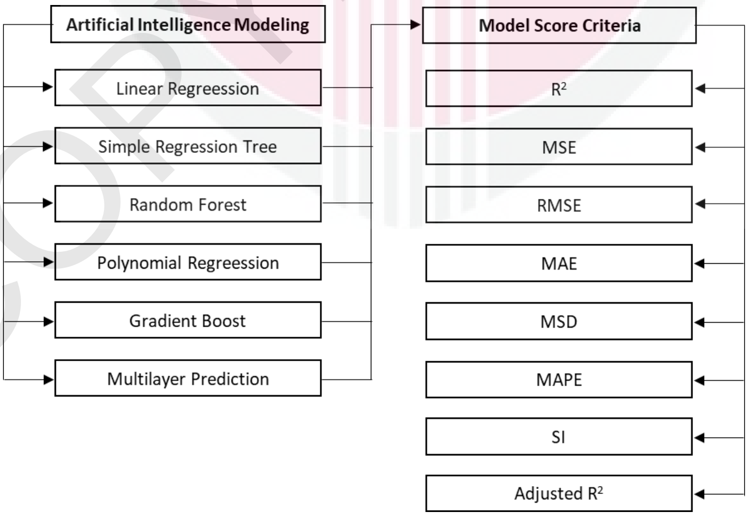

Figure 3.39: Justification and evaluation methodology for the models.

CHAPTER 4

RESULTS AND DISCUSSION

4.1 Introduction

In the current chapter, an experimental investigation was conducted with the aim of acquiring the mechanical properties of a soil reinforced with lime (L), palm oil fly ash (POFA) and calcined shale (CS). To commence the study, a comprehensive evaluation of the physical properties of the marine clay was performed. Subsequently, the behavior of POFA at various ratios was studied in conjunction with a fixed ratio of lime to assess its suitability as a soil reinforcement material. Following this, the marine clay was compacted with varying amounts of lime and calcined shale at optimal water content, incorporating the optimal POFA ratio. To observe the progression of mechanical strength over time, the reinforced specimens were subjected to testing at intervals of 7, 14, 21, 28, 56 and 90 days after treatment, under both short–term and long–term loading conditions. Furthermore, microstructural examinations were carried out to scrutinize the evolution of soil particles. The results were then compared to finite element models for triaxial samples and analyzed using machine learning techniques to discern the relationship between parameters and to develop a predictive model for the shear strength of the treated specimens under both short–term and long–term loading conditions. As a practical application, the finite element method was utilized to analyze a case study of a landslide in the Serdang area, comparing the results between the treated marine clay and the natural marine clay.

4.2 Results organization

The results discussed in the current chapter are structured into five principal sections, aligned with the objectives established in Chapter One. These sections and their respective sub–sections present the outcomes of laboratory experiments conducted during the course of the research study. The results are followed by a comprehensive discussion, providing insights and implications of each experiment. The following topics form the organization of this chapter:

1. An exploratory investigation of the original soft marine clay, aimed at providing preliminary insights.

2. An evaluation of the morphological and mechanical characteristics of soils treated with L–POFA and L–POFA–CS, using standard engineering techniques.

3. A finite element modelling approach to assess the performance of L–POFA and L–POFA–CS treated soils, providing numerical predictions and validations.

4. A finite element modelling application for geotechnical study for a landslide case to evaluate the L–POFA–CS treated marine clay as a soil fill material.

5. An exploration of the performance of L–POFA and L–POFA–CS treated soils through the application of machine learning algorithms, aimed at uncovering new trends and patterns.

4.3 Geotechnical Properties of Untreated Kuala Langat Marine Clay

Particles size distribution of Kuala Langat marine clay are presented in Table 4.1 and it is made up of 2.3% sand, and 97.7% fines. The grain size distribution shows that 2.3% of the soil is fine sand, as shown in Figure 4.1. High fractions of fine sand, silt, and clay are a common characteristic of coastal regions in Peninsular Malaysia (Anggraini et al., 2015, 2016; Azhar et al., 2018; Huat, 1994; Saad et al., 2021). The uniformity coefficient was 4.92 and the curvature was 1.08.

Table 4.1: Kuala Langat marine clay geotechnical properties

Property	**Value**				
Sieve Analysis	Sand (%)	Silt (%)	Clay (%)	USCS	
	2.3	40.7	57.0	CH	
Atterberg Limits	w_n (%)	w_{LL} (%)	w_{PL} (%)	PI	CI
	67	75.2	49.0	26.30	0.31
Physical	G_s	$\gamma_{bulk}(kg/m^3)$	$\gamma_{dry}(kg/m^3)$	Colour	
	2.56	1660 – 1796	988 – 1294	Light Grey	
Compressibility	P_C' (kPa)	C_C	C_r	C_v (m^2/yr)	
	147.5	0.200	0.086	7.88	

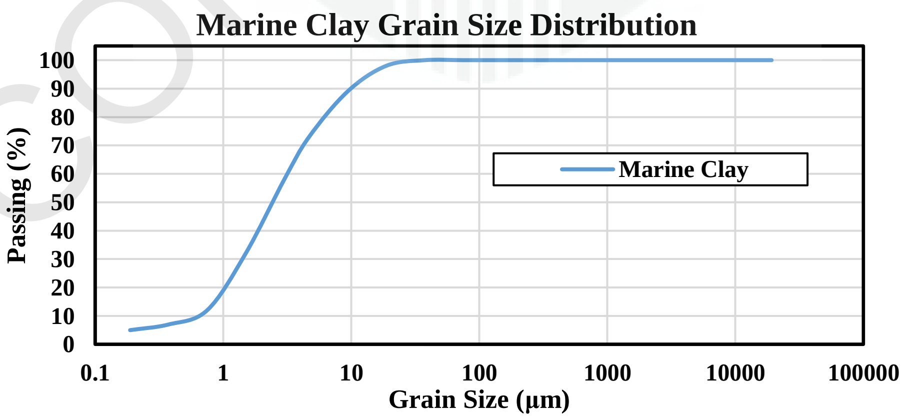

Figure 4.1: Kuala Langat marine clay grain size distribution

The natural water content, w_n, was determined to be 67%. The liquid limit, w_{LL}, was 75.2% and the plastic limit, w_{PL}, was 49.0%. The plasticity index, PI, and consistency index, CI, were 26.30 and 0.31, respectively. This observation shows that the Kuala Langat marine clay follows the same trend as the Peninsular Malaysia marine clay, where the ranges of w_n, w_{LL}, w_{PL}, and PI were at 25 to 140%, 50 to 150%, 20 to 85%, and 26.5 to 130%, respectively (Juhaizad Ahmad et al., 2011; Bergado et al., 2022; Chompoorat et al., 2022; Hoy et al., 2022; Moe et al., 2021; Ngo et al., 2021; Wang et al., 2021; Yu et al., 2021).

The specific gravity, G_s, was determined to be 2.56 and the bulk density, γ_{bulk}, ranged from 1660 to 1796 kg/m^3, while the dry density, γ_{dry}, ranged from 988 to 1294 kg/m^3. The Malaysian marine clay G_s and γ_{bulk} was found to be 2.52 to 2.72 and 1270 to 1880 kg/m^3, respectively, based on data from Anggraini et al. (2015), Hassan et al. (2019), Jang (2018), Lam et al. (2018), Ngo et al. (2020), Wang et al. (Shuyao Wang et al., 2021), and Yu et al. (2021).

For the compressibility characteristics of the Kuala Langat marine clay, the Pc' was obtained to be 147.5 kPa, C_C 0.200, C_r 0.086, and C_v 7.88 m^2/yr. These values agree with the characteristics determined by Kamaruidzaman et al. (2019), Ngo et al. (2021), Nguyen, Tran, and Dao (2020), Sarah and Soebowo (2018), Wang et al. (2021), and Zainorabidin et al. (2019) for P_C', C_C, C_r, and C_v, which ranged from 26 to 318 kPa, 0.08 to 7.48, 0.02 to 0.4, and 0.2 to 24 m^2/yr, respectively.

The chemical composition of the soil samples was indicated by XRF, as shown in Table 4.2. The major weighted percentage of the chemical composition was SiO_2, Al_2O_3, and Fe_2O_3, which followed the same trend as marine clays in previous research (Mohd Yunus et al., 2015; Tamizi et al., 2013). The XRD test showed that the normal soil was formed of kaolinite, illite, and quartz.

Table 4.2: XRF results of marine clay of Kuala Langat

Chemical Composition	SiO_2	Al_2O_3	Fe_2O_3	K_2O	SO_3	MgO	Others
Percentage	55.41	24.12	13.24	1.25	0.91	7.00	5.07

Generally, the conducted properties indicate that Kuala Langat marine clay is following the same trend of the marine clay as shown in Section 2.2. Although, the high water of the samples is less that liquid limit, the water content is high enough to reach liquid limit, that explains the reason of Kuala Langat marine clay tending to have huge plastic deformations and weak resistance to loading. In addition, the mineralogy of the sample indicates the presence of clay minerals that accumulates huge amount of water molecules due to the massive charges on their surfaces. Thus, all are reflected in the compressibility characteristics of high value in compressibility index C_C, and low value of preconsolidation stress P_C'. Accordingly, Kuala Langat marine clay requires reinforcement to resist different loading conditions.

4.4 Treatment Materials

4.4.1 Lime Properties

The lime employed in this research is hydrated lime $Ca(OH)_2$. The chemical properties of the lime are shown in Table 4.3. The specific gravity of the lime is 2.2 with a molecular weight of 78 and calcium oxides CaO content exceeding 93%.

Table 4.3: Chemical properties of lime

Chemical Composition	SiO_2	Al_2O_3	Fe_2O_3	CaO	MgO	SO_3	Others	LOI
Percentage	1.4	0.3	0.2	93.5	0.4	0.5	3.70	3.9

4.4.2 Palm Oil Fly Ash (POFA) Properties

Grain size distribution of POFA is shown in Figure 4.2, where about 40% of the POFA has size more than 300 μm. POFA was sieved using sieve of size 300 μm before been used to treat marine clay. The chemical properties of POFA are shown in Table 4.4 and specific surface area SSA is 5720 cm^2/g. POFA was specified as class CFA as per ASTM C618 – 03 Standards (2003a) mentioned in Table 2.7. The used POFA is the same properties used by Mohammed (2023), but about 40% less in CaO ratio compared by the POFA used by Khasib et. al. (2020).

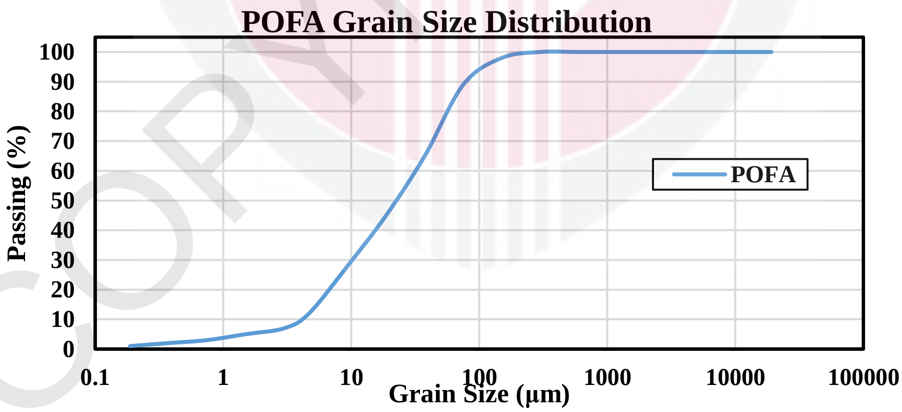

Figure 4.2: Used Palm Oil Fly Ash grain size distribution}

Table 4.4: Chemical properties of POFA

Chemical Composition	SiO_2	Al_2O_3	Fe_2O_3	CaO	MgO	SO_3	K2O	Others	LOI
Percentage	55.02	8.96	3.81	6.23	2.29	1.11	6.71	15.87	8.91

4.4.3 Calcined Shale Properties

The chemical composition of calcined shale is shown in Table 4.5. It shows that the major content is formed by both silicate SiO_2 and aluminate Al_2O_3. The calcined shale grains grading is 92% passing 600 μm, 70% passing 42.5 μm, and 23% passing 3 μm, where the grain size distribution is shown in Figure 4.3.

Table 4.5: Chemical properties of calcined shale

Chemical Composition	SiO_2	Al_2O_3	Fe_2O_3	CaO	MgO	SO_3	Others	LOI
Percentage	63.27	25.57	4.36	1.19	1.10	0.29	4.22	8.82

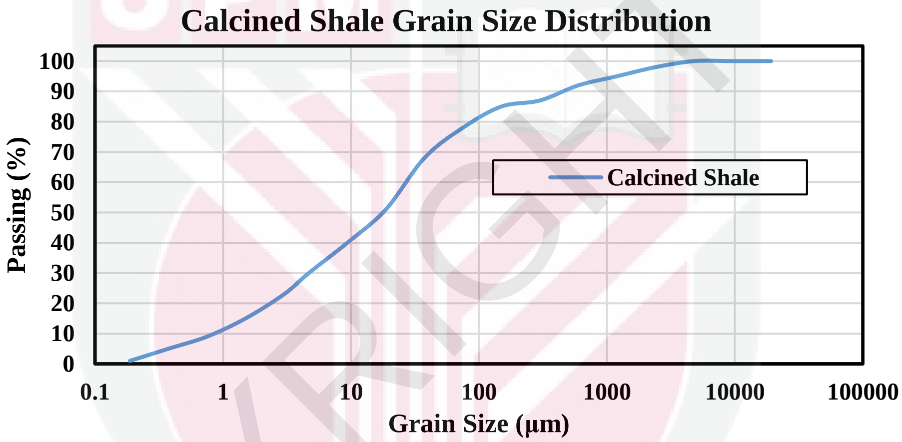

Figure 4.3: Used calcined shale grain size distribution

4.5 Treated Kuala Langat Marine Clay

4.5.1 Influence of POFA Inclusion on Mechanical Properties

Series of triaxial compression test were conducted on samples SL5P0C0–7, SL5P1C0–7, SL5P5C0–7, SL5P10C0–7, SL5P15C0–7, and SL5P20C0–7. Consolidated undrained (CU) and Unconsolidated undrained (UU) triaxial test were done. The results are shown in Figure 4.4 for natural marine clay and for treated samples. The samples were tested after 7 curing days. For UU test, the samples showed a peak increment for POFA ratio of 5% following the same behaviour of the previous research for unconfined compressive strength (Zimar et al., 2022). The undrained deviatoric stress increased gradually up to the conducted peak by 0.94 MPa for sample SL5P5C0–7, where the strength decreases significantly as the ratio of POFA increased. On the other hand, Khasib et al. (2020) observed that treated non–cohesive soil using POFA increased only from 115 kPa to 121 kPa, which indicated a slight increment in unconfined compressive strength. Thant indicates that the treatment of L–POFA–CS is more effective with cohesive soils such as marine clay.

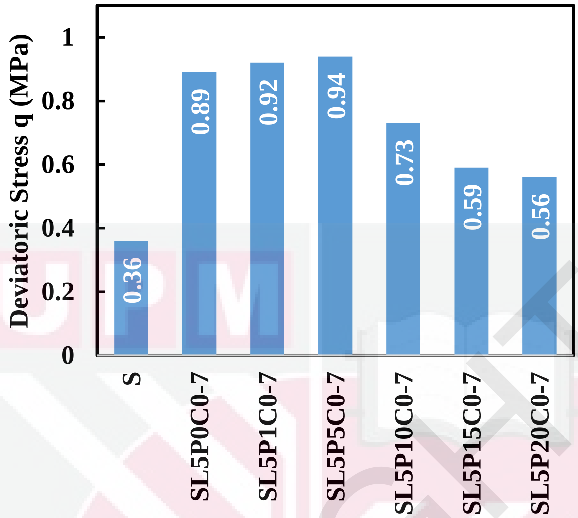

Figure 4.4: Shear strength from UU triaxial test for treated sample after 7 curing days compared to natural marine clay sample

For CU triaxial test, the samples showed a peak increment for POFA ratio of 5% for undrained cohesive strength, C and internal friction angle, ϕ. Although, the drained internal friction angle, ϕ' also significantly increased for SL5P5C0–7 specimen compared to control and other specimens, the drained cohesive strength, C' was enhanced by a range of 155 to 261% more than the control specimen, where all the results are shown in Figures from 4.5 to 4.8 as concluded from shear–vertical stress relationship shown in Appendix Figures from A1 to A7. On the same hand, White et al. (White et al., 2005) conducted the same results for treated samples with fly ash showing that the CU shear strength increased significantly. However, the specimens used by White et al. (White et al., 2005) were mixed cohesive and non–cohesive soil. Regardless soil type, both results indicate that fly ash is significant in treating soils in with respect to both short–term and long–term loading conditions, but L–POFA–CS treatment was significant in enhancing the marine clay.

Based on results, it is indicated that the increment of POFA ratio reduced both drained and undrained shear strength which could be a result of the volumetric swelling due the pozzolanic activity of POFA and the over consolidation behaviour as the POFA fines filled voids as mentioned by previous research (McCarthy et al., 2012; Mohammed, 2023) following the same conducted by previous research (Toyeb et al., 2023), where the MDD The reduction in maximum dry density (MDD) observed with the addition of POFA content is attributed to the initial combined process of clay particle flocculation and agglomeration, triggered by the cation exchange capacity. This phenomenon results in an expansion in volume and a subsequent decrease in dry density (Nik Daud et al., 2014; Toyeb et al., 2023). Hence, the optimal POFA ratio (oP) selected from the results at this stage is 5%. The optimum ratio selected was the used on the next stage, where the effect of change in lime and calcined shale ration on the treated specimen mechanical behaviour.

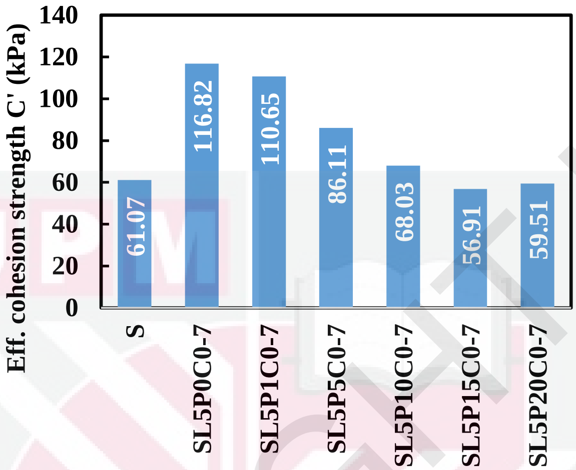

Figure 4.5: Effective cohesion strength from CU triaxial test for treated sample after 7 curing days compared to natural marine clay sample

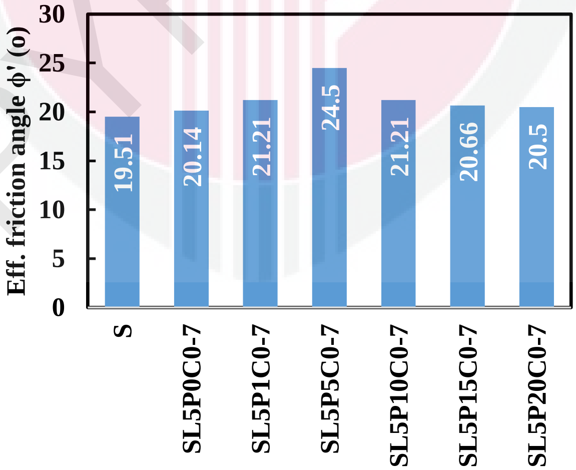

Figure 4.6: Effective internal friction angle from CU triaxial test for treated sample after 7 curing days compared to natural marine clay sample

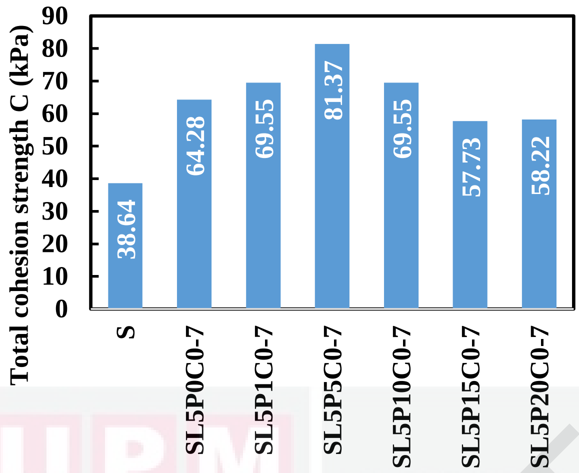

Figure 4.7: Total cohesion strength from CU triaxial test for treated sample after 7 curing days compared to natural marine clay sample

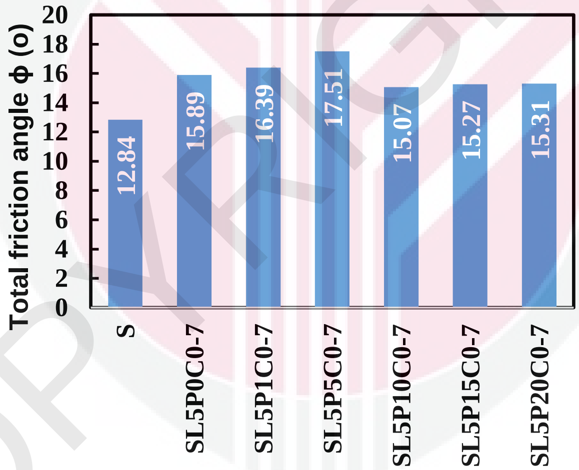

Figure 4.8: Total internal friction angle from CU triaxial test for treated sample after 7 curing days compared to natural marine clay sample

4.5.2 Influence of Lime and Calcined Shale Inclusion on Mechanical Properties

Series of CU and UU triaxial tests were conducted to investigate the effect of lime (L) and calcined shale (CS) ratios on mechanical properties of treated marine clay. UU triaxial test results shown in Figure 4.9 indicated that the optimal ratio of lime was 5%, where both drained and undrained shear strength were effectively increasing by lime ratio increment, as indicated by previous research (Al–Mukhtar et al., 2010b).

However, the ratio indicated by Al–Mukhtar et al. (2010b) was indicated to be 8% of lime as it was individual additive for soil treatment. In addition, the strength of treated specimens were enhancing by increment of curing days, which meet the same observation of previous research with respect to the optimum ratio of lime (Al–Mukhtar et al., 2010b).

Regarding calcined shale, the shear strength was also increased with CS ratio increment, where the peak was at 10% for calcined shale, which then the strength decreases significantly to 40% of control specimen from 360.0 kPa to 207.8 and 206.8 kPa for SPL3P5C20 and SPL1P5C20 respectively. That is due to the increment of the pore size due to expansion of the treated specimens during curing as indicated by previous research (Wild et al., 1997).

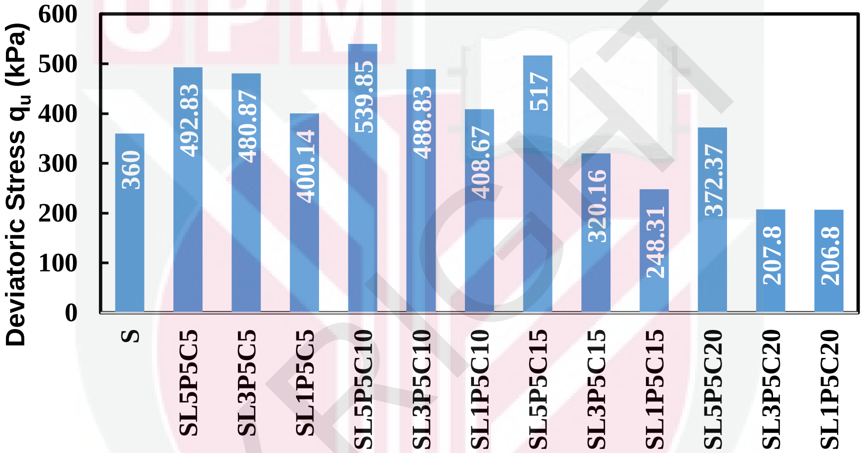

(a)

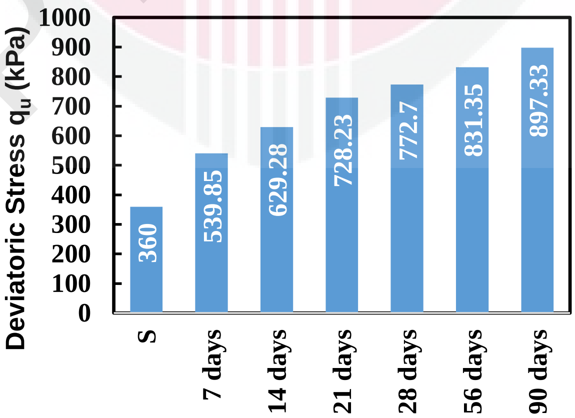

(b)

Figure 4.9: Deviatoric stress q_u of UU triaxial test for (a) 7 days curing time and (b) SL5P5C10 for 7, 14, 21, 28, 56, and 90 days curing time

Generally for CU triaxial tests, the parameters shear strength peak was for 10% of CS and 5% of L as shown in Figures from 4.10 to 4.13. The treated samples showed random trend in undrained cohesion as treatment materials ratio changed, but for the time effect it can be seen that the undrained cohesion increased with curing time increment, see Figure 4.10. On the other hand, the undrained friction angle ϕ_u was direct proportional to the content of the treatment materials and curing time, see Figure 4.11. For drained cohesion c', the peak strength was exhibited by specimen SL5P5C10, where the strength is directly proportional with curing time as shown in Figure 4.12, but unexpectedly the drained cohesion decreased to less than 50 kPa for 90 curing days. In addition, the peak drained angle of friction, ϕ' shows the same trend as the drained cohesion of treated sample as shown in Figure 4.13. Therefore, the engineering ratios based on experimental work for both drained and undrained shear strength were identified as 5% POFA, 5% lime, and 10% CS, where C_u increased by 4 times, ϕ_u increased by 50%, C' increased by 6 times, and ϕ' increased by 90%, all compared to control specimen. That indicates the behaviour of treated specimens significantly resist the loading conditions in both short–term and long–term, but in long–term of loading is more enhanced, which helps in future various geotechnical applications, where it was not covered by previous research specially for the treating mixture L–POFA–CS.

Generally, triaxial test results showed the behaviour of treated specimens on long time loading were more like the behaviour of coarse soil failure, with particularly the increment of curing duration as shown in Figure 4.14. That highlights the enhancement in long–term resistance for the treated specimens, an aspect not previously addressed in research, particularly concerning the L–POFA–CS treatment mixture.

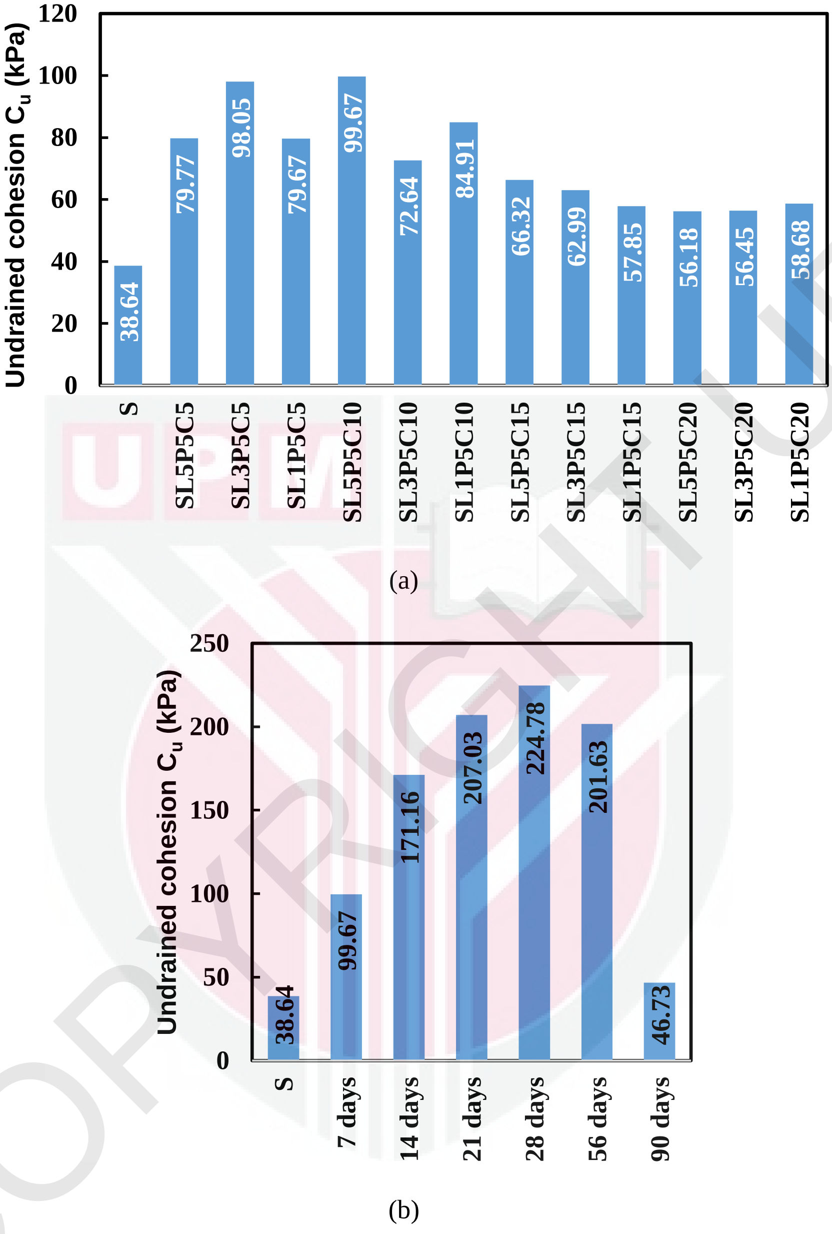

Figure 4.10: Undrained cohesion C_u of CU triaxial test for (a) 7 days curing time and (b) SL5P5C10 for 7, 14, 21, 28, 56, and 90 days curing time

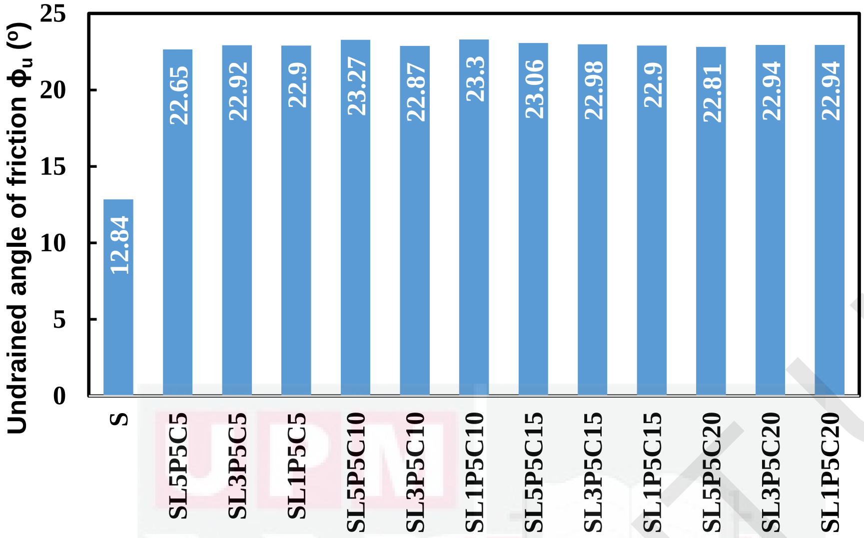

(a)

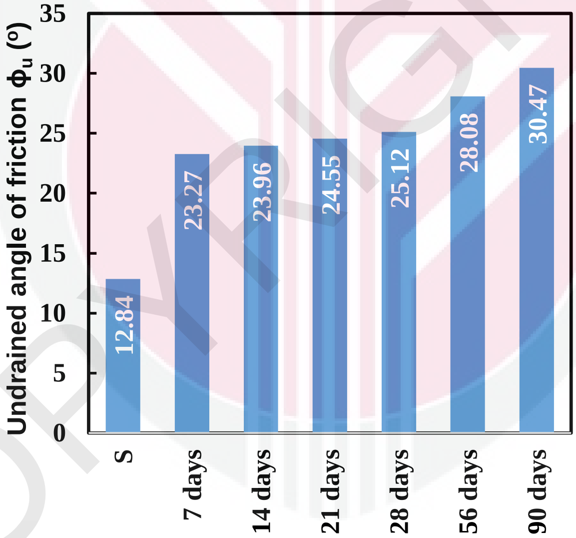

(b)

Figure 4.11: Undrained angle of friction ϕ_u of CU triaxial test for (a) 7 days curing time and (b) SL5P5C10 for 7, 14, 21, 28, 56, and 90 days curing time

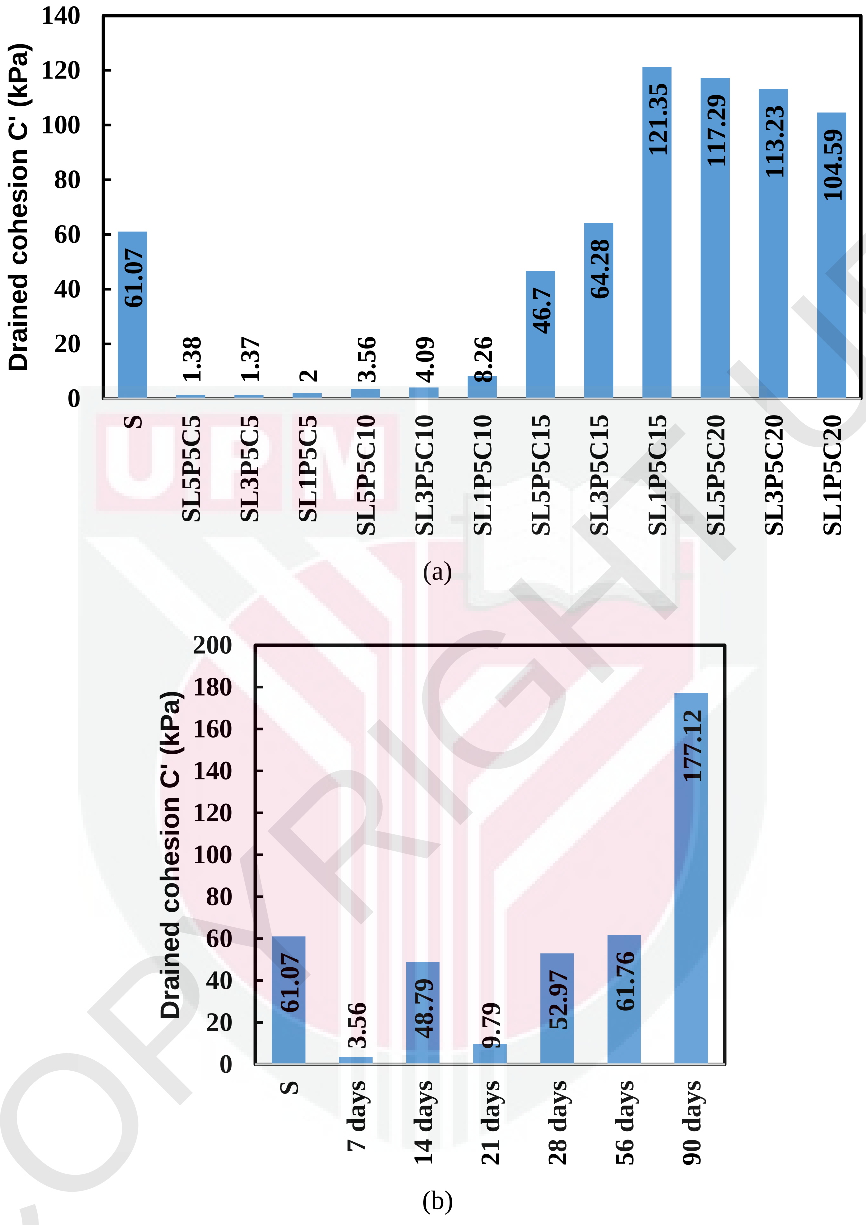

Figure 4.12: Drained cohesion C' of CU triaxial test for (a) 7 days curing time and (b) SL5P5C10 for 7, 14, 21, 28, 56, and 90 days curing time

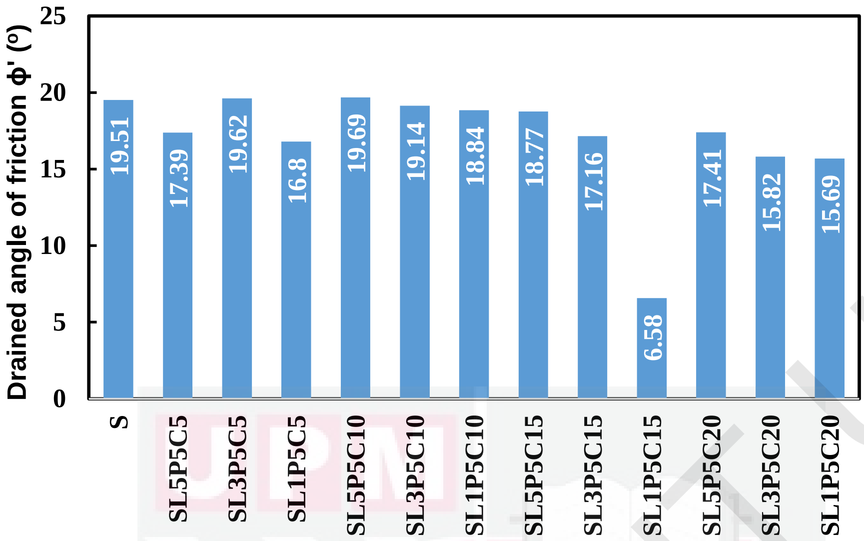

(a)

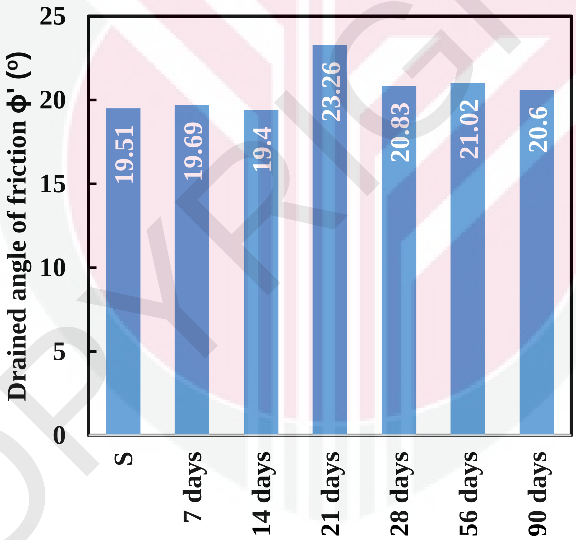

(b)

Figure 4.13: Drained angle of friction ϕ' of CU triaxial test for (a) 7 days curing time and (b) SL5P5C10 for 7, 14, 21, 28, 56, and 90 days curing time

Figure 4.14: Triaxial specimens after failure for SL5P5C10 specimens on various curing durations compared to (a) control specimen, (b) 7, (c) 14, (d) 21, (e) 28, and (f) 90 curing days

4.5.3 Effects of L–POFA–CS Treatment on Compressibility

Compressibility of treated soil specimens using L–POFA–CS mixture was investigated using one dimensional consolidation test, where the coefficients and indices derived from the 1D consolidation test are shown in Table 4.6. The findings reveal that the treatment using L–POFA–CS for specimens of SL5P5C10 mixture produced substantial enhancements in the consolidation parameters relative to specimens of other mixtures. The compressibility of the soil was significantly decreased after treatment compared to the natural soil (S) compressibility, as evidenced by the data in Table 4.6. In addition, the volume compressibility m_v was decreased after treatment and significantly the minimum for specimen SL5P5C10–7 which indicated the minimum deformation compared to other specimens in addition to the control specimen. That also was reflected on coefficient of consolidation C_v that showed the same behaviour. Moreover, the permeability of the soil increased between two and nine times as compared to natural soil (s) permeability. That helps in faster dissipation for generated pore water pressure during loading, so that the soil resistance enhanced and be able more resistible for subjected loads. The results was following the same behaviour of the treated samples conducted by Mohammed (2023). In addition the results met the same findings by Nik Daud and Mohammed (2014) but on different treatment mixture of POFA.

Table 4.6: Compressibility factors conducted from 1D consolidation test

Code	m_v	a_v	C_v	C_r	C_C	CR	K
	(m^2/ton)	(m^2/ton)	(m^2/yr)				(cm/sec)
S	1.29E–04	2.50E–04	147.5	0.086	0.086	0.0025	3.25E–08
SL5P5C5–7	0.074	0.06	3.82	0.015	0.05	0.02	7.20E–09
SL3P5C5–7	0.123	0.258	4.04	0.04	0.176	0.076	2.19E–08
SL1P5C5–7	0.0815	0.15	4.42	0.037	0.198	0.095	9.45E–09
SL5P5C10–7	0.071	0.036	3.15	0.015	0.048	0.03	6.30E–09
SL3P5C10–7	0.101	0.175	3.31	0.031	0.122	0.062	1.53E–08
SL1P5C10–7	0.0808	0.145	4.1	0.033	0.151	0.076	9.24E–09
SL5P5C15–7	0.068	0.119	6.69	0.017	0.056	0.023	5.40E–09
SL3P5C15–7	0.13	0.241	5.68	0.025	0.18	0.07	2.40E–08
SL1P5C15–7	0.118	0.225	5.52	0.041	0.161	0.079	2.04E–08
SL5P5C20–7	0.085	0.142	7.1	0.022	0.067	0.026	1.05E–08
SL3P5C20–7	0.12	0.45	7.85	0.02	0.181	0.077	2.10E–08
SL1P5C20–7	0.104	0.182	7.25	0.044	0.145	0.059	1.62E–08

4.5.4 Geotechnical Properties of Treated Marine Clay

Results of Atterberg limits showed an enhancement after treatment using various L–POFA–CS ratios in general. The Atterberg limits can be seen to be enhanced with the increment of curing duration as shown in Table 4.7. The significant change can be seen on specimens of 56 curing days, which is a reflection of the shear strength enhancement as illustrated in CU and UU triaxial tests, which was also conducted by Mohammed (2023). In addition the results were following the same trend of the treated clay soils but using different mixtures with POFA and lime (Arvind Kumar et al., 2007; Nik Daud et al., 2014). However, Kumar et. al. (2007) conducted that the duration has slight difference compared to conducted results in this research.

Table 4.7: Atterberg limits

Code	LL	PL	PI	GS	SL	USCS
S	75.20	48.95	26.25	2.56	13.71	MH
SL5P0C0–7	68.00	48.67	19.33	2.47	10.09	MH
SL5P1C0–7	67.30	45.11	22.20	2.47	11.59	MH
SL5P5C0–7	62.00	48.24	13.76	2.46	7.19	MH
SL5P10C0–7	60.30	47.95	12.35	2.46	6.45	MH
SL5P15C0–7	61.00	44.89	16.11	2.43	8.41	MH
SL5P20C0–7	65.00	52.10	12.90	2.41	6.74	MH
SL5P5C5–7	61.30	48.95	12.35	2.57	6.43	MH
SL3P5C5–7	64.55	48.67	15.88	2.62	10.71	MH
SL1P5C5–7	66.10	45.11	21.00	2.69	10.00	MH
SL5P5C10–7	59.50	48.24	11.26	2.56	5.71	MH
SL3P5C10–7	63.40	47.95	15.45	2.61	10.00	MH
SL1P5C10–7	64.30	44.89	19.41	2.61	8.57	MH
SL5P5C15–7	59.20	52.10	7.10	2.54	5.36	MH
SL3P5C15–7	60.62	48.43	12.19	2.57	8.57	MH
SL1P5C15–7	62.45	45.95	16.5	2.58	7.86	MH
SL5P5C20–7	62.80	53.44	9.36	2.53	4.29	MH
SL3P5C20–7	63.22	49.85	13.37	2.55	7.86	MH
SL1P5C20–7	66.04	47.46	18.58	2.51	7.14	MH
SL5P5C10–14	59.50	44.45	15.05	2.63	7.86	MH
SL5P5C10–21	56.50	38.67	17.83	2.64	9.31	MH
SL5P5C10–28	56.50	38.67	17.83	2.64	9.31	MH
SL5P5C10–56	54.50	34.24	20.26	2.65	10.58	MH
SL5P5C10–90	34.50	32.01	2.49	2.66	1.30	ML

4.5.5 Microstructural Properties of Treated Marine Clay

Based on results from triaxial tests, SEM test and XRD test were applied on the specimens of SL5P5C10 and control specimens (natural soil).

4.5.5.1 SEM Results

SEM test was assessed using S34OO–N HITACHI by Volts 10Kv and Probe Current of 20 ohm, where the test was assessed in Universti Putra Malaysia, Material Characterization Laboratory. Figure 4.15 provides detailed visual insight into the incorporation of L–POFA–CS treatment mixture with marine clay soil. In Figure 4.15–a, the marine clay soil is portrayed as cohesive aggregates, exhibiting a flocculated–aggregated structure indicative of its cohesive nature. Notably, the sample surface displays numerous open fissures, suggesting potential avenues for interstitial interactions. After 7 days of treatment, Figure 4.15–b showcases fine particles dispersed within the matrix, accompanied by the presence of small fissures, possibly indicating the initial stages of material homogenization. Further for 28 and 90 days of curing, Figures 4.15–c and 4.15–d unveils fine particles coexisting with larger porous agglomerates, characterized by rounded and rod–shaped morphologies with slight difference in 90 as shown in Figure 4.15–d. This morphology variation suggests a heterogeneous distribution within the sample, possibly influenced by the interplay between L–POFA–CS and the marine clay soil. Moreover, the observed scattering of grain sizes, encompassing both large and small particles, implies a complex microstructural composition, potentially contributing to the material's mechanical behavior. These detailed observations shed light on the intricate interfacial phenomena occurring between L–POFA–CS and marine clay soil, laying the groundwork for further investigation into their combined effect on material properties. Results indicated that cementation crystals coated the interfacial surfaces of clay particles as shown in Figure 4.15. The results show that the coating rate increased as the curing duration increased, and the clay layers' boundaries became sharper and interlocked together. However, cementation crystals were not in a significant difference in comparison between 28 and 90 curing days as shown in Figures 4.15–c and 4.15–d. That indicates the significant increment in shear strength of treated samples compared to the control specimen, as conducted by previous research (Nik Daud et al., 2014; Toyeb et al., 2023; Wahab et al., 2021).

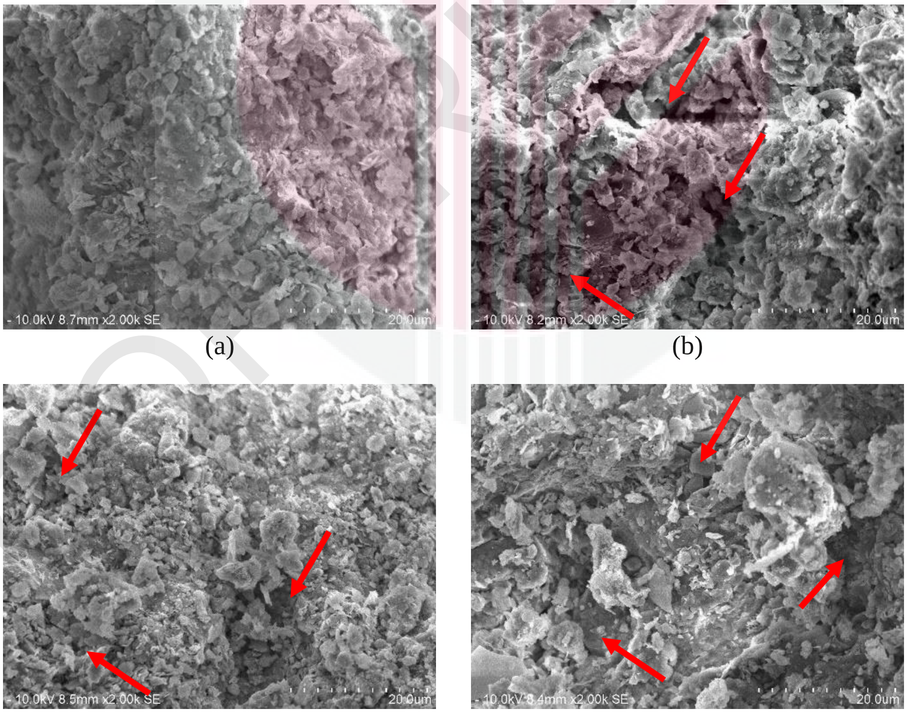

Figure 4.15: SEM results for (a) S, (b) SL5P5C10–7, (c) SL5P5C10–28, and (d) SL5P5C10–90

4.5.5.2 XRD Results

XRD test was assessed using X–RAY DIFFRACTOMETER (XRD) SHIMADZU XRD–6000 in Universti Putra Malaysia, Material Characterization Laboratory. Intensity of diffracted x–rays is evaluated based on the specimen alignment and diffraction angle 2θ. Adding lime, POFA, and CS to marine clay enhances the intensity of the calcium silicate hydrate but reduces the intensity of the calcium hydroxide. The XRD results indicated that there were evolving in calcium silicate hydrate C–S–H and calcium aluminate hydrate C–A–H for marine clay specimen treated with SL5P5C10–7, SL5P5C10–28, and SL5P5C10–90 and the natural soil (S), both of which contained mainly quartz, kaolinite, and illite. These findings are consistent with previous research on marine clay (Alabduljabbar et al., 2020; Anggraini et al., 2015; Basha et al., 2020; Saad et al., 2021; Salih et al., 2015; Swapna Thomas et al., 2022). Thus, it can be concluded that the L–POFA–CS treating mixture enhanced the formation of soil minerals, as demonstrated by the peaks in Figure 4.16. With L-POFA-CS, calcium oxide CaO well-connected floc-like and fibrous-like C-S-H phases formed, filling voids inside the marine clay. The inclusion of L-POFA-CS started C–S–H formation within the matrix. As L-POFA-CS increased and curing time, the matrix became denser, and fractured surfaces were almost completely covered by C-S-H. The calcium hydroxide reduction and enhanced microstructure were due to the consumption of CaO from L-POFA-CS mixture.

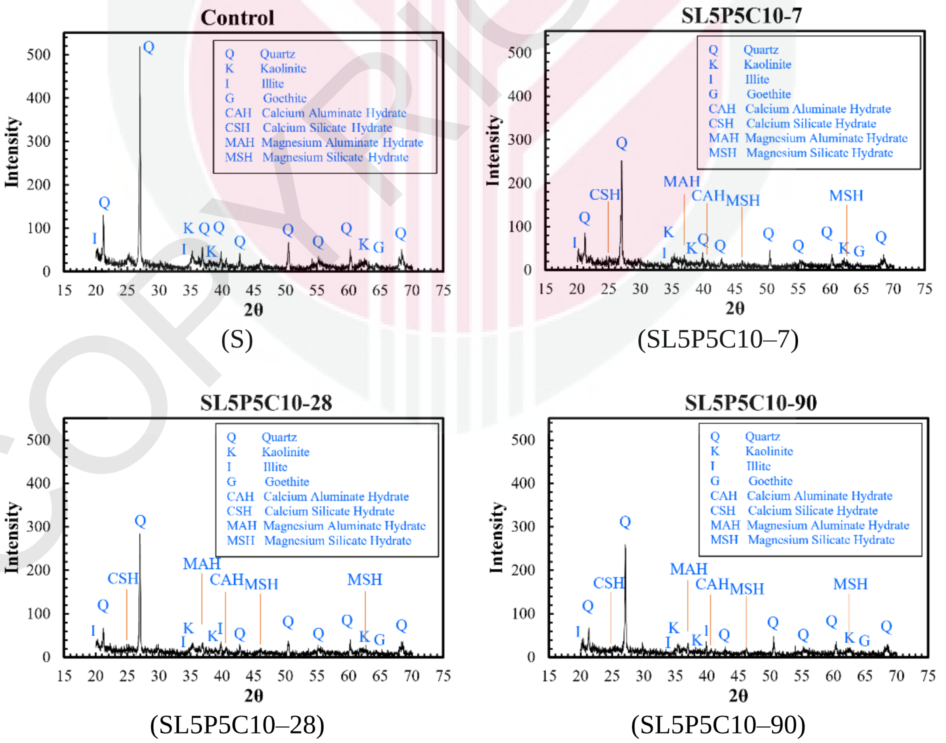

Figure 4.16: XRD results showing peaks for SL5P5C10–7, SL5P5C10–28, SL5P5C10–90 and S

4.6 Finite Element Modelling Results

Series of finite element modelling FEM were assessed using PLAXIS 2D V22 program for both following studies;

1. Consolidated undrained triaxial compression test, and
2. Simulation of Serdang landslide case for natural soil and L–POFA–CS treated soil depending on results of the optimum specimen SL5P5C10

4.6.1 Simulation of CU Triaxial Test

Total of 90 FEMs were assessed for natural marine clay and L–POFA–CS treated specimens. The models were assessed for consolidation confining pressures σ_3 of 340 kPa and axial stresses for confining pressures of 390, 440, and 490 kPa. The stress–strain relationship was conducted for the specimens soil/geotechnical parameters as per Table 3.8 identified previously in Section 3.7.1, where the results are represented in Figure 4.17 for control specimen and Figures from 4.18 to 4.19 for specimens treated by L–POFA–CS mixtures. The behaviour of the specimens through FEM can be seen to be following the same behaviour obtained through experimental work for the residual strain and stress. However, the trend showed by FEM is normal consolidated behavior (NCC), while the experimental results were following the over consolidated soil behaviour (OCC). The same outcome was indicated by previous research for Bangkok marine clay (Surarak et al., 2012). This is must be due to the OCC behaviour from experimental work which was conducted on the specimens at maximum dry density (MDD) and optimum moisture content (OMC), hence the specimens are over consolidated. Therefore, the FEM simulation through PLAXIS program can be used as a guidance in preliminary design or investigation but not for final work. Accordingly, machine learning should be involved in such investigations and predictions to enhance the accuracy of the obtained results without experimental work as indicated by previous research (Schweiger, 2002, 2009; Surarak et al., 2012).

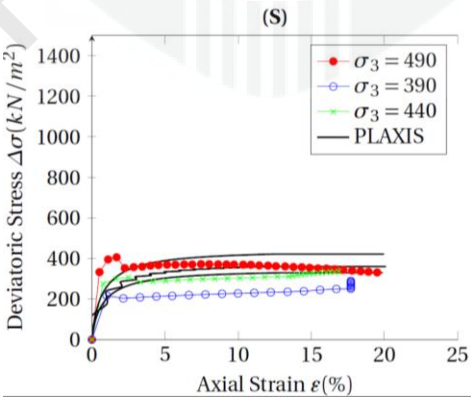

Figure 4.17: Deviatoric stress $\Delta\sigma$ of CU triaxial test of both laboratory and FEM results for natural marine clay for the confining pressures σ_3 390, 440, 490 kPa

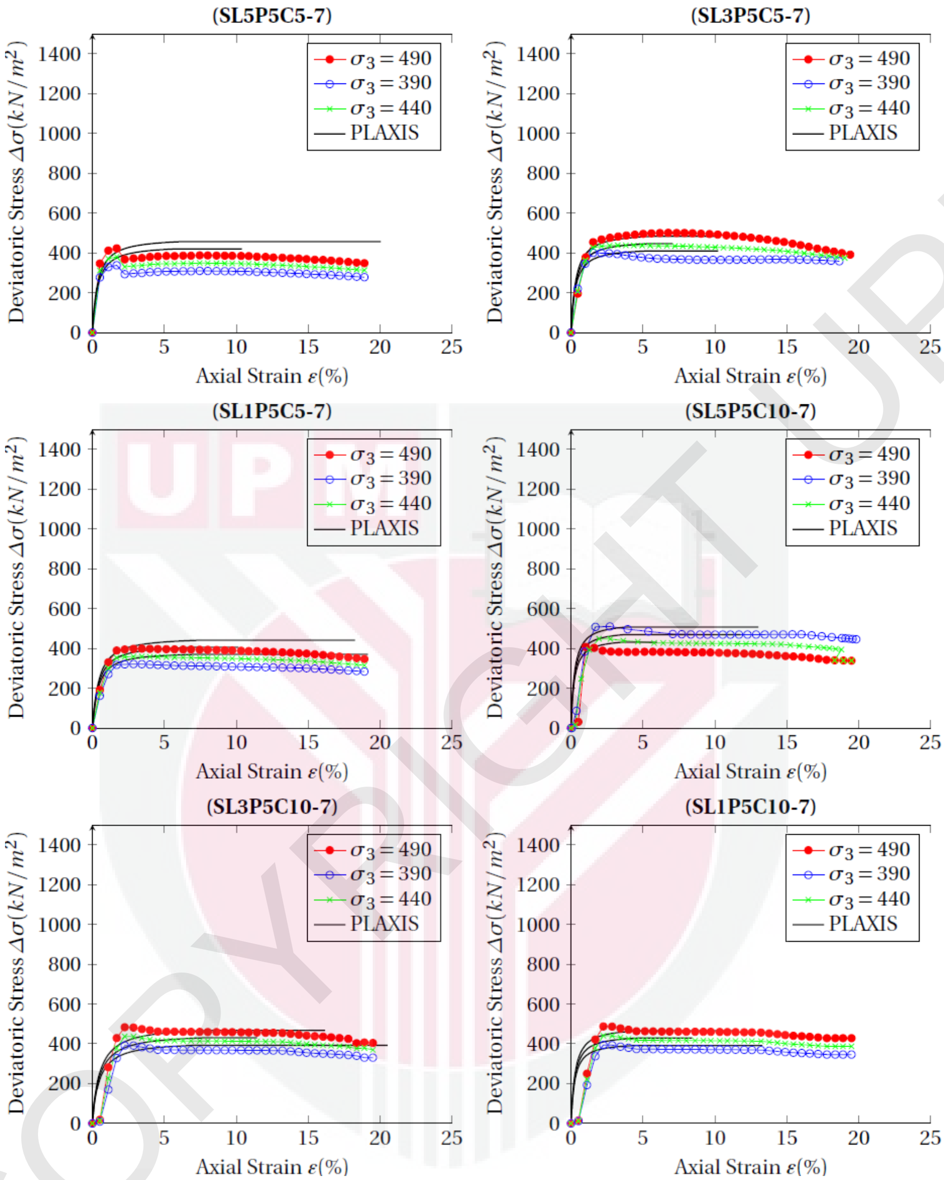

Figure 4.18: Deviatoric stress $\Delta\sigma$ of CU test of experimental and FEM results for treated samples after 7 curing days for confining pressures σ_3 390, 440, 490 kPa

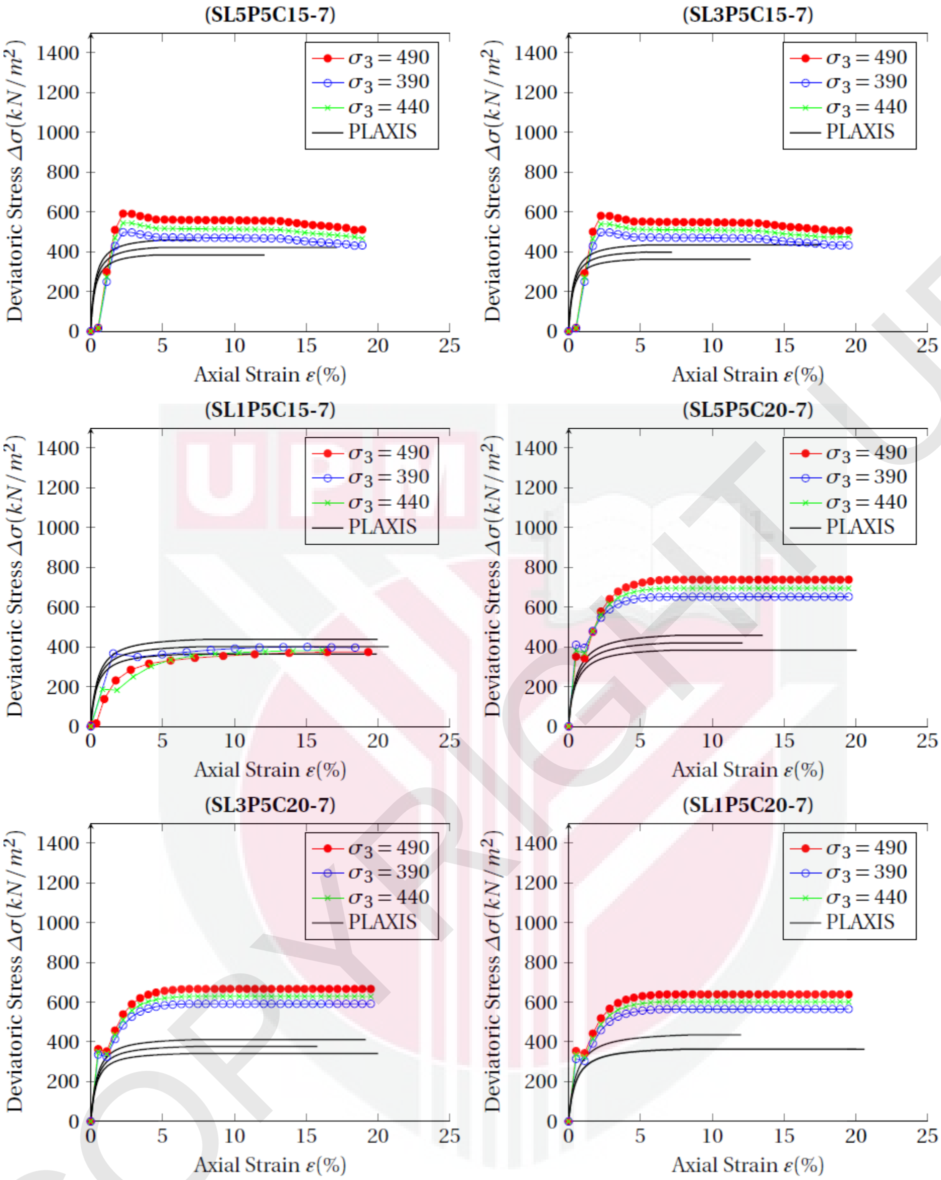

Figure 4.18: Deviatoric stress $\Delta\sigma$ of CU test of experimental and FEM results for treated samples after 7 curing days for confining pressures σ_3 390, 440, 490 kPa

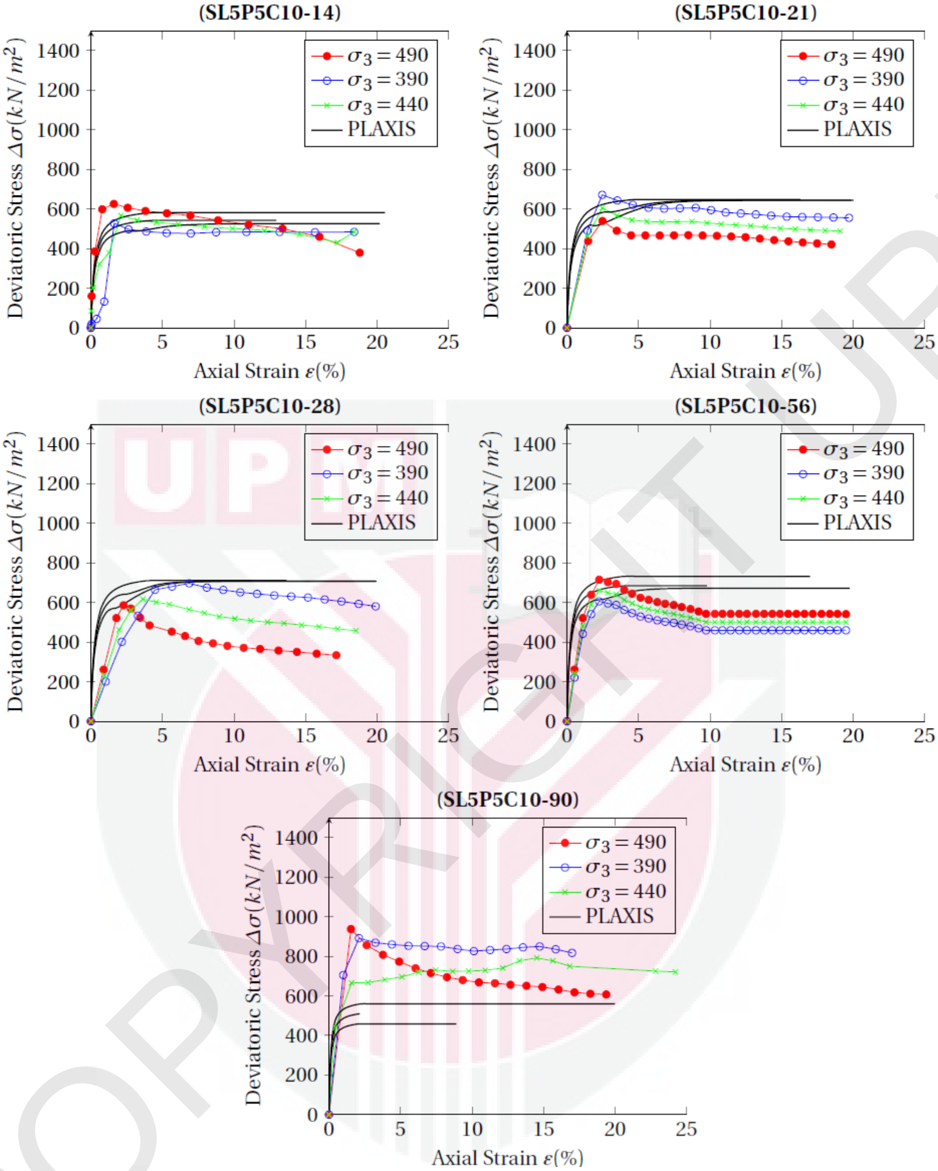

Figure 4.19: Deviatoric stress $\Delta\sigma$ of CU test of experimental and FEM results for treated samples after 7 curing days for confining pressures σ_3 390, 440, 490 kPa

4.6.2 Case Study of Serdang Landslide

Serdang landslide was investigated for its failure case and using the properties of marine clay and treated marine clay sample SL5P5C10, where the parameters were defined in Section 3.7.2 in Tables from 3.9 to 3.12. The results of the FEM showed that the soil collapsed where marine clay used as fill behind canal and retaining wall by a horizontal movement of 0.4 meters as shown in Figures 4.20 to 4.22, where the drained stresses were significantly huge behind the retaining wall as shown in Figures 4.23 to 4.25. On the other hand, the treated soil showed a significant resistance to soil collapse and deformations as shown in Figures 4.26 to 4.28, where the stresses were minimum and almost uniform in distribution as shown in Figures 4.29 to 4.31.

The simulation shows that the soil resistance for the horizontal stresses increased significantly after treatment, where the stresses decreased from 20 kN/m^2 for natural soil to 2 kN/m^2 for SL5P5C10 treated soil fill. That indicates that the soil after treatment can resist 10 times the horizontal stresses compared to the control (natural) soil for the same loading conditions. That could help in increasing the near buildings heights and can accept heavy traffic loads for the adjacent parking areas. In general, that promises more engineering, geotechnical and economic benefits using the SL5P5C10 treated soil as a soil fill behind retaining walls. Thus, treated marine clay can be proposed to be used as soil fill and help in resisting the external forces for both short–term and long–term conditions, which is compatible with the previous research (Nouman Amjad Raja et al., 2021) based on PLAXIS 3D materials model manual (Brinkgreve et al., 2012).

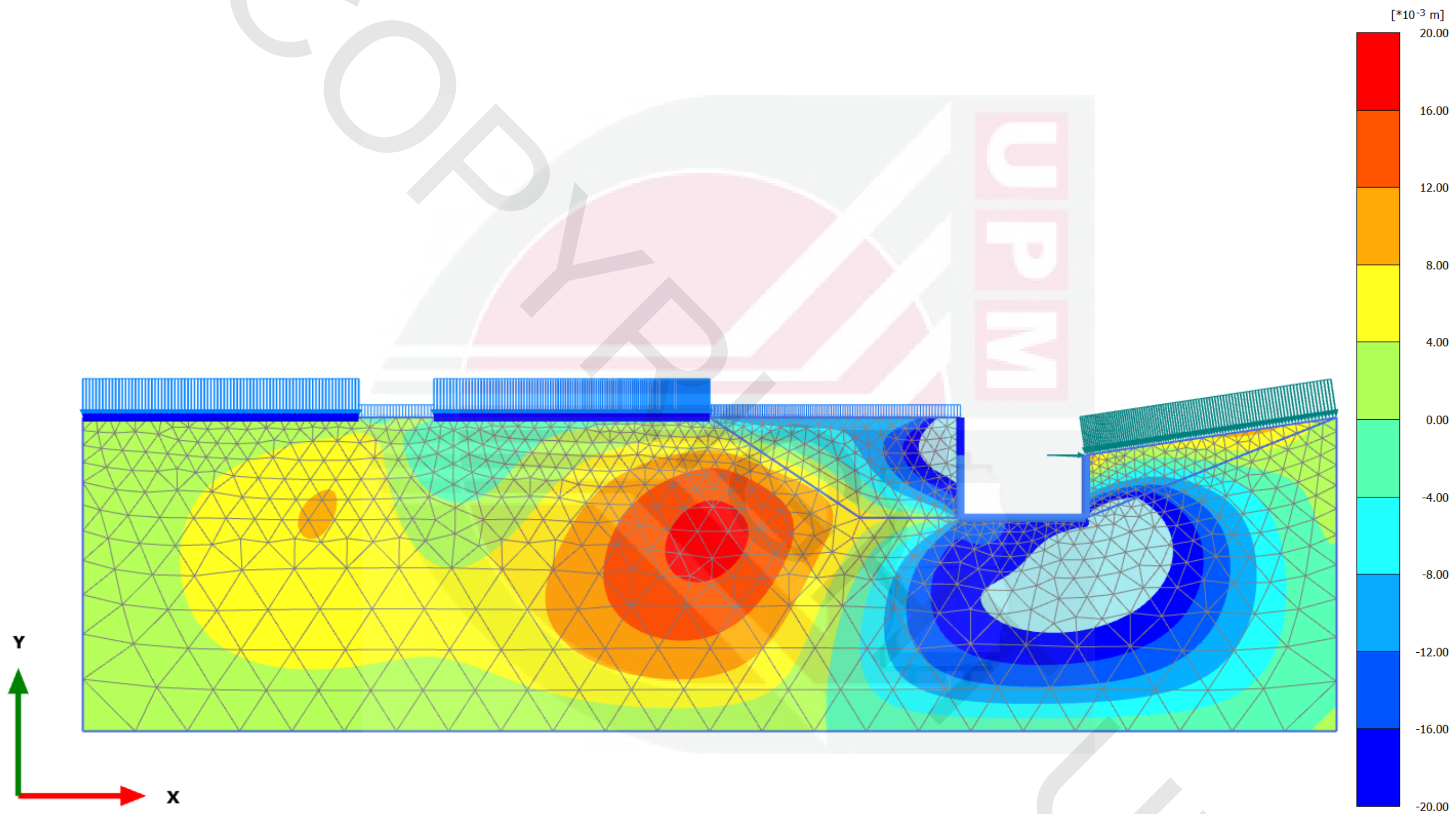

Figure 4.20: PLAXIS output showing horizontal deformations for natural marine clay

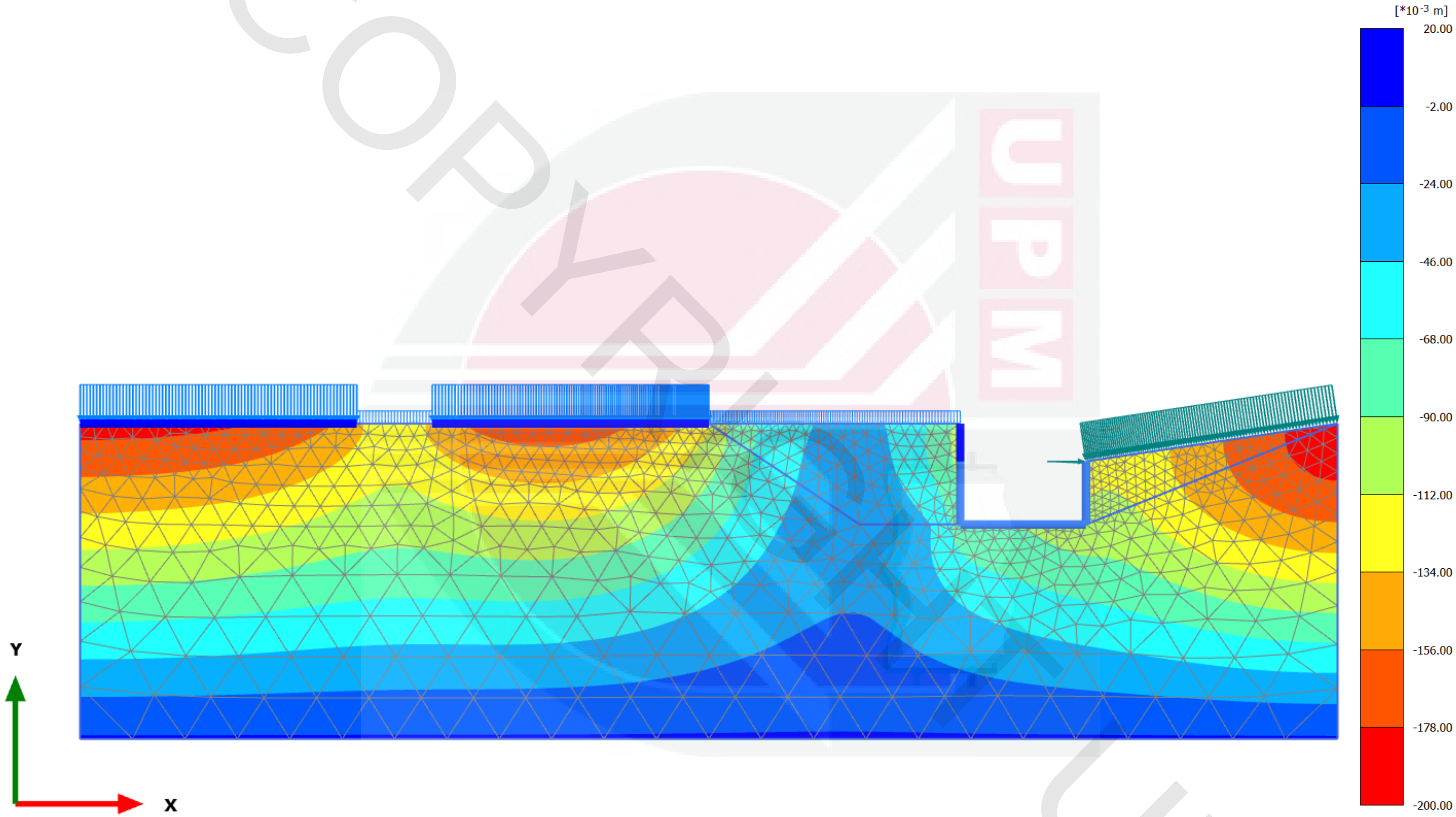

Figure 4.21: PLAXIS output showing vertical deformations for natural marine clay

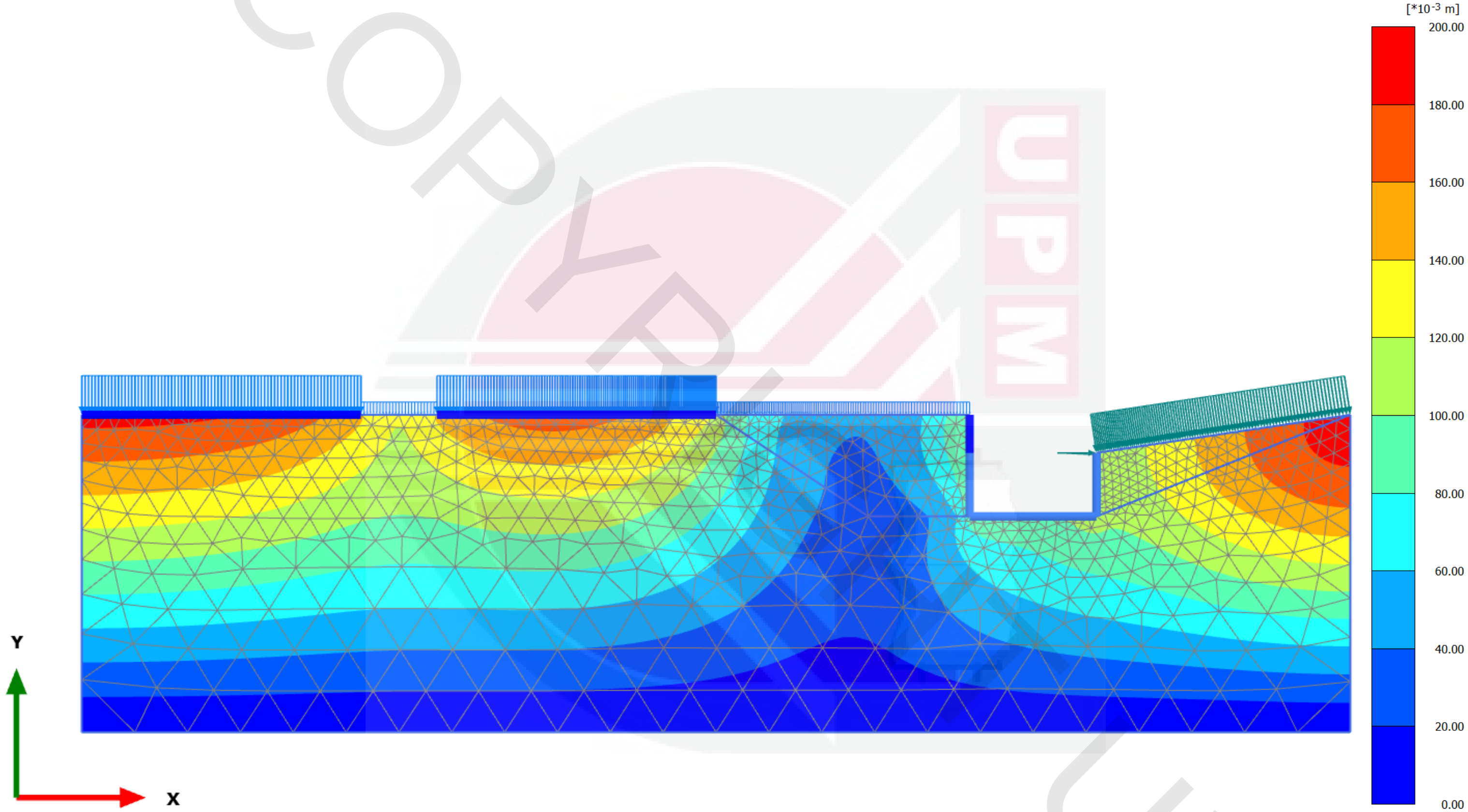

Figure 4.22: PLAXIS output showing total deformations for natural marine clay

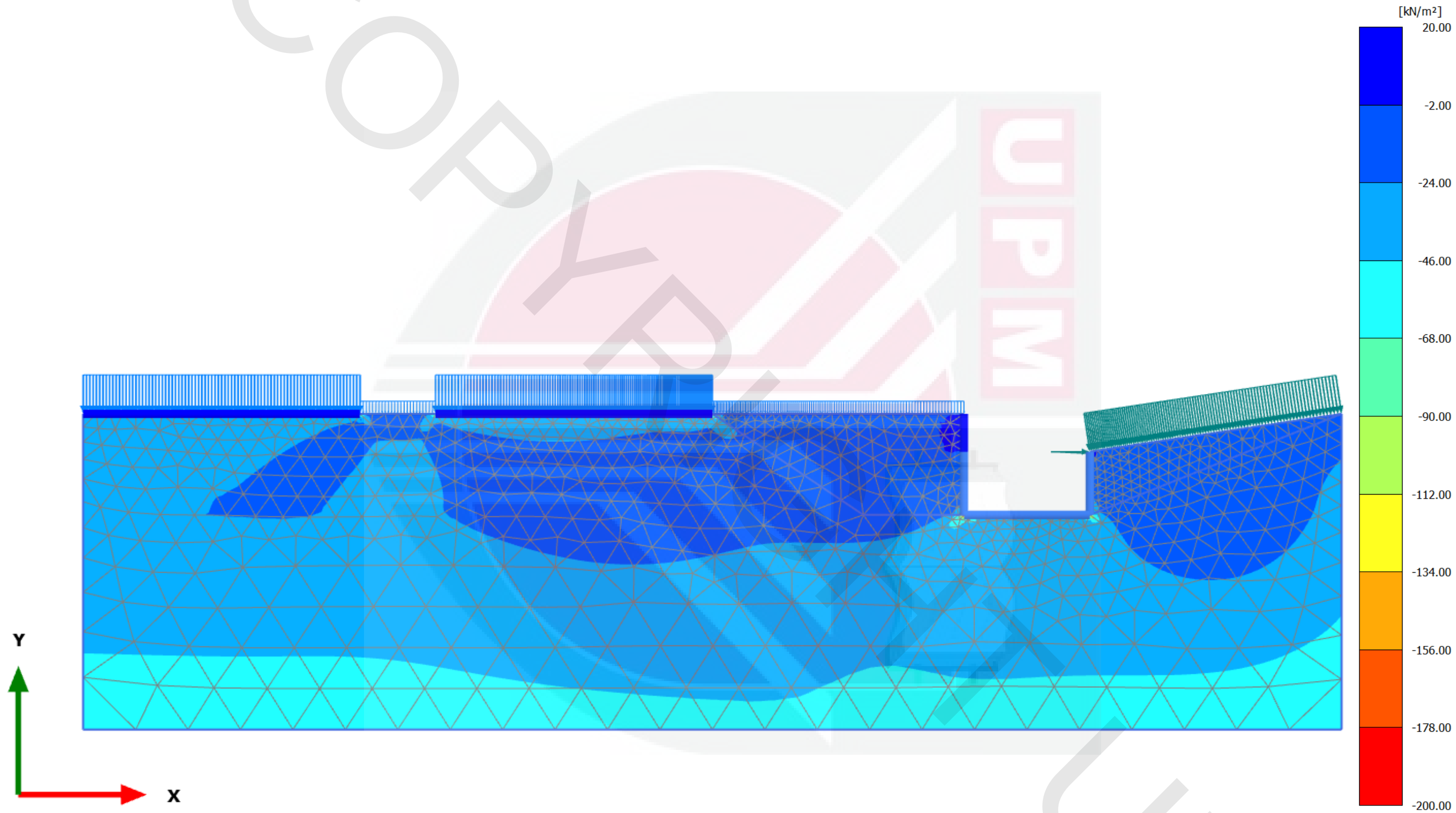

Figure 4.23: PLAXIS output showing σ'_{xx} stresses for natural marine clay

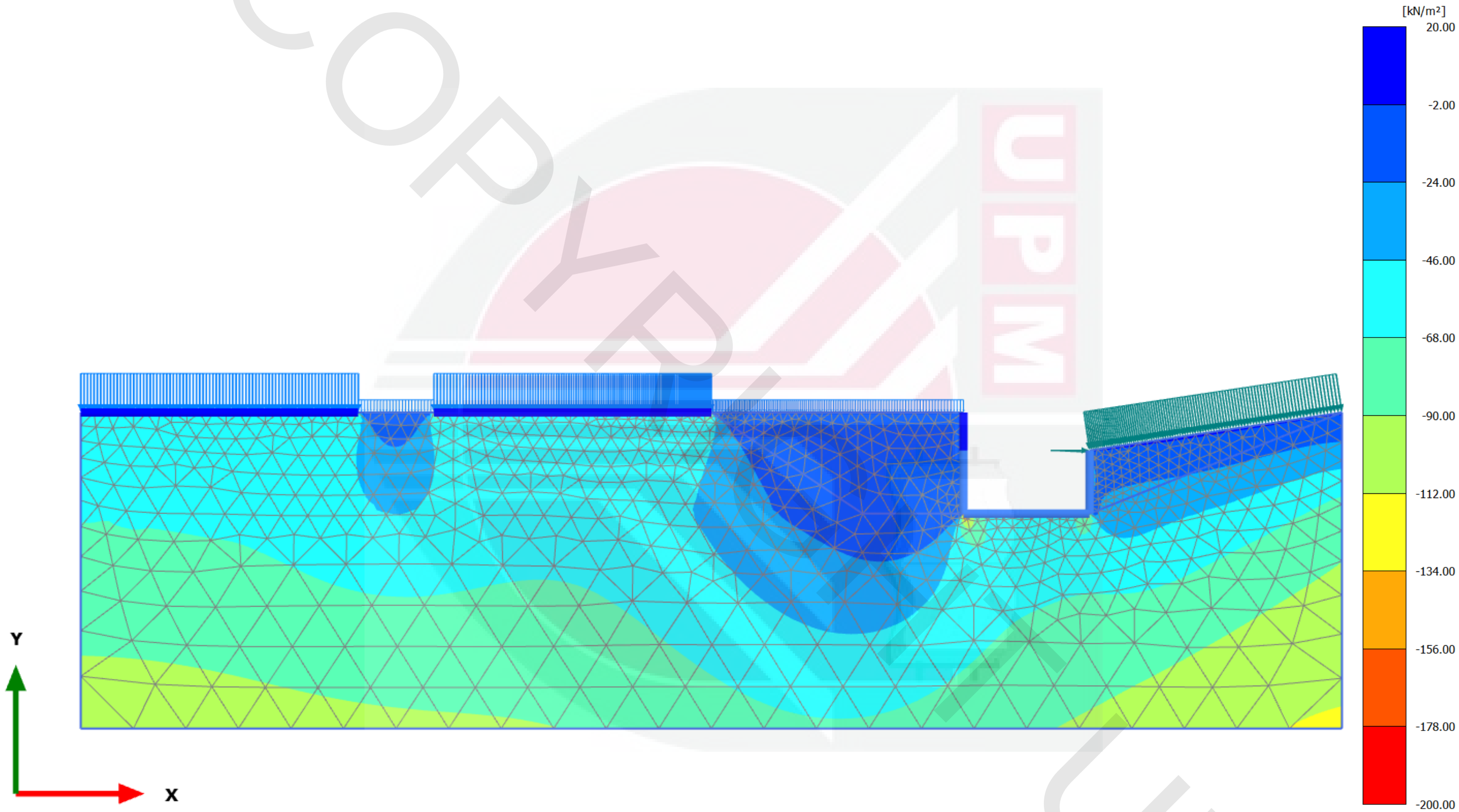

Figure 4.24: PLAXIS output showing σ'_{yy} stresses for natural marine clay

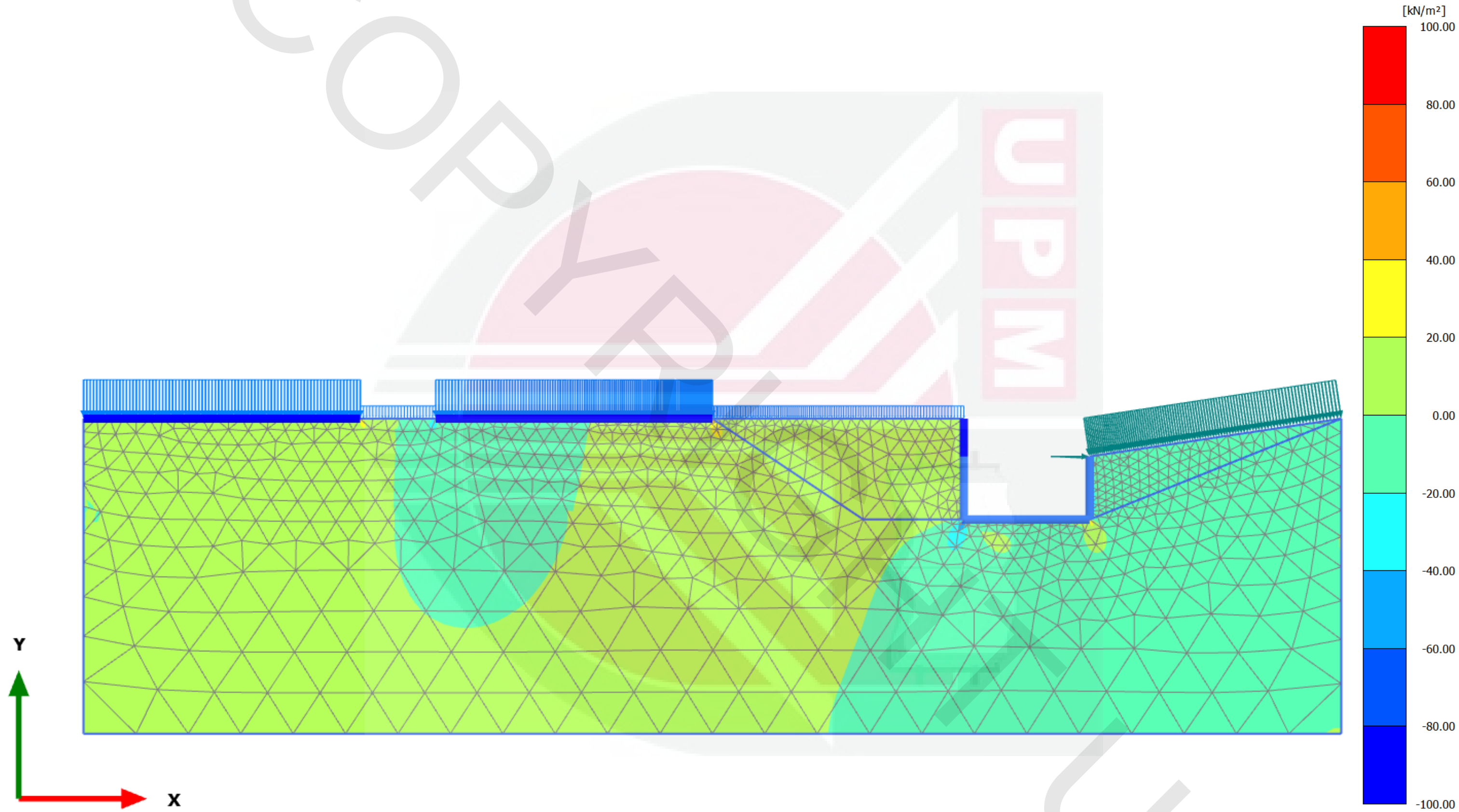

Figure 4.25: PLAXIS output showing σ'_{xy} stresses for natural marine clay

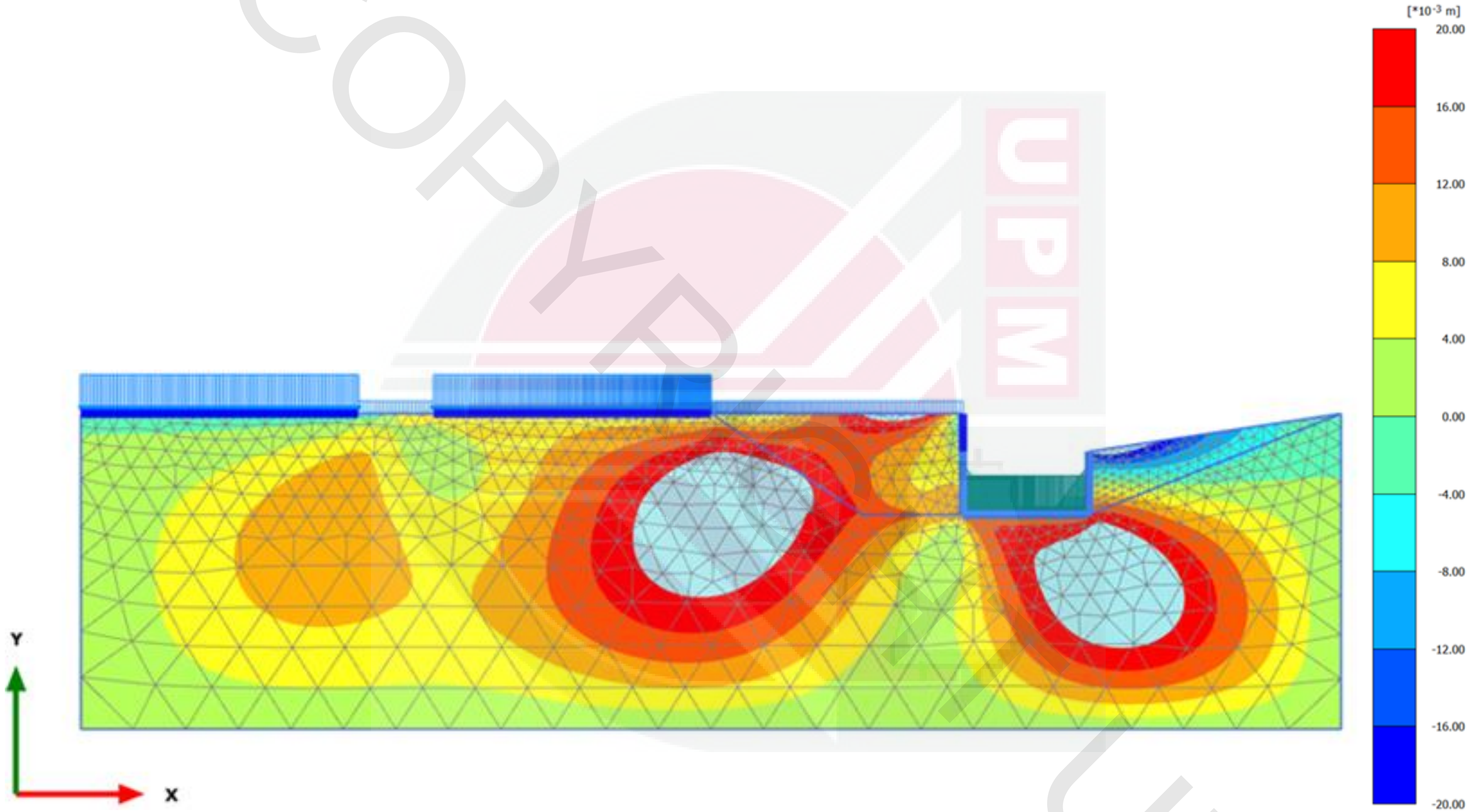

Figure 4.26: PLAXIS output showing horizontal deformations for SL5P5C10

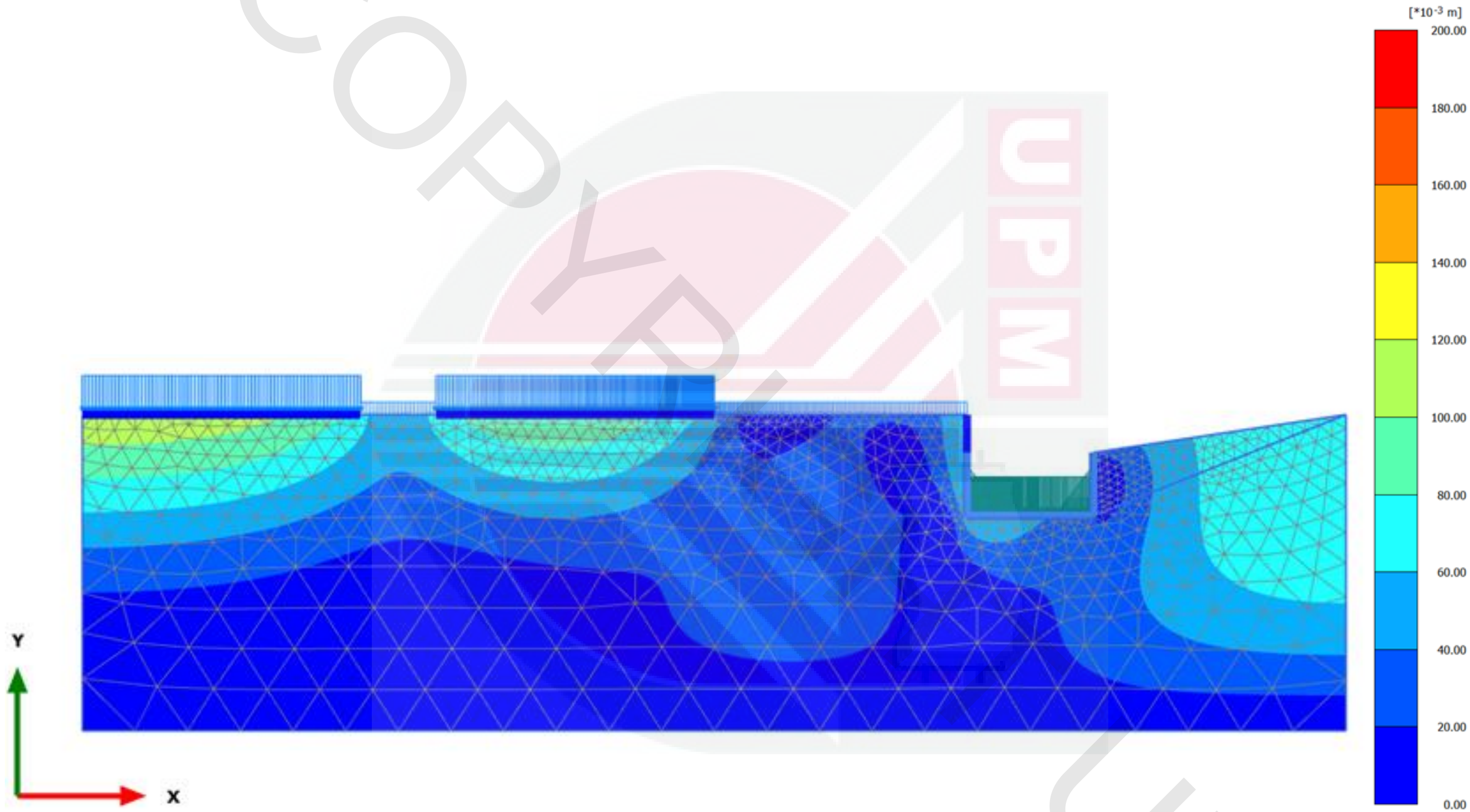

Figure 4.27: PLAXIS output showing vertical deformations for SL5P5C10

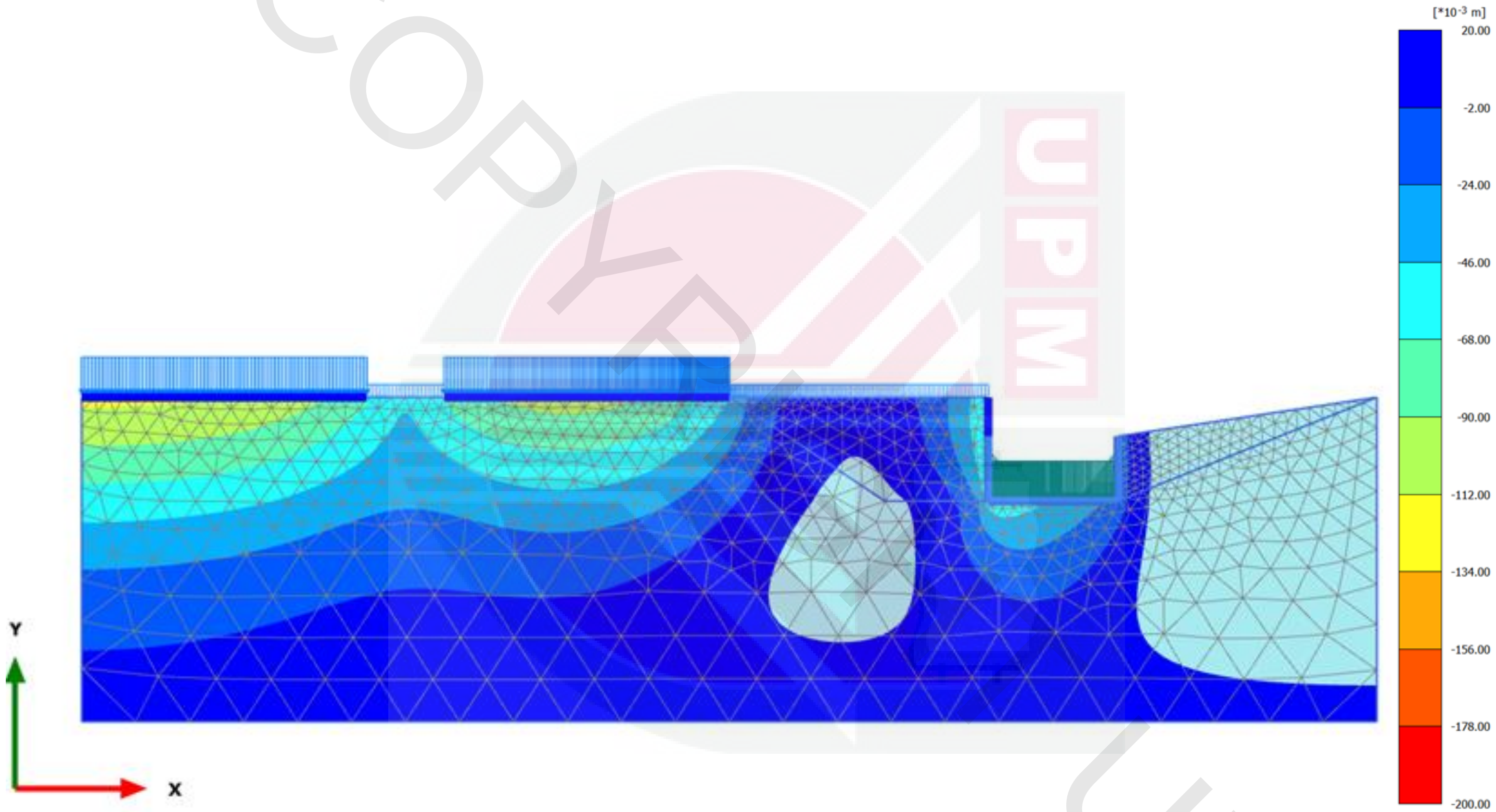

Figure 4.28: PLAXIS output showing total deformations for SL5P5C10

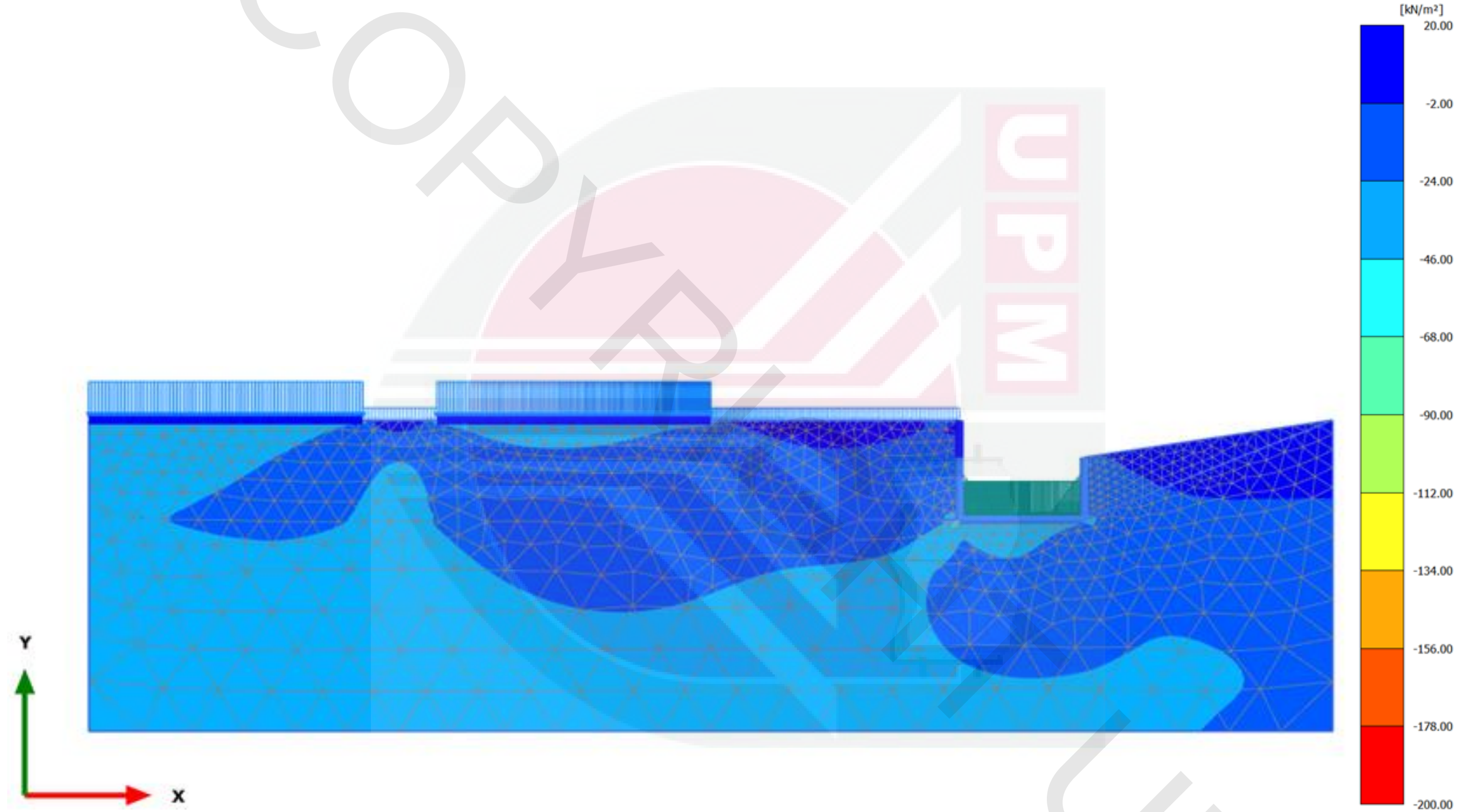

Figure 4.29: PLAXIS output showing σ'_{xx} stresses for SL5P5C10

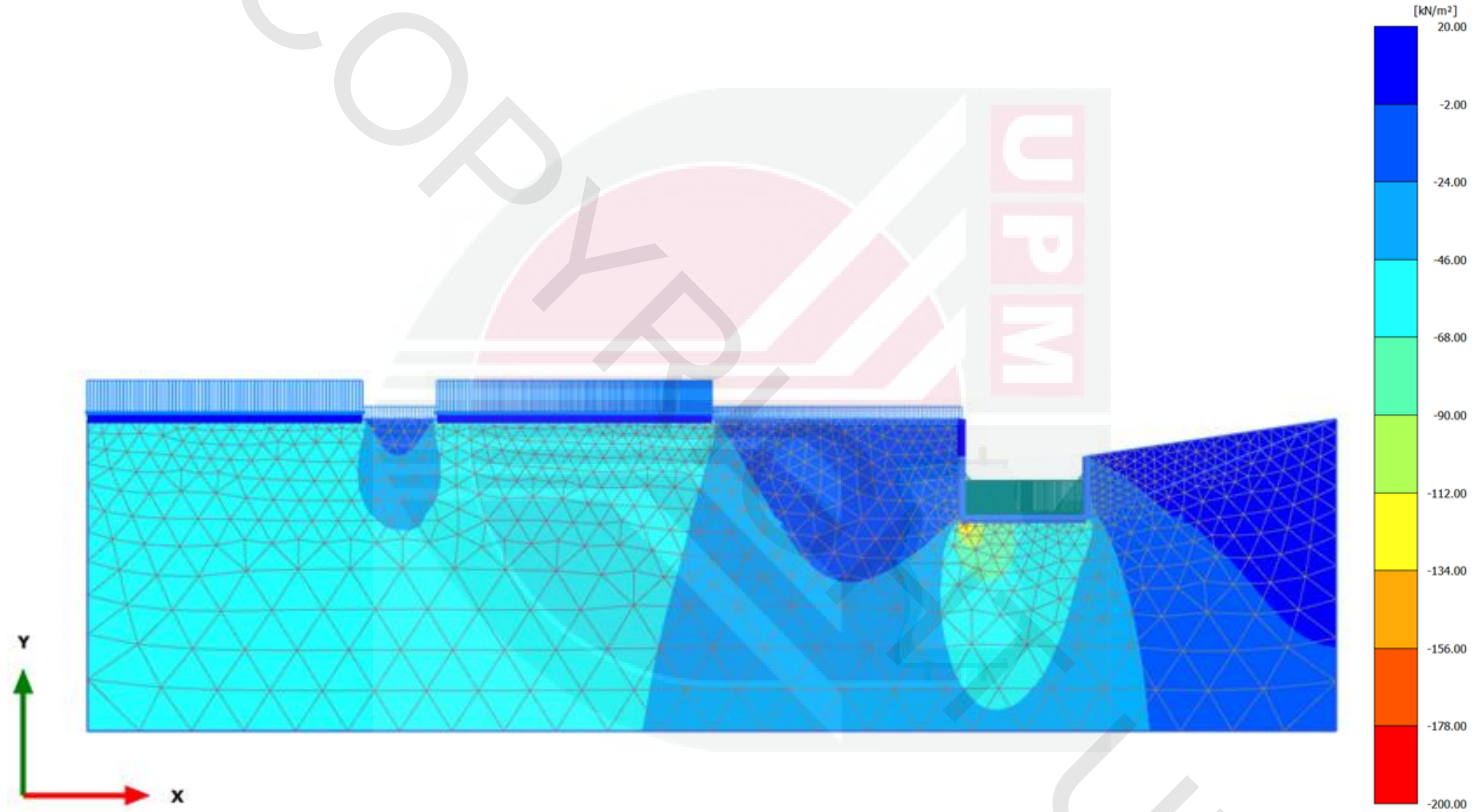

Figure 4.30: PLAXIS output showing σ'_{yy} stresses for SL5P5C10

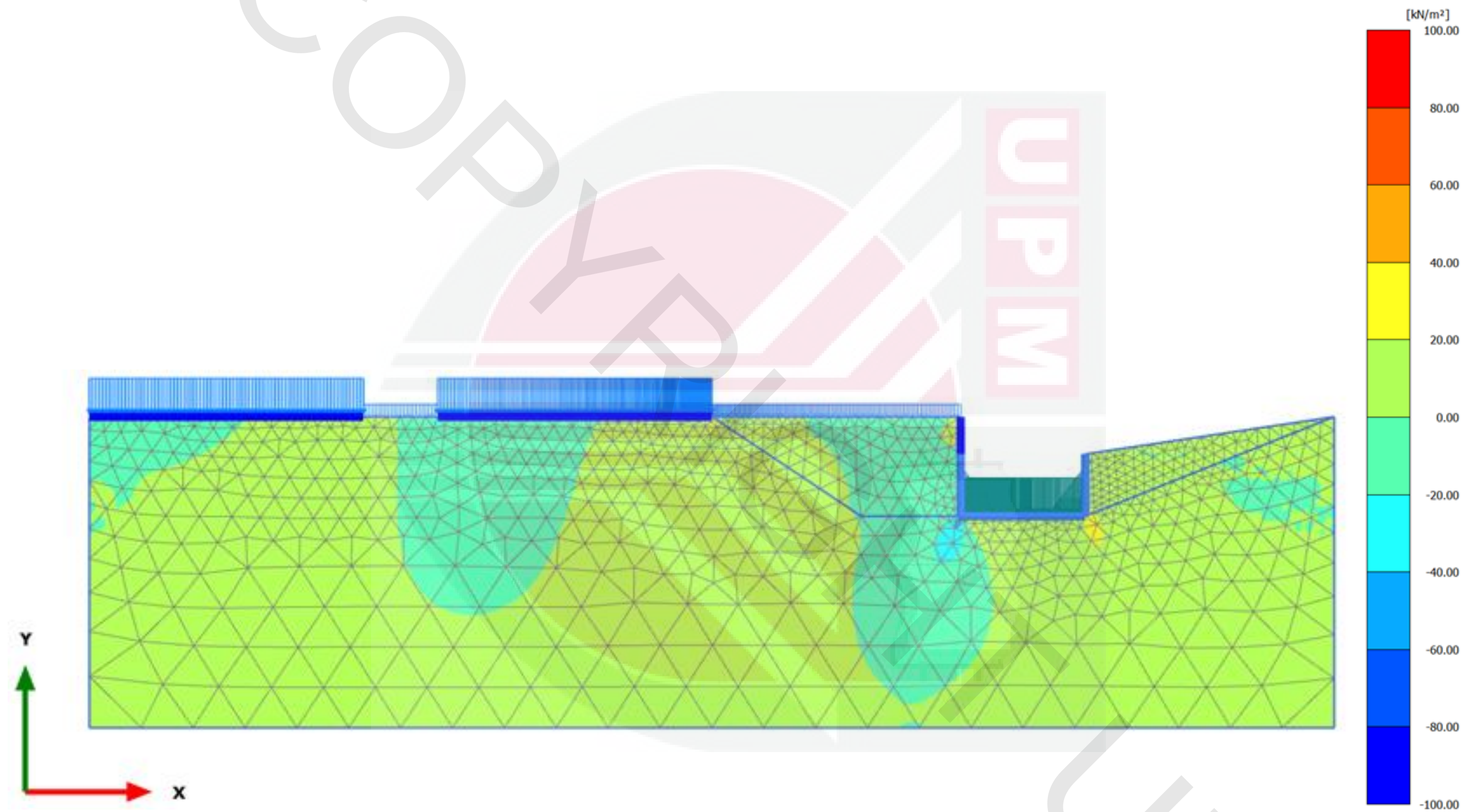

Figure 4.31: PLAXIS output showing σ'_{xy} stresses for SL5P5C10

4.7 Machine Learning Applications

Through this stage of the research, machine learning algorithms were used in prediction of short–term and long–term of loading conditions. In addition, stress–strain behaviour for long–term of loading was predicted using machine learning models. This section is divided into; (1) data collection, (2) data curing (data imputation), (3) models of manual feature selections, and (4) hybrid models for feature selections.

4.7.1 Data Collection

This study depended on previous research on the assessment of lime, palm oil fly ash, and calcined shale in strengthening marine clay in short–term loading (Mohammed, 2023). Previous research focused on 7, 28, and 90 days curing duration, and factors of unconfined shear strength UCS, flexural strength FLX, modulus of elasticity E, compression index C_C, swelling index C_s,coefficient of volume compressibility m_v, coefficient of consolidation C_V, seepage velocity k, void ratio e, maximum dry density MMD, optimum moisture content OMC and Atterberg limits as shown in Tables 4.8, 4.9, and 4.10.

Table 4.8: Collected data from previous research for compressive strength

Code	m_v	C_s	C_C	C_v	k	a_v	e
S	1.29E–04	0.086	0.2	2.50E–03	3.25E–08	2.50E–04	0.98
SL5P0C0–7	1.26E–04	0.028	0.077	1.70E–03	2.18E–08	–	0.975
SL5P1C0–7	4.10E–05	0.027	0.068	1.32E–03	5.15E–09	7.80E–05	0.932
SL5P5C0–7	4.00E–05	0.022	0.051	1.21E–03	5.00E–09	7.50E–05	0.841
SL5P10C0–7	7.90E–05	0.02	0.1	1.80E–03	1.40E–08	1.41E–04	0.798
SL5P15C0–7	9.80E–05	0.026	0.122	3.21E–03	3.22E–08	1.65E–04	0.725
SL5P20C0–7	9.60E–05	0.032	0.125	3.35E–03	3.23E–08	1.62E–04	0.675
SL5P5C5–7	3.40E–05	0.015	0.05	1.21E–03	4.60E–09	6.00E–05	0.805
SL3P5C5–7	1.53E–04	0.04	0.176	1.28E–03	2.00E–08	2.58E–04	0.811
SL1P5C5–7	8.15E–05	0.037	0.198	1.40E–03	1.20E–08	1.50E–04	0.832
SL5P5C10–7	2.10E–05	0.015	0.048	1.00E–03	2.00E–09	3.60E–05	0.775
SL3P5C10–7	1.01E–04	0.031	0.122	1.05E–03	1.00E–08	1.75E–04	0.788
SL1P5C10–7	8.08E–05	0.033	0.151	1.30E–03	1.15E–08	1.45E–04	0.79
SL5P5C15–7	6.20E–05	0.017	0.056	2.12E–03	1.28E–08	1.19E–04	0.882
SL3P5C15–7	1.30E–04	0.025	0.18	1.80E–03	2.50E–08	2.41E–04	0.845
SL1P5C15–7	1.18E–04	0.041	0.161	1.75E–03	2.01E–08	2.25E–04	0.84
SL5P5C20–7	7.50E–05	0.022	0.067	2.25E–03	1.65E–08	1.42E–04	0.891
SL3P5C20–7	2.20E–04	0.02	0.181	2.49E–03	5.80E–08	4.50E–04	0.88
SL1P5C20–7	1.04E–04	0.044	0.145	2.30E–03	2.41E–08	1.82E–04	0.846

For missing data (–) symbol is mentioned for data imputation

Table 4.9: Collected data from previous research for shear and flexural strength

Code	L	POFA	CS	Time	UCS	FLX	E	Load
S	0	0	0		0.356	0.23	1.22	185.5
SL5P0C0–7	5	0	0	7	0.885	0.37	1.78	300.6
SL5P1C0–7	5	1	0	7	0.919	0.4	2.54	323.9
SL5P5C0–7	5	5	0	7	0.948	0.41	2.56	335.4
SL5P10C0–7	5	10	0	7	0.715	0.32	2.06	258.9
SL5P15C0–7	5	15	0	7	0.592	0.254	1.63	205.4
SL5P20C0–7	5	20	0	7	0.552	–	–	–
SL5P5C5–7	5	5	5	7	0.986	0.618	4.125	512.9
SL3P5C5–7	3	5	5	7	0.948	0.576	3.35	477.7
SL1P5C5–7	1	5	5	7	0.802	0.545	2.3	452.4
SL5P5C10–7	5	5	10	7	1.103	0.64	4.489	531.2
SL3P5C10–7	3	5	10	7	0.993	0.63	4.38	522.9
SL1P5C10–7	1	5	10	7	0.82	0.55	2.853	456.5
SL5P5C15–7	5	5	15	7	1.025	0.465	3.21	386
SL3P5C15–7	3	5	15	7	0.631	0.435	2.72	361.1
SL1P5C15–7	1	5	15	7	0.483	0.355	1.756	294.7
SL5P5C20–7	5	5	20	7	0.729	0.168	2.765	139.4
SL3P5C20–7	3	5	20	7	0.422	0.35	2.2	290.5
SL1P5C20–7	1	5	20	7	0.411	0.24	1.42	199.2
SL5P5C5–28	5	5	5	28	1.206	–	–	–
SL3P5C5–28	3	5	5	28	1.074	–	–	–
SL1P5C5–28	1	5	5	28	0.805	–	–	–
SL5P5C10–28	5	5	10	28	1.563	–	–	–
SL3P5C10–28	3	5	10	28	1.294	–	–	–
SL1P5C10–28	1	5	10	28	0.814	–	–	–
SL5P5C15–28	5	5	15	28	1.02	–	–	–
SL3P5C15–28	3	5	15	28	0.716	–	–	–
SL1P5C15–28	1	5	15	28	0.502	–	–	–
SL5P5C20–28	5	5	20	28	–	–	–	–
SL3P5C20–28	3	5	20	28	–	–	–	–
SL1P5C20–28	1	5	20	28	–	–	–	–
SL5P5C5–90	5	5	5	90	1.201	–	–	–
SL3P5C5–90	3	5	5	90	1.09	–	–	–
SL1P5C5–90	1	5	5	90	0.808	–	–	–
SL5P5C10–90	5	5	10	90	1.77	–	–	–
SL3P5C10–90	3	5	10	90	1.1	–	–	–
SL1P5C10–90	1	5	10	90	0.811	–	–	–
SL5P5C15–90	5	5	15	90	1.04	–	–	–
SL3P5C15–90	3	5	15	90	0.728	–	–	–
SL1P5C15–90	1	5	15	90	0.521	–	–	–
SL5P5C20–90	5	5	20	90	–	–	–	–
SL3P5C20–90	3	5	20	90	–	–	–	–
SL1P5C20–90	1	5	20	90	–	–	–	–

For missing data (–) symbol is mentioned for data imputation

Table 4.10: Collected data from previous research for compaction and Atterberg limits

Code	LL	PL	PI	GS	SL	MDD	OMC
S	–	–	–	–	–	14.3	26
SL5P0C0–7	–	–	–	–	–	13.81	32
SL5P1C0–7	–	–	–	–	–	13.79	32.5
SL5P5C0–7	–	–	–	–	–	13.76	33
SL5P10C0–7	–	–	–	–	–	13.7	34
SL5P15C0–7	–	–	–	–	–	13.6	34.9
SL5P20C0–7	–	–	–	–	–	13.44	35
SL5P5C5–7	61.3	48.95	12.35	2.57	6.43	14.59	31.5
SL3P5C5–7	64.55	48.67	15.88	2.62	10.71	14.74	31
SL1P5C5–7	66.1	45.105	20.995	2.69	10	14.71	30.50
SL5P5C10–7	59.5	48.24	11.26	2.56	5.71	14.6	31.3
SL3P5C10–7	63.4	47.95	15.45	2.61	10	14.8	30.2
SL1P5C10–7	64.3	44.89	19.41	2.61	8.57	14.85	29.77
SL5P5C15–7	59.2	52.1	7.1	2.54	5.36	13.78	34
SL3P5C15–7	60.62	48.43	12.19	2.57	8.57	13.95	33.2
SL1P5C15–7	62.45	45.95	16.5	2.58	7.86	14.8	29.8
SL5P5C20–7	62.8	53.436	9.364	2.53	4.29	13.76	35
SL3P5C20–7	63.22	49.85	13.37	2.55	7.86	13.81	34.3
SL1P5C20–7	66.04	47.46	18.58	2.51	7.14	14.43	30.00

For missing data (–) symbol is mentioned for data imputation

The data was not enough for applying the machine learning prediction and to study long–term behaviour of treated soil, which are the core aim of this study. In addition, the assessment of the treated soil matrix and its properties in real geotechnical applications. Therefore, missing–data imputation was a compulsory through this research, where the data was completed experimentally and numerically. The data imputed were related to the missing durations for 14, 21, and 56 curing days, where UU triaxial test, 1–D consolidation test, Atterberg limits, and others. The missing data that were not able to impute using laboratory experiments were imputed using the numerical prediction using the equations mentioned in Section 4.7.2 for both experimentally and numerically, where the missing data are as shown in "—" in Tables 4.8, 4.9 and 4.10.

4.7.2 Missing Data Imputation

First, the experimental imputation for the data was assessed for Atterberg limits, while the consolidation parameters were conducted from the CU triaxial test from consolidation stage. For undrained shear strength, the data imputation was conducted using experimental work through unconfined undrained triaxial test. The results were compared to the UCS results of previous research (Mohammed, 2023), where the values were almost identical.

Missing data that could assessed experimentally, were imputed through interpolating method with accurate results depending on accepted deviation, where the experimental uncertainties could affect the results (Tsai, 2010). Impossibility to The missing data was covered using linear regression following the trend of the existing data. The linear regression was based on the standard deviation of the existing data as in Equations 4.1 and 4.2, where E_{er} is the error, y is imputed target, $\hat{y}$ is mean of targeted values, and x is input data. This method allows the data to follow the same trend by the same standard deviation, variance, and mean of the exiting data within the allowable limits. The linear regression is effective imputation method compared to other methods; mean, most frequent data, maximum, minimum, or zero (Longford, 2005), where each one of them has a defect in the data's statistical trend and performance. In addition, the dataset completed by predicted data $\hat{y}$ would seem more like what we may expect even though the values of y would not be "estimated" as well since the values of predicted y would be distributed around the regression line just as widely as the values of y that were really recorded (Longford, 2005). All data was imputed using simple regression was following the relationship between the parameters that follow the linear trend as shown in Figure 4.32. Finally, all used data in machine learning ML modelling are shown in Appendix B – Table B1, where all the features collected are 34 features in total.

$$\hat{y} - E_{er} < y < \hat{y} + E_{er} \tag{4.1}$$

$$E = t_c\, S_e \sqrt{1 + \frac{1}{n} + \frac{n\,(x_o + \bar{\bar{x}})^2}{n\,\Sigma\, x^2 - (\Sigma\, X\,)^2}} \tag{4.2}$$

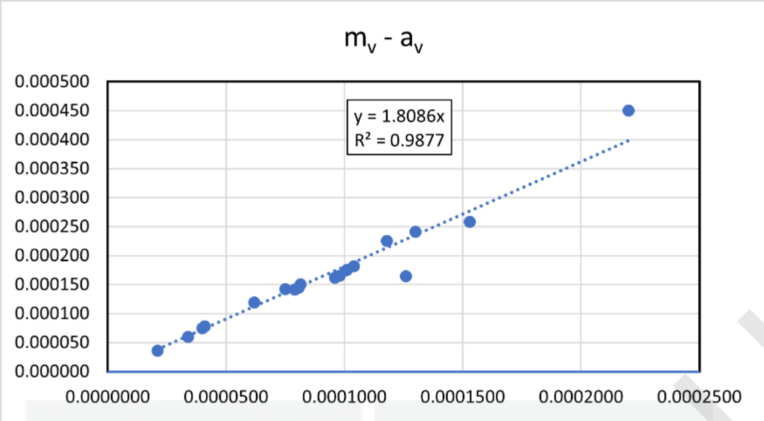

(a)

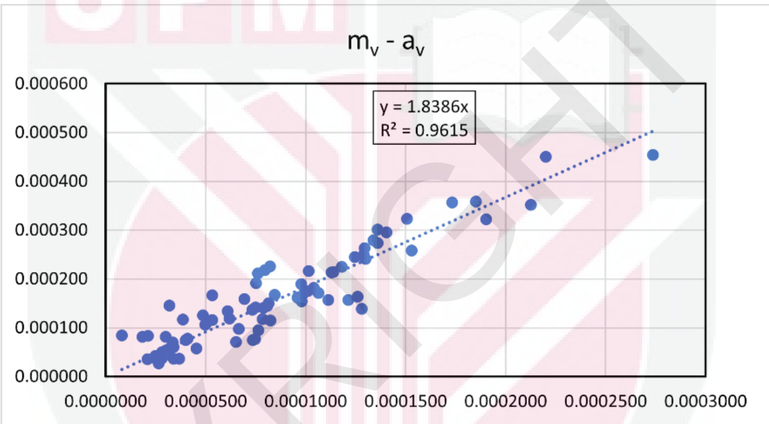

(b)

Figure 4.32: Example for predicted data for imputation of missing data using linear regression showing (a) existing data and (b) all data after prediction.

4.7.3 Data Hypothesis

The used data were tested for hypothesis test as mentioned in Section 3.8.1. First, the correlation matrix was applied to study the relationship between features, where the used features showed a significant relationship between them, and undrained shear strength conducted from UU triaxial test as shown in Figures 4.33 and 4.34. Then, t–test was assessed for all features, where all feature were significant statistically by P–value less than 0.05 as shown in Table 4.11. On the same hand, Kolmogorov–Smirnov test conducted the same trend, that all feature were significant statistically by P–value less than 0.05 as shown in Table 4.12. In addition, Bland–Atiman plot showed that all features are in the allowed statistical limits as shown in Table 4.13. Finally, skewness, kurtosis, variance and other statistical properties are shown in Table 4.14, which indicates that the dataset is reliable for machine learning modelling as mentioned in previous research (Eyo et al., 2022; Nouman Amjad Raja et al., 2021).

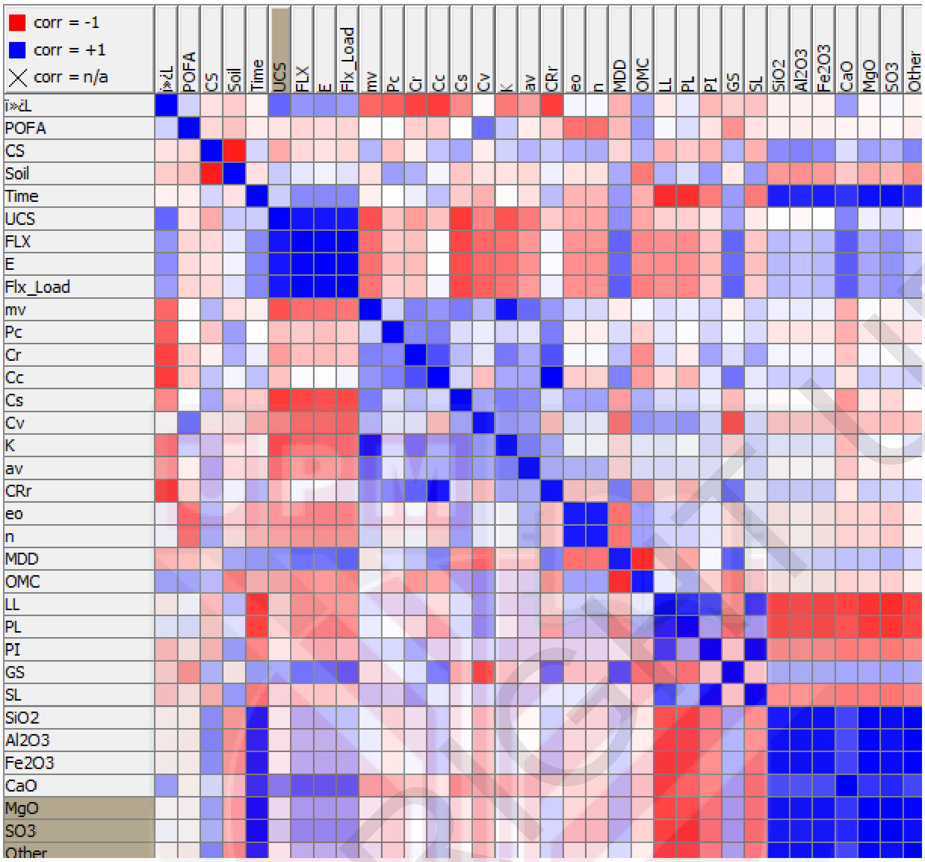

Figure 4.33: Correlation matrix for used features using colour weight

RowID	ï»¿L	POFA	CS	Soil	Time	UCS	FLX	E	Flx_Load	mv	Pc	Cr	Cc	Cs	Cv	K	av
ï»¿L	1.0	0.181	-0.120	-0.202	-0.057	0.602	0.421	0.447	0.390	-0.595	-0.630	-0.736	-0.770	-0.469	-0.031	-0.529	-0.389
POFA	0.181	1.0	-0.157	-0.240	-0.075	-0.108	-0.164	-0.140	-0.170	-0.024	-0.003	-0.187	-0.204	0.004	0.571	0.209	-0.072
CS	-0.120	-0.157	1.0	-0.888	0.165	-0.332	-0.148	-0.119	-0.158	0.292	-0.228	-0.059	0.234	0.345	-0.077	0.180	0.288
Soil	-0.202	-0.240	-0.888	1.0	-0.120	0.206	0.094	0.050	0.114	-0.124	0.384	0.311	0.040	-0.218	-0.116	-0.113	-0.156
Time	-0.057	-0.075	0.165	-0.120	1.0	0.199	0.468	0.471	0.468	-0.062	-0.008	0.066	0.247	-0.207	-0.313	-0.018	-0.125
UCS	0.602	-0.108	-0.332	0.206	0.199	1.0	0.925	0.918	0.912	-0.685	-0.248	-0.384	-0.238	-0.779	-0.485	-0.677	-0.520
FLX	0.421	-0.164	-0.148	0.094	0.468	0.925	1.0	0.988	0.990	-0.568	-0.209	-0.252	0.012	-0.728	-0.602	-0.567	-0.413
E	0.447	-0.140	-0.119	0.050	0.471	0.918	0.988	1.0	0.979	-0.566	-0.250	-0.271	-0.013	-0.703	-0.594	-0.560	-0.433
Flx_Load	0.390	-0.170	-0.158	0.114	0.468	0.912	0.990	0.979	1.0	-0.545	-0.194	-0.233	0.038	-0.719	-0.626	-0.548	-0.393
mv	-0.595	-0.024	0.292	-0.124	-0.062	-0.685	-0.568	-0.566	-0.545	1.0	0.175	0.496	0.420	0.517	0.281	0.930	0.593
Pc	-0.630	-0.003	-0.228	0.384	-0.008	-0.248	-0.209	-0.250	-0.194	0.175	1.0	0.470	0.505	0.136	0.073	0.168	0.109
Cr	-0.736	-0.187	-0.059	0.311	0.066	-0.384	-0.252	-0.271	-0.233	0.496	0.470	1.0	0.690	0.276	0.098	0.532	0.335
Cc	-0.770	-0.204	0.234	0.040	0.247	-0.238	0.012	-0.013	0.038	0.420	0.505	0.690	1.0	0.170	-0.260	0.345	0.352
Cs	-0.469	0.004	0.345	-0.218	-0.207	-0.779	-0.728	-0.703	-0.719	0.517	0.136	0.276	0.170	1.0	0.358	0.499	0.445
Cv	-0.031	0.571	-0.077	-0.116	-0.313	-0.485	-0.602	-0.594	-0.626	0.281	0.073	0.098	-0.260	0.358	1.0	0.415	0.378
K	-0.529	0.209	0.180	-0.113	-0.018	-0.677	-0.567	-0.560	-0.548	0.930	0.168	0.532	0.345	0.499	0.415	1.0	0.517
av	-0.389	-0.072	0.288	-0.156	-0.125	-0.520	-0.413	-0.433	-0.393	0.593	0.109	0.335	0.352	0.445	0.378	0.517	1.0
CRr	-0.764	-0.189	0.208	0.058	0.264	-0.210	0.038	0.014	0.064	0.407	0.508	0.683	0.999	0.144	-0.271	0.337	0.326
eo	0.039	-0.559	0.299	-0.107	-0.293	-0.350	-0.422	-0.440	-0.434	0.157	-0.065	0.033	-0.201	0.362	0.101	0.029	0.299
n	0.030	-0.571	0.321	-0.122	-0.287	-0.353	-0.418	-0.434	-0.429	0.158	-0.065	0.026	-0.181	0.368	0.075	0.022	0.298
MDD	-0.312	-0.273	-0.167	0.337	0.405	0.445	0.616	0.592	0.634	-0.076	0.138	0.260	0.495	-0.384	-0.573	-0.145	-0.177
OMC	0.371	0.389	0.304	-0.526	-0.315	-0.351	-0.473	-0.439	-0.499	0.033	-0.181	-0.451	-0.390	0.316	0.415	0.075	0.117
LL	-0.082	0.033	-0.300	0.301	-0.836	-0.189	-0.441	-0.456	-0.441	0.139	0.095	0.138	-0.152	0.147	0.380	0.089	0.133
PL	0.090	0.132	-0.212	0.137	-0.817	-0.192	-0.459	-0.451	-0.470	0.079	0.011	-0.073	-0.298	0.155	0.427	0.016	0.108
PI	-0.274	-0.111	-0.290	0.391	-0.512	-0.105	-0.233	-0.272	-0.218	0.159	0.165	0.357	0.104	0.074	0.160	0.149	0.110
GS	-0.202	-0.432	0.292	-0.083	0.392	0.356	0.609	0.575	0.622	-0.055	0.031	0.134	0.554	-0.269	-0.717	-0.171	0.005
SL	-0.239	-0.112	-0.304	0.396	-0.524	-0.084	-0.224	-0.250	-0.202	0.186	0.138	0.352	0.097	0.052	0.149	0.168	0.167
SiO2	-0.058	-0.060	0.454	-0.406	0.893	-0.006	0.270	0.278	0.270	0.062	-0.096	0.044	0.202	-0.029	-0.231	0.095	-0.032
Al2O3	-0.061	-0.072	0.493	-0.440	0.860	-0.036	0.236	0.244	0.237	0.080	-0.108	0.041	0.195	-0.001	-0.225	0.107	-0.016
Fe2O3	-0.056	-0.060	0.453	-0.406	0.894	-0.003	0.272	0.280	0.273	0.059	-0.098	0.043	0.201	-0.031	-0.232	0.094	-0.033
CaO	0.388	-0.041	0.135	-0.217	0.809	0.482	0.645	0.645	0.636	-0.326	-0.315	-0.233	-0.113	-0.406	-0.294	-0.272	-0.229
MgO	-0.031	-0.040	0.378	-0.347	0.941	0.065	0.341	0.348	0.341	0.013	-0.091	0.034	0.196	-0.092	-0.245	0.058	-0.067
SO3	0.030	-0.026	0.303	-0.293	0.966	0.157	0.423	0.429	0.422	-0.055	-0.110	0.000	0.161	-0.168	-0.261	-0.001	-0.108
Other	-0.042	-0.073	0.486	-0.437	0.866	-0.016	0.254	0.263	0.255	0.065	-0.119	0.030	0.184	-0.016	-0.230	0.093	-0.025

RowID	CRr	eo	n	MDD	OMC	LL	PL	PI	GS	SL	SiO2	Al2O3	Fe2O3	CaO	MgO	SO3	Other
ï»¿L	-0.764	0.039	0.030	-0.312	0.371	-0.082	0.090	-0.274	-0.202	-0.239	-0.058	-0.061	-0.056	0.388	-0.031	0.030	-0.042
POFA	-0.189	-0.559	-0.571	-0.273	0.389	0.033	0.132	-0.111	-0.432	-0.112	-0.060	-0.072	-0.060	-0.041	-0.040	-0.026	-0.073
CS	0.208	0.299	0.321	-0.167	0.304	-0.300	-0.212	-0.290	0.292	-0.304	0.454	0.493	0.453	0.135	0.378	0.303	0.486
Soil	0.058	-0.107	-0.122	0.337	-0.526	0.301	0.137	0.391	-0.083	0.396	-0.406	-0.440	-0.406	-0.217	-0.347	-0.293	-0.437
Time	0.264	-0.293	-0.287	0.405	-0.315	-0.836	-0.817	-0.512	0.392	-0.524	0.893	0.860	0.894	0.809	0.941	0.966	0.866
UCS	-0.210	-0.350	-0.353	0.445	-0.351	-0.189	-0.192	-0.105	0.356	-0.084	-0.006	-0.036	-0.003	0.482	0.065	0.157	-0.016
FLX	0.038	-0.422	-0.418	0.616	-0.473	-0.441	-0.459	-0.233	0.609	-0.224	0.270	0.236	0.272	0.645	0.341	0.423	0.254
E	0.014	-0.440	-0.434	0.592	-0.439	-0.456	-0.451	-0.272	0.575	-0.250	0.278	0.244	0.280	0.645	0.348	0.429	0.263
Flx_Load	0.064	-0.434	-0.429	0.634	-0.499	-0.441	-0.470	-0.218	0.622	-0.202	0.270	0.237	0.273	0.636	0.341	0.422	0.255
mv	0.407	0.157	0.158	-0.076	0.033	0.139	0.079	0.159	-0.055	0.186	0.062	0.080	0.059	-0.326	0.013	-0.055	0.065
Pc	0.508	-0.065	-0.065	0.138	-0.181	0.095	0.011	0.165	0.031	0.138	-0.096	-0.108	-0.098	-0.315	-0.091	-0.110	-0.119
Cr	0.683	0.033	0.026	0.260	-0.451	0.138	-0.073	0.357	0.134	0.352	0.044	0.041	0.043	-0.233	0.034	0.000	0.030
Cc	0.999	-0.201	-0.181	0.495	-0.390	-0.152	-0.298	0.104	0.554	0.097	0.202	0.195	0.201	-0.113	0.196	0.161	0.184
Cs	0.144	0.362	0.368	-0.384	0.316	0.147	0.155	0.074	-0.269	0.052	-0.029	-0.001	-0.031	-0.406	-0.092	-0.168	-0.016
Cv	-0.271	0.101	0.075	-0.573	0.415	0.380	0.427	0.160	-0.717	0.149	-0.231	-0.225	-0.232	-0.294	-0.245	-0.261	-0.230
K	0.337	0.029	0.022	-0.145	0.075	0.089	0.016	0.149	-0.171	0.168	0.095	0.107	0.094	-0.272	0.058	-0.001	0.093
av	0.326	0.299	0.298	-0.177	0.117	0.133	0.108	0.110	0.005	0.167	-0.032	-0.016	-0.033	-0.229	-0.067	-0.108	-0.025
CRr	1.0	-0.244	-0.225	0.527	-0.416	-0.159	-0.305	0.099	0.556	0.092	0.205	0.197	0.204	-0.102	0.203	0.172	0.186
eo	-0.244	1.0	0.999	-0.608	0.401	0.201	0.212	0.102	-0.175	0.108	-0.105	-0.065	-0.106	-0.182	-0.169	-0.217	-0.069
n	-0.225	0.999	1.0	-0.599	0.405	0.185	0.198	0.091	-0.150	0.097	-0.096	-0.055	-0.096	-0.180	-0.161	-0.210	-0.059
MDD	0.527	-0.608	-0.599	1.0	-0.904	-0.244	-0.378	0.033	0.680	0.010	0.186	0.153	0.186	0.245	0.239	0.279	0.156
OMC	-0.416	0.401	0.405	-0.904	1.0	0.086	0.276	-0.199	-0.513	-0.162	-0.100	-0.070	-0.101	-0.172	-0.150	-0.188	-0.074
LL	-0.159	0.201	0.185	-0.244	0.086	1.0	0.867	0.757	-0.447	0.762	-0.764	-0.739	-0.765	-0.743	-0.803	-0.829	-0.746
PL	-0.305	0.212	0.198	-0.378	0.276	0.867	1.0	0.331	-0.516	0.358	-0.744	-0.720	-0.744	-0.679	-0.778	-0.796	-0.725
PI	0.099	0.102	0.091	0.033	-0.199	0.757	0.331	1.0	-0.170	0.976	-0.472	-0.455	-0.473	-0.517	-0.501	-0.525	-0.462
GS	0.556	-0.175	-0.150	0.680	-0.513	-0.447	-0.516	-0.170	1.0	-0.165	0.330	0.321	0.331	0.344	0.345	0.357	0.325
SL	0.092	0.108	0.097	0.010	-0.162	0.762	0.358	0.976	-0.165	1.0	-0.484	-0.467	-0.485	-0.523	-0.513	-0.537	-0.474
SiO2	0.205	-0.105	-0.096	0.186	-0.100	-0.764	-0.744	-0.472	0.330	-0.484	1.0	0.997	1.000	0.735	0.992	0.965	0.998
Al2O3	0.197	-0.065	-0.055	0.153	-0.070	-0.739	-0.720	-0.455	0.321	-0.467	0.997	1.0	0.997	0.709	0.980	0.946	1.000
Fe2O3	0.204	-0.106	-0.096	0.186	-0.101	-0.765	-0.744	-0.473	0.331	-0.485	1.000	0.997	1.0	0.738	0.992	0.966	0.998
CaO	-0.102	-0.182	-0.180	0.245	-0.172	-0.743	-0.679	-0.517	0.344	-0.523	0.735	0.709	0.738	1.0	0.791	0.855	0.728
MgO	0.203	-0.169	-0.161	0.239	-0.150	-0.803	-0.778	-0.501	0.345	-0.513	0.992	0.980	0.992	0.791	1.0	0.990	0.983
SO3	0.172	-0.217	-0.210	0.279	-0.188	-0.829	-0.796	-0.525	0.357	-0.537	0.965	0.946	0.966	0.855	0.990	1.0	0.952
Other	0.186	-0.069	-0.059	0.156	-0.074	-0.746	-0.725	-0.462	0.325	-0.474	0.998	1.000	0.998	0.728	0.983	0.952	1.0

Figure 4.34: Correlation matrix for used features using factors weight

Table 4.11: Results of paired t–test

Pair	Label	t	df	p–value (2–tailed)	Mean	STD	Standard Error Mean	Confidence Interval Probability	Lower Bound	Upper Bound
Pair 1	UCS – L	–13.00	78	3.25E–21	–2.23E+00	1.53E+00	1.72E–01	0.95	–2.57	–1.89
Pair 2	UCS – POFA	–16.30	78	7.67E–27	–4.32E+00	2.36E+00	2.65E–01	0.95	–4.85	–3.79
Pair 3	UCS – CS	–14.23	78	2.18E–23	–1.05E+01	6.56E+00	7.38E–01	0.95	–11.98	–9.04
Pair 4	UCS – Soil	–107.46	78	1.57E–86	–7.94E+01	6.57E+00	7.39E–01	0.95	–80.88	–77.94
Pair 5	UCS – Time	–10.02	78	1.16E–15	–3.25E+01	2.88E+01	0.24E+00	0.95	–38.91	–26.01
Pair 6	UCS – FLX	17.79	78	3.56E–29	2.87E–01	1.44E–01	1.61E–02	0.95	0.26	0.32
Pair 7	UCS – E	–23.57	78	3.18E–37	–2.85E+00	1.08E+00	1.21E–01	0.95	–3.09	–2.61
Pair 8	UCS – FLX Load	–24.92	78	6.92E–39	–4.82E+02	1.72E+02	1.94E+01	0.95	–521.01	–443.92
Pair 9	UCS – mv	21.07	78	6.16E–34	7.89E–01	3.33E–01	3.75E–02	0.95	0.71	0.86
Pair 10	UCS – P_c’	–17.94	78	2.07E–29	–1.06E+02	5.24E+01	5.90E+00	0.95	–117.57	–94.09
Pair 11	UCS – C_r	23.65	78	2.54E–37	8.49E–01	3.19E–01	3.59E–02	0.95	0.78	0.92
Pair 12	UCS – C_c	20.58	78	2.99E–33	7.63E–01	3.29E–01	3.71E–02	0.95	0.69	0.84
Pair 13	UCS – C_s	23.59	78	3.00E–37	8.57E–01	3.23E–01	3.63E–02	0.95	0.78	0.93
Pair 14	UCS – C_v	24.87	78	7.98E–39	8.81E–01	3.15E–01	3.54E–02	0.95	0.81	0.95
Pair 15	UCS – K	–7.33	78	1.86E–10	–8.66E–01	1.05E+00	1.18E–01	0.95	–1.10	–0.63
Pair 16	UCS – a_v	18.56	78	2.44E–30	7.14E–01	3.42E–01	3.85E–02	0.95	0.64	0.79
Pair 17	UCS – CR_r	22.57	78	6.13E–36	8.16E–01	3.21E–01	3.62E–02	0.95	0.74	0.89
Pair 18	UCS – e_o	1.78	78	7.83E–02	6.75E–02	3.36E–01	3.78E–02	0.95	–0.01	0.14
Pair 19	UCS – n	12.03	78	1.87E–19	4.34E–01	3.20E–01	3.61E–02	0.95	0.36	0.51
Pair 20	UCS – MDD	–289.74	78	4.95E–120	–1.36E+01	4.18E–01	4.71E–02	0.95	–13.73	–13.55
Pair 21	UCS – OMC	–137.55	78	7.54E–95	–3.02E+01	1.95E+00	2.19E–01	0.95	–30.62	–29.75
Pair 22	UCS – LL	–45.67	78	4.78E–58	–5.17E+01	1.01E+01	1.13E+00	0.95	–53.98	–49.47
Pair 23	UCS – PL	–49.46	78	1.17E–60	–3.89E+01	7.00E+00	7.87E–01	0.95	–40.51	–37.37
Pair 24	UCS – PI	–19.90	78	2.68E–32	–1.19E+01	5.32E+00	5.98E–01	0.95	–13.09	–10.71
Pair 25	UCS – G_S	–50.68	78	1.85E–61	–1.71E+00	3.01E–01	3.38E–02	0.95	–1.78	–1.65
Pair 26	UCS – SL	–18.56	78	2.41E–30	–5.82E+00	2.79E+00	3.14E–01	0.95	–6.45	–5.20

Table 4.12: Conducted Kolmogorov–Smirnov test

Reject H0	Statistic	p–Value
1	1	0
1	1	0
1	0.48	2.30561E–08
1	0.95	0
1	1	0
1	0.99	0
1	0.96	0
1	0.91	0
1	1	0
1	1	0
1	1	0
1	1	0
1	1	0
1	0.59	1.43641E–12
1	0.99	0
1	1	0
1	0.46	1.50107E–07
1	0.89	0
1	1	0
1	1	0
1	0.89	0
1	0.97	0
1	0.97	0
1	0.95	0
1	0.96	0
1	0.96	0
1	0.7	0
1	1	0
1	1	0
1	0.99	0
1	1	0

Table 4.13: Bland–Atiman plot limits

Feature	Bias	Upper limit of agreement	Lower limit of agreement
L	–2.232	0.759	–5.222
POFA	–4.320	0.296	–8.936
CS	–10.510	2.353	–23.373
Soil	–79.409	–66.535	–92.282
Time	–32.459	23.977	–88.896
UCS	0.287	0.569	0.006
FLX	–2.853	–0.745	–4.962
E	–482.464	–145.149	–819.779
Flx Load	0.789	1.442	0.137
m_v	–105.828	–3.072	–208.584
P_c’	0.849	1.475	0.224
C_r	0.763	1.408	0.117
C_c	0.857	1.489	0.224
C_s	0.881	1.498	0.264
C_v	–0.866	1.193	–2.925
K	0.714	1.385	0.044
a_v	0.816	1.446	0.186
CR	0.067	0.726	–0.591
e_o	0.434	1.062	–0.194
n	–13.641	–12.821	–14.461
MDD	–30.182	–26.360	–34.005
OMC	–51.721	–31.993	–71.450
LL	–38.938	–25.224	–52.652
PL	–11.901	–1.483	–22.319
PI	–1.714	–1.125	–2.304
G_S	–5.824	–0.358	–11.290
SL	–352.767	331.284	–1036.817
SiO_2	–119.394	124.133	–362.922
Al_2O_3	–23.624	23.722	–70.970
Fe_2O_3	–109.018	116.53	–334.566
CaO	–7.894	8	–23.787
MgO	–2.684	3.484	–8.851
SO_3	–96.563	99.047	–292.174

Table 4.14: Statistical properties of features

Feature	Min	Max	Mean	STD	VAR	Skewness	Kurtosis	Sum	Missing	Median	Num
L	0	5	3.114	1.695	2.871	–0.150	–1.519	246	0	3	79
POFA	0	20	5.203	2.3	5.292	4.251	26.284	411	0	5	79
CS	0	20	11.392	6.452	41.626	–0.136	–1.122	900	0	10	79
Soil	70	100	80.291	6.626	43.901	0.382	–0.213	6343	0	80	79
Time	0	90	33.342	28.855	832.612	1.01	–0.349	2634	0	21	79
UCS	0.36	1.79	0.882	0.315	0.099	0.404	–0.085	69.71	0	0.88	79
FLX	0.21	1.23	0.595	0.211	0.045	0.424	–0.025	47.01	0	0.58	79
E	1.22	7.75	3.736	1.358	1.843	0.364	–0.149	295.12	0	3.67	79
Flx_Load	139.4	993.1	483.3	172.4	29717.1	0.317	–0.038	38184.36	0	477.75	79
mv	0.04	0.13	0.093	0.026	0.001	–0.345	–1.011	7.34	0	0.1	79
Pc	33.9	223.7	106.7	52.3	2740.3	0.699	–0.064	8430.13	0	106.9	79
Cr	0.01	0.09	0.033	0.011	0	1.256	4.87	2.63	0	0.03	79
Cc	0.02	0.18	0.12	0.048	0.002	–0.417	–0.883	9.47	0	0.12	79
Cs	0	0.05	0.026	0.01	0	–0.020	–0.670	2.04	0	0.03	79
Cv	0	0	0.001	0	0	2.959	9.806	0.12	0	0	79
K	0.36	3.25	1.748	0.812	0.659	–0.102	–1.137	138.13	0	1.87	79
av	0.04	0.45	0.168	0.048	0.002	2.268	15.579	13.29	0	0.17	79
CR	0.01	0.1	0.066	0.027	0.001	–0.377	–0.941	5.23	0	0.06	79
eo	0.68	0.98	0.815	0.052	0.003	0.615	1.549	64.38	0	0.81	79

Table 4.14: Continued

Feature	Min	Max	Mean	STD	VAR	Skewness	Kurtosis	Sum	Missings	Median	Num
n	0.4	0.49	0.449	0.015	0	0.359	1.243	35.44	0	0.45	79
MDD	13.44	15.3	14.523	0.449	0.202	–0.379	–0.670	1147.33	0	14.59	79
OMC	26	35	31.065	1.818	3.304	0.104	–0.185	2454.12	0	30.94	79
LL	33.86	75.2	52.604	10.001	100	–0.246	–0.889	4155.68	0	54.37	79
PL	24.14	53.44	39.82	6.93	48.022	–0.069	–1.005	3145.81	0	40.01	79
PI	0.62	26.25	12.783	5.273	27.804	0.175	–0.467	1009.87	0	12.35	79
G_S	2.41	2.69	2.597	0.05	0.002	–2.119	4.598	205.14	0	2.61	79
SL	0.33	13.71	6.706	2.745	7.533	0.148	–0.465	529.8	0	6.45	79
SiO_2	0	1392.8	353.6	349	121803.3	1.473	1.56	27938.3	0	216.65	79
Al_2O_3	0	501.93	120.276	124.237	15434.826	1.576	1.97	9501.84	0	78.08	79
Fe_2O_3	0	96.53	24.506	24.153	583.376	1.47	1.547	1935.99	0	15.02	79
CaO	0	470.21	109.9	115.227	13277.2	1.754	2.547	8682.12	0	70.64	79
MgO	0	31.91	8.776	8.123	65.987	1.29	0.826	693.3	0	5.31	79
SO_3	0	12.47	3.566	3.181	10.119	1.176	0.355	281.71	0	2.38	79
Other	0	408.5	97.4	99.8	9959.2	1.559	1.902	7698.21	0	63.54	79

4.7.4 ANOVA Analysis

ANOVA test was assessed using IBM SPSS Statistics 26 program. The analysis was derived using the multivariant analysis of variation test MANOVA for the data mentioned in Table 3.13, Section 3.8.1.2. The used test was Tukey Post Hoc Analysis which is showed in Tables 4.15 to 4.22 as generated by SPSS program (Hang Lee, 2014). The results showed that the significance was high for all factors except for effective cohesion factor C' and total cohesion factor C_u. That reflects that the optimum selection of the ratios must relay on results of UCS, ϕ_u and ϕ', where set of "S+5%L+5%P+10%C (Case 2)" showed the least significance value compared to the other sets, where the P value for UCS was 0.000, 0.003, 0.000, and 0.000 related to S (Control Sample), S+5%L+x%P (Case 1), S+5%L+5%P+15%C (Case 2), and S+3%L+5%P+20%C (Case 2) sets respectively as shown in Table 4.22 for Post Hoc Tests using Tukey method. The P–values for ϕ' and ϕ_c were following the same trend of significance. However, P–values for C_u and C' were not significant, which makes the controlling parameters are UCS, ϕ' and ϕ_c as observed in previous research (Yong et al., 2019). That supports the selection of specimen SL5P5C10 as the optimum ratios for optimum engineering targeted shear strength values for both drained and undrained conditions as mentioned in Figures 4.4 to 4.13.

Table 4.15: Generated details of SPSS report for “General Linear Model”

Notes

Output Created		14–MAR–2024 12:04:04
Comments		
Input	Data	C:\Users\ROG\Desktop\spss\trial 1.sav
	Active Dataset	DataSet0
	Filter	<none>
	Weight	<none>
	Split File	<none>
	N of Rows in Working Data File	80
Missing Value Handling	Definition of Missing	User–defined missing values are treated as missing.
	Cases Used	Statistics are based on all cases with valid data for all variables in the model.
Syntax		GLM UCS Eff_C Eff_Phi Tot_C Tot_Phi BY Case /METHOD=SSTYPE(3) /INTERCEPT=INCLUDE /POSTHOC=Case(TUKEY) /PRINT=DESCRIPTIVE PARAMETER HOMOGENEITY /PLOT=RESIDUALS /CRITERIA=ALPHA(.05) /DESIGN= Case.
Resources	Processor Time	00:00:00.09
	Elapsed Time	00:00:00.23

Table 4.16: Descriptive Statistics

	Case	Mean	Std. Deviation	N
UCS	S (Control Sample)	.3600	.00000	2
	S+5%L+x%P (Case 1)	.7717	.16964	6
	S+5%L+5%P+x%C (Case 2)	1.1771	.24699	24
	S+3%L+5%P+x%C (Case 2)	.8579	.26978	24
	S+1%L+5%P+x%C (Case 2)	.6600	.19397	24
	Total	.8754	.31797	80
Eff_C	S (Control Sample)	61.0700	.00000	2
	S+5%L+x%P (Case 1)	83.0050	25.97905	6
	S+5%L+5%P+x%C (Case 2)	111.2633	47.42494	24
	S+3%L+5%P+x%C (Case 2)	100.1296	27.05796	24
	S+1%L+5%P+x%C (Case 2)	103.4383	25.81606	24
	Total	102.2015	34.67342	80
Eff_Phi	S (Control Sample)	19.5100	.00000	2
	S+5%L+x%P (Case 1)	21.3700	1.58884	6
	S+5%L+5%P+x%C (Case 2)	24.7967	2.12008	24
	S+3%L+5%P+x%C (Case 2)	24.6471	1.66734	24
	S+1%L+5%P+x%C (Case 2)	24.6767	1.82841	24
	Total	24.3266	2.15356	80
Tot_C	S (Control Sample)	38.6400	.00000	2
	S+5%L+x%P (Case 1)	66.7833	8.82768	6
	S+5%L+5%P+x%C (Case 2)	50.6463	38.66274	24
	S+3%L+5%P+x%C (Case 2)	58.9671	37.82978	24
	S+1%L+5%P+x%C (Case 2)	82.0604	45.27158	24
	Total	63.4769	40.38596	80
Tot_Phi	S (Control Sample)	12.8400	.00000	2
	S+5%L+x%P (Case 1)	15.9067	.92368	6
	S+5%L+5%P+x%C (Case 2)	19.8917	1.24472	24
	S+3%L+5%P+x%C (Case 2)	19.0450	1.30340	24
	S+1%L+5%P+x%C (Case 2)	17.6696	2.60412	24
	Total	18.4959	2.27682	80

Table 4.17: Box's Test of Equality of Covariance Matrices[a]

Box's M	169.692
F	2.935
df1	45
df2	1324.353
Sig.	.000

Tests the null hypothesis that the observed covariance matrices of the dependent variables are equal across groups.
a. Design: Intercept + Case

Table 4.18: Multivariate Tests[a]

Effect		Value	F	Hypothesis df	Error df	Sig.
Intercept	Pillai's Trace	.992	1657.130[b]	5.000	71.000	.000
	Wilks' Lambda	.008	1657.130[b]	5.000	71.000	.000
	Hotelling's Trace	116.699	1657.130[b]	5.000	71.000	.000
	Roy's Largest Root	116.699	1657.130[b]	5.000	71.000	.000
Case	Pillai's Trace	1.098	5.601	20.000	296.000	.000
	Wilks' Lambda	.215	6.971	20.000	236.430	.000
	Hotelling's Trace	2.283	7.934	20.000	278.000	.000
	Roy's Largest Root	1.424	21.076[c]	5.000	74.000	.000

a. Design: Intercept + Case
b. Exact statistic
c. The statistic is an upper bound on F that yields a lower bound on the significance level.

Table 4.19: Levene's Test of Equality of Error Variances[a]

		Levene Statistic	df1	df2	Sig.
UCS	Based on Mean	3.022	4	75	.023
	Based on Median	2.989	4	75	.024
	Based on Median and with adjusted df	2.989	4	44.405	.029
	Based on trimmed mean	3.014	4	75	.023
Eff_C	Based on Mean	2.628	4	75	.041
	Based on Median	1.792	4	75	.139
	Based on Median and with adjusted df	1.792	4	41.163	.149
	Based on trimmed mean	2.348	4	75	.062
Eff_Phi	Based on Mean	1.761	4	75	.146
	Based on Median	.997	4	75	.415
	Based on Median and with adjusted df	.997	4	67.256	.415
	Based on trimmed mean	1.605	4	75	.182
Tot_C	Based on Mean	3.381	4	75	.013
	Based on Median	3.096	4	75	.020
	Based on Median and with adjusted df	3.096	4	64.919	.021
	Based on trimmed mean	3.275	4	75	.016
Tot_Phi	Based on Mean	.957	4	75	.436
	Based on Median	.790	4	75	.536
	Based on Median and with adjusted df	.790	4	37.749	.539
	Based on trimmed mean	.806	4	75	.525

Tests the null hypothesis that the error variance of the dependent variable is equal across groups.
a. Design: Intercept + Case

Table 4.20: Tests of Between–Subjects Effects

Source	Dependent Variable	Type III Sum of Squares	df	Mean Square	F	Sig.
Corrected Model	UCS	3.901[a]	4	.975	17.899	.000
	Eff_C	7705.180[b]	4	1926.295	1.655	.169
	Eff_Phi	109.557[c]	4	27.389	7.998	.000
	Tot_C	14026.805[d]	4	3506.701	2.290	.067
	Tot_Phi	174.583[e]	4	43.646	13.933	.000
Intercept	UCS	18.497	1	18.497	339.486	.000
	Eff_C	266014.669	1	266014.669	228.608	.000
	Eff_Phi	16705.384	1	16705.384	4878.306	.000
	Tot_C	111494.750	1	111494.750	72.825	.000
	Tot_Phi	9202.257	1	9202.257	2937.551	.000
Case	UCS	3.901	4	.975	17.899	.000
	Eff_C	7705.180	4	1926.295	1.655	.169
	Eff_Phi	109.557	4	27.389	7.998	.000
	Tot_C	14026.805	4	3506.701	2.290	.067
	Tot_Phi	174.583	4	43.646	13.933	.000
Error	UCS	4.086	75	.054		
	Eff_C	87272.284	75	1163.630		
	Eff_Phi	256.832	75	3.424		
	Tot_C	114824.200	75	1530.989		
	Tot_Phi	234.947	75	3.133		
Total	UCS	69.290	80			
	Eff_C	930589.193	80			
	Eff_Phi	47709.164	80			
	Tot_C	451196.098	80			
	Tot_Phi	27777.321	80			
Corrected Total	UCS	7.987	79			
	Eff_C	94977.465	79			
	Eff_Phi	366.389	79			
	Tot_C	128851.005	79			
	Tot_Phi	409.530	79			

a. R Squared = .488 (Adjusted R Squared = .461)
b. R Squared = .081 (Adjusted R Squared = .032)
c. R Squared = .299 (Adjusted R Squared = .262)
d. R Squared = .109 (Adjusted R Squared = .061)
e. R Squared = .426 (Adjusted R Squared = .396)

Table 4.21: Parameter Estimates

Dependent Variable	Parameter	B	Std. Error	t	Sig.	95% Confidence Interval	
						Lower Bound	Upper Bound
UCS	Intercept	.660	.048	13.852	.000	.565	.755
	[Case=1.00]	–.300	.172	–1.746	.085	–.642	.042
	[Case=2.00]	.112	.107	1.048	.298	–.101	.324
	[Case=3.00]	.517	.067	7.674	.000	.383	.651
	[Case=4.00]	.198	.067	2.937	.004	.064	.332
	[Case=5.00]	0[a]	.	.	.	.	.
Eff_C	Intercept	103.438	6.963	14.855	.000	89.567	117.310
	[Case=1.00]	–42.368	25.106	–1.688	.096	–92.382	7.645
	[Case=2.00]	–20.433	15.570	–1.312	.193	–51.450	10.584
	[Case=3.00]	7.825	9.847	.795	.429	–11.792	27.442
	[Case=4.00]	–3.309	9.847	–.336	.738	–22.926	16.308
	[Case=5.00]	0[a]	.	.	.	.	.
Eff_Phi	Intercept	24.677	.378	65.328	.000	23.924	25.429
	[Case=1.00]	–5.167	1.362	–3.794	.000	–7.880	–2.454
	[Case=2.00]	–3.307	.845	–3.915	.000	–4.989	–1.624
	[Case=3.00]	.120	.534	.225	.823	–.944	1.184
	[Case=4.00]	–.030	.534	–.055	.956	–1.094	1.035
	[Case=5.00]	0[a]	.	.	.	.	.
Tot_C	Intercept	82.060	7.987	10.274	.000	66.150	97.971
	[Case=1.00]	–43.420	28.797	–1.508	.136	–100.788	13.947
	[Case=2.00]	–15.277	17.859	–.855	.395	–50.855	20.301
	[Case=3.00]	–31.414	11.295	–2.781	.007	–53.915	–8.913
	[Case=4.00]	–23.093	11.295	–2.045	.044	–45.595	–.592
	[Case=5.00]	0[a]	.	.	.	.	.
Tot_Phi	Intercept	17.670	.361	48.908	.000	16.950	18.389
	[Case=1.00]	–4.830	1.303	–3.708	.000	–7.425	–2.235
	[Case=2.00]	–1.763	.808	–2.182	.032	–3.372	–.154
	[Case=3.00]	2.222	.511	4.349	.000	1.204	3.240
	[Case=4.00]	1.375	.511	2.692	.009	.358	2.393
	[Case=5.00]	0[a]	.	.	.	.	.

a. This parameter is set to zero because it is redundant.

Table 4.22: Post Hoc Tests

Multiple Comparisons
Tukey HSD

Dependent Variable	(I) Case	(J) Case	Mean Difference (I–J)	Std. Error	Sig.	95% Confidence Interval	
						Lower Bound	Upper Bound
UCS	S (Control Sample)	S+5%L+x%P (Case 1)	–.4117	.19059	.206	–.9444	.1211
		S+5%L+5%P+x%C (Case 2)	–.8171*	.17179	.000	–1.2973	–.3369
		S+3%L+5%P+x%C (Case 2)	–.4979*	.17179	.038	–.9781	–.0177
		S+1%L+5%P+x%C (Case 2)	–.3000	.17179	.412	–.7802	.1802
	S+5%L+x%P (Case 1)	S (Control Sample)	.4117	.19059	.206	–.1211	.9444
		S+5%L+5%P+x%C (Case 2)	–.4054*	.10654	.003	–.7032	–.1076
		S+3%L+5%P+x%C (Case 2)	–.0863	.10654	.927	–.3841	.2116
		S+1%L+5%P+x%C (Case 2)	.1117	.10654	.832	–.1861	.4095
	S+5%L+5%P+x%C (Case 2)	S (Control Sample)	.8171*	.17179	.000	.3369	1.2973
		S+5%L+x%P (Case 1)	.4054*	.10654	.003	.1076	.7032
		S+3%L+5%P+x%C (Case 2)	.3192*	.06738	.000	.1308	.5075
		S+1%L+5%P+x%C (Case 2)	.5171*	.06738	.000	.3287	.7054
	S+3%L+5%P+x%C (Case 2)	S (Control Sample)	.4979*	.17179	.038	.0177	.9781
		S+5%L+x%P (Case 1)	.0863	.10654	.927	–.2116	.3841
		S+5%L+5%P+x%C (Case 2)	–.3192*	.06738	.000	–.5075	–.1308
		S+1%L+5%P+x%C (Case 2)	.1979*	.06738	.035	.0096	.3863
	S+1%L+5%P+x%C (Case 2)	S (Control Sample)	.3000	.17179	.412	–.1802	.7802
		S+5%L+x%P (Case 1)	–.1117	.10654	.832	–.4095	.1861
		S+5%L+5%P+x%C (Case 2)	–.5171*	.06738	.000	–.7054	–.3287
		S+3%L+5%P+x%C (Case 2)	–.1979*	.06738	.035	–.3863	–.0096
Eff_C	S (Control Sample)	S+5%L+x%P (Case 1)	–21.9350	27.85235	.933	–99.7893	55.9193
		S+5%L+5%P+x%C (Case 2)	–50.1933	25.10577	.276	–120.3702	19.9836
		S+3%L+5%P+x%C (Case 2)	–39.0596	25.10577	.530	–109.2365	31.1173

Table 4.22: Continued

		S+1%L+5%P+x%C (Case 2)	–42.3683	25.10577	.448	–112.5452	27.8086
	S+5%L+x%P (Case 1)	S (Control Sample)	21.9350	27.85235	.933	–55.9193	99.7893
		S+5%L+5%P+x%C (Case 2)	–28.2583	15.56994	.373	–71.7802	15.2635
		S+3%L+5%P+x%C (Case 2)	–17.1246	15.56994	.806	–60.6465	26.3973
		S+1%L+5%P+x%C (Case 2)	–20.4333	15.56994	.684	–63.9552	23.0885
	S+5%L+5%P+x%C (Case 2)	S (Control Sample)	50.1933	25.10577	.276	–19.9836	120.3702
		S+5%L+x%P (Case 1)	28.2583	15.56994	.373	–15.2635	71.7802
		S+3%L+5%P+x%C (Case 2)	11.1338	9.84729	.790	–16.3919	38.6594
		S+1%L+5%P+x%C (Case 2)	7.8250	9.84729	.931	–19.7007	35.3507
	S+3%L+5%P+x%C (Case 2)	S (Control Sample)	39.0596	25.10577	.530	–31.1173	109.2365
		S+5%L+x%P (Case 1)	17.1246	15.56994	.806	–26.3973	60.6465
		S+5%L+5%P+x%C (Case 2)	–11.1338	9.84729	.790	–38.6594	16.3919
		S+1%L+5%P+x%C (Case 2)	–3.3088	9.84729	.997	–30.8344	24.2169
	S+1%L+5%P+x%C (Case 2)	S (Control Sample)	42.3683	25.10577	.448	–27.8086	112.5452
		S+5%L+x%P (Case 1)	20.4333	15.56994	.684	–23.0885	63.9552
		S+5%L+5%P+x%C (Case 2)	–7.8250	9.84729	.931	–35.3507	19.7007
		S+3%L+5%P+x%C (Case 2)	3.3088	9.84729	.997	–24.2169	30.8344
Eff_Phi	S (Control Sample)	S+5%L+x%P (Case 1)	–1.8600	1.51094	.733	–6.0835	2.3635
		S+5%L+5%P+x%C (Case 2)	–5.2867*	1.36195	.002	–9.0936	–1.4797
		S+3%L+5%P+x%C (Case 2)	–5.1371*	1.36195	.003	–8.9441	–1.3301
		S+1%L+5%P+x%C (Case 2)	–5.1667*	1.36195	.003	–8.9736	–1.3597
	S+5%L+x%P (Case 1)	S (Control Sample)	1.8600	1.51094	.733	–2.3635	6.0835
		S+5%L+5%P+x%C (Case 2)	–3.4267*	.84464	.001	–5.7877	–1.0657
		S+3%L+5%P+x%C (Case 2)	–3.2771*	.84464	.002	–5.6381	–.9161
		S+1%L+5%P+x%C (Case 2)	–3.3067*	.84464	.002	–5.6677	–.9457
	S+5%L+5%P+x%C (Case 2)	S (Control Sample)	5.2867*	1.36195	.002	1.4797	9.0936
		S+5%L+x%P (Case 1)	3.4267*	.84464	.001	1.0657	5.7877

Table 4.22: Continued

		S+3%L+5%P+x%C (Case 2)	.1496	.53420	.999	–1.3436	1.6428
		S+1%L+5%P+x%C (Case 2)	.1200	.53420	.999	–1.3732	1.6132
	S+3%L+5%P+x%C (Case 2)	S (Control Sample)	5.1371*	1.36195	.003	1.3301	8.9441
		S+5%L+x%P (Case 1)	3.2771*	.84464	.002	.9161	5.6381
		S+5%L+5%P+x%C (Case 2)	–.1496	.53420	.999	–1.6428	1.3436
		S+1%L+5%P+x%C (Case 2)	–.0296	.53420	1.000	–1.5228	1.4636
	S+1%L+5%P+x%C (Case 2)	S (Control Sample)	5.1667*	1.36195	.003	1.3597	8.9736
		S+5%L+x%P (Case 1)	3.3067*	.84464	.002	.9457	5.6677
		S+5%L+5%P+x%C (Case 2)	–.1200	.53420	.999	–1.6132	1.3732
		S+3%L+5%P+x%C (Case 2)	.0296	.53420	1.000	–1.4636	1.5228
Tot_C	S (Control Sample)	S+5%L+x%P (Case 1)	–28.1433	31.94776	.903	–117.4453	61.1587
		S+5%L+5%P+x%C (Case 2)	–12.0063	28.79732	.994	–92.5020	68.4895
		S+3%L+5%P+x%C (Case 2)	–20.3271	28.79732	.955	–100.8228	60.1686
		S+1%L+5%P+x%C (Case 2)	–43.4204	28.79732	.561	–123.9161	37.0753
	S+5%L+x%P (Case 1)	S (Control Sample)	28.1433	31.94776	.903	–61.1587	117.4453
		S+5%L+5%P+x%C (Case 2)	16.1371	17.85934	.895	–33.7842	66.0584
		S+3%L+5%P+x%C (Case 2)	7.8163	17.85934	.992	–42.1051	57.7376
		S+1%L+5%P+x%C (Case 2)	–15.2771	17.85934	.912	–65.1984	34.6442
	S+5%L+5%P+x%C (Case 2)	S (Control Sample)	12.0063	28.79732	.994	–68.4895	92.5020
		S+5%L+x%P (Case 1)	–16.1371	17.85934	.895	–66.0584	33.7842
		S+3%L+5%P+x%C (Case 2)	–8.3208	11.29524	.947	–39.8939	23.2522
		S+1%L+5%P+x%C (Case 2)	–31.4142	11.29524	.052	–62.9872	.1589
	S+3%L+5%P+x%C (Case 2)	S (Control Sample)	20.3271	28.79732	.955	–60.1686	100.8228
		S+5%L+x%P (Case 1)	–7.8163	17.85934	.992	–57.7376	42.1051
		S+5%L+5%P+x%C (Case 2)	8.3208	11.29524	.947	–23.2522	39.8939
		S+1%L+5%P+x%C (Case 2)	–23.0933	11.29524	.255	–54.6664	8.4797

Table 4.22: Continued

	S+1%L+5%P+x%C (Case 2)	S (Control Sample)	43.4204	28.79732	.561	–37.0753	123.9161
		S+5%L+x%P (Case 1)	15.2771	17.85934	.912	–34.6442	65.1984
		S+5%L+5%P+x%C (Case 2)	31.4142	11.29524	.052	–.1589	62.9872
		S+3%L+5%P+x%C (Case 2)	23.0933	11.29524	.255	–8.4797	54.6664
Tot_Phi	S (Control Sample)	S+5%L+x%P (Case 1)	–3.0667	1.44514	.222	–7.1062	.9729
		S+5%L+5%P+x%C (Case 2)	–7.0517*	1.30263	.000	–10.6928	–3.4105
		S+3%L+5%P+x%C (Case 2)	–6.2050*	1.30263	.000	–9.8462	–2.5638
		S+1%L+5%P+x%C (Case 2)	–4.8296*	1.30263	.004	–8.4708	–1.1884
	S+5%L+x%P (Case 1)	S (Control Sample)	3.0667	1.44514	.222	–.9729	7.1062
		S+5%L+5%P+x%C (Case 2)	–3.9850*	.80786	.000	–6.2432	–1.7268
		S+3%L+5%P+x%C (Case 2)	–3.1383*	.80786	.002	–5.3965	–.8802
		S+1%L+5%P+x%C (Case 2)	–1.7629	.80786	.198	–4.0211	.4952
	S+5%L+5%P+x%C (Case 2)	S (Control Sample)	7.0517*	1.30263	.000	3.4105	10.6928
		S+5%L+x%P (Case 1)	3.9850*	.80786	.000	1.7268	6.2432
		S+3%L+5%P+x%C (Case 2)	.8467	.51093	.466	–.5815	2.2749
		S+1%L+5%P+x%C (Case 2)	2.2221*	.51093	.000	.7939	3.6503
	S+3%L+5%P+x%C (Case 2)	S (Control Sample)	6.2050*	1.30263	.000	2.5638	9.8462
		S+5%L+x%P (Case 1)	3.1383*	.80786	.002	.8802	5.3965
		S+5%L+5%P+x%C (Case 2)	–.8467	.51093	.466	–2.2749	.5815
		S+1%L+5%P+x%C (Case 2)	1.3754	.51093	.065	–.0528	2.8036
	S+1%L+5%P+x%C (Case 2)	S (Control Sample)	4.8296*	1.30263	.004	1.1884	8.4708
		S+5%L+x%P (Case 1)	1.7629	.80786	.198	–.4952	4.0211
		S+5%L+5%P+x%C (Case 2)	–2.2221*	.51093	.000	–3.6503	–.7939
		S+3%L+5%P+x%C (Case 2)	–1.3754	.51093	.065	–2.8036	.0528

Based on observed means.
The error term is Mean Square(Error) = 3.133.
*. The mean difference is significant at the .05 level.

4.7.5 Data Prediction Models Using Manual Feature Selection

Manual feature selection was identified according to type of geotechnical test, where the features weight conducted from the correlation matrix. Therefore, there were eight ML models were assessed as identified in Table 3.13 in Section 3.8.2, where the models 1 to 7 definitions for the relation between undrained compressive strength (UCS) and other geotechnical parameters are as follows: (1) model 1 using duration & treating materials ratios, (2) model 2 using physical properties, (3) model 3 using flexural strength, (4) model 4 using chemical content, (5) model 5 using consolidation parameters, (6) model 6 using compaction parameters, (7) model 7 using all conducted parameters and for model 8 the relationship was between cu stress–strain, duration and treating materials ratios. The machine learning algorithms were applied according to the selected features for targeted strength prediction and optimisation.

The first model was predicting the relationship between undrained shear strength, and treating materials ratio, and duration of curing, where the model has the highest accuracy for ANN algorithm by R^2 value of 0.994, 1.000, and 0.999 for Test, Train, and Validation respectively. In addition, PR, GBoost, xGBoost and RF were having high accuracy as shown in Table 4.23. The LR model was low in accuracy about 0.5 for R^2 value as shown in Figures 4.35 to 4.37. The figures show that variance for ANN, xGBoost and GBoost was the least compared to the other algorithms for training, testing and validation datasets. For testing dataset, the variance was the least for ANN which reflects the best accuracy of ANN as a prediction algorithm, besides the indication of the first model applicability in prediction using ANN as conducted by previous research (Mozumder et al., 2015; Prasad et al., 2016; Rezazadeh Eidgahee et al., 2020; Shah et al., 2020). Accordingly, ANN is the best model for predicting and controlling UCS of treated marine clay using POFA, lime and calcined shale through manual feature selection for the first model.

Table 4.23: 1st model R^2 values for different used algorithms

Algorithm	Test	Train	Validation
LR	0.444	0.573	0.559
PR	0.806	0.880	0.871
ANN	0.994	1.000	0.999
xGBoost	0.912	1.000	0.979
GBoost	0.806	1.000	0.947
RF	0.833	0.952	0.937

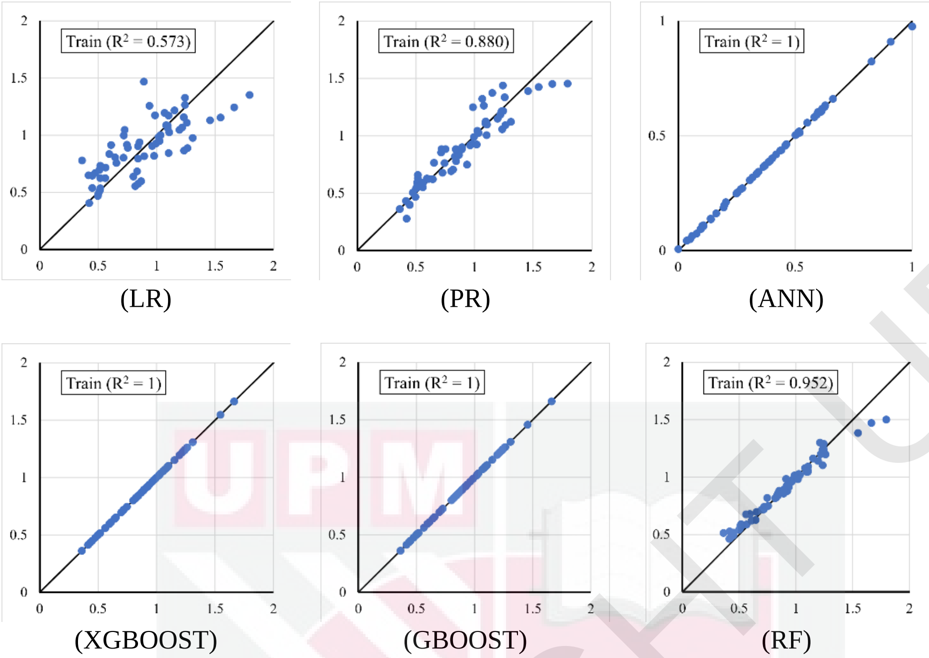

Figure 4.35: Accuracy of model 1 results for LR, PR, ANN, XGBOOST, GBOOST, and RF algorithms for training data

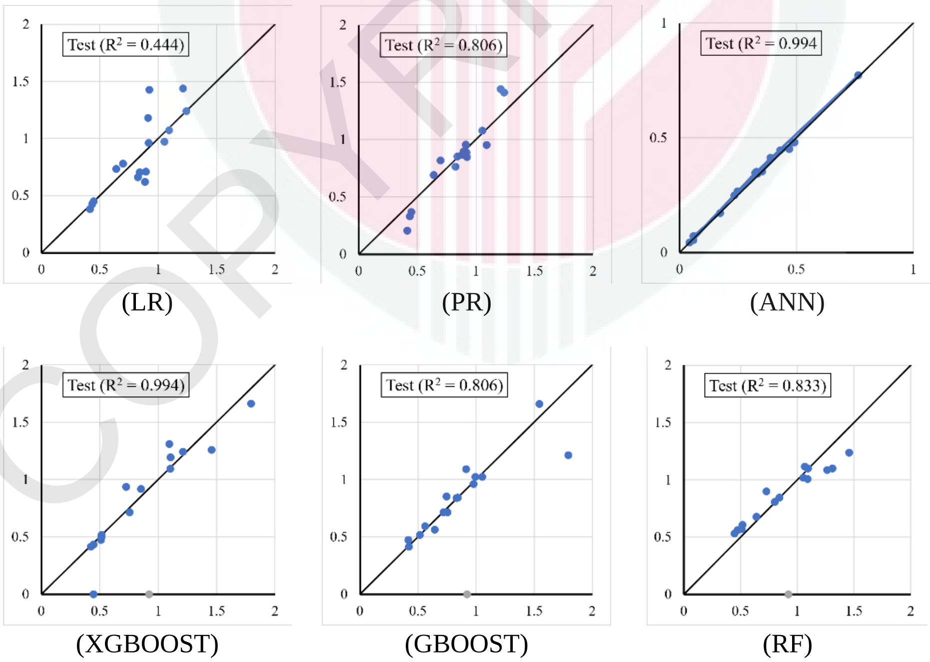

Figure 4.36: Accuracy of model 1 results for LR, PR, ANN, XGBOOST, GBOOST, and RF algorithms for testing data

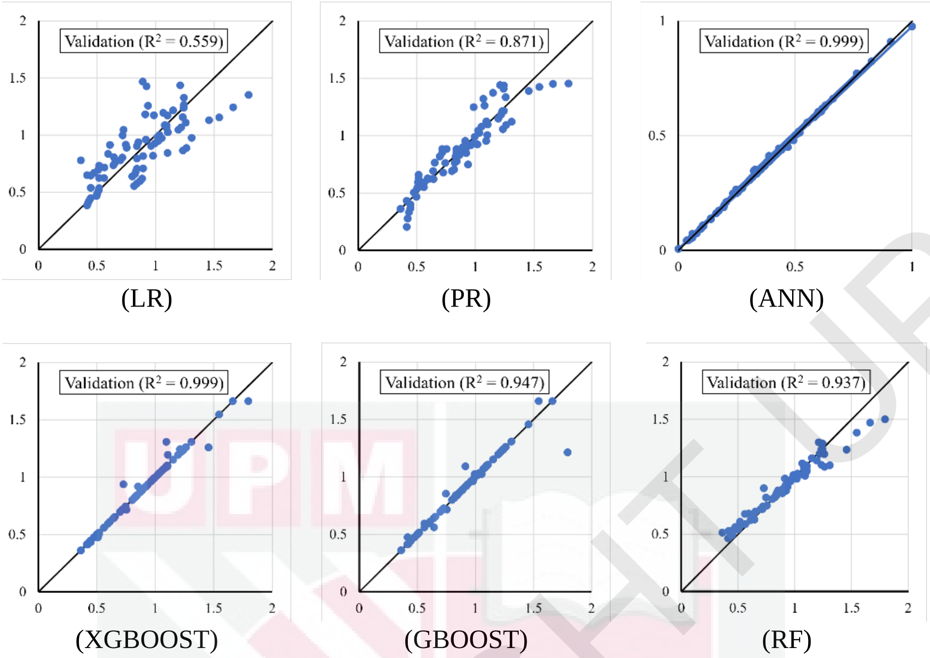

Figure 4.37: Accuracy of model 1 results for LR, PR, ANN, XGBOOST, GBOOST, and RF algorithms for validation data

The second model was predicting the relationship between undrained shear strength and features conducted from flexural strength test, where the model has the highest accuracy for ANN algorithm by R^2 value of 0.907, 0.993, and 0.981 for Test, Train, and Validation respectively. In addition, LR, PR, GBoost, xGBoost and RF were having high accuracy as shown in Table 4.24. Although LR and PR models were the lowest in accuracy about 0.86 for R^2 value as shown in Figures 4.38 to 4.40, their accuracy was acceptable. The figures show that variance for ANN, RF and GBoost techniques was the least compared to the other algorithms for training, testing and validation datasets. For testing dataset, the variance was the least for ANN which reflects the best accuracy of ANN as a prediction algorithm, besides the indication of the second model applicability in prediction using ANN as conducted by previous research (Mozumder et al., 2015; Prasad et al., 2016; Nouman Amjad Raja et al., 2021; Rezazadeh Eidgahee et al., 2020; Shah et al., 2020). Therefore, the best model for predicting and controlling UCS of treated marine clay using POFA, lime and calcined shale through manual feature selection is ANN technique for the second model, where the other algorithms are with acceptable high accuracy. On the other hand, xGBoost technique show high variation in testing and validation datasets compared to GBoost technique, although the high performance of xGBoost compared to GBoost statistically. That indicates that the random selection of the data for testing and training was not suitable for xGBoost which can be solved by increasing the number of readings (samples) (Mozumder et al., 2015). However, the model was in acceptable accuracy.

Table 4.24: 2nd model R^2 values for different used algorithms

Algorithm	Test	Train	Validation
LR	0.840	0.858	0.857
PR	0.840	0.858	0.857
ANN	0.907	0.993	0.981
xGBoost	0.728	1.000	0.890
GBoost	0.865	1.000	0.963
RF	0.804	0.971	0.943

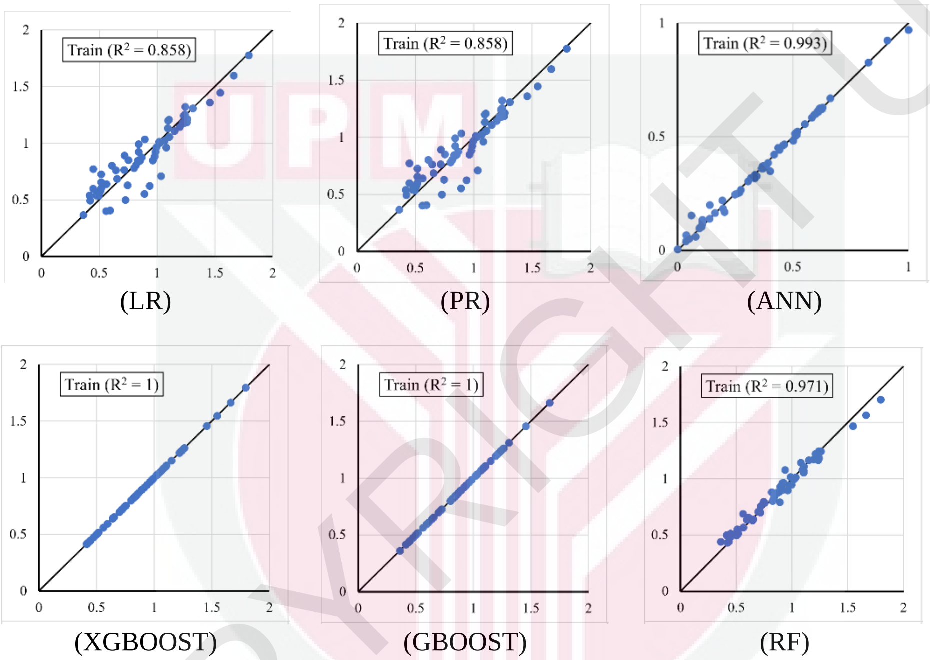

Figure 4.38: Accuracy of model 2 results for LR, PR, ANN, XGBOOST, GBOOST, and RF algorithms for training data

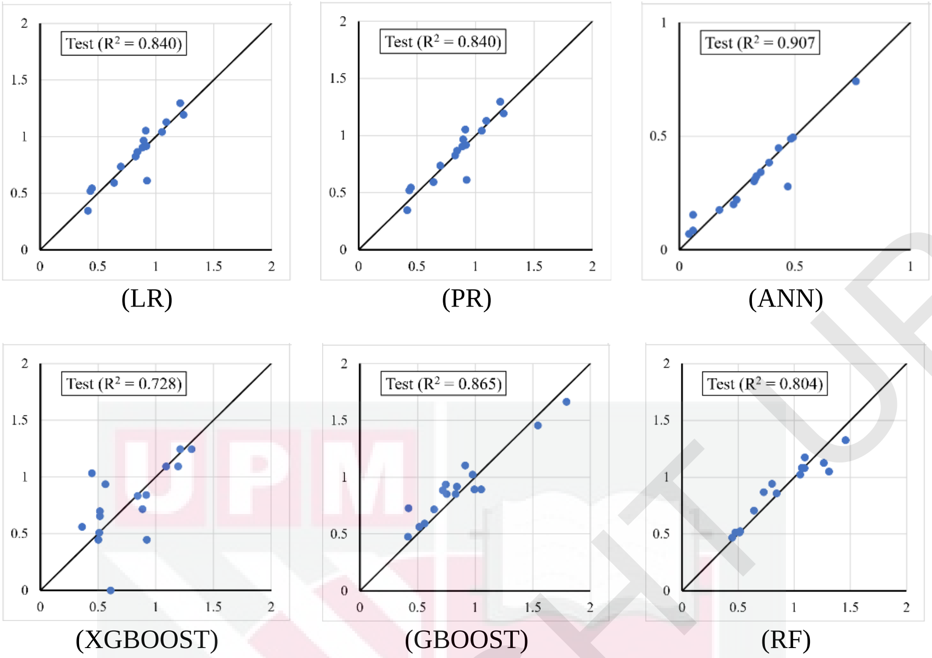

Figure 4.39: Accuracy of model 2 results for LR, PR, ANN, XGBOOST, GBOOST, and RF algorithms for testing data

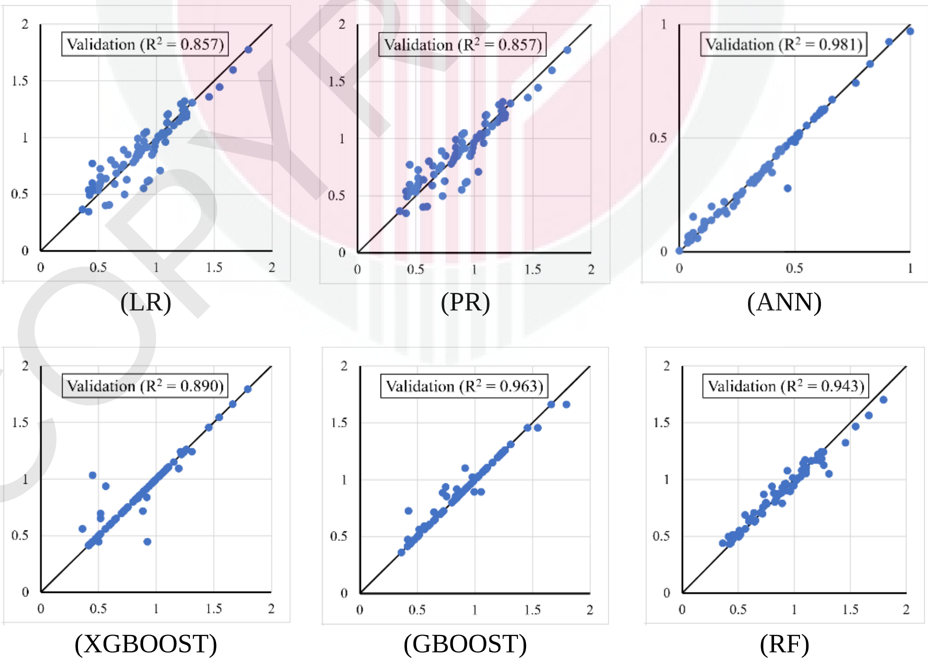

Figure 4.40: Accuracy of model 2 results for LR, PR, ANN, XGBOOST, GBOOST, and RF algorithms for validation data

The third model was predicting the relationship between undrained shear strength and the features conducted from consolidation test, where the model has the highest accuracy for ANN algorithm by R^2 value of 0.947, 0.990, and 0.984 for Test, Train, and Validation respectively. In addition, PR, GBoost, xGBoost and RF were having high accuracy as shown in Table 4.25. However, GBoost and xGBoost were more accurate in training accuracy by 1.000 R^2 value, which is related to the methodology and structure of training using both algorithms as shown in Figures 4.41 to 4.43. The figures show that variance for ANN and xGBoost techniques was the least compared to the other algorithms for training, for testing and validation datasets. For testing dataset, the variance was the least for ANN which reflects the best accuracy of ANN as a prediction algorithm, besides the indication of the applicability of the third model in prediction using ANN as conducted by previous research (Mozumder et al., 2015; Prasad et al., 2016; Nouman Amjad Raja et al., 2021; Rezazadeh Eidgahee et al., 2020; Shah et al., 2020). Therefore, the best model for predicting and controlling UCS of treated marine clay using POFA, lime and calcined shale through manual feature selection is ANN technique for the third model, where the other algorithms are with acceptable high accuracy. On the other hand, GBoost and xGBoost technique show high variation in testing and validation datasets compared to RF technique, although the high performance of xGBoost compared to GBoost statistically. That indicates that the random selection of the data for testing and training was not suitable for GBoost and xGBoost which can be solved by increasing the number of readings (samples) (Mozumder et al., 2015). However, the model was in acceptable accuracy.

Table 4.25: 3rd model R^2 values for different used algorithms

Algorithm	Test	Train	Validation
LR	0.649	0.813	0.793
PR	0.649	0.813	0.793
ANN	0.947	0.990	0.984
xGBoost	0.564	1.000	0.967
GBoost	0.677	1.000	0.912
RF	0.812	0.976	0.961

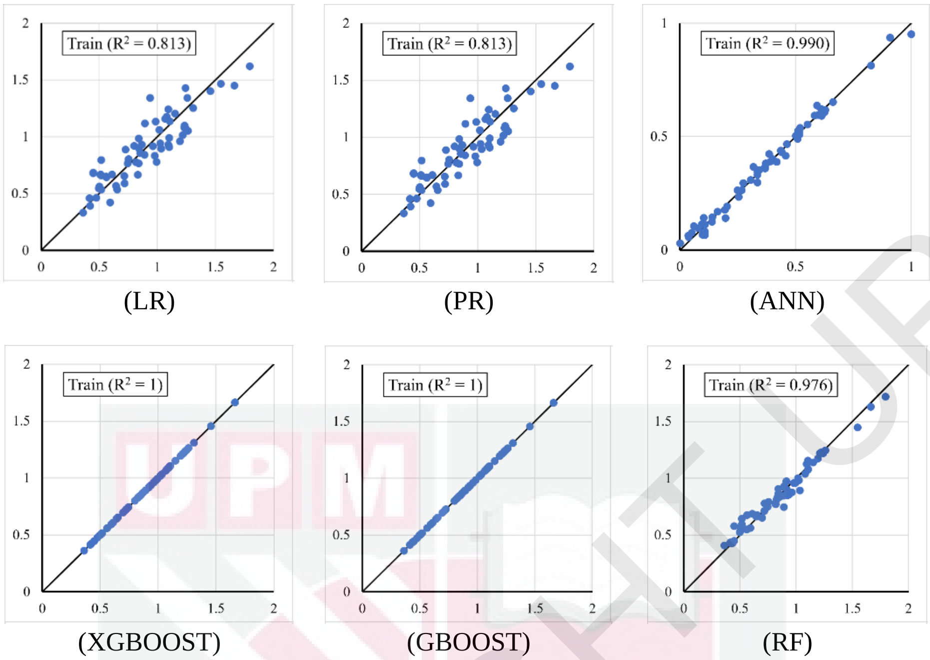

Figure 4.41: Accuracy of model 3 results for LR, PR, ANN, XGBOOST, GBOOST, and RF algorithms for training data

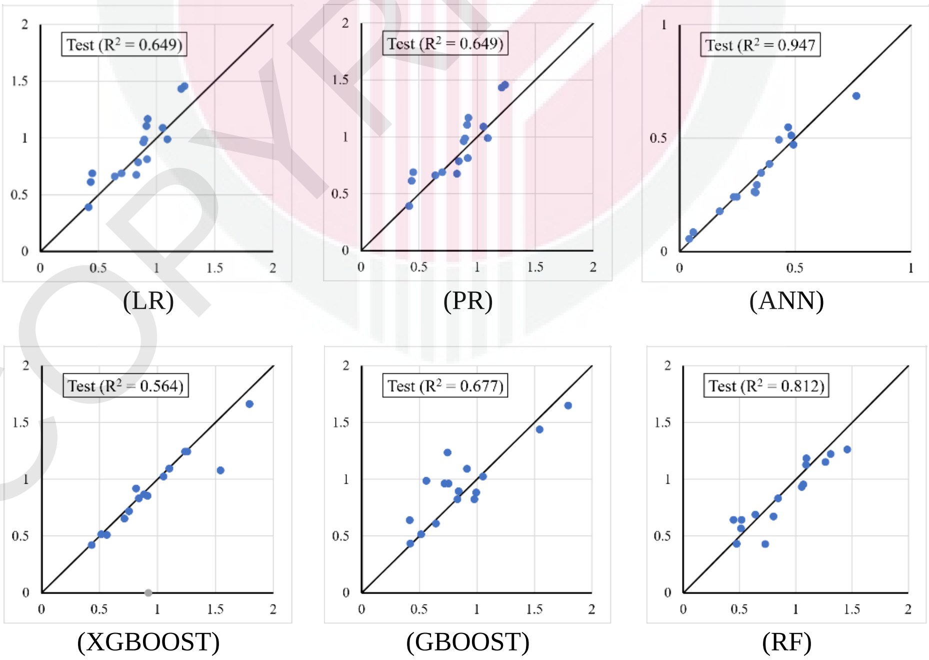

Figure 4.42: Accuracy of model 3 results for LR, PR, ANN, XGBOOST, GBOOST, and RF algorithms for testing data

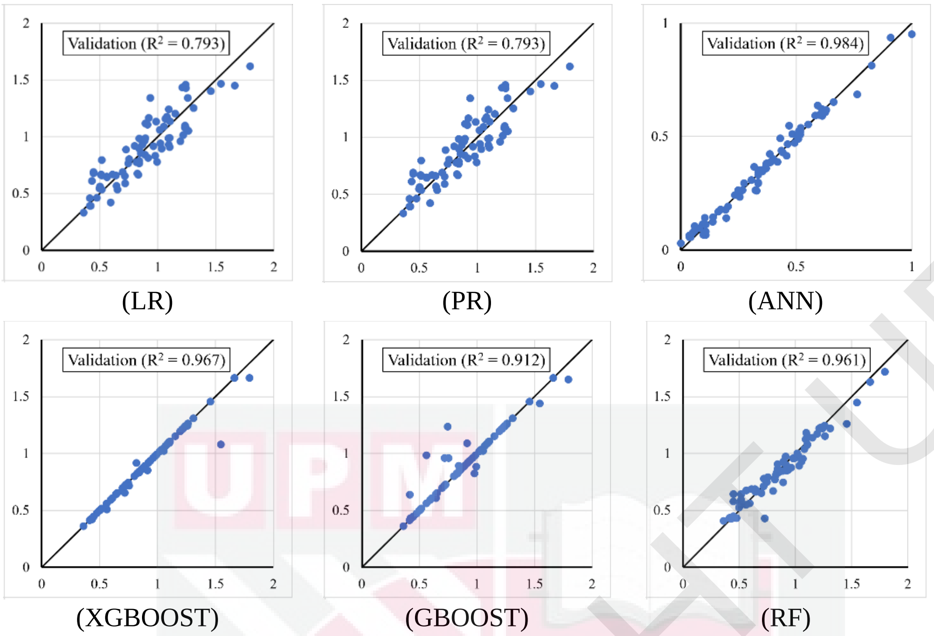

Figure 4.43: Accuracy of model 3 results for LR, PR, ANN, XGBOOST, GBOOST, and RF algorithms for validation data

The fourth model was predicting the relationship between undrained shear strength and the features conducted from compaction test, where the model has the highest accuracy for ANN algorithm by R^2 value of 0.462, 0.453, and 0.459 for Test, Train, and Validation respectively. However, GBoost and xGBoost were more accurate in training accuracy by 1.000 R^2 value, which is related to the methodology and structure of training using both algorithms. The validation R^2 value was also high for GBoost, xGBoost and RF algorithms as the training data and testing data were combined in validation set. In addition, PR, GBoost, xGBoost and RF were having math error or weak accuracy as shown in Table 4.26, which indicates that the testing points are far away from training model. Therefore, that indicates this model was the worst prediction model and the least accurate model among the other models as shown in Figures 4.44 to 4.46. That indicates that the huge variation in the datasets of the fourth model, which makes the model inaccurate and unapplicable for prediction and controlling UCS of treated marine clay specimens.

Table 4.26: 4th model R^2 values for different used algorithms

Algorithm	Test	Train	Validation
LR	–0.005	0.238	0.210
PR	0.264	0.497	0.470
ANN	0.462	0.453	0.459
xGBoost	–0.117	1.000	0.782
GBoost	0.064	1.000	0.745
RF	–0.020	0.857	0.693

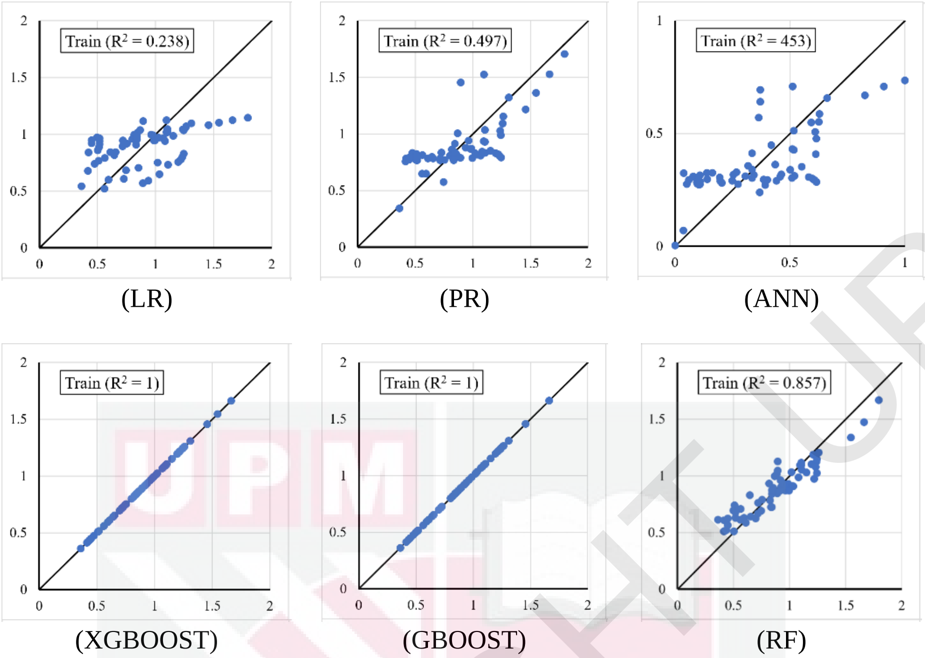

Figure 4.44: Accuracy of model 4 results for LR, PR, ANN, XGBOOST, GBOOST, and RF algorithms for training data

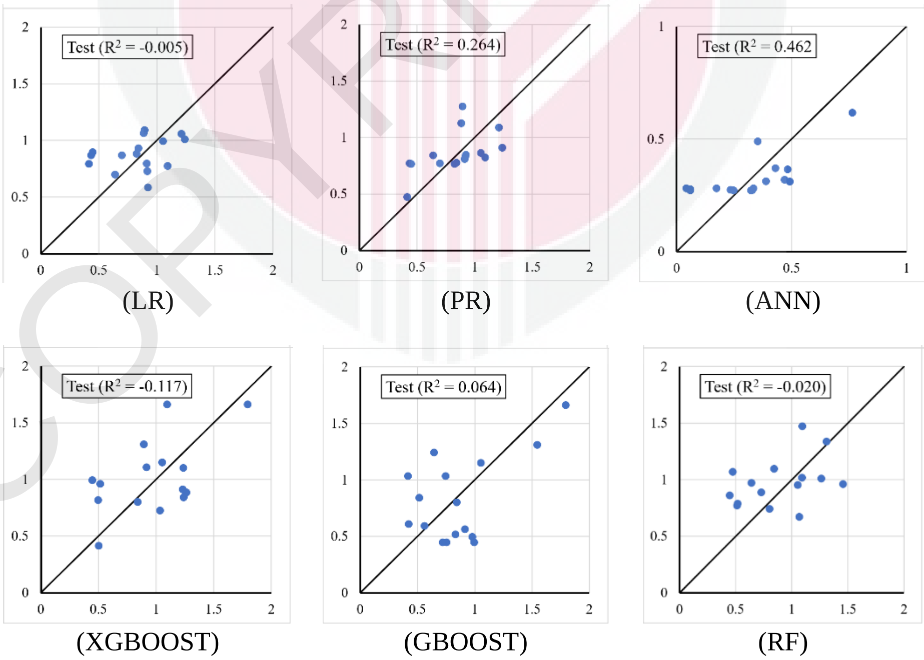

Figure 4.45: Accuracy of model 4 results for LR, PR, ANN, XGBOOST, GBOOST, and RF algorithms for testing data

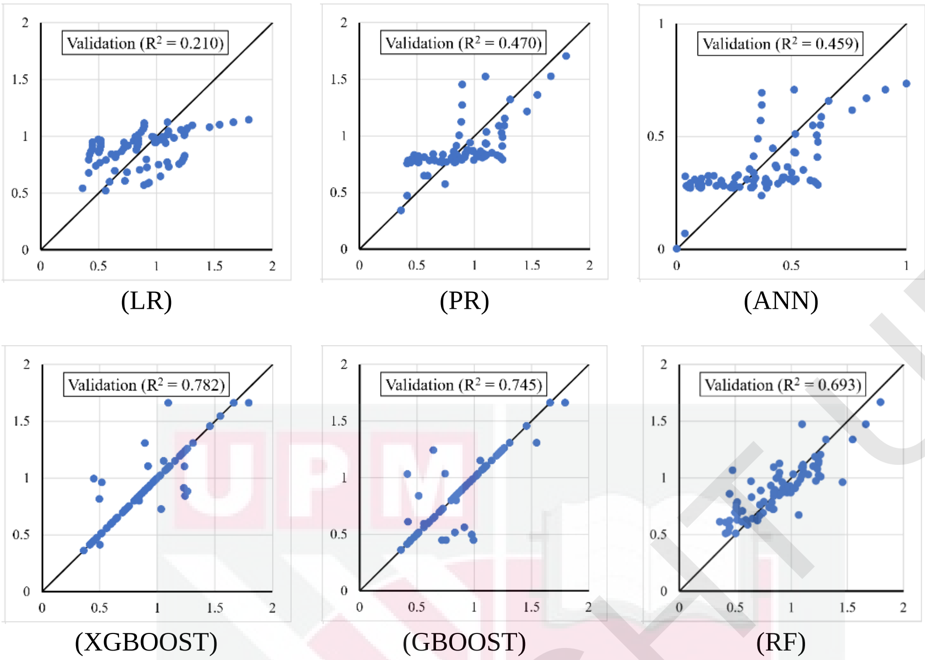

Figure 4.46: Accuracy of model 4 results for LR, PR, ANN, XGBOOST, GBOOST, and RF algorithms for validation data

The fifth model was predicting the relationship between undrained shear strength and the features conducted from Atterberg limits, where the model has the highest accuracy for ANN algorithm by R^2 value of 0.714, 0.876, and 0.853 for Test, Train, and Validation respectively. In addition, LR and PR were weak in prediction, while GBoost, xGBoost and RF were having high accuracy as shown in Table 4.27. However, GBoost and xGBoost were more accurate in training accuracy by 1.000 R^2 value, which is related to the methodology and structure of training using both algorithms and their accuracy for testing was doubted as shown in Figures 4.47 to 4.49. Despite the dataset variances and the comparatively lower accuracy of the ANN technique, its performance remained acceptable, establishing ANN as the optimal technique for predicting and controlling UCS for the fifth model as conducted by previous studies (Prasad et al., 2016; Shah et al., 2020). Moreover, the accuracy of the model suggests that the random selection of data was unsuitable for RF, GBoost and xGBoost, an issue that could potentially be resolved by increasing the number of samples (Mozumder & Laskar, 2015).

Table 4.27: 5th model R^2 values for different used algorithms

Algorithm	Test	Train	Validation
LR	0.098	0.132	0.132
PR	0.120	0.338	0.313
ANN	0.714	0.876	0.853
xGBoost	–0.079	1.000	0.738
GBoost	0.182	1.000	0.777
RF	0.425	0.927	0.828

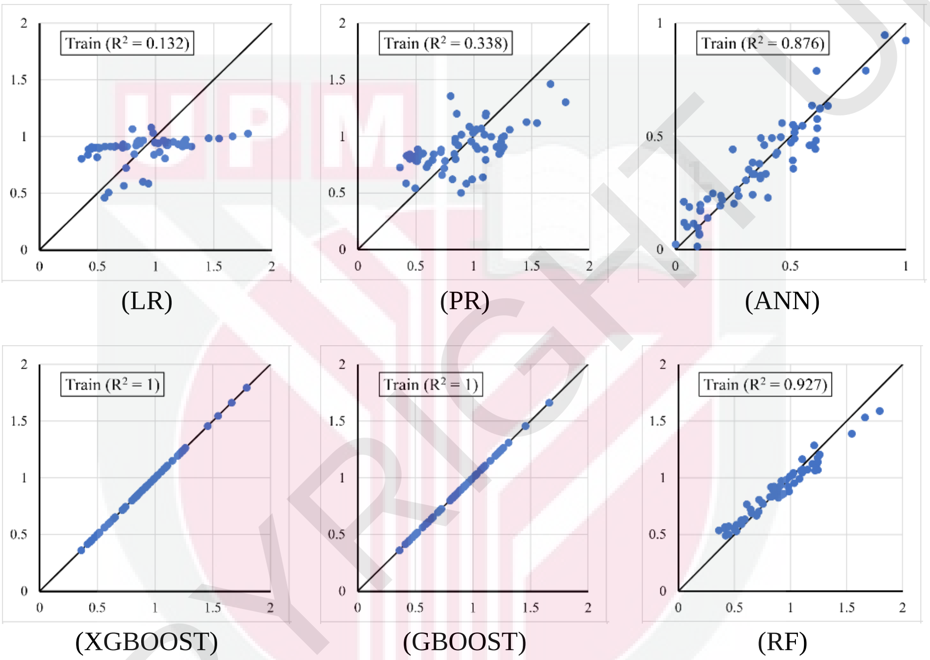

Figure 4.47: Accuracy of model 5 results for LR, PR, ANN, XGBOOST, GBOOST, and RF algorithms for training data

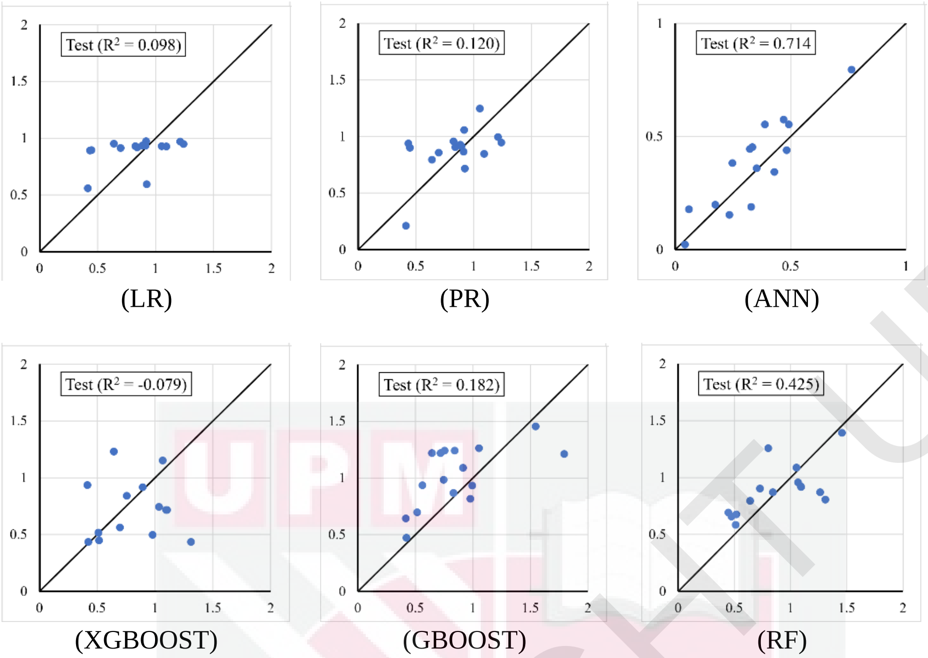

Figure 4.48: Accuracy of model 5 results for LR, PR, ANN, XGBOOST, GBOOST, and RF algorithms for testing data

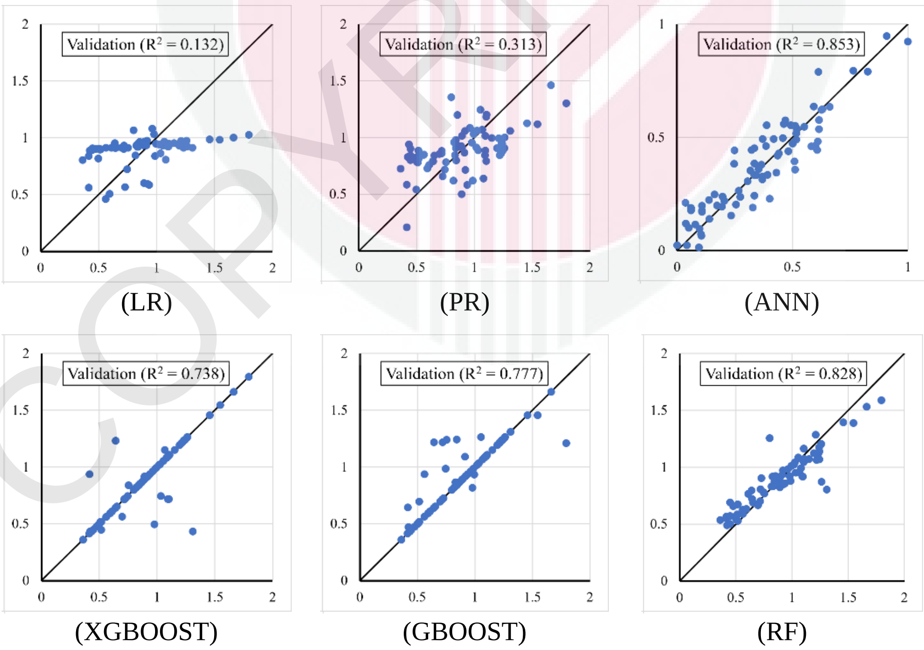

Figure 4.49: Accuracy of model 5 results for LR, PR, ANN, XGBOOST, GBOOST, and RF algorithms for validation data

The sixth model was predicting the relationship between undrained shear strength and the features of weight compounds and duration, where the model has the highest accuracy for ANN algorithm by R^2 value of 0.977, 0.997, and 0.994 for Test, Train, and Validation respectively as shown in Table 4.28. In addition, LR and PR were weak in prediction, while GBoost, xGBoost and RF were having high accuracy in training and validation but weak in testing as shown in Figures 4.50 to 4.52. ANN technique, its performance remained acceptable, establishing ANN as the optimal technique for predicting and controlling UCS for the sixth model as conducted by previous studies (Prasad et al., 2016; Shah et al., 2020). Moreover, the accuracy of the model suggests that the random selection of data was unsuitable for RF, GBoost and xGBoost, an issue that could potentially be resolved by increasing the number of samples (Mozumder & Laskar, 2015) although their high accuracy in training and validation datasets.

Table 4.28: 6th model R^2 values for different used algorithms

Algorithm	Test	Train	Validation
LR	0.107	0.556	0.501
PR	0.281	0.646	0.601
ANN	0.977	0.997	0.994
xGBoost	0.023	1.000	0.939
GBoost	–0.082	1.000	0.705
RF	0.400	0.903	0.825

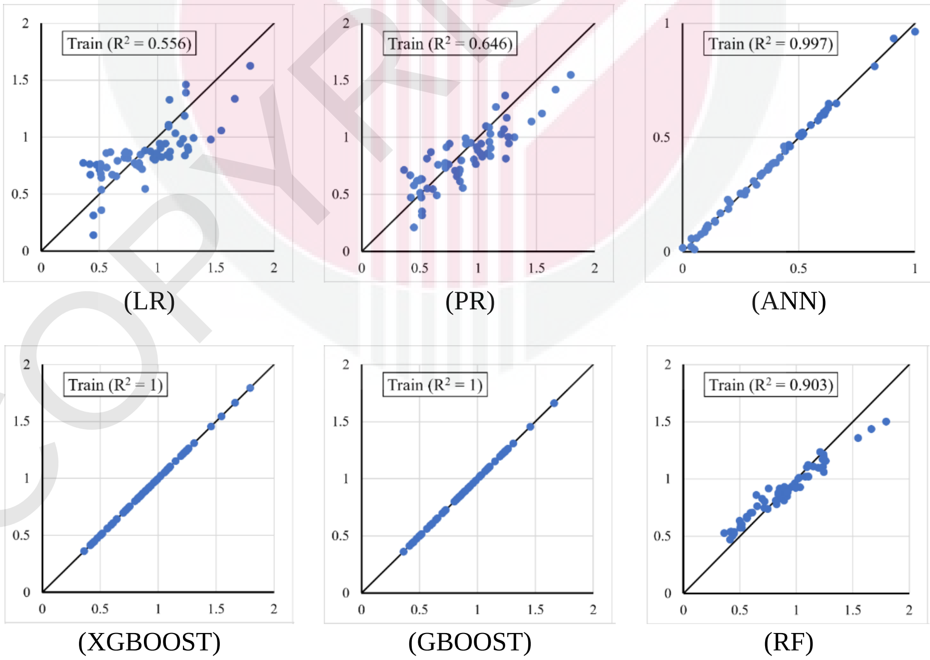

Figure 4.50: Accuracy of model 6 results for LR, PR, ANN, XGBOOST, GBOOST, and RF algorithms for training data

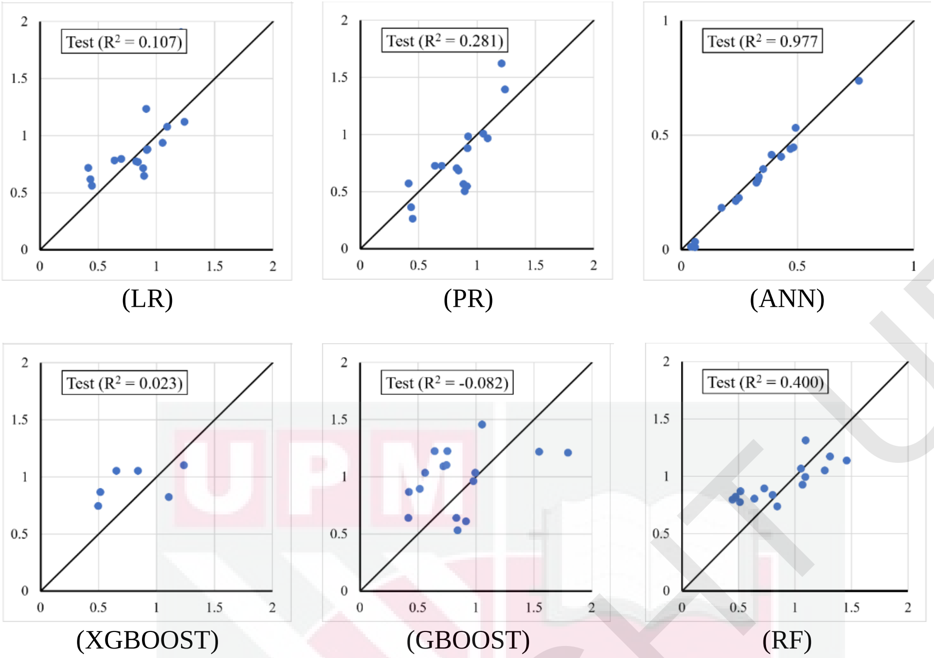

Figure 4.51: Accuracy of model 6 results for LR, PR, ANN, XGBOOST, GBOOST, and RF algorithms for testing data

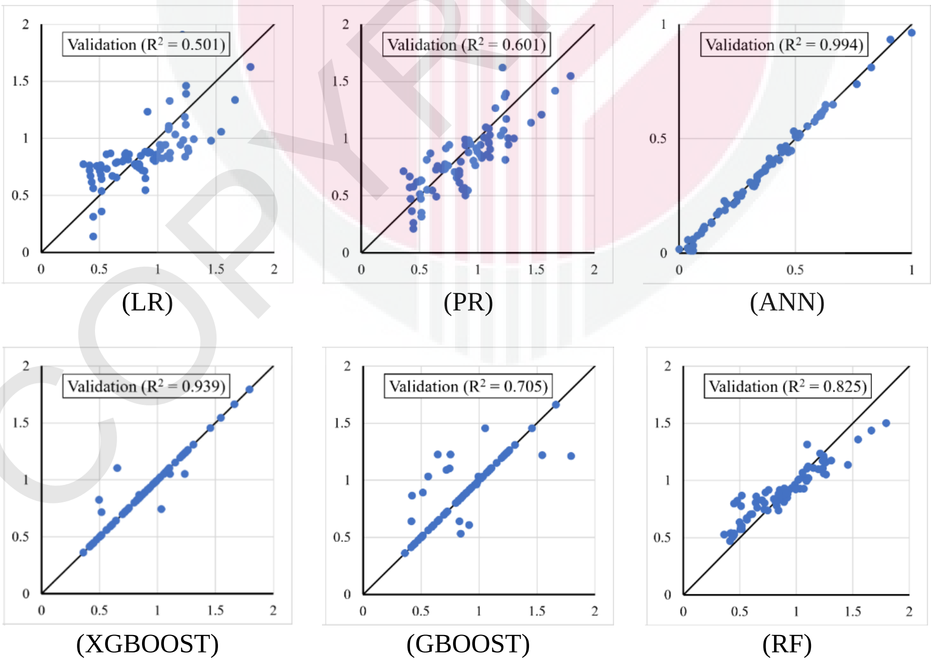

Figure 4.52: Accuracy of model 6 results for LR, PR, ANN, XGBOOST, GBOOST, and RF algorithms for validation data

The seventh model was predicting the relationship between undrained shear strength and the all mentioned features, where the model has the highest accuracy for ANN algorithm by R^2 value of 0.996, 1.000, and 0.999 for Test, Train, and Validation respectively as shown in Figures 4.53 to 4.55. In addition, LR, PR, GBoost, xGBoost and RF were having a significant high accuracy in training, testing and validation as shown in Table 4.29. Accordingly, this model is one of the best conducted models through this research as the variance of the datasets for training, testing, and validation is the minimum for all algorithms compared to other models. As per conducted figures, the best model for predicting and controlling UCS of treated marine clay using POFA, lime and calcined shale through manual feature selection is ANN technique. On the other hand, xGBoost, GBoost and RF techniques show high variation in testing and validation datasets compared to LR and PR techniques, although the high performance of xGBoost, GBoost and RF compared to LR and PR statistically. That indicates that the random selection of the data for testing and training was not suitable for xGBoost, GBoost and RF which can be solved by increasing the number of readings (samples) (Mozumder et al., 2015). However, the model was significantly high accuracy for xGBoost, GBoost and RF algorithms.

Table 4.29: 7th model R^2 values for different used algorithms

Algorithm	Test	Train	Validation
LR	0.953	0.993	0.988
PR	0.953	0.993	0.988
ANN	0.996	1.000	0.999
xGBoost	0.839	1.000	0.988
GBoost	0.844	1.000	0.957
RF	0.864	0.984	0.977

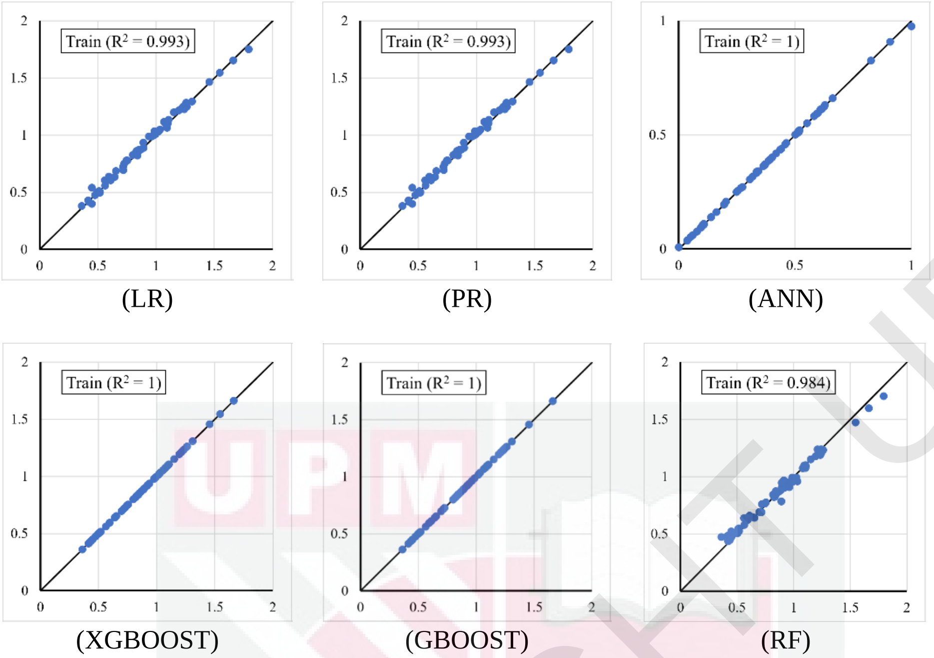

Figure 4.53: Accuracy of model 7 results for LR, PR, ANN, XGBOOST, GBOOST, and RF algorithms for training data

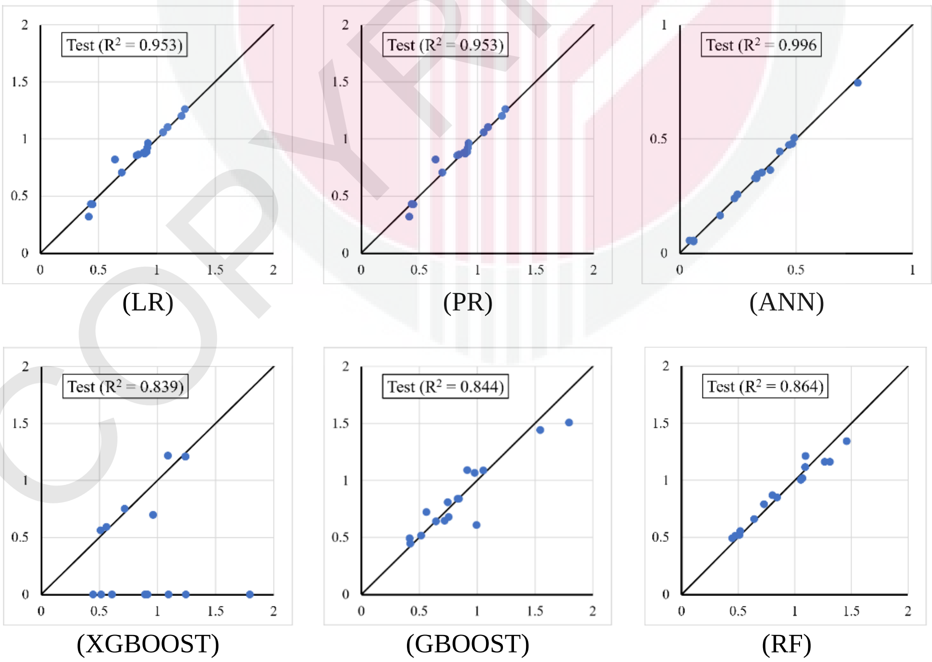

Figure 4.54: Accuracy of model 7 results for LR, PR, ANN, XGBOOST, GBOOST, and RF algorithms for testing data

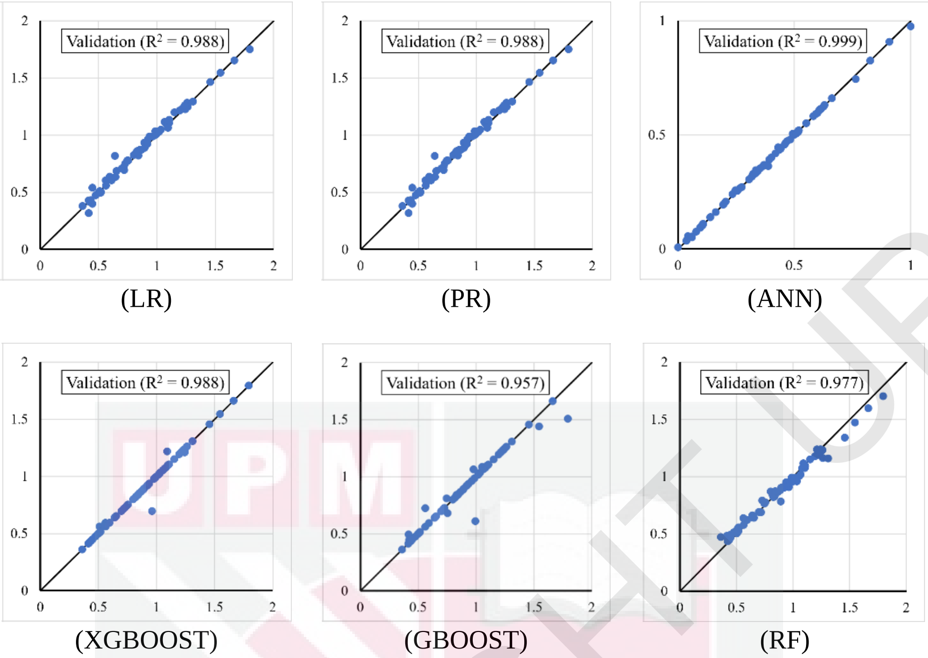

Figure 4.55: Accuracy of model 7 results for LR, PR, ANN, XGBOOST, GBOOST, and RF algorithms for validation data

The eighth model was predicting the stress–strain relationship using features conducted from CU triaxial test, curing duration, and treating materials ratio, where the model has the highest accuracy for xGBoost algorithm by R^2 value of 0.842, 0952, and 0.933 for Test, Train, and Validation respectively as shown in Figures 4.56 to 4.58. In addition, LR and PR showed low accuracy, where GBoost, ANN and RF were having a significant high accuracy in training, testing and validation as shown in Table 4.30. In addition, the variance of the datasets for training, testing, and validation is the minimum for ANN, GBoost, xGBoost and RF algorithms. As per conducted figures, the best model for predicting and controlling UCS of treated marine clay using POFA, lime and calcined shale through manual feature selection is xGBoost technique with a slightly difference compared to GBoost. On the other hand, xGBoost, GBoost and RF techniques show a surprisingly significant better performance compared to ANN algorithm, which was the reason for the number of readings dataset that was sufficient for xGBoost, GBoost and RF algorithms in training, testing and validation (Mozumder et al., 2015). However, the model was significantly accurate for ANN algorithm. Accordingly, this model is better in prediction of stress–strain relationship of CU triaxial test better than FEM results conducted from PLAXIS program. That promises easier, accurate prediction for CU behaviour of soil without applying triaxial test.

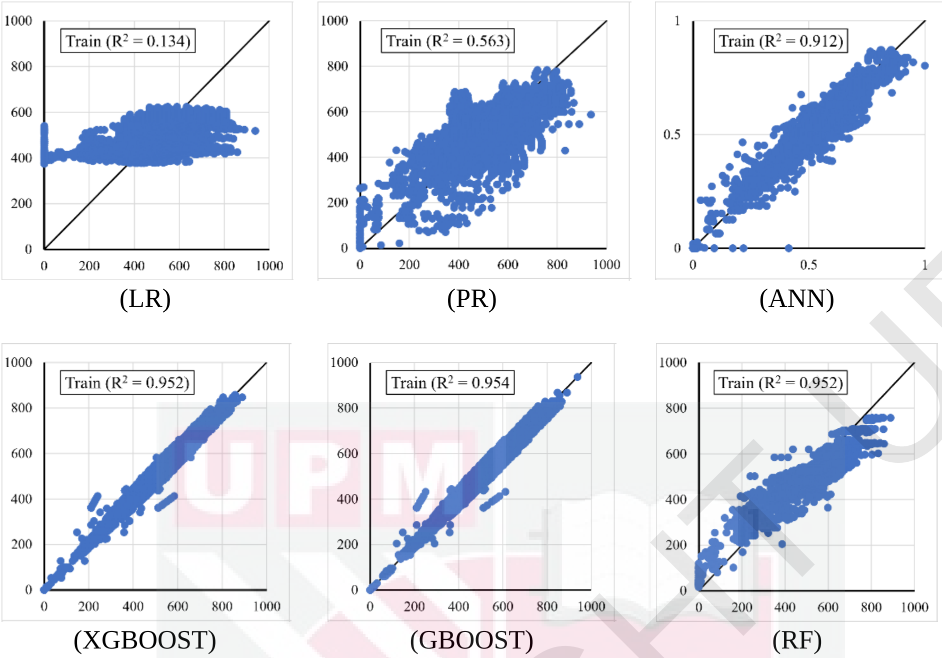

Figure 4.56: Accuracy of model 8 results for LR, PR, ANN, XGBOOST, GBOOST, and RF algorithms for training data

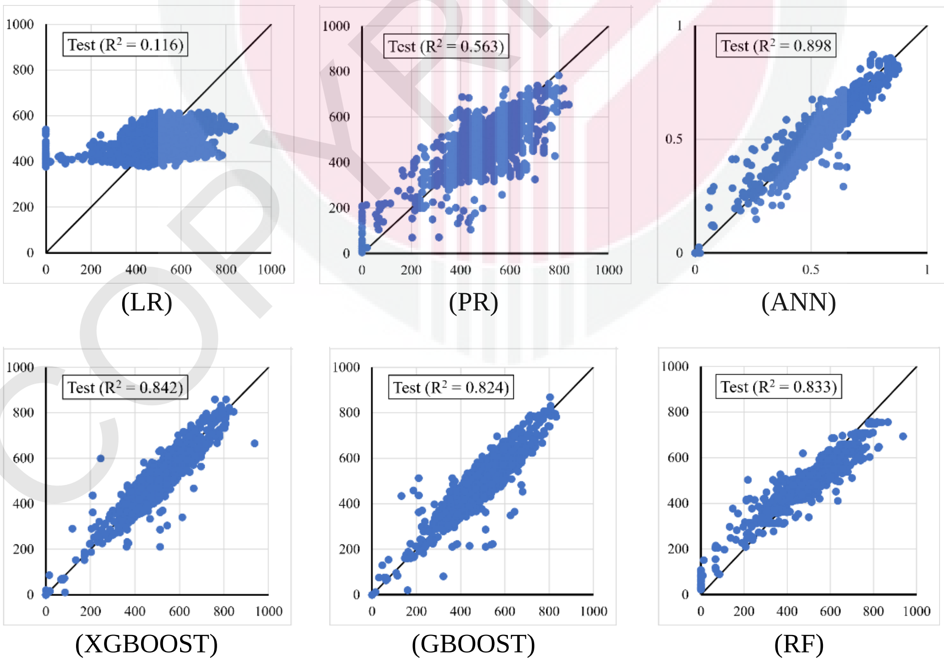

Figure 4.57: Accuracy of model 8 results for LR, PR, ANN, XGBOOST, GBOOST, and RF algorithms for testing data

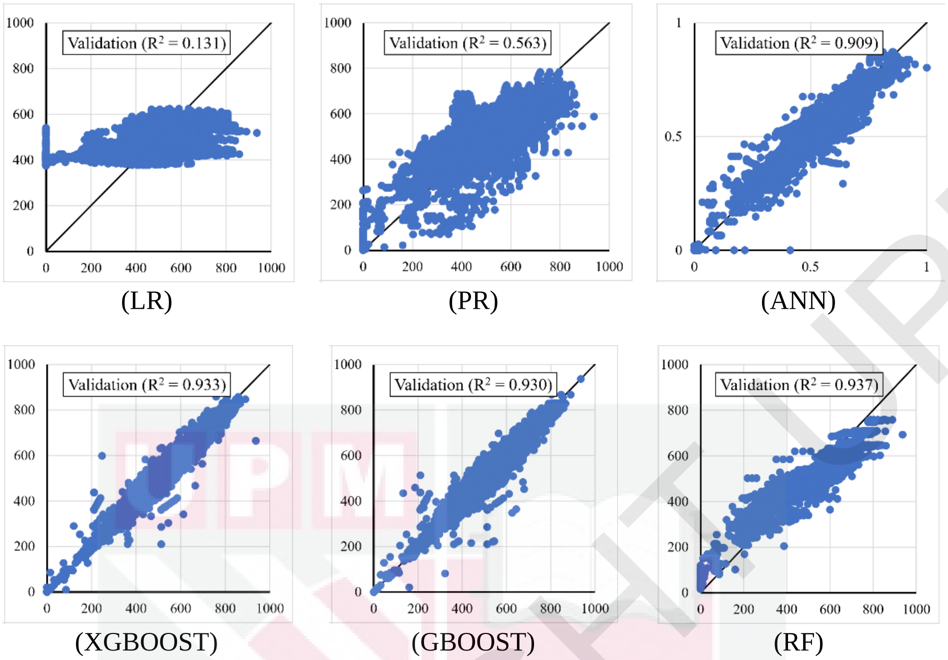

Figure 4.58: Accuracy of model 8 results for LR, PR, ANN, XGBOOST, GBOOST, and RF algorithms for validation data

Table 4.30: 8th model R^2 values for different used algorithms

Algorithm	**Test**	**Train**	**Validation**
LR	0.116	0.134	0.131
PR	0.563	0.563	0.563
ANN	0.898	0.912	0.909
xGBoost	0.842	0.952	0.933
GBoost	0.824	0.954	0.930
RF	0.859	0.872	0.870

4.7.6 Data Prediction Models Using Hybrid Algorithms

Machine learning feature selection was based on using Genetic feature selection GS, forward feature selection FS and backward feature selection BS through RF, GBoost, and xGBoost. All conducted features were used in this stage, but the algorithms were selecting the best features giving the highest accuracy using the three different selection methods. Therefore there were nine ML models were assessed as identified in Table 3.14 in Section 3.8.2.

The ninth model was GS through RF algorithm for predicting undrained shear strength using the selected features, where the model has the highest accuracy for ANN algorithm by R^2 value of 0.992, 0.999, and 0.998 for Test, Train, and Validation respectively as shown in Figures 4.59 to 4.61. In addition, LR, PR, GBoost, xGBoost and RF were having high accuracy as shown in Table 4.31. In addition, the variance of the datasets for training, testing, and validation is the minimum for ANN, GBoost, xGBoost and RF algorithms. As per conducted figures, the best model for predicting and controlling UCS of treated marine clay using POFA, lime and calcined shale through hybrid feature selection is ANN technique with a significant difference compared to other algorithms as conducted by previous studies (Iravanian, Kassem, & Gokcekus, 2022; Nouman Amjad Raja et al., 2021). On the other hand, xGBoost, LR and PR techniques show significant better performance compared to GBoost and RF algorithms, which was the reason for the number of readings dataset that was sufficient for GBoost and RF algorithms in training, testing and validation (Mozumder et al., 2015). However, the models were significantly accurate for all algorithms.

Table 4.31: 9th model R^2 values for different used algorithms

Algorithm	Test	Train	Validation
LR	0.987	0.982	0.982
PR	0.987	0.982	0.982
ANN	0.992	0.999	0.998
xGBoost	0.875	1.000	0.981
GBoost	0.872	1.000	0.965
RF	0.857	0.983	0.973

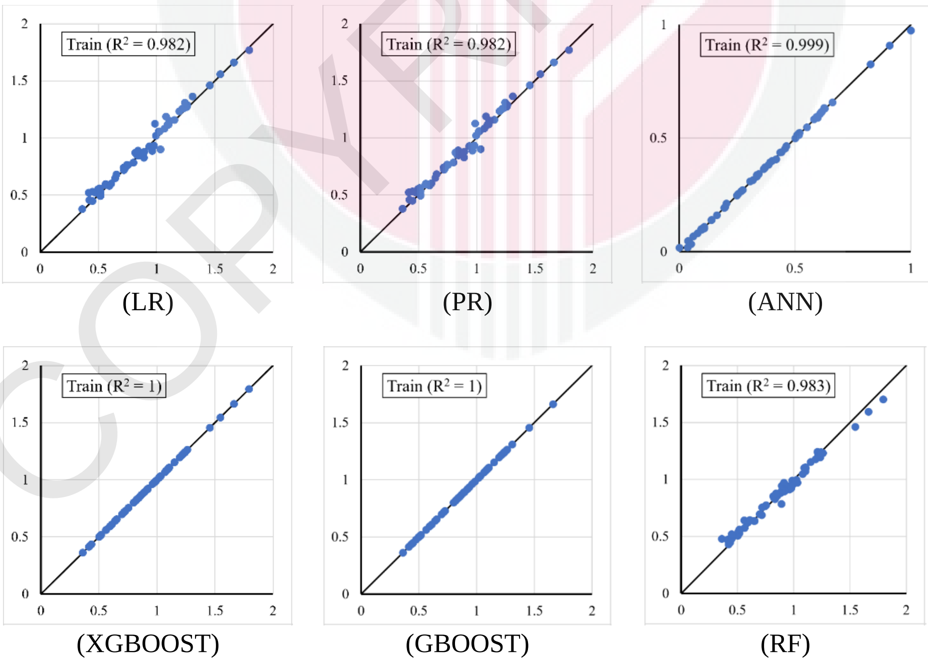

Figure 4.59: Accuracy of model 9 results for LR, PR, ANN, XGBOOST, GBOOST, and RF algorithms for training data

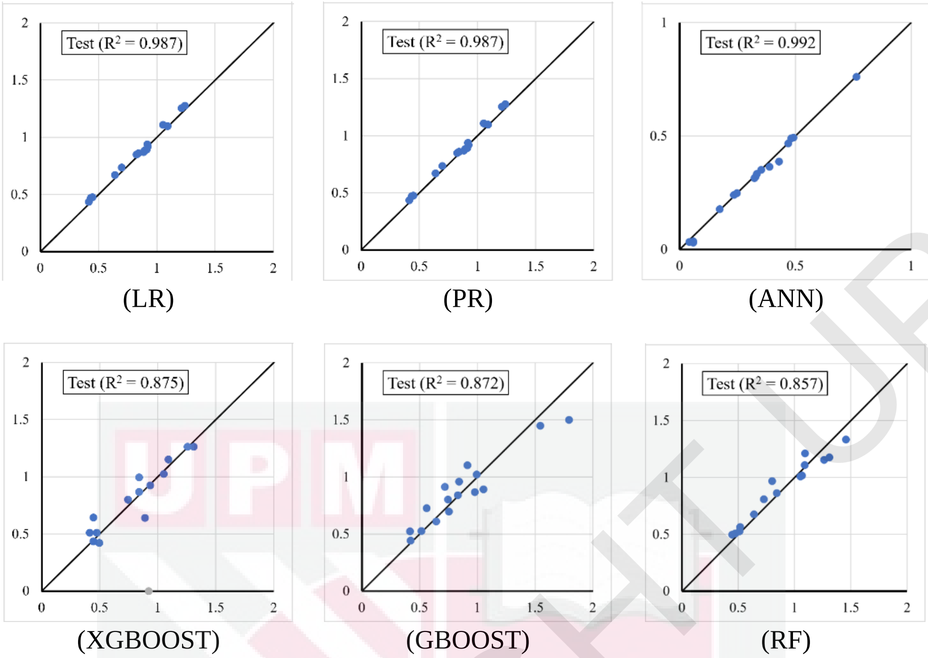

Figure 4.60: Accuracy of model 9 results for LR, PR, ANN, XGBOOST, GBOOST, and RF algorithms for testing data

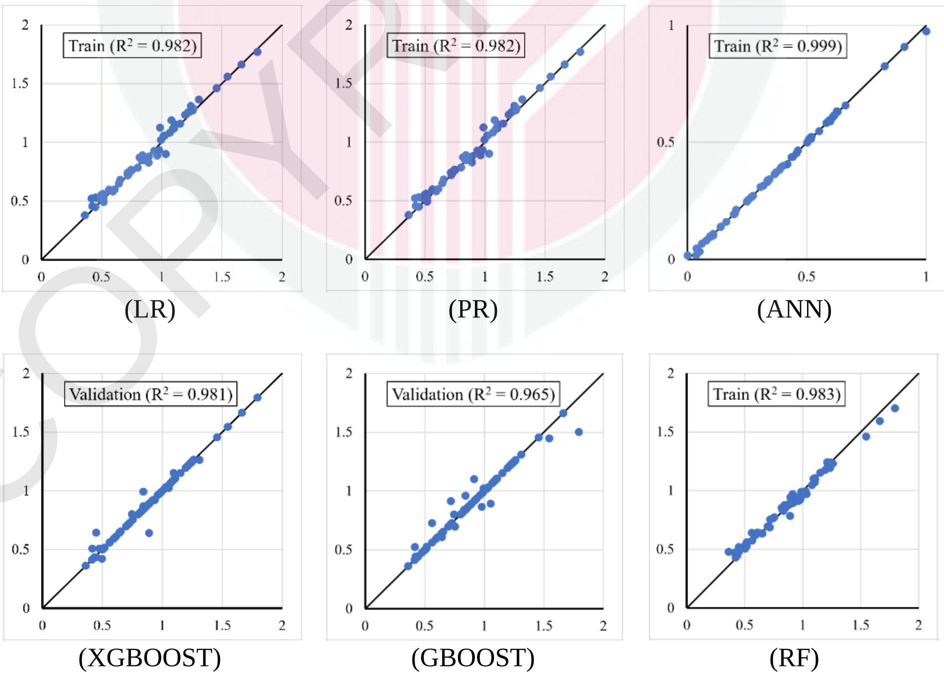

Figure 4.61: Accuracy of model 9 results for LR, PR, ANN, XGBOOST, GBOOST, and RF algorithms for validation data

The tenth model was FS through RF algorithm for predicting undrained shear strength using the selected features, where the model has the highest accuracy for ANN algorithm by R^2 value of 0.976, 0.999, and 0.996 for Test, Train, and Validation respectively as shown in Figures 4.62 to 4.64. In addition, LR and PR were low accuracy models, while GBoost, xGBoost and RF were having high accuracy models as shown in Table 4.32. Furthermore, the variance among the training, testing, and validation datasets was minimal for ANN, GBoost, xGBoost, and RF algorithms. Based on these findings, the ANN technique emerged as the most suitable model for predicting and controlling undrained shear strength in treated marine clay using hybrid feature selection as conducted by previous studies (Iravanian, Kassem, & Gokcekus, 2022; Nouman Amjad Raja et al., 2021). Additionally, xGBoost and RF techniques outperformed the GBoost algorithm significantly, particularly in terms of testing dataset accuracy, which was notably poor for GBoost. This discrepancy can be attributed to the random selection of datasets, which lacked sufficient readings (Mozumder et al., 2015).

Table 4.32: 10th model R^2 values for different used algorithms

Algorithm	Test	Train	Validation
LR	0.217	0.746	0.679
PR	0.265	0.689	0.636
ANN	0.976	0.999	0.996
xGBoost	0.737	1.000	0.962
GBoost	0.280	1.000	0.804
RF	0.760	0.971	0.951

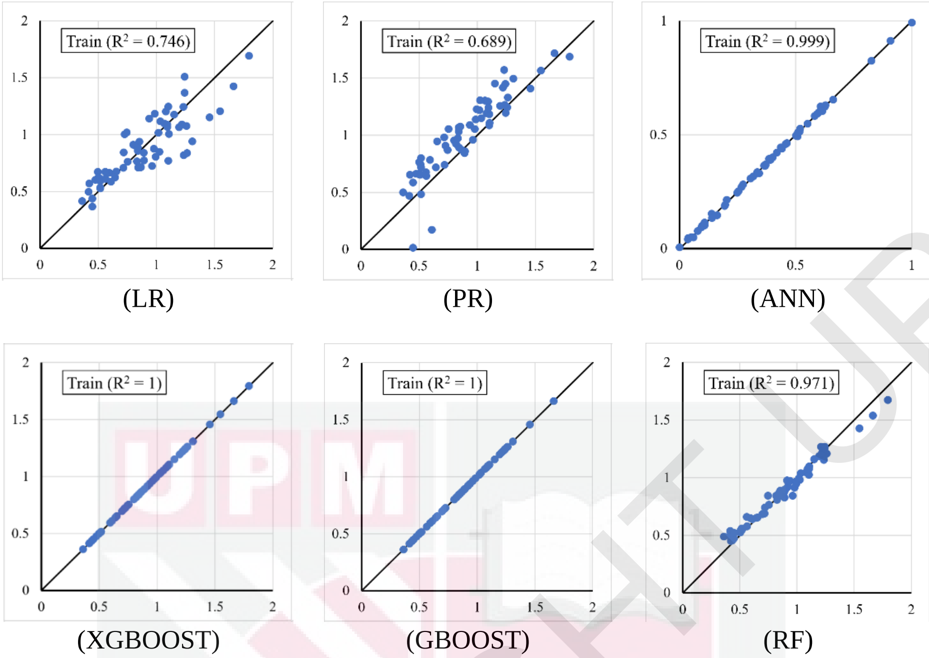

Figure 4.62: Accuracy of model 10 results for LR, PR, ANN, XGBOOST, GBOOST, and RF algorithms for training data

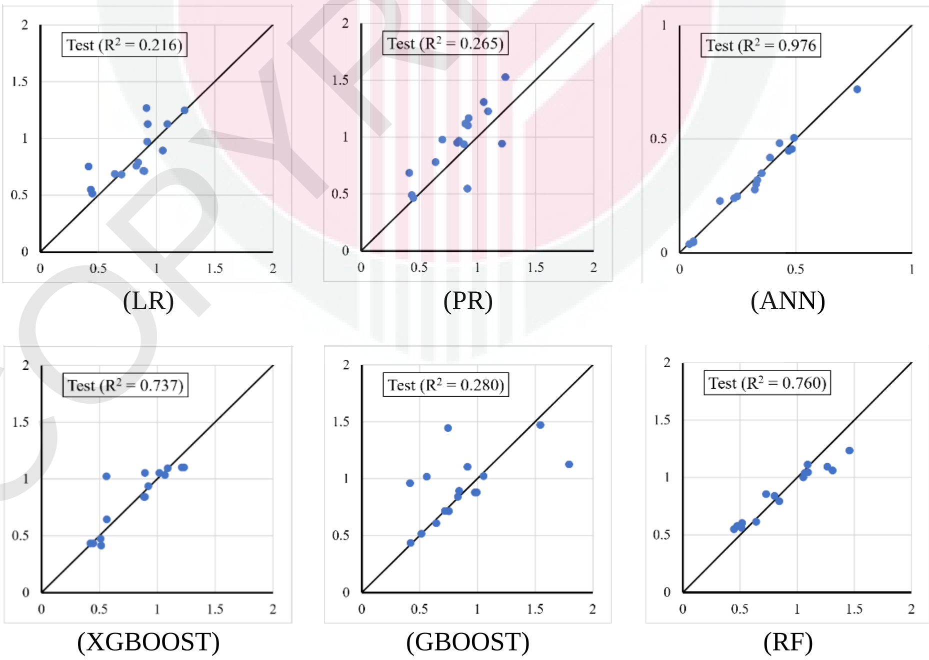

Figure 4.63: Accuracy of model 10 results for LR, PR, ANN, XGBOOST, GBOOST, and RF algorithms for testing data

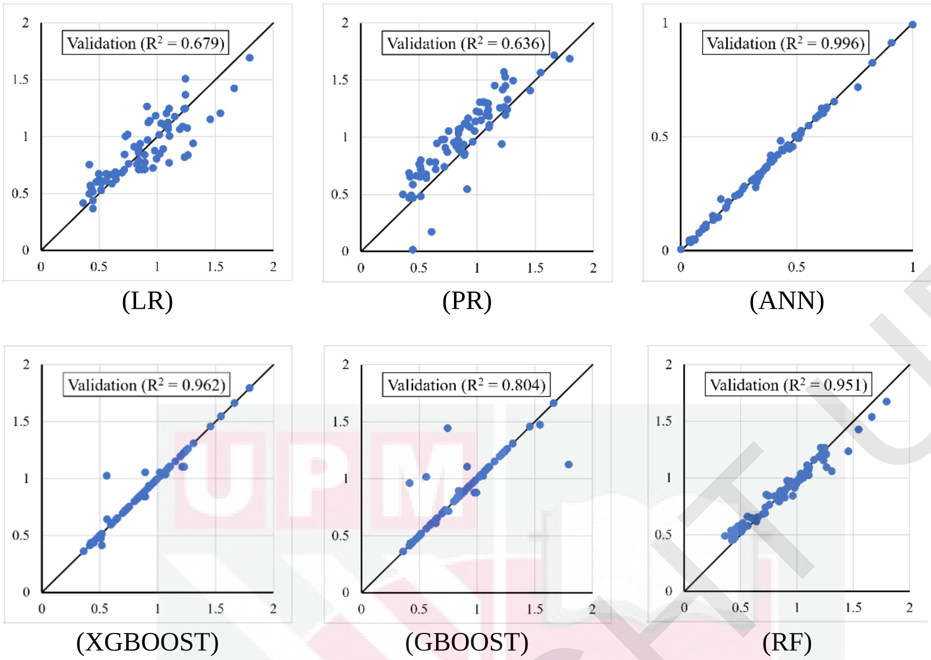

Figure 4.64: Accuracy of model 10 results for LR, PR, ANN, XGBOOST, GBOOST, and RF algorithms for validation data

The eleventh model was BS through RF algorithm for predicting undrained shear strength using the selected features, where the model has the highest accuracy for ANN algorithm by R^2 value of 1, 0.996, and 0.999 for Test, Train, and Validation respectively. In addition, PR was a low accurate model, while LR, GBoost, xGBoost and RF were having high accuracy as shown in Table 4.33. That shows that BS is better than GS and FS using RF algorithm in feature selection. Furthermore, the variance among the datasets was minimal for ANN, GBoost, xGBoost, and RF algorithms as shown in Figures 4.65 to 4.67. Accordingly, the ANN technique emerged as the most suitable model for predicting and controlling undrained shear strength in treated marine clay using hybrid feature selection as conducted by previous studies (Iravanian, Kassem, & Gokcekus, 2022; Nouman Amjad Raja et al., 2021). Additionally, RF techniques outperformed GBoost and xGBoost algorithms significantly, particularly in terms of testing dataset accuracy, which was surprisingly poor for xGBoost. This inconsistency can be attributed to the random selection of datasets, which required sufficient readings (Mozumder et al., 2015).

Table 4.33: 11th model R^2 values for different used algorithms

Algorithm	Test	Train	Validation
LR	0.953	0.993	0.988
PR	0.265	0.689	0.636
ANN	1.000	0.996	0.999
xGBoost	0.810	1.000	0.937
GBoost	0.844	1.000	0.957
RF	0.864	0.984	0.977

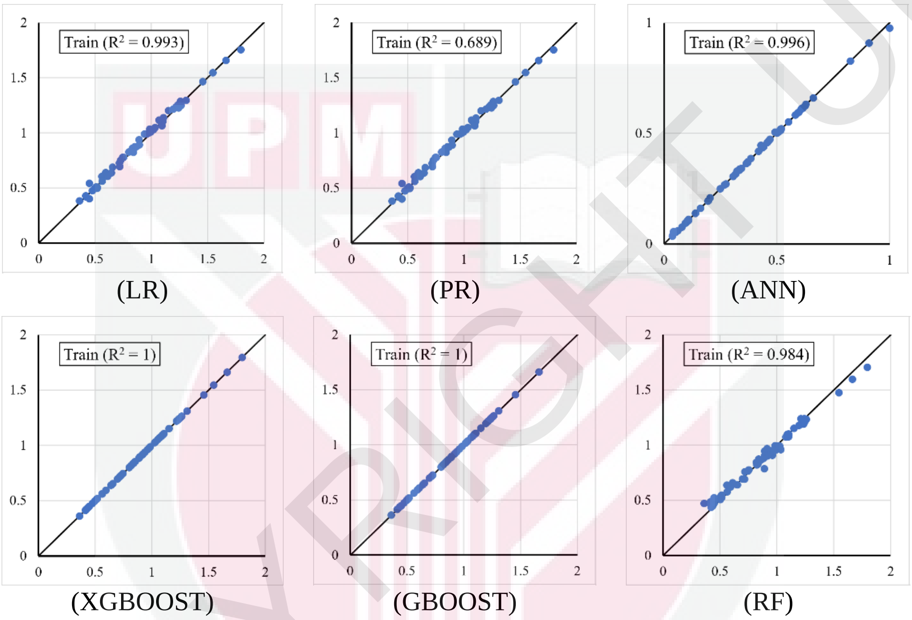

Figure 4.65: Accuracy of model 11 results for LR, PR, ANN, XGBOOST, GBOOST, and RF algorithms for training data

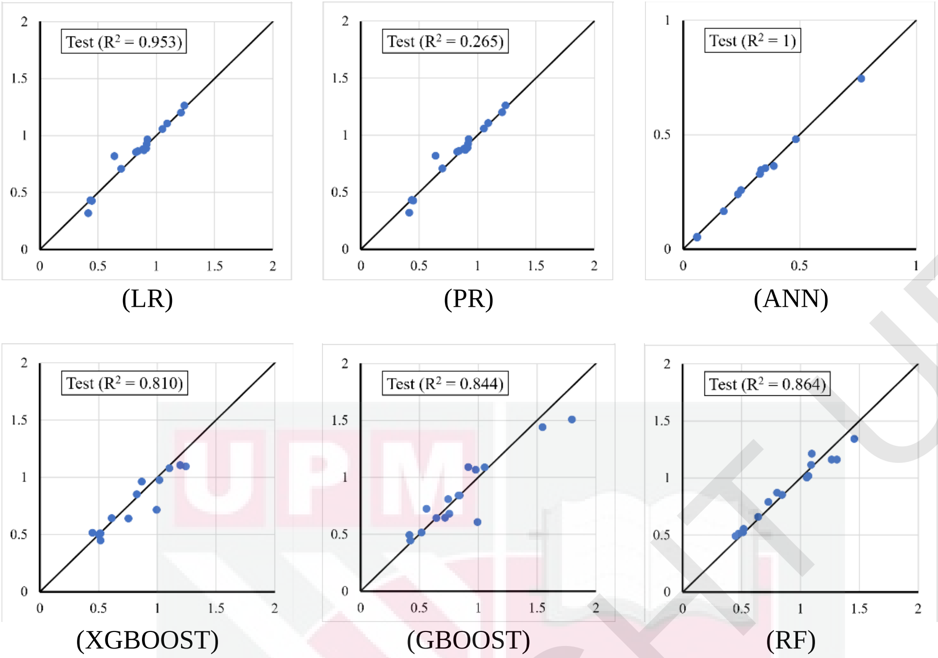

Figure 4.66: Accuracy of model 11 results for LR, PR, ANN, XGBOOST, GBOOST, and RF algorithms for testing data

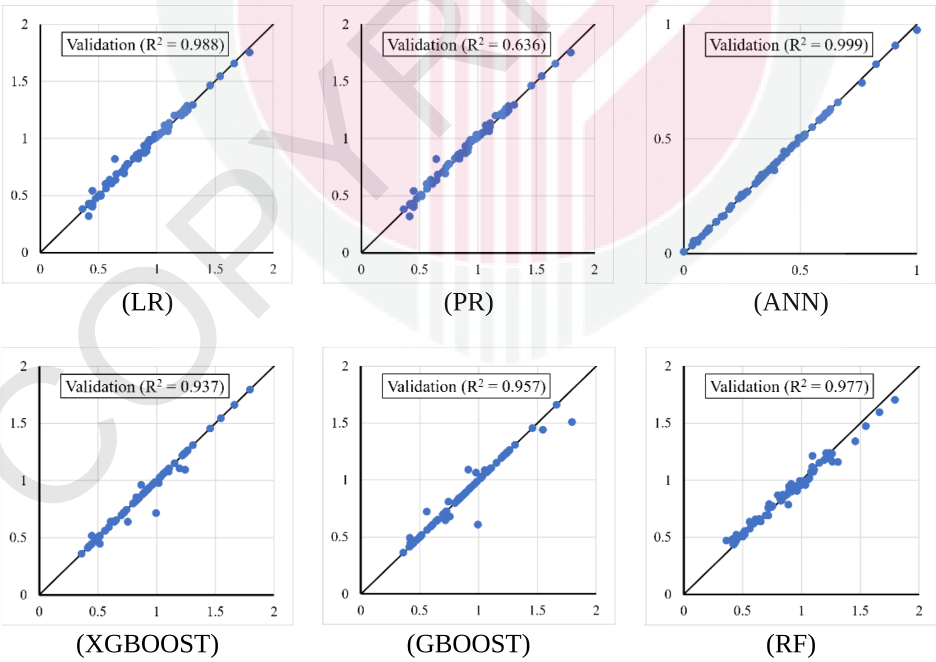

Figure 4.67: Accuracy of model 11 results for LR, PR, ANN, XGBOOST, GBOOST, and RF algorithms for validation data

The twelfth model was GS through GBoost algorithm for predicting undrained shear strength using the selected features, where the model has the highest accuracy for ANN algorithm by R^2 value of 0.994, 0.999, and 0.999 for Test, Train, and Validation respectively. In addition, LR, PR, GBoost, xGBoost and RF were having high accuracy as shown in Table 4.34. Both PR and LR were more accurate compared to RF, xGBoost, and GBoost, where the selected features were better in direct relationships compared to family of tree regression method. This inconsistency can be attributed to the random selection of datasets, which required sufficient readings to overcome that issue (Mozumder et al., 2015). Furthermore, the variance among the training, testing, and validation datasets was minimal for ANN, LR, PR, and RF algorithms as shown in Figures 4.68 to 4.70. Based on these findings, the ANN technique emerged as the most suitable model for predicting and controlling undrained shear strength in treated marine clay using hybrid feature selection as conducted by previous studies (Iravanian, Kassem, & Gokcekus, 2022; Nouman Amjad Raja et al., 2021).

Table 4.34: 12th model R^2 values for different used algorithms

Algorithm	Test	Train	Validation
LR	0.991	0.986	0.987
PR	0.991	0.986	0.987
ANN	0.994	0.999	0.999
xGBoost	0.677	1.000	0.958
GBoost	0.796	1.000	0.945
RF	0.846	0.982	0.972

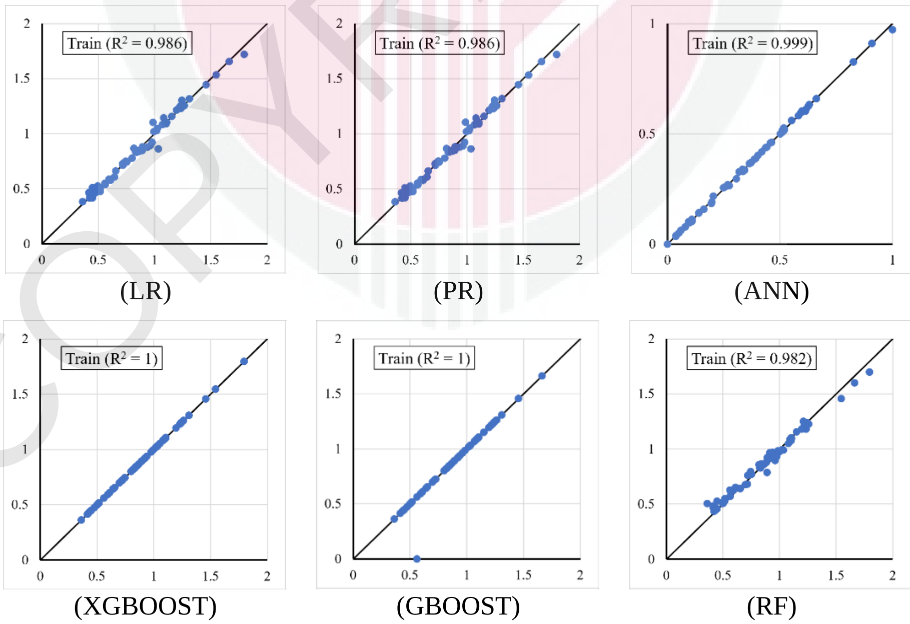

Figure 4.68: Accuracy of model 12 results for LR, PR, ANN, XGBOOST, GBOOST, and RF algorithms for training data

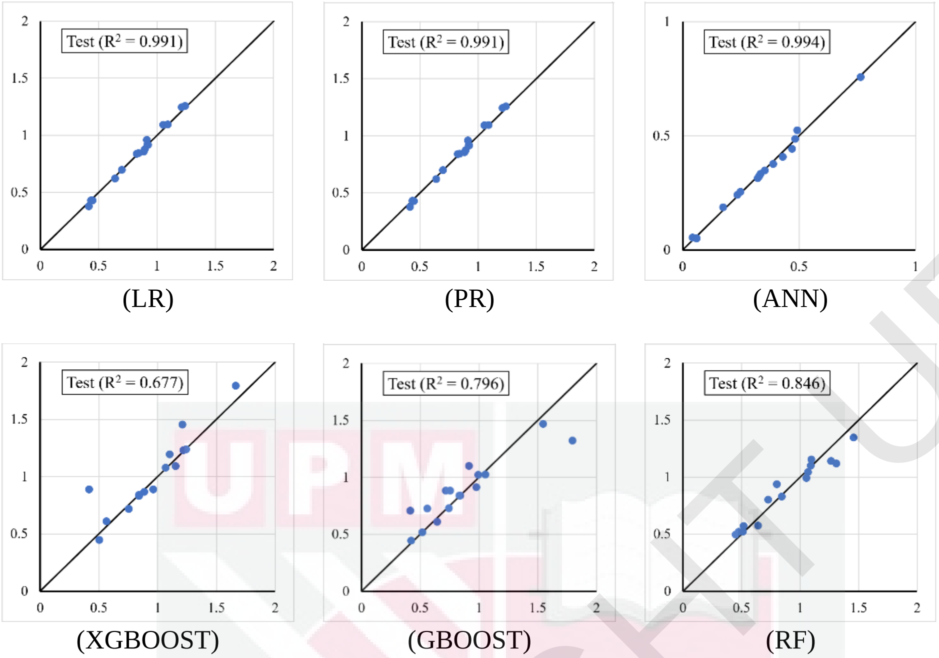

Figure 4.69: Accuracy of model 12 results for LR, PR, ANN, XGBOOST, GBOOST, and RF algorithms for testing data

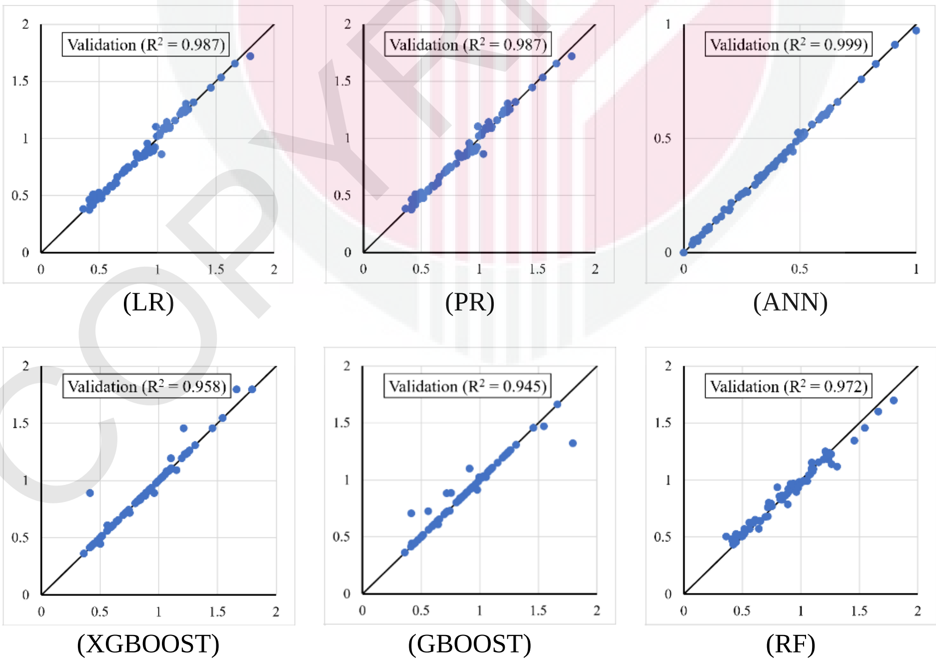

Figure 4.70: Accuracy of model 12 results for LR, PR, ANN, XGBOOST, GBOOST, and RF algorithms for validation data

The thirteenth model was FS through GBoost algorithm for predicting undrained shear strength using the selected features, where the model has the highest accuracy for ANN algorithm by R^2 value of 0.976, 0.999, and 0.996 for Test, Train, and Validation respectively. In addition, LR and PR were giving acceptable accuracy, while GBoost, xGBoost and RF were having high accuracy as shown in Table 4.35. Furthermore, the variance among the training, testing, and validation datasets was minimal for ANN, GBoost, xGBoost, and RF algorithms as shown in Figures 4.71 to 4.73. Based on these findings, the ANN technique appeared as the most suitable model for predicting and controlling UCS in treated marine clay using hybrid feature selection as conducted by previous studies (Iravanian, Kassem, & Gokcekus, 2022; Nouman Amjad Raja et al., 2021). RF algorithm for testing dataset was significantly poor in accuracy. This inconsistency can be attributed to the random selection of datasets, which required sufficient readings to overcome that issue (Mozumder et al., 2015).

Table 4.35: 13th model R^2 values for different used algorithms

Algorithm	Test	Train	Validation
LR	0.217	0.746	0.679
PR	0.265	0.689	0.636
ANN	0.976	0.999	0.996
xGBoost	0.789	1.000	0.930
GBoost	0.280	1.000	0.804
RF	0.760	0.971	0.951

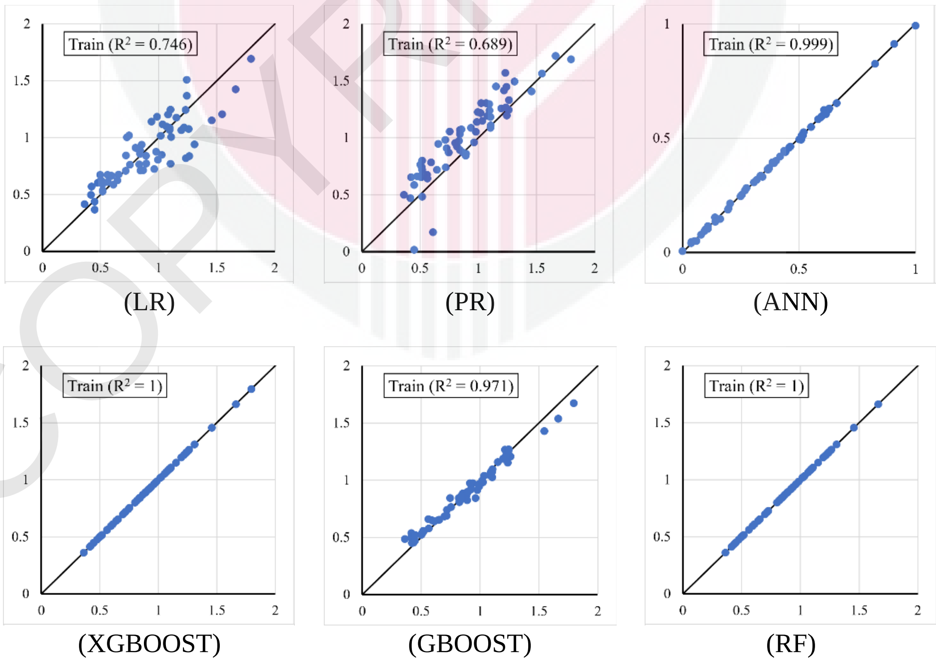

Figure 4.71: Accuracy of model 13 results for LR, PR, ANN, XGBOOST, GBOOST, and RF algorithms for training data

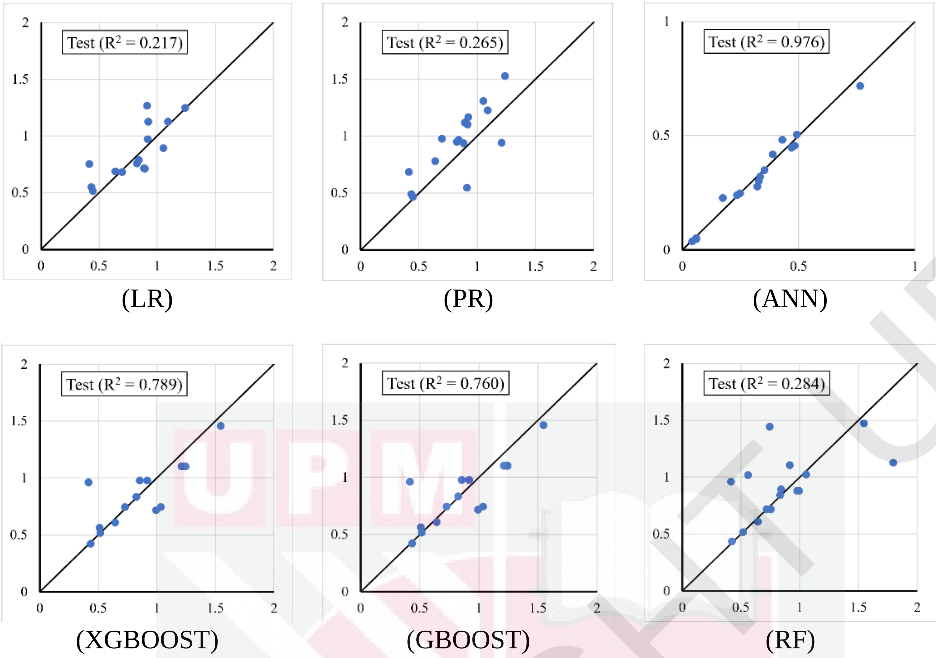

Figure 4.72: Accuracy of model 13 results for LR, PR, ANN, XGBOOST, GBOOST, and RF algorithms for testing data

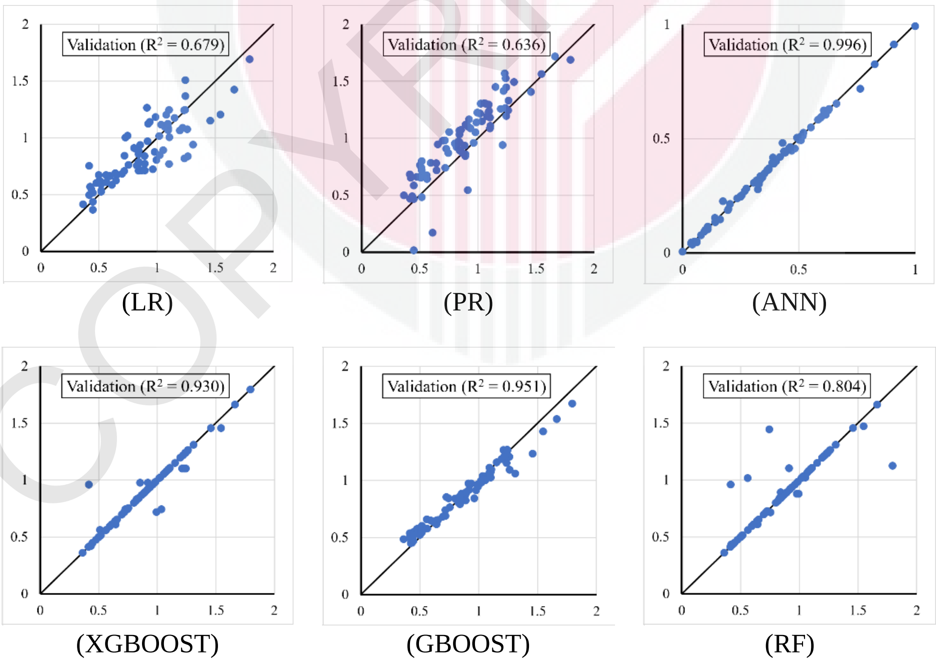

Figure 4.73: Accuracy of model 13 results for LR, PR, ANN, XGBOOST, GBOOST, and RF algorithms for validation data

The fourteenth model was BS through GBoost algorithm for predicting undrained shear strength using the selected features, where the model has the highest accuracy for ANN algorithm by R^2 value of 0.996, 1.000, and 0.999 for Test, Train, and Validation respectively. In addition, LR, PR, GBoost, xGBoost and RF were having high accuracy as shown in Table 4.36. Both PR and LR were more accurate compared to RF, xGBoost, and GBoost, where the selected features were better in direct relationships compared to family of tree regression method. This inconsistency can be attributed to the random selection of datasets, which required sufficient readings to overcome that issue (Mozumder et al., 2015).That shows that BS is better than GS and FS using RF algorithm in feature selection. However, the variance among the training, testing, and validation datasets was minimal for all algorithms as shown in Figures 4.74 to 4.76. Accordingly, the ANN technique appeared as the most suitable model for predicting and controlling UCS in treated marine clay using hybrid feature selection as conducted by previous studies (Iravanian, Kassem, & Gokcekus, 2022; Nouman Amjad Raja et al., 2021).

Table 4.36: 14th model R^2 values for different used algorithms

Algorithm	Test	Train	Validation
LR	0.953	0.993	0.988
PR	0.953	0.993	0.988
ANN	0.996	1.000	0.999
xGBoost	0.773	1.000	0.979
GBoost	0.844	1.000	0.957
RF	0.864	0.984	0.977

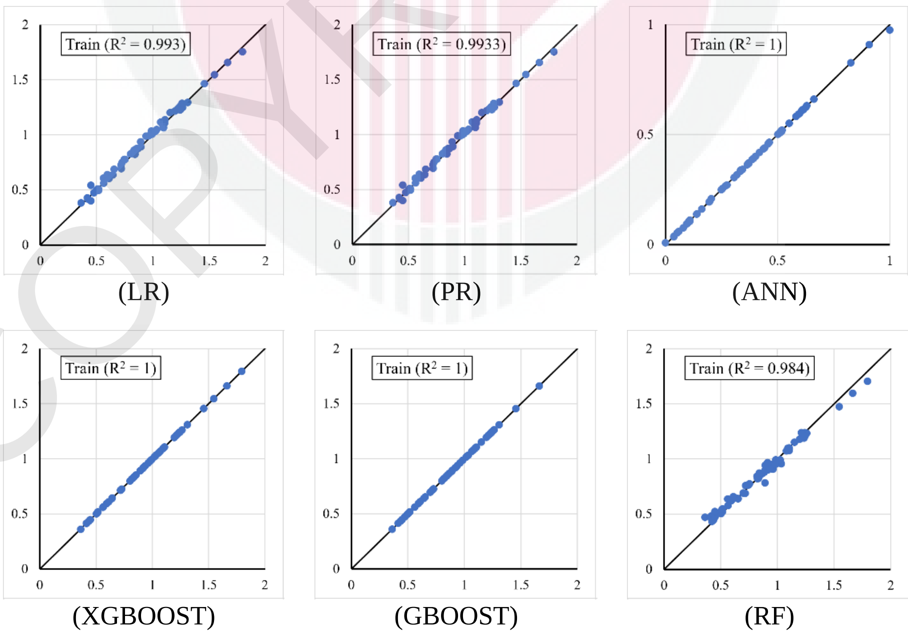

Figure 4.74: Accuracy of model 14 results for LR, PR, ANN, XGBOOST, GBOOST, and RF algorithms for training data

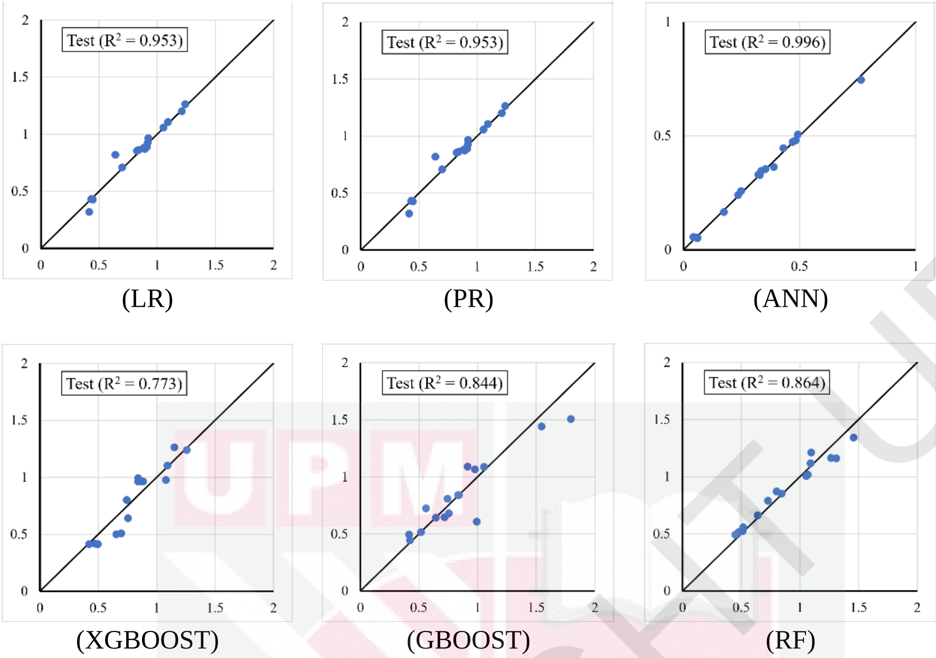

Figure 4.75: Accuracy of model 14 results for LR, PR, ANN, XGBOOST, GBOOST, and RF algorithms for testing data

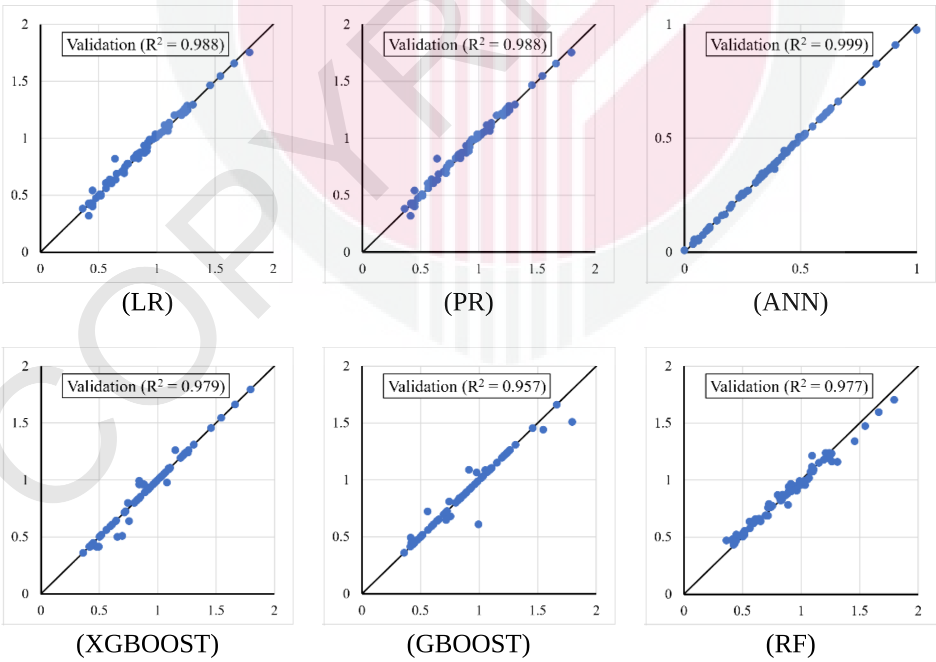

Figure 4.76: Accuracy of model 14 results for LR, PR, ANN, XGBOOST, GBOOST, and RF algorithms for validation data

The fifteenth model was GS through xGBoost algorithm for predicting undrained shear strength using the selected features, where the model has the highest accuracy for ANN algorithm by R^2 value of 0.988, 0.999, and 0.997 for Test, Train, and Validation respectively. In addition, LR and PR were significantly accurate, while GBoost, xGBoost and RF were slightly less accurate compared to LR, PR and ANN as shown in Table 4.37, where the selected features were better in direct relationships compared to family of tree regression method. This inconsistency can be attributed to the random selection of datasets, which required sufficient readings to overcome that issue (Mozumder et al., 2015). However, the variance among the training, testing, and validation datasets was minimal for all algorithms as shown in Figures 4.77 to 4.79. Accordingly, the ANN technique appeared as the most suitable model for predicting and controlling UCS in treated marine clay using hybrid feature selection as conducted by previous studies (Iravanian, Kassem, & Gokcekus, 2022; Nouman Amjad Raja et al., 2021).

Table 4.37: 15th model R^2 values for different used algorithms

Algorithm	Test	Train	Validation
LR	0.982	0.990	0.989
PR	0.982	0.990	0.989
ANN	0.988	0.999	0.997
xGBoost	0.742	1.000	0.971
GBoost	0.830	1.000	0.954
RF	0.853	0.983	0.976

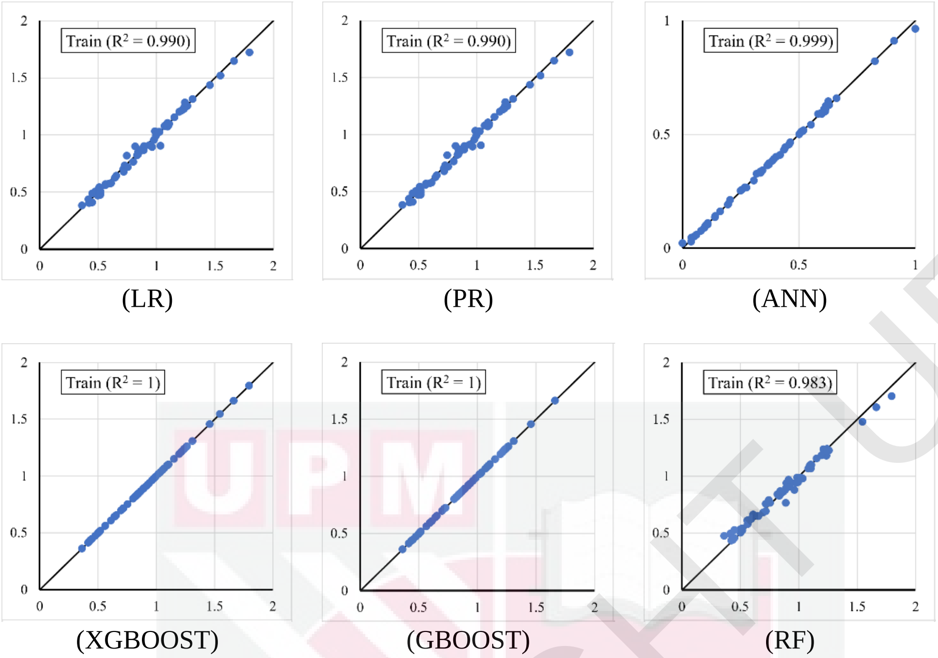

Figure 4.77: Accuracy of model 15 results for LR, PR, ANN, XGBOOST, GBOOST, and RF algorithms for validation results

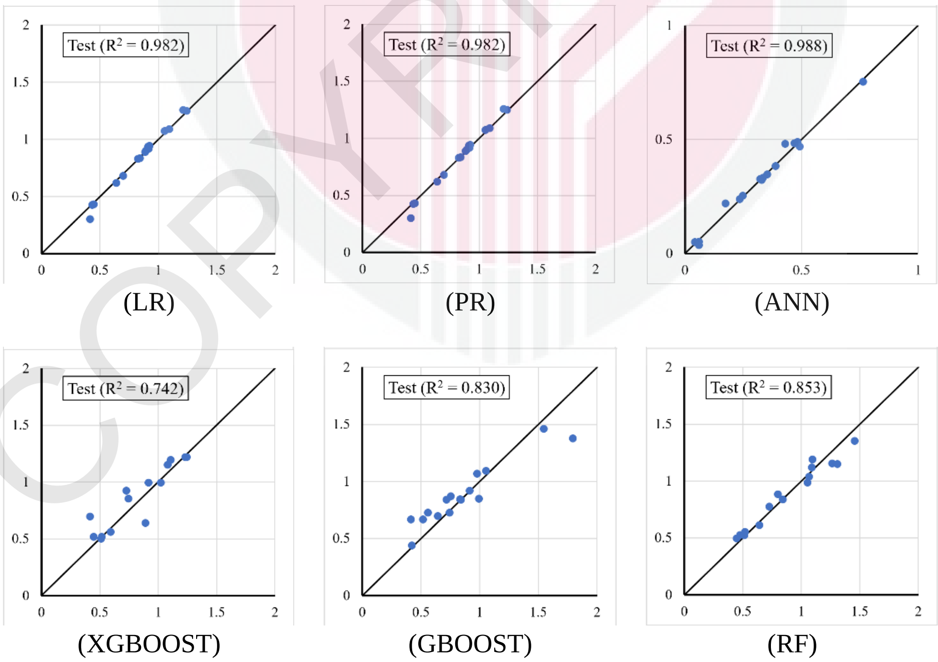

Figure 4.78: Accuracy of model 15 results for LR, PR, ANN, XGBOOST, GBOOST, and RF algorithms for validation results

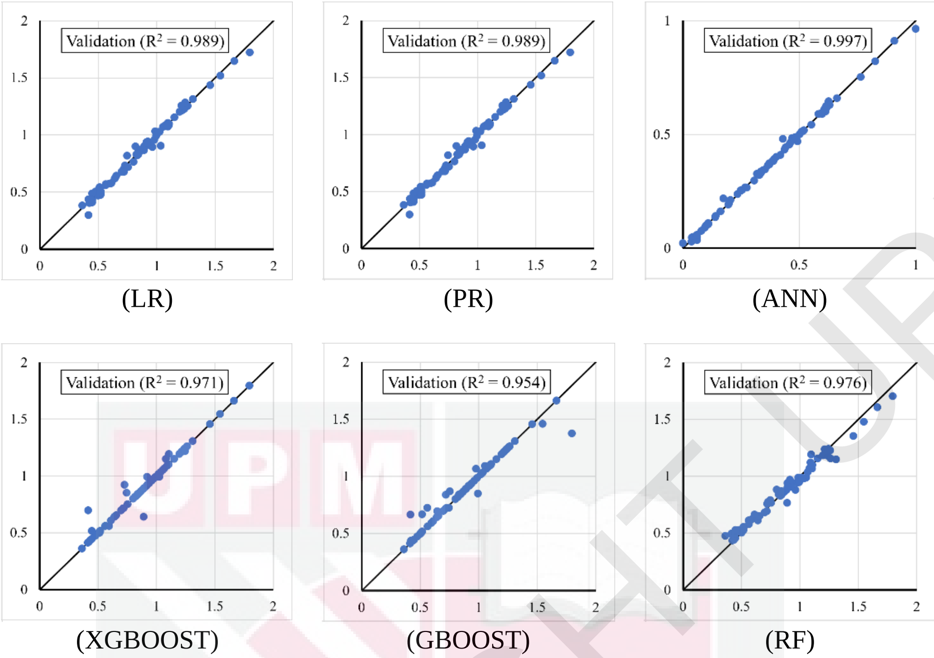

Figure 4.79: Accuracy of model 15 results for LR, PR, ANN, XGBOOST, GBOOST, and RF algorithms for validation results

The sixteenth model was FS through xGBoost algorithm for predicting undrained shear strength using the selected features, where the model has the highest accuracy for ANN algorithm by R^2 value of 0.989, 1.000, and 0.998 for Test, Train, and Validation respectively. In addition, LR and PR, GBoost, xGBoost and RF were having high accuracy as shown in Table 4.38. In addition, the variance among the training, testing, and validation datasets was minimal for ANN, xGBoost and RF algorithms as shown in Figures 4.80 to 4.82. Furthermore, the ANN technique was the most suitable model for predicting and controlling UCS in treated marine clay using hybrid feature selection as conducted by previous studies (Iravanian, Kassem, & Gokcekus, 2022; Nouman Amjad Raja et al., 2021).

Table 4.38: 16th model R^2 values for different used algorithms

Algorithm	Test	Train	Validation
LR	0.669	0.901	0.872
PR	0.669	0.901	0.872
ANN	0.989	1.000	0.998
xGBoost	0.660	1.000	0.942
GBoost	0.569	1.000	0.883
RF	0.805	0.976	0.968

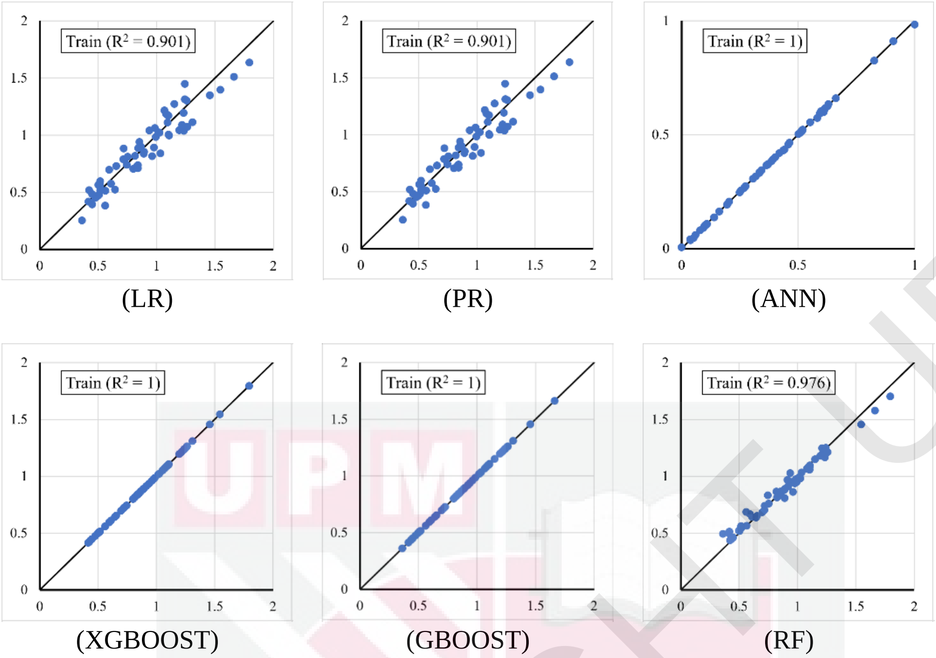

Figure 4.80: Accuracy of model 16 results for LR, PR, ANN, XGBOOST, GBOOST, and RF algorithms for training data

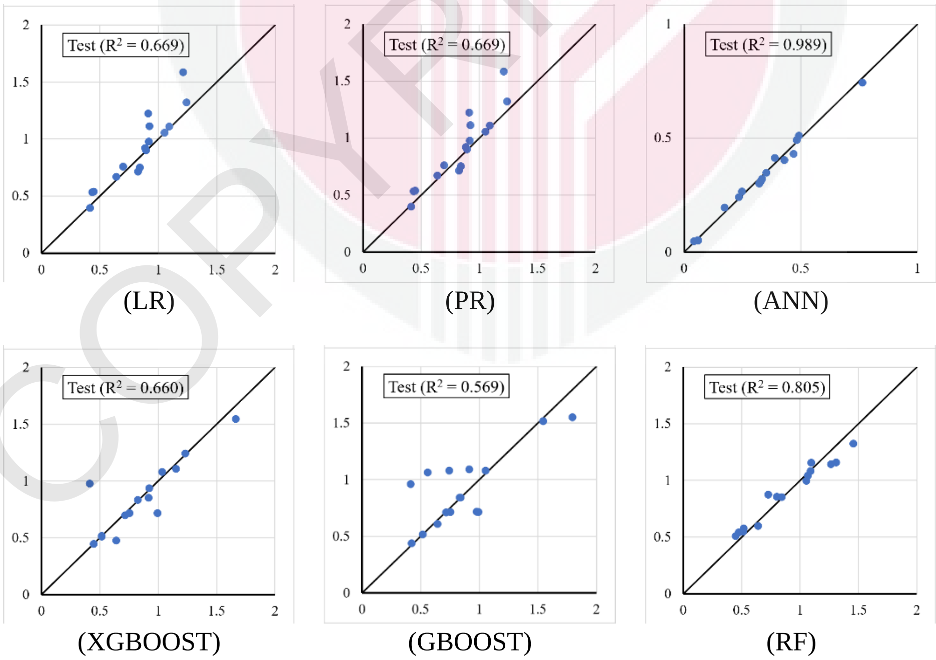

Figure 4.81: Accuracy of model 16 results for LR, PR, ANN, XGBOOST, GBOOST, and RF algorithms for testing data

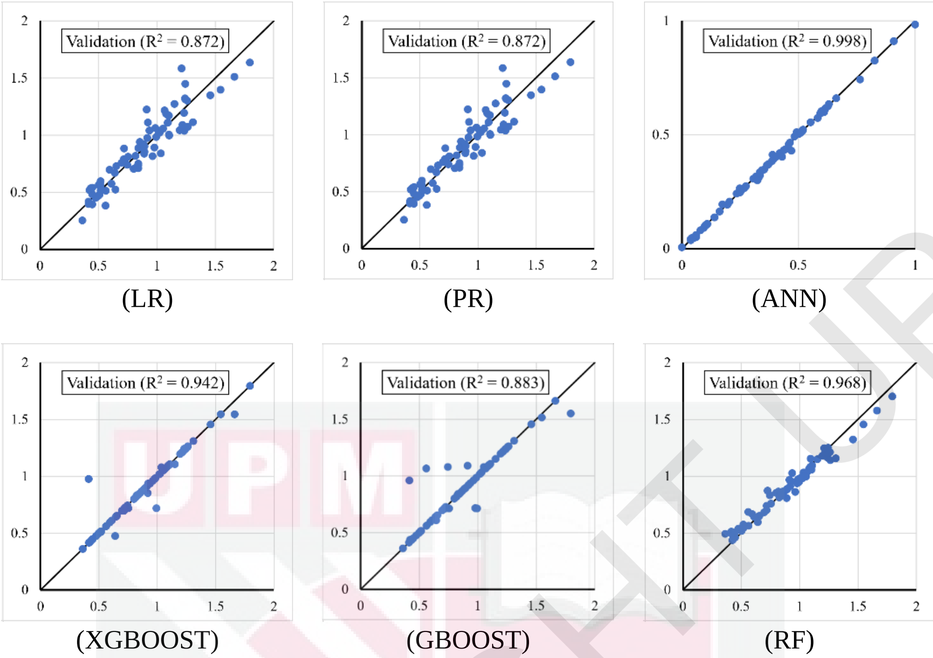

Figure 4.82: Accuracy of model 16 results for LR, PR, ANN, XGBOOST, GBOOST, and RF algorithms for validation data

The seventeenth model was BS through xGBoost algorithm for predicting undrained shear strength using the selected features, where the model has the highest accuracy for ANN algorithm by R^2 value of 0.992, 1.000, and 0.999 for Test, Train, and Validation respectively. In addition, LR, PR, GBoost, xGBoost and RF were having high accuracy as shown in Table 4.39. Both PR and LR were more accurate compared to RF, xGBoost, and GBoost, where the selected features were better in direct relationships compared to family of tree regression method. This inconsistency can be attributed to the random selection of datasets, which required sufficient readings to overcome that issue (Mozumder et al., 2015). That shows that BS is better than GS and FS using RF algorithm in feature selection. In addition, the variance among the training, testing, and validation datasets was minimal for all algorithms excluding xGBoost as shown in Figures 4.83 to 4.85. Furthermore, the ANN technique was the most suitable model for predicting and controlling UCS in treated marine clay using hybrid feature selection as conducted by previous studies (Iravanian, Kassem, & Gokcekus, 2022; Nouman Amjad Raja et al., 2021).

Table 4.39: 17th model R^2 values for different used algorithms

Algorithm	Test	Train	Validation
LR	0.948	0.995	0.989
PR	0.948	0.995	0.989
ANN	0.992	1.000	0.999
xGBoost	0.612	1.000	0.947
GBoost	0.844	1.000	0.957
RF	0.866	0.984	0.977

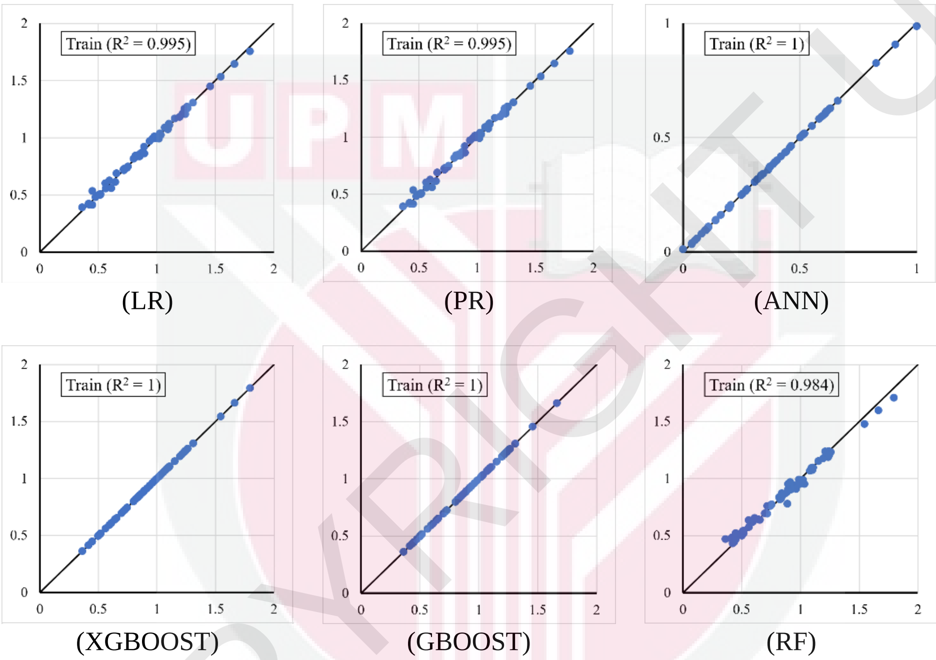

Figure 4.83: Accuracy of model 17 results for LR, PR, ANN, XGBOOST, GBOOST, and RF algorithms for training data

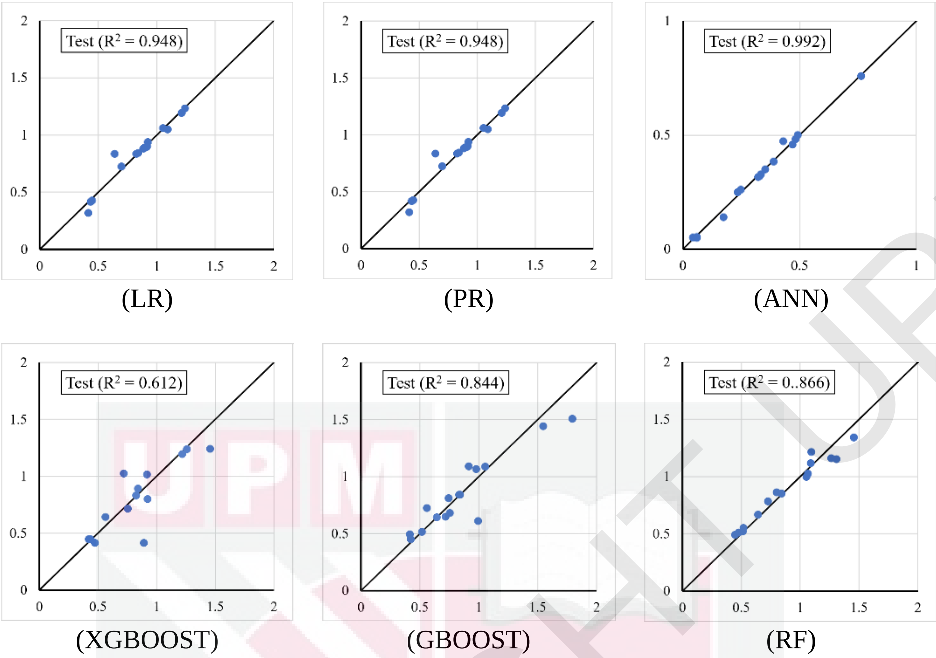

Figure 4.84: Accuracy of model 17 results for LR, PR, ANN, XGBOOST, GBOOST, and RF algorithms for testing data

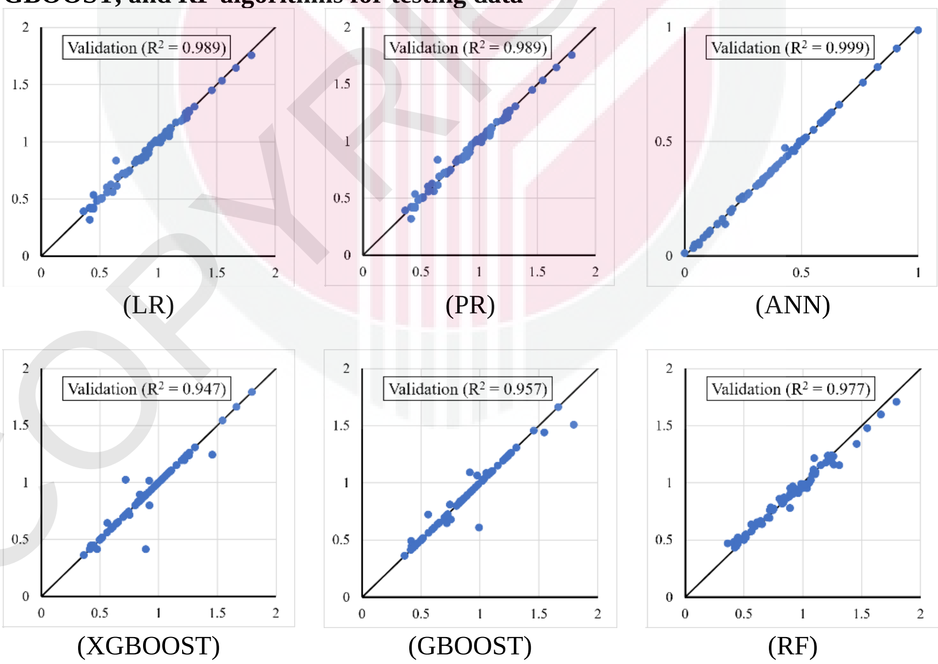

Figure 4.85: Accuracy of model 17 results for LR, PR, ANN, XGBOOST, GBOOST, and RF algorithms for validation data

Generally, hybrid algorithms produced a significant high accurate models compared to manual feature selection models. ANN algorithm is an important tool in regression and prediction of undrained shear strength and stress–strain relationship that promises various applications in future work and research for various geotechnical applications and could be used as a significant tool instead of FEM programs. However, significant research should cover this gap.

In order predict soil's undrained shear strength and stress-strain correlations, the study also used machine learning approaches. In order to forecast the mechanical properties of soil, the most significant features were determined using both automatic and manual feature selection techniques. Generally speaking, random forests (RF), gradient boosting (GBoost), extreme gradient boosting (xGBoost), and artificial neural networks (ANN) demonstrated excellent accuracy. However, the most accurate models differed based on the kind of test performed to gather the features. In most models, the accuracy of polynomial and linear regressions was low.

CHAPTER 5

CONCLUSION AND RECOMMENDATIONS

5.1. Summary

Marine clay is classified as weak soils that can experience significant deformations when loaded due to high moisture content. This can result in considerable variations in undrained shear strength and compressibility, which in turn can cause differential movement and severe damage to structures such as roads, embankments, and canal linings.

The study investigated the effect of different ratios of palm oil fly ash (POFA), lime, and calcined shale on the mechanical properties of Marine clay through a series of UU and CU triaxial tests for short–term and long–term behaviour. The results showed that an optimal ratio of 5% POFA, 5% lime, and 10% calcined shale provided the best mechanical properties, including a 4 times increment in undrained cohesion, a 50% increment in undrained internal friction angle, 6 times increment in drained cohesion, and a 90% increment in drained internal friction angle. The treated specimens also demonstrated on increased resistance to soil failure under both short–term and long–term loading conditions, making them suitable for various geotechnical applications.

In addition to the triaxial tests, one–dimensional consolidation tests were also performed, which showed a substantial decrease in soil compressibility and permeability after treatment. The Atterberg limits also showed enhancements after treatment, and the improvement increased with the increment of curing duration. The XRD analysis revealed that the treatment enhanced the formation of soil minerals, particularly the calcium silicate hydrate.

Finite element modelling was also used to simulate stress–strain relationships, which were consistent with the experimental data, although the FEM simulations showing towards normal consolidated behavior, while the experimental results were more over consolidated. As a result, FEM simulations through PLAXIS can provide preliminary design or investigation guidance, but machine learning techniques should be utilized to enhance the accuracy of the results for final work without experimental work.

The study also employed machine learning techniques to predict undrained shear strength and stress–strain relationships in soil. The manual and automated feature selection methods were used to identify the most important features for predicting the mechanical properties of soil. The most accurate models varied depending on the type of test used to obtain the features, but generally artificial neural networks (ANN), gradient boosting (GBoost), extreme gradient boosting (xGBoost), and random forest

(RF) showed high accuracy. Linear regression (LR) and polynomial regression (PR) showed low accuracy in most models.

Using the PLAXIS 2D programme, a case study of the Serdang landslide was investigated utilising treated clay sample SL5P5C10 and marine clay. The treated soil exceeded the natural soil in terms of resistance to soil collapse and deformations, and the treatment significantly improved the soil's resistance to horizontal stresses.

Overall, the study demonstrated that the inclusion of POFA and CS is an effective and promising method for improving the mechanical properties of Marine clay. The combination of triaxial tests, one–dimensional consolidation tests, finite element modelling, and machine learning techniques provided a comprehensive understanding the mechanical properties of treated Marine clay, and can be applied to other geotechnical problems in the future.

5.2. Conclusions

1. Triaxial compression tests on natural marine clay showed increased undrained deviatoric stress and internal friction angle with a 5% POFA ratio. The drained internal friction angle increased significantly for SL5P5C0–7 specimen compared to control and other specimens, while the drained cohesive strength increment was 155 to 261% more than the control specimen. However, volumetric swelling and over consolidation behavior reduced shear strength. An optimal POFA ratio of 5% was chosen for further study on lime and calcined shale ratio's effect on treated specimens' mechanical behavior.

2. The study found that the optimal lime L and calcined shale CS ratios significantly affect the mechanical properties of treated Marine clay. The optimal lime ratio was 5%, and shear strength increased with increased ratios, with peak strength at 10% calcined shale.

3. The drained cohesion of treated specimens, particularly specimen SL5P5C10, peaks with curing time, but decreases after 90 curing days to less than 50 kPa. Long-term loading specimens are more resistant to soil failure.

4. The experimental work showed that the mixture of 5% POFA, 5% lime, and 10% CS (SL5P5C10) significantly increased the shear strength of treated specimens, resulting in a 4 times increase in c_u, 50% increase in $Ø_u$, 6 times increase in c', and 90% increase in Ø'.

5. The L–POFA–CS treatment mixture significantly improved the mechanical properties of Marine clay, reducing soil compressibility and permeability. The Atterberg limits also showed enhancements, with the improvement increasing with curing duration, where compression index C_v reduced significantly from 147.5 to 3.15 m^2/yr and permeability k reduced significantly from 3.25E–08 to 6.30E–09

cm/sec after 7 curing days for SL5P5C10 treated specimens promising significant deformation resistance.

6. L–POFA–CS mixture has been proven to be an effective and promising method for improving the geotechnical properties of Marine clay. The XRD analysis showed that the treatment enhanced the formation of soil minerals, particularly calcium silicate hydrate.

7. The FEMs produced stress–strain relationships that were consistent with the experimental data, although the FEMs trended towards normal consolidated behavior, while the experimental results were more over consolidated. As a result, FEM simulations through PLAXIS can provide preliminary design or investigation guidance.

8. The study utilized manual feature selection to identify crucial features for predicting undrained shear strength and stress-strain relationship in soil using eight machine learning models, with the findings revealing the following:

    i. For predicting undrained shear strength, the best models varied depending on the type of test used to obtain the features, but generally ANN, GBoost, xGBoost, and RF showed high accuracy above 0.800 for R^2 values.

    ii. For predicting stress–strain relationship, xGBoost was the most accurate model, outperforming FEM results obtained from PLAXIS program by R^2 of 0.933, 0.845, and 0.952 for validation, test and train data respectively.

    iii. The seventh model, which used all the features, showed high accuracy for predicting undrained shear strength and is considered one of the best models in this research for the manual feature selection method, where ANN results were the most accurate by R^2 values of 0.999, 1.000, and 0.996 for validation, test and train data respectively.

    iv. The fourth model, which used features from compaction test, was the least accurate model for predicting undrained shear strength, where the test accuracy was out of the training model as R^2 values were below zero for xGBoost, RF, and LR algorithms.

    v. LR and PR showed low accuracy in most models, while GBoost, xGBoost, and RF generally showed high accuracy in training, testing, and validation, where their accuracy was higher than 0.85 for R^2 values.

9. The study utilized automated feature selection to predict undrained shear strength and stress-strain relationship in soil using nine machine learning models. The backward feature selection method was the most accurate, with genetic and forward feature selections also showing close accuracy, with R^2 values above 0.900.

10. For case study of Serdang landslide, the results showed that the treated soil SL5P5C10 showed significant resistance to soil collapse and deformations, while the natural soil showed significant drained stresses. The treatment also increased

soil resistance to horizontal stresses, decreasing stresses from 20 kN/m^2 to 2 kN/m^2.

5.3. Contribution of this work

This study assessed the improvement for long–term strength of marine clay using L–POFA–CS treatment mixture. FEM were generated using PLAXIS program showing that FEM has acceptable accuracy for the prediction and simulating CU triaxial test for L–POFA–CS treated marine clay. Assessment of machine learning applications in prediction of shear strength and stress–strain relationship for treated and untreated marine clay using L–POFA–CS mixture with a highly significant accuracy has been made. Overall, the research makes a valuable contribution to the development of innovative solutions for treating marine clay in civil engineering applications, and the proposed approach has the potential to improve the performance and sustainability of civil engineering projects using machine learning algorithms.

5.4. Recommendations

As per the limitation of this study using green materials such as POFA and calcined shale, it is recommended to investigate another green mixtures such as; coir fibers, recycled concrete, recycled aggregate, and other byproduct materials. Therefore, it is recommended to investigate these materials mixtures as follows:

1. Green fibers, such as coir fibers, effect as additional reinforcing material to the existing mixture.

2. Simulation relationship to the predicted triaxial data of future recommended green mixtures (Such as ABACUS).

3. Artificial intelligence regression/predictive models for the future recommended green mixtures.

4. Effect of temperature change on reinforced marine clay used reinforcing mixtures through this research.

5. Unsaturated behaviour of improved marine clay after using the future recommended green mixtures.

6. Saturated behaviour of improved marine clay after using the future recommended green mixtures.

7. Artificial intelligence regression/predictive models for different stress–path and/or strain path.

8. Investigation the difference between the future recommended green mixtures and the mixture used through this research.

9. Include additional factors such as cost of used reinforcing materials, marine clay source (type), and number of specimens used in feeding AI models.

10. Study the effect of other factors on the strength of treaded specimens such as zeta potential.

11. Study of the behaviour of treated marine clay on advanced clay models such as CAM Clay

BIBLIOGRAPHY

Aamir, M., Mahmood, Z., Nisar, A., Farid, A., Khan, T. A., Abbas, M., Ismaeel, M., Shah, S. A. R., & Waseem, M. (2019). Performance evaluation of sustainable soil stabilization process using waste materials. *Processes*, *7*(6).

Abbas, J. M., Ibrahim, A. M., & Shihab, A. M. (2020). Investigation to some Preliminary Geotechnical Properties of Soft Clay Stabilized by Fly Ash Based Geopolymers. *Key Engineering Materials*, *857*, 259–265.

Abdalla, A., Salih Mohammed, A., & Mohammed, A. S. (2022). Surrogate Models to Predict the Long–Term Compressive Strength of Cement–Based Mortar Modified with Fly Ash. *Archives of Computational Methods in Engineering*.

Abdi, M. R., Nakhaei, P., & Safdari Seh Gonbad, M. (2021). Prediction of Enhanced Soil–Anchored Geogrid Interactions in Direct Shear Mode Using Gene Expression Programming. *Geotechnical and Geological Engineering*, *39*(2), 957–972.

Abuel–Naga, Hossam. M., Bergado, Dennes. T., Bouazza, A., & Pender, Michael. J. (2009). Thermal conductivity of soft Bangkok clay from laboratory and field measurements. *Engineering Geology*, *105*(3–4), 211–219.

Adeboje, A. O., Bankole, S. O., Apata, A. C., Olawuyi, O. A., & Busari, A. A. (2021). Modification of Lateritic Soil with Selected Agricultural Waste Materials for Sustainable Road Pavement Construction. *International Journal of Pavement Research and Technology*.

Adi Tirta, B., Nugroho, M. A., Parahita, B., & Jaspers Focks, D.–J. J. (2018). Observational Method for More Reliable Settlement Prediction for Reclamation on the Holocene Marine Clay Deposit in Jakarta Bay. *MATEC Web of Conferences*, *147*, 07007.

Afrin, H. (2017). A Review on Different Types Soil Stabilization Techniques. *International Journal of Transportation Engineering and Technology*, *3*(2), 19.

Ahmad, A., Sutanto, M. H., Al–Bared, M. A. M., Harahap, I. S. H., Abad, S. V. A. N. K., & Khan, M. A. (2021). Physio–Chemical Properties, Consolidation, and Stabilization of Tropical Peat Soil Using Traditional Soil Additives — A State of the Art Literature Review. *KSCE Journal of Civil Engineering*, *25*(10), 3662–3678.

Ahmad, J., Abdul Rahman, A. S., Mohd Ali, M. R., & Khif, K. F. (2011). Peat soil treatment using POFA. *2011 IEEE Colloquium on Humanities, Science and Engineering, CHUSER 2011*, 66–70.

Ahmed, H. U., Mohammed, A. S., Faraj, R. H., Qaidi, S. M. A., & Mohammed, A. A. (2022). Compressive strength of geopolymer concrete modified with nano–silica: Experimental and modeling investigations. *Case Studies in Construction Materials*, *16*(March), e01036.

Akbulut, S., & Arasan, S. (2010). The Variations of Cation Exchange Capacity, pH and Zeta Potential in Expansive Soils Treated by Additives. *International Journal of Civil and Structural Engineering*, *1*(2), 139 – 154.

Alabduljabbar, H., Huseien, G. F., Sam, A. R. M., Alyouef, R., Algaifi, H. A., & Alaskar, A. (2020). Engineering properties of waste sawdust–based lightweight alkali–activated concrete: Experimental assessment and numerical prediction. *Materials*, *13*(23), 1–30.

Alagesh, T. N. (2021). *Landslide, road closure in Kinta not Cameron Highlands, clarifies Pahang MB*. https://www.nst.com.my/news/nation/2021/09/728880/landslide–road–closure–kinta–not–cameron–highlands–clarifies–pahang–mb

Al–Bared, M. A. M., & Marto, A. (2019). Evaluating the Compaction Behaviour of Soft Marine Clay Stabilized with Two Sizes of Recycled Crushed Tiles. In B. Pradhan (Ed.), *Lecture Notes in Civil Engineering* (Vol. 9, pp. 1273–1284). Springer Singapore.

Al–Bared, M. A. M., Marto, A., Harahap, I. S. H., & Kasim, F. (2018). Compaction and Plasticity Comparative Behaviour of Soft Clay Treated with Coarse and Fine Sizes of Ceramic Tiles. *E3S Web of Conferences*, *34*.

Al–Bared, M. A. M., Marto, A., & Latifi, N. (2018). Utilization of Recycled Tiles and Tyres in Stabilization of Soils and Production of Construction Materials – A State–of–the–Art Review. *KSCE Journal of Civil Engineering*, *22*(10), 3860–3874.

Aleem, M. I. A., & Arumairaj, P. D. (2012). Geopolymer concrete – a review. *International Journal of Engineering Sciences & Emerging Technologies*, *1*(2), 118–122.

Al–Mukhtar, M., Lasledj, A., & Alcover, J. F. (2010a). Behaviour and mineralogy changes in lime–treated expansive soil at 20°C. *Applied Clay Science*, *50*(2), 191–198.

Al–Mukhtar, M., Lasledj, A., & Alcover, J. F. (2010b). Behaviour and mineralogy changes in lime–treated expansive soil at 50°C. *Applied Clay Science*, *50*(2), 199–203.

Al–Swaidani, A., Hammoud, I., & Meziab, A. (2016). Effect of adding natural pozzolana on geotechnical properties of lime–stabilized clayey soil. *Journal of Rock Mechanics and Geotechnical Engineering*, *8*(5), 714–725.

Al–Tabbaa, A., & Perera, A. S. R. (2006). UK stabilization/solidification treatment and remediation – Part I: binders, technologies, testing and research. *Land Contamination & Reclamation*, *14*(1), 1–22.

Al–Taie, A. J. (2020). Improve Geotechnical Properties of Soils Using Industrial Wastes: A Review. *Civil Engineering Beyond Limits*, *1*(4), 28–34.

Al–Zboon, K., Al–Harahsheh, M. S., & Hani, F. B. (2011). Fly ash–based geopolymer for Pb removal from aqueous solution. *Journal of Hazardous Materials*, *188*(1–3), 414–421.

Amini Kiasari, M., Pakbaz, M. S., & Ghezelbash, G. R. (2018). Increasing of Soil Urease Activity by Stimulation of Indigenous Bacteria and Investigation of Their Role on Shear Strength. *Geomicrobiology Journal*, *35*(10), 821–828.

Amuda, A. G., Sahdi, F., Hasan, A., Taib, S. N. L., Boylan, N., & Mohamad, A. (2019). Measurement of Amorphous Peat Shear Strength in the Direct Shear Box at High Displacement Rates. *Geotechnical and Geological Engineering*, *37*(2), 1059–1072.

Anggraini, V., Asadi, A., Farzadnia, N., Jahangirian, H., & Huat, B. B. K. (2016). Effects of coir fibres modified with Ca(OH) 2 and Mg(OH) 2 nanoparticles on mechanical properties of lime–treated marine clay. *Geosynthetics International*, *23*(3), 206–218.

Anggraini, V., Asadi, A., Syamsir, A., & Huat, B. B. K. (2017). Three point bending flexural strength of cement treated tropical marine soil reinforced by lime treated natural fiber. *Measurement: Journal of the International Measurement Confederation*, *111*(July), 158–166.

Anggraini, V., Huat, B. B. K., Asadi, A., & Nahazanan, H. (2015). Effect of Coir Fibers on the Tensile and Flexural Strength of Soft Marine Clay. *Journal of Natural Fibers*, *12*(2), 185–200.

Aprianti S, E. (2017). A huge number of artificial waste material can be supplementary cementitious material (SCM) for concrete production – a review part II. *Journal of Cleaner Production*, *142*, 4178–4194.

Aravind, N., Nagajothi, S., & Elavenil, S. (2021). Machine learning model for predicting the crack detection and pattern recognition of geopolymer concrete beams. *Construction and Building Materials*, *297*, 123785.

Ardhira, P. J., & Sathyan, D. (2022). A comparative study of normal and self–compacting geopolymer mortar and its strength prediction using tensor flow approach. *Materials Today: Proceedings*.

ASTM. (1996). (D2435–96) Standard test method for one–dimensional consolidation properties of soils. *ASTM International*.

ASTM. (1998). (D422–63R98) Standard test method for particle–size analysis of soils. *ASTM International*.

ASTM. (2000a). (D2487–00) Standard practice for classification of soils for engineering purposes. *ASTM International*.

ASTM. (2000b). (D4220–95) Standard Practices for Preserving and Transporting Soil Samples. *ASTM International*.

ASTM. (2003a). ASTM C618 – 03: Standard Specification for Coal Fly Ash and Raw or Calcined Natural Pozzolan for Use Concrete. In *ASTM Volume 04.02: Concrete And Aggregates* (pp. 3–6). ASTM International.

ASTM. (2003b). (D4767–95) Standard Test Method for Consolidated Undrained Triaxial Compression Test for Cohesive Soils. *ASTM International*, *04*(January), 1–15.

ASTM. (2007). (D2850–03aR07) Standard Test Method for Unconsolidated–Undrained Triaxial Compression Test on Cohesive Soils. *ASTM International*.

ASTM. (2019). (D2216–19) Standard Test Methods for Laboratory Determination of Water (Moisture) Content of Soil and Rock by Mass. *ASTM International*, *January*, 1–5.

ASTM International. (2000). D854–00: Standard Test Method for Specific Gravity of Soils. *ASTM International*, *D*.

Atiş, C. D. (2003). Accelerated carbonation and testing of concrete made with fly ash. *Construction and Building Materials*, *17*(3), 147–152.

Ayininuola, G. M., & Oladotun, P. O. (2016). Geotechnical Properties of Coconut Coir Fiber Soil Mixture. *Journal of Civil Engineering Research*, *6*(4), 79–85.

Azhar, A. T. S., Nordin, N. S., Azmi, M. A. M., Embong, Z., Sunar, N., Hazreek, Z. A. M., & Aziman, M. (2018). The Physical Behavior of Stabilised Soft Clay by Electrokinetic Stabilisation Technology. *Journal of Physics: Conference Series*, *995*(1), 1—11.

Azim, M. A. M., Baizura Hamid, N., Mokhtar, M., Hudai Abdullah, N., Azhar Ahmad Tajudin, S., Shahidan, S., Abdullah, N., Ahmad Tajudin, S., Shahidan, S., Hudai Abdullah, N., Azhar Ahmad Tajudin, S., & Shahidan, S. (2021). A Review on The Binder Used to Remediate the Contaminated Soil by Stabilisation Method. *Multidisciplinary Applied Research and Innovation*, *23*(21), 7–13.

Aziz, I. H. (2022). *“Kejadian itu tanah runtuh, bukan tanah mendap.”* https://www.bharian.com.my/berita/nasional/2022/01/915888/kejadian–itu–tanah–runtuh–bukan–tanah–mendap

Balasubramaniam, A., Balasubramaniam, A. S., Cai, H., Zhu, D., Surarak, C., & N Oh, E. Y. (2010). Settlements of Embankments in Soft Soils. *Geotechnical Engineering Journal of the SEAGS & AGSSEA*, *41*(2).

Barak, S., & Sadegh, S. S. (2016). Forecasting energy consumption using ensemble ARIMA–ANFIS hybrid algorithm. *International Journal of Electrical Power and Energy Systems*, *82*, 92–104.

Baral, P., Rujikiatkamjorn, C., Indraratna, B., Leroueil, S., & Yin, J.–H. (2019). Radial Consolidation Analysis Using Delayed Consolidation Approach. *Journal of Geotechnical and Geoenvironmental Engineering*, *145*(10).

Basack, S., Siahaan, F., Indraratna, B., & Rujikiatkamjorn, C. (2018). Stone Column–Stabilized Soft–Soil Performance Influenced by Clogging and Lateral Deformation: Laboratory and Numerical Evaluation. *International Journal of Geomechanics*, *18*(6).

Basha, S. I., Aziz, A., Maslehuddin, M., Ahmad, S., Hakeem, A. S., & Rahman, M. M. (2020). Characterization, Processing, and Application of Heavy Fuel Oil Ash, an Industrial Waste Material – A Review. *The Chemical Record*, *20*(12), 1568–1595.

Behnood, A. (2018). Soil and clay stabilization with calcium– and non–calcium–based additives: A state–of–the–art review of challenges, approaches and techniques. *Transportation Geotechnics*, *17*(May), 14–32.

Bell, F. G. (1996). Lime stabilization of clay minerals and soils. *Engineering Geology*, *42*(4), 223–237.

Bergado, D. T., Jamsawang, P., Jongpradist, P., Likitlersuang, S., Pantaeng, C., Kovittayanun, N., & Baez, F. (2022). Case study and numerical simulation of PVD improved soft Bangkok clay with surcharge and vacuum preloading using a modified air–water separation system. *Geotextiles and Geomembranes*, *50*(1), 137–153.

Bhavani Chowdary, T., & Ranga Rao, V. (2022). Design and Analysis of Lightweight Alkali–Activated Slag and Fly Ash Geopolymer Mortars using ANFIS–SSO. *Iranian Journal of Science and Technology–Transactions of Civil Engineering*, *46*(2), 1211–1224.

Binal, A. (2016). The Effects of High Alkaline Fly Ash on Strength Behaviour of a Cohesive Soil. *Advances in Materials Science and Engineering*, *2016*, 12–14.

Binal, A., & Binal, B. E. (2020). Ternary Diagrams for Predicting Strength of Soil Ameliorated with Different Types of Fly Ash. *Arabian Journal for Science and Engineering*, *45*(10), 8199–8217.

Blissett, R. S. S., & Rowson, N. A. A. (2012). A review of the multi–component utilisation of coal fly ash. *Fuel*, *97*, 1–23.

Bo, M. W., Lwin, T., & Choa, V. (2019). Application of specialised in situ tests in Changi East reclamation projects, Singapore. *Geotechnical Research*, *6*(1), 3–18.

Borhan, M. N., Ismail, A., & Rahmat, R. A. (2010). Evaluation of palm oil fuel ash (POFA) on asphalt mixtures. *Australian Journal of Basic and Applied Sciences*, *4*(10), 5456–5463.

Bouazza, A., Kwan, P. S., & Chapman, G. (2004). Strength properties of cement treated Coode Island silt by the soil mixing method. *Geotechnical Engineering for Transportation Projects*, 1421–1428.

Breiman, L. (2001). *Random forests*. *7*(6), 1–33.

Breiman, L., Friedman, J. H., Olshen, R. A., & Stone, C. J. (1984). Classification and Regression Trees. In *Biometrics* (Vol. 40, Issue 3).

Brinkgreve, R. B. J., Engin, E., & Swolfts, W. M. (2012). PLAXIS 3D Material Models Manual 2012. *Plaxis Bv*.

British Standards Institution. (1996). *BS 6399–1: Loading for buildings code of practice for dead and imposed loads*.

British Standards Institution. (2021). *BS 22475–1: Technical principles for the sampling methods and of soil, rock and groundwater*.

BS1377. (1990). British Standard Methods of test for soils for civil engineering purposes. In *British Standards: Vol. Parts 1–* (Issue August).

BSI. (1990a). In–situ tests (BS1377–9). In *British Standards Institution*. British Standards Institution.

BSI. (1990b). Shear strength tests – effective stress (BS1377–8). In *British Standards Institution*. British Standards Institution.

Bumrongjaroen, W., Muller, I., Schweitzer, J., & Livingston, R. A. (2007). Application of Glass Corrosion Tests to the Reactivity of Fly Ash. *World of Coal Ash*, *January*.

Cao, X. Y., Yue, Q. Y., Song, L. Y., Li, M., & Zhao, Y. C. (2007). The performance and application of fly ash modified by PDMDAAC. *Journal of Hazardous Materials*, *147*(1–2), 133–138.

Carlson, C. L., & Adriano, D. C. (1993). Environmental Impacts of Coal Combustion Residues. *Journal of Environmental Quality*, *22*(2), 227–247.

Chai, T., & Draxler, R. R. (2014). Root mean square error (RMSE) or mean absolute error (MAE)? –Arguments against avoiding RMSE in the literature. *Geoscientific Model Development*, *7*(3), 1247–1250.

Chen, S., Zhao, Y., & Bie, Y. (2020). The prediction analysis of properties of recycled aggregate permeable concrete based on back–propagation neural network. *Journal of Cleaner Production*, *276*.

Cherian, C., Siddiqua, S., Sustainability, S. S.–, 2019, undefined, & Siddiqua, S. (2019). Pulp and Paper Mill Fly Ash: A Review. *Sustainability*, *11*(16), 4394.

Chittoori, B. C. S., Burbank, M., & Islam, M. T. (2018). Evaluating the Effectiveness of Soil–Native Bacteria in Precipitating Calcite to Stabilize Expansive Soils. *Geotechnical Special Publication*, *2018–March*(GSP 296), 59–68.

Chompoorat, T., Thepumong, T., Khamplod, A., & Likitlersuang, S. (2022). Improving mechanical properties and shrinkage cracking characteristics of soft clay in deep soil mixing. *Construction and Building Materials*, *316*(November 2021), 125858.

Chu, H.–H., Khan, M. A., Javed, M., Zafar, A., Ijaz Khan, M., Alabduljabbar, H., & Qayyum, S. (2021). Sustainable use of fly–ash: Use of gene–expression programming (GEP) and multi–expression programming (MEP) for forecasting the compressive strength geopolymer concrete. *Ain Shams Engineering Journal*, *12*(4), 3603–3617.

Chua, S., Switzer, A. D., Kearsey, T. I., Bird, M. I., Rowe, C., Chiam, K., & Horton, B. P. (2020). A new quaternary stratigraphy of the Kallang River Basin, Singapore: Implications for urban development and geotechnical engineering in Singapore. *Journal of Asian Earth Sciences*, *200*(May), 104430.

Cordoba, G., & Irassar, E. F. (2021). Sulfate performance of calcined illitic shales. *Construction and Building Materials*, *291*, 123215.

Dal, K., Cansiz, O. F., Ornek, M., & Turedi, Y. (2019). Prediction of footing settlements with geogrid reinforcement and eccentricity. *Geosynthetics International*, *26*(3), 297–308.

Damineli, B. L., Kemeid, F. M., Aguiar, P. S., & John, V. M. (2010). Measuring the eco–efficiency of cement use. *Cement and Concrete Composites*, *32*(8), 555–562.

Dao, D., Ly, H.–B. H.–B., Trinh, S. H., Le, T.–T. T.–T., Pham, B. T., Van Dao, D., Ly, H.–B. H.–B., Trinh, S. H., Le, T.–T. T.–T., & Pham, B. T. (2019). Artificial Intelligence Approaches for Prediction of Compressive Strength of Geopolymer Concrete. *Materials*, *12*(6), 983.

Dao, D., Trinh, S. H., Ly, H.–B. H.–B., Pham, B. T., Van Dao, D., Trinh, S. H., Ly, H.–B. H.–B., & Pham, B. T. (2019). Prediction of Compressive Strength of Geopolymer Concrete Using Entirely Steel Slag Aggregates: Novel Hybrid Artificial Intelligence Approaches. *Applied Sciences*, *9*(6), 1113.

Dash, S. K., & Hussain, M. (2012). Lime Stabilization of Soils: Reappraisal. *Journal of Materials in Civil Engineering*, *24*(6), 707–714.

Davidson, G. R., & Bassett, R. L. (1993). Application of boron isotopes for identifying contaminants such as fly ash leachate in groundwater. *Environmental Science & Technology*, *27*(1), 172–176.

Dehghanbanadaki, A., Khari, M., Arefnia, A., Ahmad, K., & Motamedi, S. (2019). A Study on UCS of Stabilized Peat with Natural Filler: A Computational Estimation Approach. *KSCE Journal of Civil Engineering*, *23*(4), 1560–1572.

DeJong, J. T., Fritzges, M. B., & Nüsslein, K. (2006). Microbially Induced Cementation to Control Sand Response to Undrained Shear. *Journal of Geotechnical and Geoenvironmental Engineering*, *132*(11), 1381–1392.

Duan, P., Yan, C., Zhou, W., & Ren, D. (2016). Development of fly ash and iron ore tailing based porous geopolymer for removal of Cu(II) from wastewater. *Ceramics International*, *42*(12), 13507–13518.

Ebrahimi, A., Saffari, M., Milani, D., Montoya, A., Valix, M., & Abbas, A. (2017). Sustainable transformation of fly ash industrial waste into a construction cement blend via CO2 carbonation. *Journal of Cleaner Production*, *156*, 660–669.

El–Habaak, G., Askalany, M., & Abdel–Hakeem, M. (2018). The effect of mineralogy of calcined shales on the alkali activation and geopolymerization reactions: A case study from Abu–Tartur plateau, Western Desert, Egypt. *Applied Clay Science*, *162*(June), 90–100.

Elimbi, A., Tchakoute, H. K., & Njopwouo, D. (2011). Effects of calcination temperature of kaolinite clays on the properties of geopolymer cements. *Construction and Building Materials*, *25*(6), 2805–2812.

Emmanuel, E., Lau, C. C., Anggraini, V., & Pasbakhsh, P. (2019). Stabilization of a soft marine clay using halloysite nanotubes: A multi–scale approach. *Applied Clay Science*, *173*, 65–78.

Estabragh, A. R., Khajepour, H., Javadi, A. A., & Amini, M. (2022). Effect of forced carbonation on the behaviour of a magnesia–stabilised clay soil. *International Journal of Pavement Engineering*, *23*(5), 1691–1705.

Eyo, E. U., Abbey, S. J., & Booth, C. A. (2022). Strength Predictive Modelling of Soils Treated with Calcium–Based Additives Blended with Eco–Friendly Pozzolans—A Machine Learning Approach. *Materials*, *15*(13).

Faridmehr, I., Nehdi, M. L., Huseien, G. F., Baghban, M. H., Sam, A. R. M., & Algaifi, H. A. (2021). Experimental and Informational Modeling Study of Sustainable Self–Compacting Geopolymer Concrete. *Sustainability*, *13*(13), 7444.

Faridmehr, I., Nehdi, M. L., Nikoo, M., Huseien, G. F., & Ozbakkaloglu, T. (2021). Life–cycle assessment of alkali–activated materials incorporating industrial by-products. *Materials*, *14*(9).

Faris, F. (2022). *Cracks seen at Seri Kembangan site a day after landslide*. https://www.nst.com.my/news/nation/2022/01/766629/cracks–seen–seri–kembangan–site–day–after–landslide

Farooq, F., Jin, X., Faisal Javed, M., Akbar, A., Izhar Shah, M., Aslam, F., Alyousef, R., Farooq, F., Xin, J., Javed, M. F., Akbar, A., Shah, M. I., Alyousef, R., Jin, X., Faisal Javed, M., Akbar, A., Izhar Shah, M., Aslam, F., & Alyousef, R. (2021). Geopolymer concrete as sustainable material: A state of the art review. *Construction and Building Materials*, *306*(September), 124762.

Fasihihour, N., Abad, J. M. N., Karimipour, A., & Mohebbi, M. R. (2022). Experimental and numerical model for mechanical properties of concrete containing fly ash: Systematic review. *Measurement: Journal of the International Measurement Confederation*, *188*.

Fiore, S., Dumontet, S., Huertas, F. J., & Pasquale, V. (2011). Bacteria–induced crystallization of kaolinite. *Applied Clay Science*, *53*(4), 566–571.

Gao, J., Wang, J., Wei, Y., Jiao, S., Jing, M., Gao, J., & Wang, C. (2020). Study on Treatment of Loess Landslide Based on Nanosilica and Fly Ash Composite Stabilizer Filling Fissures. *Advances in Civil Engineering*, *2020*.

Garg, N., & Skibsted, J. (2015). *Heated Montmorillonite: Structure, Reactivity, and Dissolution* (pp. 117–124).

Ghani, S., Kumari, S., Choudhary, A. K., & Jha, J. N. (2021). Experimental and computational response of strip footing resting on prestressed geotextile–reinforced industrial waste. *Innovative Infrastructure Solutions*, *6*(2), 98.

Ghorbani, B., Yaghoubi, E., & Arulrajah, A. (2021). Thermal and mechanical characteristics of recycled concrete aggregates mixed with plastic wastes: experimental investigation and mathematical modeling. *Acta Geotechnica*.

Gmür, R., Thienel, K. C., & Beuntner, N. (2016). Influence of aging conditions upon the properties of calcined clay and its performance as supplementary cementitious material. *Cement and Concrete Composites*, *72*, 114–124.

Gouw, T. L. (2020). Case Histories on the Application of Vacuum Preloading and Geosynthetic–Reinforced Soil Structures in Indonesia. *Indian Geotechnical Journal*, *50*(2), 213–237.

Grim, R. E., & others. (1962). *Applied clay mineralogy*.

Haeri, S. M., & Valishzadeh, A. (2021). Evaluation of Using Different Nanomaterials to Stabilize the Collapsible Loessial Soil. *International Journal of Civil Engineering*, *19*(5), 583–594.

Hagan, M. T., Demuth, H. B., Beale, M. H., De Jess, O., & Hagan, M. T. (1997). *Neural Network Design* (2nd ed.). PWS Publishing Co.

Hardjito, D., & Rangan, B. V. (2005). *Development and properties of low–calcium fly ash–based geopolymer concrete*.

Hassan, N., Wan Hassan, W. H., Rashid, A. S. A., Latifi, N., Mohd Yunus, N. Z., Horpibulsuk, S., & Moayedi, H. (2019). Microstructural characteristics of organic soils treated with biomass silica stabilizer. *Environmental Earth Sciences*, *78*(12), 367.

Hassett, D. J., & Eylands, K. E. (1997). Heat of hydration of fly ash as a predictive tool. *Fuel*, *76*(8 SPEC. ISS.), 807–809.

He, H., Lin, Y., Li, J., & Zhang, N. (2018). Immersed tunnel foundation on marine clay improved by sand compaction piles. *Marine Georesources and Geotechnology*, *36*(2), 218–226.

He, Z., Lin, D., Lau, T., & Wu, M. (2019). *Gradient Boosting Machine : A Survey*. 1–9.

Hebib, S., & Farrell, E. R. (2017). Some experience of stabilising Irish organic soils. In *Dry Mix Methods for Deep Soil Stabilization* (pp. 81–84). Routledge.

Hendriks, C. A., Worrell, E., Price, L., Martin, N., Ozawa Meida, L., de Jager, D., & Riemer, P. (1999). Emission reduction of greenhouse gases from the cement industry. In *Greenhouse Gas Control Technologies 4* (pp. 939–944). Elsevier.

Hewlett, P. C., & Liska, M. (2019). *Lea's Chemistry of Cement and Concrete*. Elsevier.

Hicks, R. G. (2002). Alaska Soil Stabilization Design Guide. In *State of Alaska Department of Transportation and Public Facilities Research & Technology Transfer Fairbanks, AK 99709–5399*.

Hou, P., Muzenda, T. R., Li, Q., Chen, H., Kawashima, S., Sui, T., Yong, H., Xie, N., & Cheng, X. (2021). Mechanisms dominating thixotropy in limestone calcined clay cement (LC3). *Cement and Concrete Research*, *140*(March 2020), 106316.

Hoy, M., Udomchai, A., Yeanyong, C., Horpibulsuk, S., & Arulrajah, A. (2022). Stability investigation of the flood protection structure at Nava Nakorn industrial estate, Thailand. *Engineering Failure Analysis*, *137*(March), 106279.

Hsieh, P. G., & Ou, C. Y. (2018). Mechanism of buttress walls in restraining the wall deflection caused by deep excavation. *Tunnelling and Underground Space Technology*, *82*(September), 542–553.

Huat, B. B. K. (1994). Behaviour of Soft Clay Foundation beneath an Embankment. *Pertanika Journal of Science & Technology*, *2*(October 1993), 215–235.

Hunter, D. (1988). Lime-Induced Heave in Sulfate-Bearing Clay Soils. *Journal of Geotechnical Engineering*, *114*(2), 150–167.

Huseien, G. F., Mirza, J., Hussin, M. W., & Mohd Ariffin, M. A. (2016). POTENTIAL USE COCONUT MILK AS ALTERNATIVE TO ALKALI SOLUTION FOR GEOPOLYMER PRODUCTION. *Jurnal Teknologi*, *78*(11), 133–139.

Ibrahim, H. A., & Abdul Razak, H. (2016). Effect of palm oil clinker incorporation on properties of pervious concrete. *Construction and Building Materials*, *115*, 70–77.

Iravanian, A., Kassem, Y., & Gokcekus, H. (2022). Stress–strain behavior of modified expansive clay soil: experimental measurements and prediction models. *ENVIRONMENTAL EARTH SCIENCES*, *81*(4).

Iravanian, A., Kassem, Y., & Gökçekuş, H. (2022). Stress–strain behavior of modified expansive clay soil: experimental measurements and prediction models. *Environmental Earth Sciences*, *81*(4), 107.

Ishak, S. A., & Hashim, H. (2015). Low carbon measures for cement plant – A review. *Journal of Cleaner Production*, *103*, 260–274.

Jafari, S. H., Lajevardi, S. H., Sharifipour, M., & Kamalian, M. (2021). Evaluation of small strain stiffness characteristics of soft clay treated with lime and nanosilica and correlation with UCS (q u). *Bulletin of Engineering Geology and the Environment*, *80*(4), 3163–3175.

Jang, W. Y. (2018). Behaviors of Embankment on PVD–Improved Haiphong Clay. *Soil Mechanics and Foundation Engineering*, *55*(2), 120–126.

Javdanian, H., & Lee, S. (2019). Evaluating unconfined compressive strength of cohesive soils stabilized with geopolymer: a computational intelligence approach. *Engineering with Computers*, *35*(1), 191–199.

John Lu, Z. Q. (2010). The Elements of Statistical Learning: Data Mining, Inference, and Prediction. *Journal of the Royal Statistical Society: Series A (Statistics in Society)*, *173*(3), 693–694.

John, S. K., Cascardi, A., Nadir, Y., Aiello, M. A., & Girija, K. (2021). A New Artificial Neural Network Model for the Prediction of the Effect of Molar Ratios on Compressive Strength of Fly Ash–Slag Geopolymer Mortar. *Advances in Civil Engineering*, *2021*, 1–17.

Jotisankasa, A., & Rurgchaisri, N. (2018). Shear strength of interfaces between unsaturated soils and composite geotextile with polyester yarn reinforcement. *Geotextiles and Geomembranes*, *46*(3), 338–353.

Kamaruidzaman, N. S., Talib, M. K. A., Alias, N. A., Adnan, Z., Madun, A., Abidin, H. Z., & Dan, M. F. M. (2019). Peat stabilization by using Sugarcane Bagasse Ash (SCBA) as a partial cement replacement materials. *International Journal of Integrated Engineering*, *11*(6), 204–213.

Kaniraj, S. R., & Havanagi, V. G. (2001). Behavior of Cement–Stabilized Fiber–Reinforced Fly Ash–Soil Mixtures. *Journal of Geotechnical and Geoenvironmental Engineering*, *127*(7), 574–584.

Kannan, G., Sujatha, E. R., Silicon, E. S.–, & 2021, U. (2021). A review on the Choice of Nano–Silica as Soil Stabilizer. *Silicon*.

Kavazanjian, E., Almajed, A., & Hamdan, N. (2017). Bio–Inspired Soil Improvement Using EICP Soil Columns and Soil Nails. *Grouting 2017*, 13–22.

Kee, C. G. (2016). Effects of base grouting and deep cement mixing on deep foundation bored piles at Marina Bay Financial Centre and a study on the geotechnical design parameters for deep foundation bored piles in various soil formations in Singapore. *Japanese Geotechnical Society Special Publication*, *2*(75), 2565–2570.

Keykha, H., Huat, B. B. K., & Asadi, A. (2015). Electro–biogrouting stabilisation of soft soil. *Environmental Geotechnics*, *2*(5), 292–300.

Keykha, H., Huat, B. B. K. K., & Asadi, A. (2014). Electrokinetic Stabilization of Soft Soil Using Carbonate–Producing Bacteria. *Geotechnical and Geological Engineering*, *32*(4), 739–747.

Khajeh, A., Jamshidi Chenari, R., Payan, M., Chenari, R. J., Geological, M. P.–G. and, & 2020, undefined. (2020). A Simple Review of Cemented Non–conventional Materials: Soil Composites. *Geotechnical and Geological Engineering*, *38*(2), 1019–1040.

Khalid, U., Ye, G. lin, Yadav, S. K., & Yin, Z. Y. (2019). A simple experimental method to regain the mechanical behavior of naturally structured marine clays. *Applied Ocean Research*, *88*(March), 275–287.

Khasib, I. A., & Daud, N. N. N. (2020). Physical and Mechanical Study of Palm Oil Fuel Ash (POFA) based Geopolymer as a Stabilizer for Soft Soil. *Pertanika Journal of Science and Technology*, *28*(S2), 149–160.

Kim, D., Sekhar Roy, S., Länsivaara, T., Deo, R., & Samui, P. (2018). *Handbook of Research on Predictive Modeling and Optimization Methods in Science and Engineering* (D. Kim, S. Sekhar Roy, T. Länsivaara, R. Deo, & P. Samui, Eds.). IGI Global.

Kolias, S., Kasselouri–Rigopoulou, V., & Karahalios, A. (2005). Stabilisation of clayey soils with high calcium fly ash and cement. *Cement and Concrete Composites*, *27*(2), 301–313.

Koňáková, D., Pommer, V. V. V. V., Jerman, M. M., Keppert, M., Černý, R., Vejmelková, E., Konakova, D., Pommer, V. V. V. V., Jerman, M. M., Keppert, M., Cerny, R., Vejmelkova, E., Koňáková, D., Pommer, V. V. V. V., Jerman, M. M., Keppert, M., Černý, R., & Vejmelková, E. (2022). Utilization of ceramic powder, calcined shale and sintered mullite as partial replacements of calcium aluminate cement. *Construction and Building Materials*, *326*(February), 126824.

Korpa, A., Xhaxhiu, K., Mele, A., & Spahiu, E. (2012). Contributing to Ecosystem Conservation via Utilization of Beneficiated High Carbon Fly Ash for Greener Cement …. *Journal of International Environmental Application and Science*, *7*(5), 847–857.

Kroehong, W., Sinsiri, T., Jaturapitakkul, C., & Chindaprasirt, P. (2011). Effect of palm oil fuel ash fineness on the microstructure of blended cement paste. *Construction and Building Materials*, *25*(11), 4095–4104.

Kuhn, M., & Johnson, K. (2013). Applied predictive modeling. In *Applied Predictive Modeling*.

Kumar, A., Walia, B. S., & Bajaj, A. (2007). Influence of Fly Ash, Lime, and Polyester Fibers on Compaction and Strength Properties of Expansive Soil. *Journal of Materials in Civil Engineering*, *19*(3), 242–248.

Kumar, D. R., Samui, P., & Burman, A. (2022). Prediction of Probability of Liquefaction Using Soft Computing Techniques. *Journal of The Institution of Engineers (India): Series A*, *103*(4), 1195–1208.

Kumar, V., & Kumar, A. (2018). Predicting the Settlement of Raft Resting on Sand Reinforced with Planar and Geocell Using Generalized Regression Neural Networks (GRNN) and Back Propagated Neural Networks (BPNN). *International Journal of Geosynthetics and Ground Engineering*, *4*(4).

Kurda, R., de Brito, J., & Silvestre, J. D. (2017). Influence of recycled aggregates and high contents of fly ash on concrete fresh properties. *Cement and Concrete Composites*, *84*(September), 198–213.

Lal, D., Sankar, N., & Chandrakaran, S. (2018). An artificial neural network–based model for predicting the bearing capacity of square footing on coir geotextile reinforced soil. In R. Vanchipura & K. S. Jiji (Eds.), *Emerging Trends in Engineering, Science and Technology for Society, Energy and Environment* (pp. 253–257). CRC Press.

Lam, K. P., Kou, H. lei, Xie, B., Chu, J., & He, J. (2018). Use of a Waste–Based Binder for High Water Content Soil Treatment. *Journal of Materials in Civil Engineering*, *30*(8).

Lam, K. P., Wu, S., & Chu, J. (2020). Field trial of a membraneless vacuum preloading system for soft soil improvement. *Proceedings of the Institution of Civil Engineers: Ground Improvement*, *173*(1), 40–50.

Lat, D. C., Ali, N., Jais, I. B. M. M., Baharom, B., Yunus, N. Z. M. M., Salleh, S. M., & Azmi, N. A. C. C. (2018). Compressibility characteristics of Sabak Bernam Marine Clay. *IOP Conference Series: Materials Science and Engineering*, *342*(1), 012082.

Latifi, N., Meehan, C. L., Majid, Muhd. Z. Z. A., & Horpibulsuk, S. (2016). Strengthening montmorillonitic and kaolinitic clays using a calcium–based non–traditional additive: A micro–level study. *Applied Clay Science*, *132–133*, 182–193.

Lee, E. C. (2015). Electrokinetic Improvement of Soft Clay Using Electrical Vertical Drains. In *Ground Improvement Case Histories: Chemical, Electrokinetic, Thermal and Bioengineering Methods* (Vol. 15, Issue December). Elsevier.

Lee, H. (2014). *Foundations of Applied Statistical Methods*. Springer International Publishing.

Li, D. P., Sun, T., Yao, M. S., Liu, S. Y., & Jia, H. T. (2019). Characteristic of soil CO2 emission under different plant communities in the shores of saline lake in arid region. *China Environmental Science*, *39*(5), 1879–1889.

Lin, D. F., Lin, K. L., Hung, M. J., & Luo, H. L. (2007). Sludge ash/hydrated lime on the geotechnical properties of soft soil. *Journal of Hazardous Materials*, *145*(1–2), 58–64.

Lin, S., Zheng, H., Han, C., Han, B., & Li, W. (2021). Evaluation and prediction of slope stability using machine learning approaches. *Frontiers of Structural and Civil Engineering*, *15*(4), 821–833.

Lingyu, T., Dongpo, H., Jianing, Z., & Hongguang, W. (2021). Durability of geopolymers and geopolymer concretes: A review. *Reviews on Advanced Materials Science*, *60*(1), 1–14.

Liu, H., Li, C., & Wei, H. (2009). Experimental Research on the Mechanical Parameter of Fly Ash Soil. *ICCTP 2009*, 1–8.

Liu, Y., Xiang, B., & Fu, M. (2019). Observed Performance of a Large–Scale Deep Triangular Excavation in Shanghai Soft Clays. *Geotechnical and Geological Engineering*, *37*(4), 2791–2809.

Longford, N. T. (2005). *Missing Data and Small–Area Estimation*. Springer–Verlag.

Lothenbach, B., Scrivener, K., & Hooton, R. D. (2011). Supplementary cementitious materials. *Cement and Concrete Research*, *41*(12), 1244–1256.

Mair, C., Kadoda, G., Lefley, M., Phalp, K., Schofield, C., Shepperd, M., & Webster, S. (2000). An Investigation of machine learning based prediction systems. *Journal of Systems and Software*, *53*(1), 23–29.

Majeed, Z. H., Taha, M. R., Hameed Majeed, Z., & Taha, M. R. (2012). Effect of nanomaterial treatment on geotechnical properties of a Penang soft soil. *Journal of Asian Scientific Research*, *2*(11), 587.

Marshall, C., Large, D. J., Athab, A., Evers, S. L., Sowter, A., Marsh, S., & Sjögersten, S. (2018). Monitoring tropical peat related settlement using ISBAS InSAR, Kuala Lumpur International Airport (KLIA). *Engineering Geology*, *244*(July), 57–65.

Marto, A., Mohd Yunus, N. Z., Pakir, F., Latifi, N., Mat Nor, A. H., & Tan, C. S. (2014). Stabilization of Marine Clay by Biomass Silica (Non–Traditional) Stabilizers. *Applied Mechanics and Materials*, *695*, 93–97.

McCarthy, M. J., Csetenyi, L. J., Sachdeva, A., & Dhir, R. K. (2012). Identifying the role of fly ash properties for minimizing sulfate–heave in lime–stabilized soils. *Fuel*, *92*(1), 27–36.

Md Zain, N. H., & Zulastry, M. I. (2020). *Compressive Strength of Peat Soil Treated with Waste Tyre Granules* (pp. 185–192).

Micic, S., Shang, J. Q., Lo, K. Y., Lee, Y. N., & Lee, S. W. (2001). Electrokinetic strengthening of a marine sediment using intermittent current. *Canadian Geotechnical Journal*, *38*(2), 287–302.

Mindess, S. (2019). *Developments in the Formulation and Reinforcement of Concrete*. Woodhead Publishing.

Mo, K. H., Alengaram, U. J., & Jumaat, M. Z. (2016). Structural performance of reinforced geopolymer concrete members: A review. *Construction and Building Materials*, *120*, 251–264.

Moe, K. W. S., Bo, M. W., Arulrajah, A., & Horpibulsuk, S. (2021). Stiffness parameters from cone pressuremeter tests at Changi East, Singapore. *Proceedings of the Institution of Civil Engineers: Ground Improvement*, *174*(3), 206–218.

Mohajerani, A., Hui, S.–Q. Q., Mirzababaei, M., Arulrajah, A., Horpibulsuk, S., Kadir, A. A., Rahman, M. T., Maghool, F., Rahman, T., Maghool, F., Abdul Kadir, A., Rahman, M. T., & Maghool, F. (2019). Amazing Types, Properties, and Applications of Fibres in Construction Materials. *Materials*, *12*(16), 2513.

Mohamad Ali Ridho, B. K. A. A., Ngamkhanong, C., Wu, Y., Kaewunruen, S., B K A, M. A. R., Ngamkhanong, C., Wu, Y., & Kaewunruen, S. (2021). Recycled Aggregates Concrete Compressive Strength Prediction Using Artificial Neural Networks (ANNs). *Infrastructures*, *6*(2), 17.

Mohamad, H. M., Zainorabidin, A., & Zolkefle, S. N. A. (2020). Determination of The Post–Cyclic Yield Strength and Initial Stiffness of Two Peat Soils. *International Journal of GEOMATE*, *18*(70), 172–177.

Mohamad, N., Afif Iman, M., Aziz Abdul Samad, A., Othuman Mydin, M. A., Jusoh, S., Sofia, A., Aziz, K., & Lee, B. (2019). Flexure Behaviour of Foamed Concrete Incorporating Banana Skin Powder and Palm Oil Fuel Ash Strengthened with Carbon Fibre Reinforced Plate. *IOP Conference Series: Materials Science and Engineering*, *601*(1), 012025.

Mohamed Jais, I. B., Abdullah, N., Md Ali, M. A., & Johar, M. A. (2019). Peat modification integrating Geopolymer and fly ash. *IOP Conference Series: Materials Science and Engineering*, *527*(1), 012021.

Mohammed, A. A. (2023). *Evaluation of Calcined Shale and POFA as a New Sustainable Low–Cost Reinforcement and Cementatious Materials to Enhance The Performance of Marine Clay* (Issue November). Universiti Putra Malaysia.

Mohammed, A. A., Nahazanan, H., Nasir, N. A. M., Huseien, G. F., & Saad, A. H. (2023). Calcium–Based Binders in Concrete or Soil Stabilization: Challenges, Problems, and Calcined Clay as Partial Replacement to Produce Low–Carbon Cement. *Materials*, *16*(5), 2020.

Mohd Yunus, N. Z., Marto, A., Pakir, F., Kasran, K., Jamal, M. A. A., Jusoh, S. N., & Abdullah, N. (2015). Performance of Lime–Treated Marine Clay on Strength and Compressibility Chracteristics. *International Journal of Geomate*, *8*(2), 1232–1238.

Mohd Zambri, N., & Mohd Ghazaly, Z. (2018). Peat Soil Stabilization using Lime and Cement. *E3S Web of Conferences*, *34*, 01034.

Momeni, E., Yarivand, A., Dowlatshahi, M. B., & Armaghani, D. J. (2021). An efficient optimal neural network based on gravitational search algorithm in predicting the deformation of geogrid–reinforced soil structures. *Transportation Geotechnics*, *26*(September 2020), 100446.

Montes–Hernandez, G., Pérez–López, R., Renard, F., Nieto, J. M., & Charlet, L. (2009). Mineral sequestration of CO2 by aqueous carbonation of coal combustion fly–ash. *Journal of Hazardous Materials*, *161*(2–3), 1347–1354.

Mozumder, R. A., & Laskar, A. I. (2015). Prediction of unconfined compressive strength of geopolymer stabilized clayey soil using Artificial Neural Network. *Computers and Geotechnics*, *69*, 291–300.

Mudgal, A., Sarkar, R., Sahu, A. K., & Delhi, N. (2014). Effect of Lime and Stone Dust in the. *Int. J. of GEOMATE*, *7*(2), 1033–1039.

Muhammad Nazrin Akmal, A. Z., Muthusamy, K., Mat Yahaya, F., Mohd Hanafi, H., & Nur Azzimah, Z. (2017). Utilization of fly ash as partial sand replacement in oil palm shell lightweight aggregate concrete. *IOP Conference Series: Materials Science and Engineering*, *271*(1).

Mujah, D., Rahman, M. E., & Zain, N. H. M. (2015). Performance evaluation of the soft soil reinforced ground palm oil fuel ash layer composite. *Journal of Cleaner Production*, *95*, 89–100.

Naveed, M., Duan, J., Uddin, S., Suleman, M., Hui, Y., & Li, H. (2020). Application of microbially induced calcium carbonate precipitation with urea hydrolysis to improve the mechanical properties of soil. *Ecological Engineering*, *153*, 105885.

Nayak, K., Lin, A. T. S., Huang, K. F., Liu, Z., Babonneau, N., Ratzov, G., Pillutla, R. K., Das, P., & Hsu, S. K. (2021). Clay–mineral distribution in recent deep–sea sediments around Taiwan: Implications for sediment dispersal processes. *Tectonophysics*, *814*.

Neville, A. M. (1995). Properties of concrete. In *Computational Modelling of Concrete Structures* (4th ed.). Longman Scientific and Technical.

Ng, Y. C. H., Xiao, H., Armediaz, Y., Pan, Y., & Lee, F. H. (2020). Effect of short fibre reinforcement on the yielding behaviour of cement–admixed clay. *Soils and Foundations*, *60*(2), 439–453.

Ngo, D. H., Horpibulsuk, S., Suddeepong, A., Hoy, M., Udomchai, A., Doncommul, P., Rachan, R., & Arulrajah, A. (2020). Consolidation behavior of dredged ultra–soft soil improved with prefabricated vertical drain at the Mae Moh mine, Thailand. *Geotextiles and Geomembranes*, *48*(4), 561–571.

Ngo, D. H., Horpibulsuk, S., Suddeepong, A., Samingthong, W., Udomchai, A., Doncommul, P., Arulrajah, A., & Bo, M. W. (2021). Full scale consolidation test on ultra–soft soil improved by prefabricated vertical drains in MAE MOH mine, Thailand. *Geotextiles and Geomembranes*, *49*(1), 72–80.

Nguyen, C. O., Tran, T. T., & Dao, V. T. T. (2020). Consolidation Analysis with Application of Constant Rate of Strain Consolidation Tests for Vietnam Clays. *Geotechnical and Geological Engineering*, *38*(1), 833–847.

Nik Daud, N. N., & Mohammed, A. S. (2014). Material characterization of palm oil fuel ash (POFA) mixed with granite residual soil. *Advanced Materials Research*, *955–959*, 2093–2097.

Nik Daud, N. N., Muhammed, A. S., & Kundiri, A. M. (2017). Hydraulic Conductivity of Compacted Granite Residual Soil Mixed with Palm Oil Fuel Ash in Landfill Application. *Geotechnical and Geological Engineering*, *35*(5), 1967–1976.

Nikliоć, I., Marković, S., Janković – Častvan, I., Radmilović, V. V., Karanović, L., Babić, B., & Radmilović, V. R. (2016). Modification of mechanical and thermal properties of fly ash–based geopolymer by the incorporation of steel slag. *Materials Letters*, *176*, 301–305.

Northcutt, C. G., Athalye, A., & Mueller, J. (2021). *Pervasive Label Errors in Test Sets Destabilize Machine Learning Benchmarks*. *NeurIPS*.

Ondova, M., & Stevulova, N. (2012). Benefits of fly ash utilization in concrete road cover. *Theoretical Foundations of Chemical Engineering*, *46*(6), 713–718.

Osinubi, K. J., & Nwaiwu, C. M. (2006). Compaction Delay Effects on Properties of Lime–Treated Soil. *Journal of Materials in Civil Engineering*, *18*(2), 250–258.

Parthiban, D., Vijayan, D. S., Koda, E., Vaverkova, M. D., Piechowicz, K., Osinski, P., & Duc, B. Van. (2022). Role of industrial based precursors in the stabilization of weak soils with geopolymer – A review. *Case Studies in Construction Materials*, *16*(October 2021), e00886.

Pasquale, V., Fiore, S., Hlayem, D., Lettino, A., Huertas, F. J., Chianese, E., & Dumontet, S. (2019). Biomineralization of carbonates induced by the fungi Paecilomyces inflatus and Plectosphaerella cucumerina. *International Biodeterioration & Biodegradation*, *140*, 57–66.

Pazouki, G., & Pourghorban, A. (2021). Using a hybrid artificial intelligence method for estimating the compressive strength of recycled aggregate self–compacting concrete. *European Journal of Environmental and Civil Engineering*.

Petry, T. M., & Little, D. N. (2002). Review of Stabilization of Clays and Expansive Soils in Pavements and Lightly Loaded Structures—History, Practice, and Future. *Journal of Materials in Civil Engineering*, *14*(6), 447–460.

Poulos, H. G., Lee, C. Y., & Small, J. C. (1989). Prediction of embankment performance on Malaysian marine clays. *International Symposium on Trial Embankments on Malaysian Marine Clays.*, *1987*, 22–31.

Prasad, P. S., & Ramana, G. V. (2016). Imperial smelting furnace (zinc) slag as a structural fill in reinforced soil structures. *Geotextiles and Geomembranes*, *44*(3), 406–428.

Radhakrishnan, G., & Gopalakrishnan, V. (2020). Applications of internet of things (IOT) to improve the stability of a grid connected power system using interline power flow controller. *Microprocessors and Microsystems*, *76*.

Rafieizonooz, M., Mirza, J., Salim, M. R., Hussin, M. W., & Khankhaje, E. (2016). Investigation of coal bottom ash and fly ash in concrete as replacement for sand and cement. *Construction and Building Materials*, *116*, 15–24.

Rahmat, M. N., & Ismail, N. (2018). Effect of optimum compaction moisture content formulations on the strength and durability of sustainable stabilised materials. *Applied Clay Science*, *157*, 257–266.

Rahmi, A., Taib, S. N. L., & Sahdi, F. (2018). Investigation of the Application of Various Water Additive Ratios on Unconfined Compressive Strength of Cement–Stabilized Amorphous Peat at Different Natural Moisture Contents. *Advances in Civil Engineering*, *2018*, 1–9.

Raja, M. N. A., & Shukla, S. K. (2021). Multivariate adaptive regression splines model for reinforced soil foundations. *Geosynthetics International*, *28*(4), 368–390.

Raja, N. A., & Shukla, S. K. (2021). Predicting the settlement of geosynthetic–reinforced soil foundations using evolutionary artificial intelligence technique. *Geotextiles and Geomembranes*, *49*(5), 1280–1293.

Rajakumar, C., & Reddy babu, G. (2021). Experimental study and neural network modelling of expansive sub grade stabilized with industrial waste by–products and geogrid. *Materials Today: Proceedings*, *46*(xxxx), 131–137.

Ramli, M. B., & Alonge, O. R. (2016). Characterization of metakaolin and study on early age mechanical strength of hybrid cementitious composites. *Construction and Building Materials*, *121*, 599–611.

Ranjbar, N., Mehrali, M., Alengaram, U. J., Metselaar, H. S. C., & Jumaat, M. Z. (2014). Compressive strength and microstructural analysis of fly ash/palm oil fuel ash based geopolymer mortar under elevated temperatures. *Construction and Building Materials*, *65*, 114–121.

Razali, S. N. M., Zainorabidin, A., Bakar, I., & Mohamad, H. M. (2018). Strength changes in peat–polymer stabilization process. *International Journal of Integrated Engineering*, *10*(9), 136–141.

Rendana, M., Idris, W. M. R., Rahim, S. A., Rahman, Z. A., & Lihan, T. (2021). Rubber bark dust–zeolite composite improves mechanical strength and microstructural characteristics of soft paddy soil. *Sains Tanah*, *18*(2), 194–202.

Rezazadeh Eidgahee, D., Rafiean, A. H., Haddad, A., Eidgahee, D. R., Rafiean, A. H., Haddad, A., Rezazadeh Eidgahee, D., Rafiean, A. H., & Haddad, A. (2020). A Novel Formulation for the Compressive Strength of IBP–Based Geopolymer Stabilized Clayey Soils Using ANN and GMDH–NN Approaches. *Iranian Journal of Science and Technology – Transactions of Civil Engineering*, *44*(1), 219–229.

Riedmiller, M., & Braun, H. (1993). Direct adaptive method for faster backpropagation learning: The RPROP algorithm. *1993 IEEE International Conference on Neural Networks*, 586–591.

Rogers, J., Olshansky, R., & Rogers, R. (1993). Modification of clay soils using lime. *Proceeding of the Seminar Held at Loughborough University on Lime Stabilization*, 99–114.

Saad, A. H., Nahazanan, H., Yusoff, Z. B. M., Mustafa, M., Elseknidy, M. H., & Mohammed, A. A. (2021). Evaluating Biosedimentation for Strength Improvement in Acidic Soil. *Applied Sciences*, *11*(22), 10817.

Sabat, A. K., & Moharana, R. K. (2015). Effect of compaction energy on engineering properties of fly ash –granite dust stabilized expansive soil. *International Journal of Engineering and Technology*, *7*(5), 1617–1624.

Sahu, R., Patra, C. R., Sivakugan, N., & Das, B. M. (2018). Bearing Capacity Prediction of Inclined Loaded Strip Footing on Reinforced Sand by ANN. In S. K.

Shukla & E. Guler (Eds.), *Sustainable Civil Infrastructures* (Issue 2016, pp. 97–109).

Said–Mansour, M., Kadri, E. H., Kenai, S., Ghrici, M., & Bennaceur, R. (2011). Influence of calcined kaolin on mortar properties. *Construction and Building Materials*, *25*(5), 2275–2282.

Salih, M. A., Farzadnia, N., Abang Ali, A. A., & Demirboga, R. (2015). Development of high strength alkali activated binder using palm oil fuel ash and GGBS at ambient temperature. *Construction and Building Materials*, *93*, 289–300.

Sapar, N. I. F., Matlan, S. J., Mohamad, H. M., Alias, R., & Ibrahim, A. (2020). A Study on Physical and Morphological Characteristics of. *International Journal of Advanced Research in Engineering and Technology*, *11*(11), 542–553.

Sarah, D., & Soebowo, E. (2018). Land subsidence threats and its management in the North Coast of Java. *IOP Conference Series: Earth and Environmental Science*, *118*(1).

Schweiger, H. F. (2002). Some remarks on pore pressure parameter A and B in undrained analyses with the Hardening Soil Model. *Plaxis Bulletin*, *12*, 6–9.

Schweiger, H. F. (2009). Influence of constitutive model and EC7 design approach in FE analysis of deep excavations. *Proceeding of ISSMGE International Seminar on Deep Excavations and Retaining Structures, Budapest*, 99–114.

Senol, A., Etminan, E., Y. Ozudogru, T., & Yildirim, H. (2011). Stabilization of a Low Plasticity Clay Soil by Alternative Materials. *International Symposium on Advances in Ground Technology & Geo–Information*, *June 2016*, 271–277.

Seraj, S., Cano, R., Ferron, R. P., Juenger, M. C. G. G., Natural, Á., & Calcined, Á. (2015). Calcined Shale as Low Cost Supplementary Cementitious Material. In *RILEM Bookseries* (Vol. 10, pp. 531–537). Springer, Dordrecht.

Shah, S. A. R., Mahmood, Z., Nisar, A., Aamir, M., Farid, A., & Waseem, M. (2020). Compaction performance analysis of alum sludge waste modified soil. *Construction and Building Materials*, *230*, 116953.

Shariatmadari, N., Hasanzadehshooiili, H., Ghadir, P., Saeidi, F., & Moharami, F. (2021). Compressive Strength of Sandy Soils Stabilized with Alkali–Activated Volcanic Ash and Slag. *Journal of Materials in Civil Engineering*, *33*(11), 04021295.

Sheikh, I. R., Wani, K. M. N. S., Jalal, F. E., & Shah, M. Y. (2022). An Investigation on the Behaviour of Geosynthetic Reinforced Quarry Waste Bases (QWB) Under Vertical loading. *Environmental Science and Pollution Research*, *29*(28), 43385–43400.

Shen, S.–L., Wu, H.–N., Cui, Y.–J., & Yin, Z.–Y. (2014). Long–term settlement behaviour of metro tunnels in the soft deposits of Shanghai. *Tunnelling and Underground Space Technology*, *40*(2014), 309–323.

Sherwood, P. T. (1993). Soil Stabilization with Cement and Lime: State–of–the–Art Review. In *Trl State of the Art Review*.

Soleimanbeigi, A., & Hataf, N. (2006). Prediction of settlement of shallow foundations on reinforced soils using neural networks. *Geosynthetics International*, *13*(4), 161–170.

Sprent, P., & Smeeton, N. C. (2004). *Applied nonparametric statistical methods* (3rd ed.). Chapman & Hall.

Stegemann, J. A., & Buenfeld, N. R. (2003). Prediction of unconfined compressive strength of cement paste containing industrial wastes. *Waste Management*, *23*(4), 321–332.

Sumanth Kumar, B., Sen, A., & Rama Seshu, D. (2020). *Shear Strength of Fly Ash and GGBS Based Geopolymer Concrete* (pp. 105–117).

Surarak, C., Likitlersuang, S., Wanatowski, D., Balasubramaniam, A., Oh, E., & Guan, H. (2012). Stiffness and strength parameters for hardening soil model of soft and stiff Bangkok clays. *Soils and Foundations*, *52*(4), 682–697.

Tajudin, S. A. A., Nordin, N. S., Marto, A., Madun, A., Mohd Hazreek Zainal Abidin5, I. J., Azmi, M. A. M. M., & Ahmad Tajudin1, S. A. (2016). the Monitoring and Cementation Behavior of Electrokinetic Stabilisation Technique on Batu Pahat Marine Clay. *International Journal of Geomate*, *11*(26), 2581–2588.

Tamizi, S. M., Al Bakri, A. M. M., Kamarudin, H., Ruzaidi, C. M., Liyana, J., & Aeslina, A. K. (2013). Feasibility Study on Composition and Mechanical Properties of Marine Clay Based Geopolymer Brick. *Key Engineering Materials*, *594–595*(JANUARY 2014), 401–405.

Tan, Y. C., Gue, S. S., Ng, H. B., & Lee, P. T. (2004). Some Geotechnical Properties of Klang Clay. *Proc. of Malaysian Geotechnical Conference*, 179–186.

Tang, J., Zheng, C., Liu, Z., Li, L., & Li, X. (2021). Simulation of microbial enhanced recycled aggregate preparation system based on artificial intelligence and embedded processor. *Microprocessors and Microsystems*, *80*(December 2020), 103620.

Tangchirapat, W., Tangpakasit, J., Waew–kum, S., & Jaturapitakkul, C. (2003). A new pozzolanic material from palm oil fuel ash. *KMUTT Research and Development Journal*, *26*(4), 459–474.

Tate, R. B., Tan, D. N. K., & Ng, T. F. (Eds.). (2008). *Geological Map of Peninsular Malaysia* (Issue December). Geological Society of Malaysia & University Malaya.

Teerawattanasuk, C., & Voottipruex, P. (2019). Comparison between cement and fly ash geopolymer for stabilized marginal lateritic soil as road material. *International Journal of Pavement Engineering*, *20*(11), 1264–1274.

Thomas, B. S., Kumar, S., & Arel, H. S. (2017). Sustainable concrete containing palm oil fuel ash as a supplementary cementitious material – A review. *Renewable and Sustainable Energy Reviews*, *80*(July 2016), 550–561.

Thomas, S., Chandrakaran, S., & Sankar, N. (2022). Nanocomposites are state–of–the–art in the field of ground improvement– a review. *Materials Today: Proceedings*, *xxxx*.

Tironi, A., Castellano, C. C., Bonavetti, V. L., Trezza, M. A., Scian, A. N., & Irassar, E. F. (2014). Kaolinitic calcined clays – Portland cement system: Hydration and properties. *Construction and Building Materials*, *64*, 215–221.

Tironi, A., Trezza, M. A., Scian, A. N., & Irassar, E. F. (2012). Kaolinitic calcined clays: Factors affecting its performance as pozzolans. *Construction and Building Materials*, *28*(1), 276–281.

Tironi, A., Trezza, M. A., Scian, A. N., & Irassar, E. F. (2013). Assessment of pozzolanic activity of different calcined clays. *Cement and Concrete Composites*, *37*(1), 319–327.

Toyeb, M., Hakam, A., Fauzan, F., & Andriani, A. (2023). Palm Oil Fuel Ash (Pofa) As Agro–Waste To Modern Stabilization on Subgrade. *Jurnal Teknik Sipil*, *12*(2), 165–171.

Tran–Nguyen, H.–H., Kitazume, M., Luong, B. T., & Bui, T. T. (2014). Laboratory investigation on An Giang soil mixed with dry cement. *Malaysian Journal of Civil Engineering*, *26*(1), 77–88.

Trümer, A., Ludwig, H.–M. M., Schellhorn, M., & Diedel, R. (2019). Effect of a calcined Westerwald bentonite as supplementary cementitious material on the long–term performance of concrete. *Applied Clay Science*, *168*(October 2018), 36–42.

Tsai, F. (2010). *Prediction of Reflection Cracking in Hot Mix Asphalt Overlays*. Texas A&M University.

Turan, C. C., Javadi, A., Consoli, N. C., Turan, C. C., Vinai, R., Cuisinier, O., Russo, G., Turan, C. C., Javadi, A., Consoli, N. C., Turan, C. C., Vinai, R., Cuisinier, O., & Russo, G. (2019). Mechanical properties of calcareous fly ash stabilized soil. *Eurocoalash 2019*, *1*, 184–194.

Turner, L. K., & Collins, F. G. (2013). Carbon dioxide equivalent (CO2–e) emissions: A comparison between geopolymer and OPC cement concrete. *Construction and Building Materials*, *43*, 125–130.

Tyagi, A., Xiao, H. W., Chin, K. G., & Lee, F. H. (2019). Model for predicting the unit weight of cement–treated soils. *Soils and Foundations*, *59*(6), 1921–1932.

Tyugu, E. Kh. (Ėnn K., & Enn. (2007). *Algorithms and architectures of artificial intelligence*. IOS Press.

Van Paassen, L. A., Ghose, R., Van der Linden, T. J. M., Van der Star, W. R. L., & Van Loosdrecht, M. C. M. (2010). Quantifying Biomediated Ground Improvement by Ureolysis: Large–Scale Biogrout Experiment. *Journal of Geotechnical and Geoenvironmental Engineering*, *136*(12), 1721–1728.

Van Paassen, L. A., Harkes, M. P., Van Zwieten, G. A., Van Der Zon, W. H., Van Der Star, W. R. L. L. L., & Van Loosdrecht, M. C. M. M. M. (2009). Scale up of BioGrout: A biological ground reinforcement method. *Proceedings of the 17th International Conference on Soil Mechanics and Geotechnical Engineering: The Academia and Practice of Geotechnical Engineering*, *3*(January 2009), 2328–2333.

Vejmelková, E., Koňáková, D., Doleželová, M., Scheinherrová, L., Svora, P., Keppert, M., Reiterman, P., & Černý, R. (2018). Effect of calcined Czech claystone on the properties of high performance concrete: Microstructure, strength and durability. *Construction and Building Materials*, *168*, 966–974.

Wahab, N., Talib, M. K. B. A., Xin, C. J., Basri, K., Leh, F. L. N., & Rashid, A. S. A. (2021). Performance of palm oil fuel ash (Pofa) in peat soil stabilization. *Malaysian Construction Research Journal*, *13*(SUPPL.2), 197–211.

Wang, H., Pan, X., Zhang, S., & Zhang, P. (2021). Simulation analysis of implementation effects of construction and demolition waste disposal policies. *Waste Management*, *126*, 684–693.

Wang, H., Wu, S., Qi, X., & Chu, J. (2021). Site characterization of reclaimed lands based on seismic cone penetration test. *Engineering Geology*, *280*.

Wang, J., Ban, H., Teng, X., Wang, H., & Ladwig, K. (2006). Impacts of pH and ammonia on the leaching of Cu(II) and Cd(II) from coal fly ash. *Chemosphere*, *64*(11), 1892–1898.

Wang, L., Chen, S. S., Tsang, D. C. W. W., Poon, C. S., & Shih, K. (2016). Value–added recycling of construction waste wood into noise and thermal insulating cement–bonded particleboards. *Construction and Building Materials*, *125*, 316–325.

Wang, S., Adekunle, A., Tartakovsky, B., & Raghavan, V. (2021). Synthesizing developments in the usage of solid organic matter in microbial fuel cells: A review. *Chemical Engineering Journal Advances*, *8*, 100140.

Wang, X. (2021). Optimization Design of Green Building Landscape Space Environment Based on VR Virtual Technology. *Journal of Physics: Conference Series*, *1852*(3).

Wang, Y.–K. K., Guo, L., Gao, Y.–F. F., Qiu, Y., Hu, X.–Q. Q., & Zhang, Y. (2016). Anisotropic Drained Deformation Behavior and Shear Strength of Natural Soft Marine Clay. *Marine Georesources and Geotechnology*, *34*(5), 493–502.

Wang, Z. S. (2011). Influence of fly ash on the mechanical properties of frame concrete. *Sustainable Cities and Society*, *1*(3), 164–169.

Whiffin, V. S., van Paassen, L. A., & Harkes, M. P. (2007). Microbial Carbonate Precipitation as a Soil Improvement Technique. *Geomicrobiology Journal*, *24*(5), 417–423.

White, D. J., Harrington, D., & Thomas, Z. (2005). Fly Ash Soil Stabilization for Non–Uniform Subgrade Soils, Volume I: Engineering Properties and Construction Guidelines. In *Iowa Department of Transportation (IHRB Project TR–461): Vol. I* (Issue April).

Wild, S., Khatib, J. M., & O'Farrell, M. (1997). Sulphate resistance of mortar, containing ground brick clay calcined at different temperatures. *Cement and Concrete Research*, *27*(5), 697–709.

Woolard, C. D., Strong, J., & Erasmus, C. R. (2003). Erratum: Evaluation of the use of modified coal ash as a potential sorbent for organic waste streams (Applied Geochemistry (2002) 17 (1159–1164). *Applied Geochemistry*, *18*(8), 1279.

Xia, C., He, X., Li, Y., & others. (2000). Comparative sorption studies of toxic ocresol on fly ash and impregnated fly ash. *Technol. Equip. Environ. Pollut. Control*, *2*, 82–86.

Xu, G., Zhang, J., Liu, H., & Ren, C. (2018). Shanghai center project excavation induced ground surface movements and deformations. *Frontiers of Structural and Civil Engineering*, *12*(1), 26–43.

Xu, H., & Van Deventer, J. S. J. (2000). The geopolymerisation of alumino–silicate minerals. *International Journal of Mineral Processing*, *59*(3), 247–266.

Xue, Z., Tang, X., & Yang, Q. (2017). Influence of voltage and temperature on electro–osmosis experiments applied on marine clay. *Applied Clay Science*, *141*, 13–22.

Yaghoubi, M., Arulrajah, A., Disfani, M. M., Horpibulsuk, S., Darmawan, S., & Wang, J. (2019). Impact of field conditions on the strength development of a geopolymer stabilized marine clay. *Applied Clay Science*, *167*, 33–42.

Yan, W., Feng, Y. L., Yu, M. G., & Chao, Y. H. (2012). Comprehensive utilization of fly ash. *Advanced Materials Research*, *518–523*, 701–704.

Yang, Q., Ren, Y., Niu, J., Cheng, K., Hu, Y., & Wang, Y. (2018). Characteristics of soft marine clay under cyclic loading: a review. *Bulletin of Engineering Geology and the Environment*, *77*(3), 1027–1046.

Yang, Z., Zhang, Q., Shi, W., Lv, J., Lu, Z., & Ling, X. (2020). Advances in Properties of Rubber Reinforced Soil. *Advances in Civil Engineering*, *2020*, 1–16.

Yaseen, Z. M., Deo, R. C., Hilal, A., Abd, A. M., Bueno, L. C., Salcedo–Sanz, S., & Nehdi, M. L. (2018). Predicting compressive strength of lightweight foamed concrete using extreme learning machine model. *Advances in Engineering Software*, *115*(July 2017), 112–125.

Yong, L. L., Perera, S. V. A. D. N. J., Syamsir, A., Emmanuel, E., Paul, S. C., & Anggraini, V. (2019). Stabilization of a residual soil using calcium and magnesium hydroxide nanoparticles: A quick precipitation method. *Applied Sciences (Switzerland)*, *9*(20).

Yoobanpot, N., Jamsawang, P., & Horpibulsuk, S. (2017). Strength behavior and microstructural characteristics of soft clay stabilized with cement kiln dust and fly ash residue. *Applied Clay Science*, *141*, 146–156.

Young, B. A., Hall, A., Pilon, L., Gupta, P., & Sant, G. (2019). Can the compressive strength of concrete be estimated from knowledge of the mixture proportions?: New insights from statistical analysis and machine learning methods. *Cement and Concrete Research*, *115*(July 2018), 379–388.

Yu, H., Yi, Y., Yao, K., Romagnoli, A., Tan, W. L., & Chang, A. B. P. (2021). Effect of water/cement ratio on properties of cement–stabilized Singapore soft marine clay for wet deep mixing application. *International Journal of Geotechnical Engineering*, *15*(9), 1198–1205.

Yuriz, Y., Hasanah, T. N., Ismail, T. N. H. T., Normunira, N., Hassan, M., Hassan, N. N. M., Hasanah, T. N., Ismail, T. N. H. T., Normunira, N., Hassan, M., & Hassan, N. N. M. (2020). An overview of waste materials for sustainable road construction. *International Journal of Sustainable Construction Engineering and Technology*, *11*(1), 215–229.

Yusof, N. Z., Samsuddin, N. S., Hanif, M. F., & Syed Osman, S. B. (2018). Peat soils stabilization using Effective Microorganisms (EM). *IOP Conference Series: Earth and Environmental Science*, *140*(1), 012088.

Zainorabidin, A., Abdurahman, M. N., Kassim, A., Azlan, M. F. M. D., Razali, S. N., & Ab Rahman, E. S. E. (2019). Settlement behaviour of Parit Nipah peat under static embankment. *International Journal of GEOMATE*, *17*(60), 151–155.

Zeng, S., & Wang, J. (2016). Characterization of mechanical and electric properties of geopolymers synthesized using four locally available fly ashes. *Construction and Building Materials*, *121*, 386–399.

Zhang, J., & Solis, R. (2008). Fly–ash–stabilized gypsiferous soil as an embankment material. *Geotechnical Engineering for Disaster Mitigation and Rehabilitation – Proceedings of the 2nd International Conference GEDMAR08*, *1981*, 809–814.

Zhang, L., Jing, L., Wang, N., Fang, C., Shan, Z., & Li, Y. (2018). Electro–Osmotic Chemical Treatment of Marine Clayey Soil Using CaCl2 Solution. In *Proceedings of the 2nd International Symposium on Asia Urban GeoEngineering* (Issue 204379, pp. 36–48). Springer.

Zhang, M., Zhao, M., Zhang, G., Mann, D., Lumsden, K., & Tao, M. (2016). Durability of red mud–fly ash based geopolymer and leaching behavior of heavy metals in sulfuric acid solutions and deionized water. *Construction and Building Materials*, *124*, 373–382.

Zhang, Y., Wang, X., & Chen, K. (2013). Growth and Distributive Effects of Public Infrastructure Investments in China. *Economic Studies in Inequality, Social Exclusion and Well–Being*, 87–116.

Zhu, W., Yan, J., & Yu, G. (2018). Vacuum preloading method for land reclamation using hydraulic filled slurry from the sea: A case study in coastal China. *Ocean Engineering*, *152*(November 2017), 286–299.

Zimar, Z., Robert, D., Zhou, A., Giustozzi, F., Setunge, S., & Kodikara, J. (2022). Application of coal fly ash in pavement subgrade stabilisation: A review. *Journal of Environmental Management*, *312*, 114926.

APPENDICES

APPENDIX A

FIGURES AND EQUATIONS

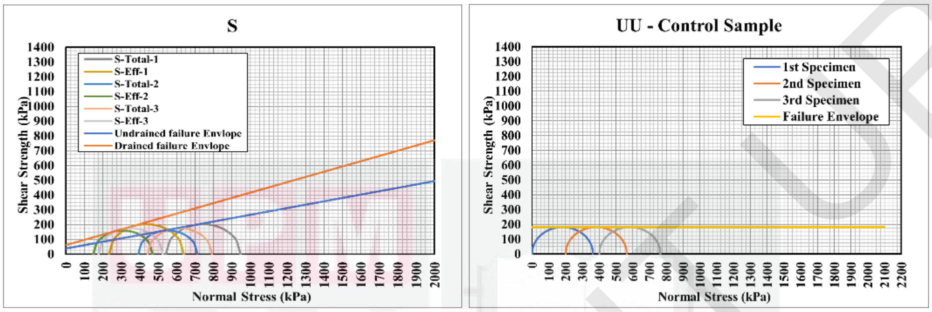

(a) (b)

Figure A.1: Results of (a) UU and (b) CU triaxial tests of sample S

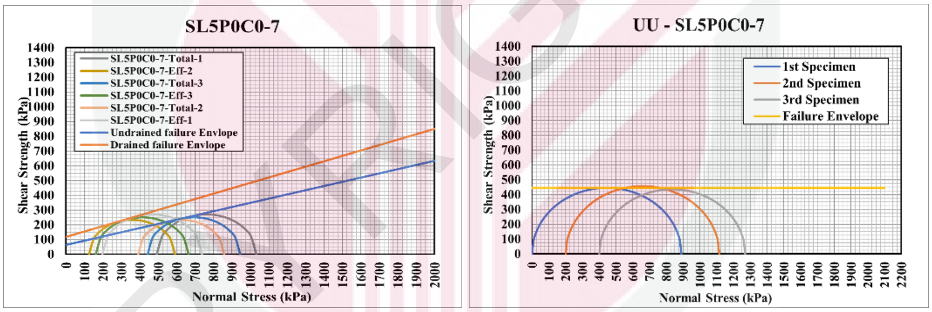

(a) (b)

Figure A.2: Results of (a) UU and (b) CU triaxial tests of sample SL5P0C0–7

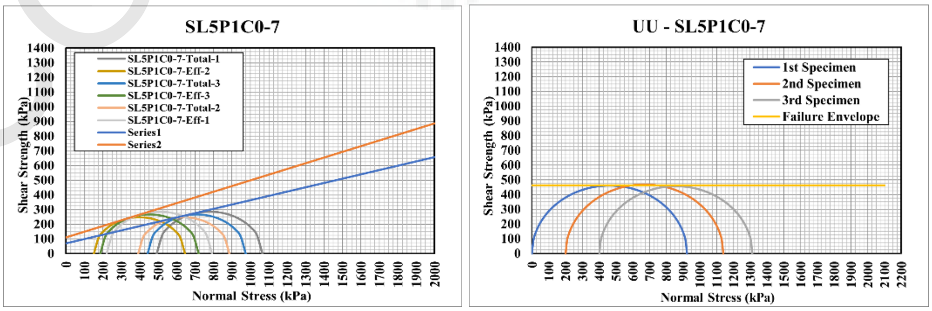

(a) (b)

Figure A.3: Results of (a) UU and (b) CU triaxial tests of sample SL5P1C0–7

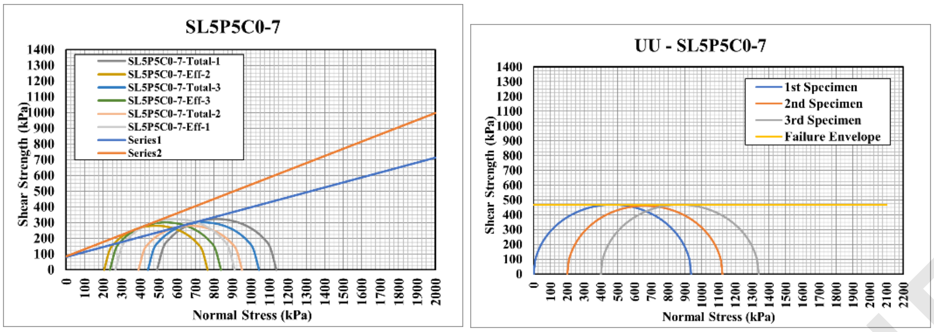

(a) (b)

Figure A.4: Results of (a) UU and (b) CU triaxial tests of sample SL5P5C0–7

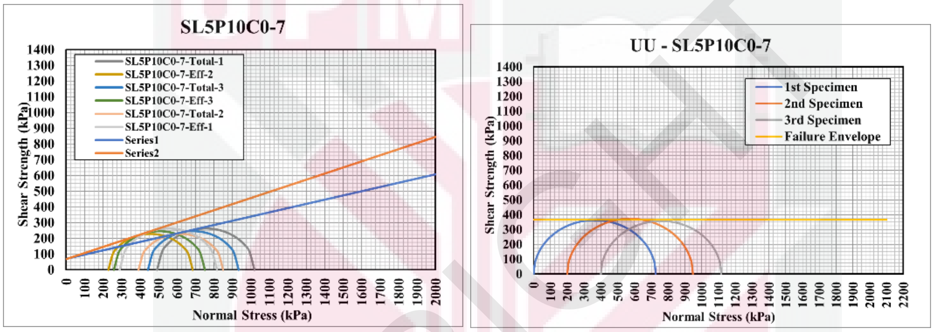

(a) (b)

Figure A.5: Results of (a) UU and (b) CU triaxial tests of sample SL5P10C0–7

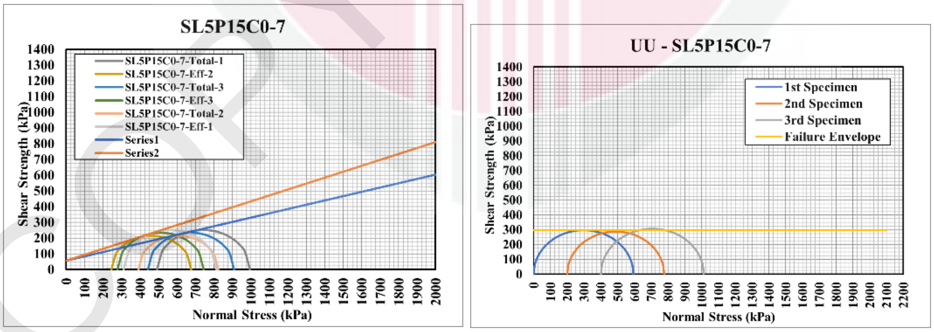

(a) (b)

Figure A.6: Results of (a) UU and (b) CU triaxial tests of sample SL5P15C0–7

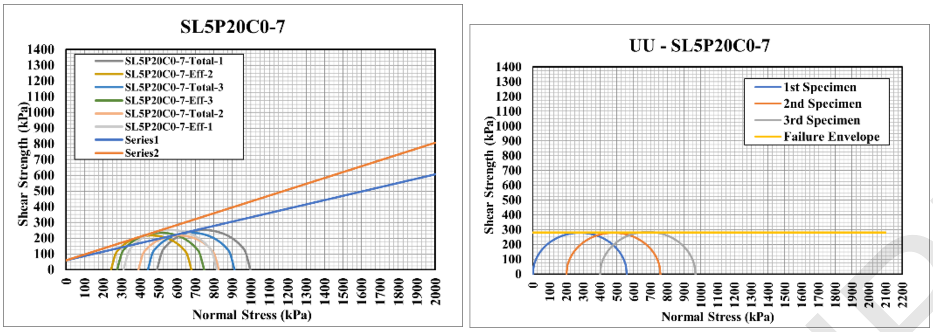

(a) (b)

Figure A.7: Results of (a) UU and (b) CU triaxial tests of sample SL5P20C0–7

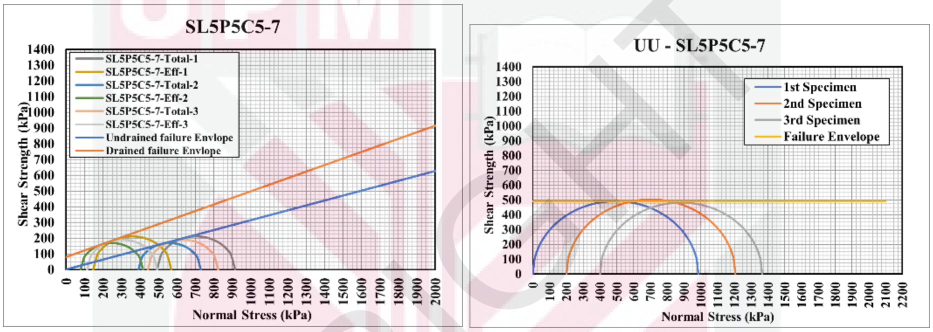

(a) (b)

Figure A.8: Results of (a) UU and (b) CU triaxial tests of sample SL5P5C5–7

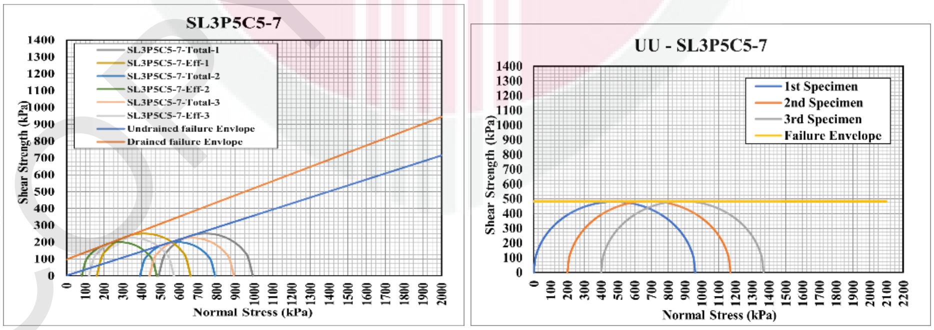

(a) (b)

Figure A.9: Results of (a) UU and (b) CU triaxial tests of sample SL3P5C5–7

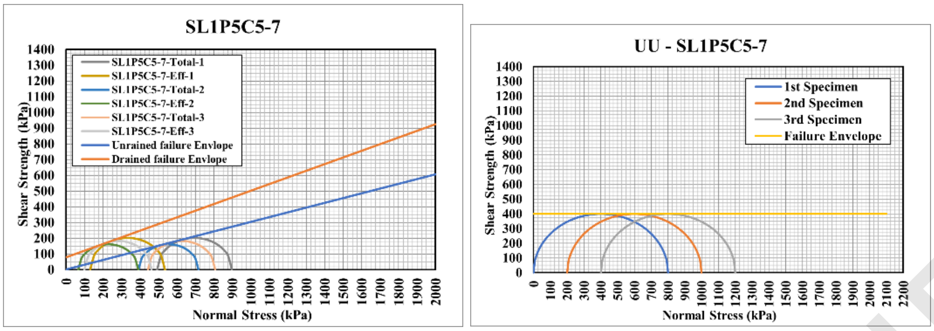

(a) (b)

Figure A.10: Results of (a) UU and (b) CU triaxial tests of sample SL1P5C5–7

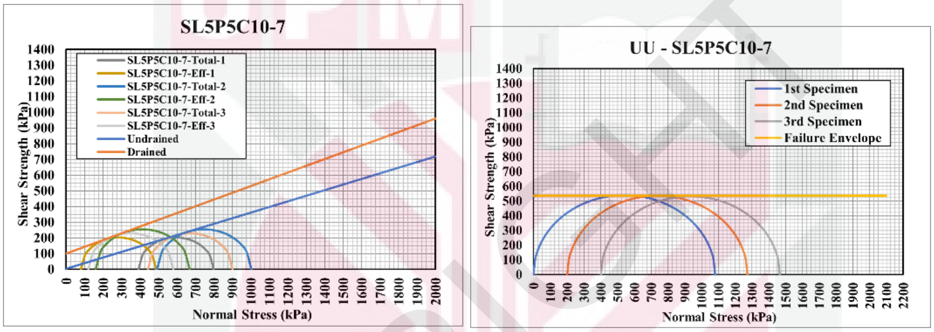

(a) (b)

Figure A.11: Results of (a) UU and (b) CU triaxial tests of sample SL5P5C10–7

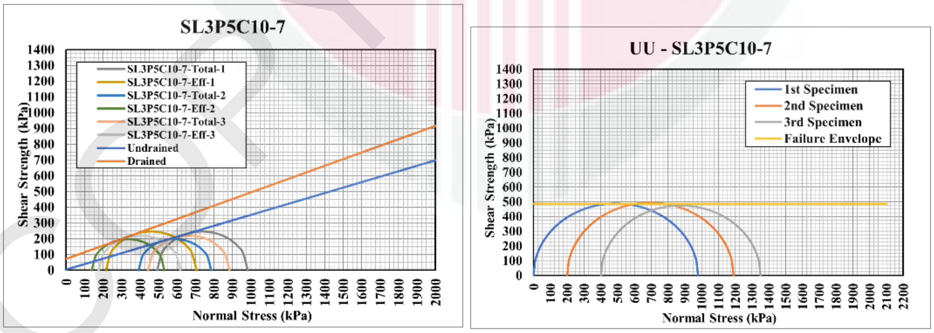

(a) (b)

Figure A.12: Results of (a) UU and (b) CU triaxial tests of sample SL3P5C10–7

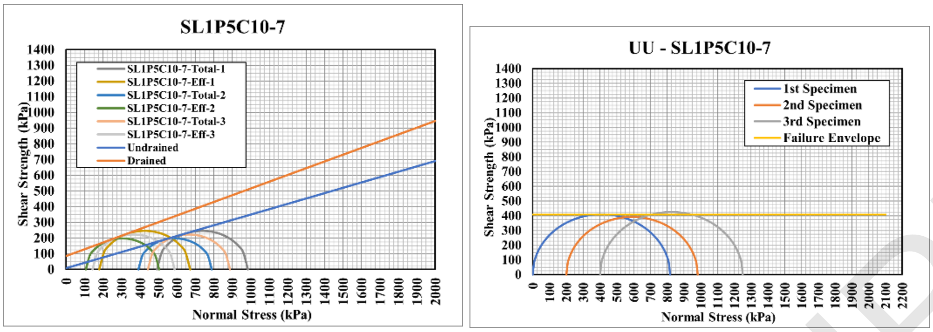

(a) (b)

Figure A.13: Results of (a) UU and (b) CU triaxial tests of sample SL1P5C10–7

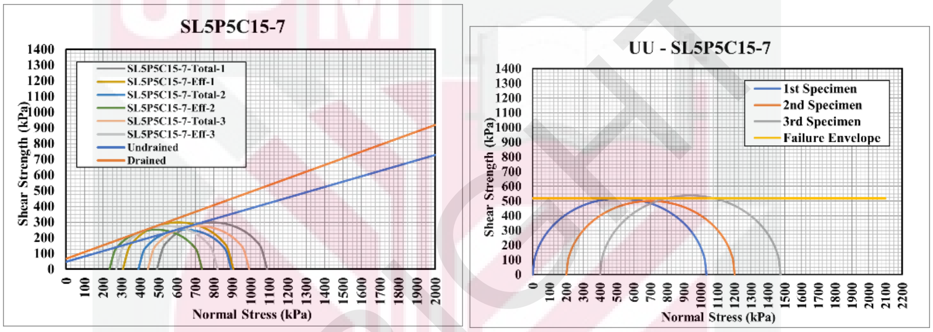

(a) (b)

Figure A.14: Results of (a) UU and (b) CU triaxial tests of sample SL5P5C15–7

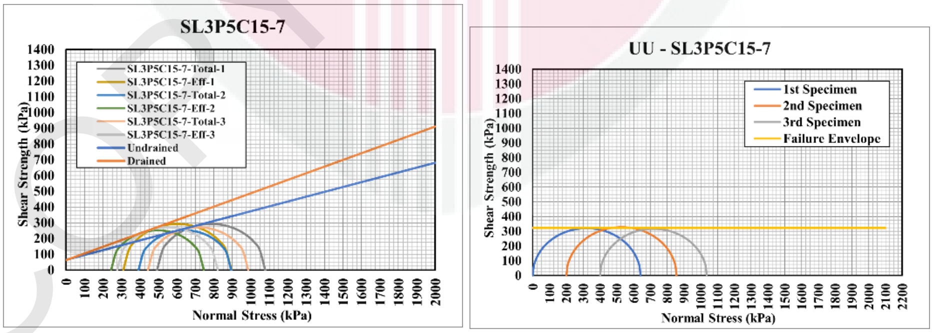

(a) (b)

Figure A.15: Results of (a) UU and (b) CU triaxial tests of sample SL3P5C15–7

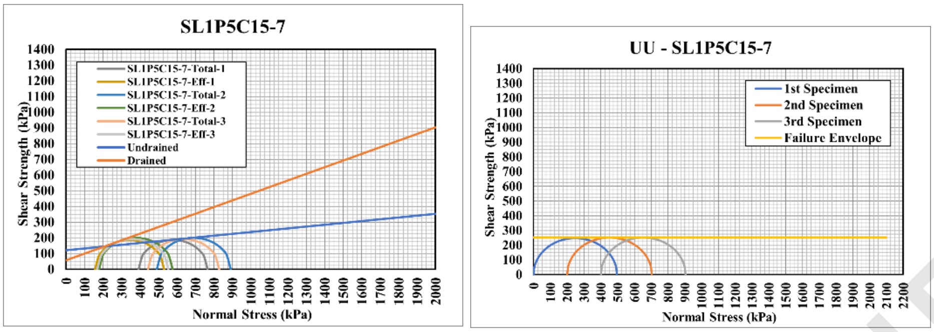

(a) (b)

Figure A.16: Results of (a) UU and (b) CU triaxial tests of sample SL1P5C15–7

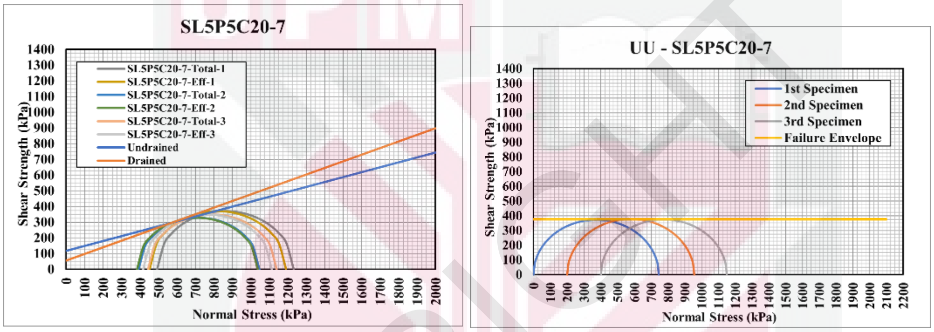

(a) (b)

Figure A.17: Results of (a) UU and (b) CU triaxial tests of sample SL5P5C20–7

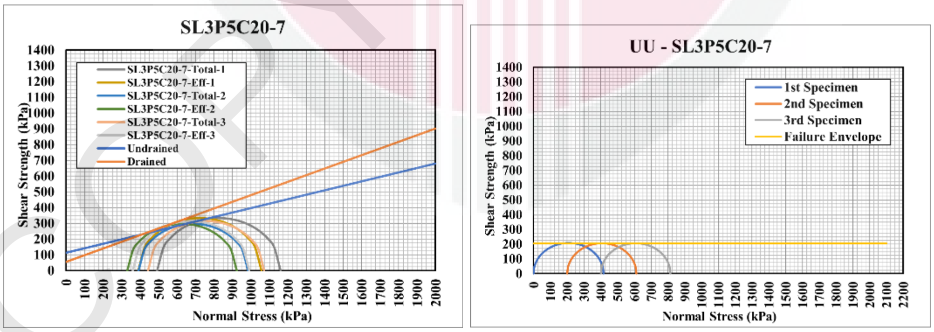

(a) (b)

Figure A.18: Results of (a) UU and (b) CU triaxial tests of sample SL3P5C20–7

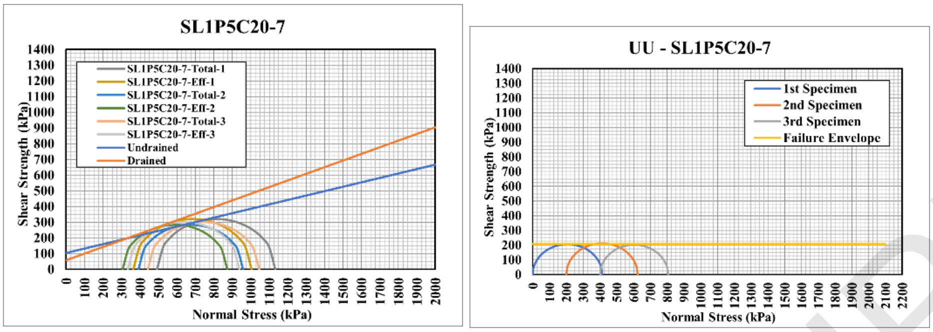

(a) (b)

Figure A.19: Results of (a) UU and (b) CU triaxial tests of sample SL1P5C20–7

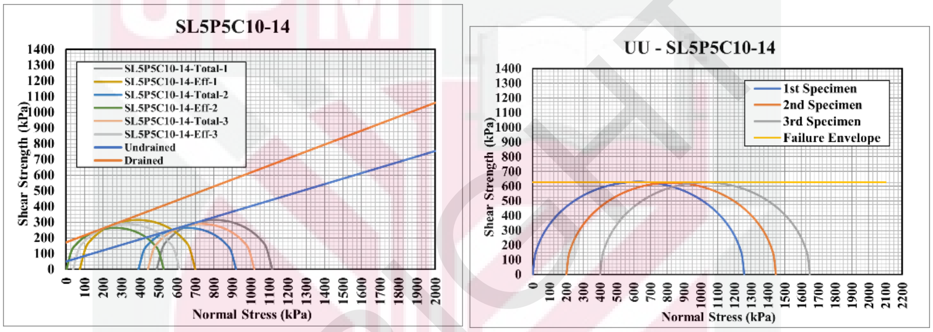

(a) (b)

Figure A.20: Results of (a) UU and (b) CU triaxial tests of sample SL5P5C10–14

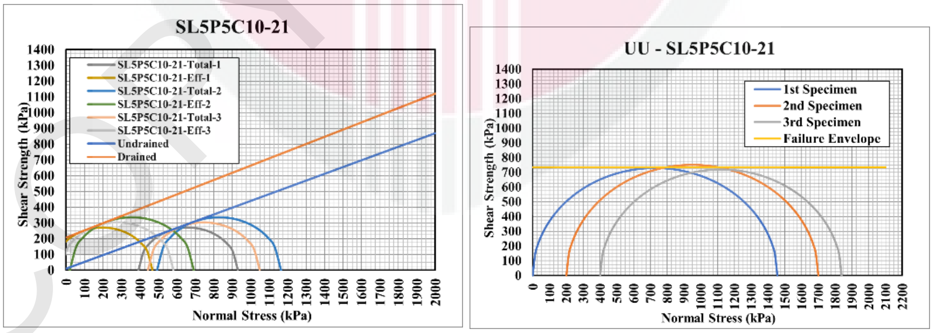

(a) (b)

Figure A.21: Results of (a) UU and (b) CU triaxial tests of sample SL5P5C10–21

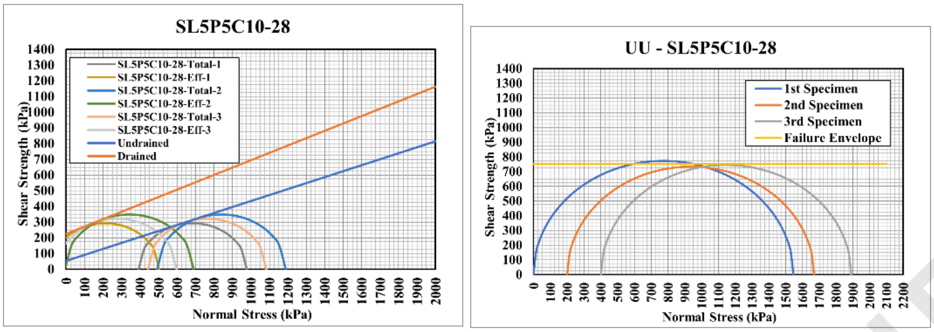

(a) (b)

Figure A.22: Results of (a) UU and (b) CU triaxial tests of sample SL5P5C10–28

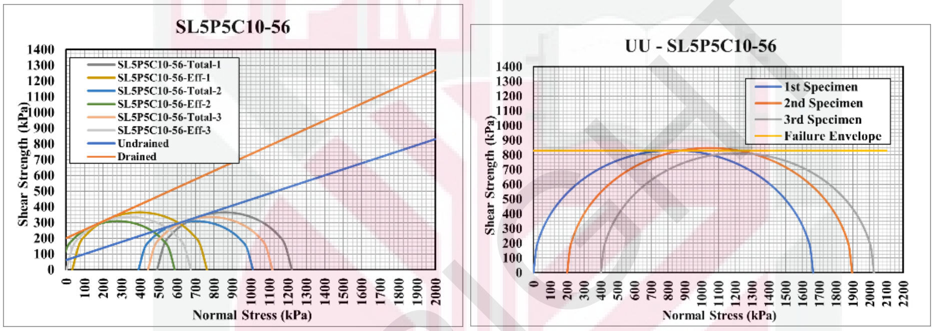

(a) (b)

Figure A.23: Results of (a) UU and (b) CU triaxial tests of sample SL5P5C10–56

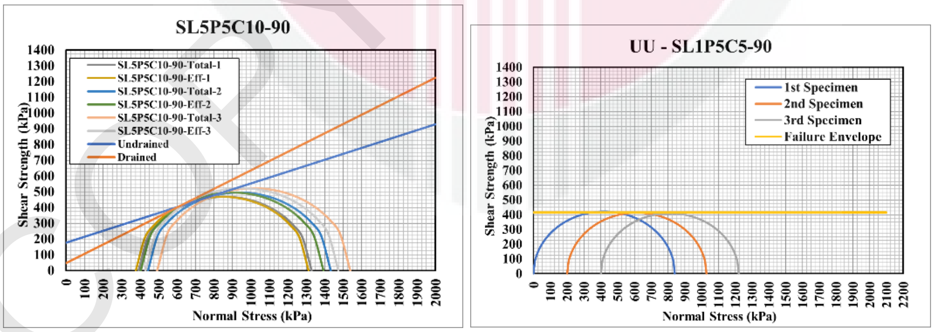

(a) (b)

Figure A.24: Results of (a) UU and (b) CU triaxial tests of sample SL5P5C10–90

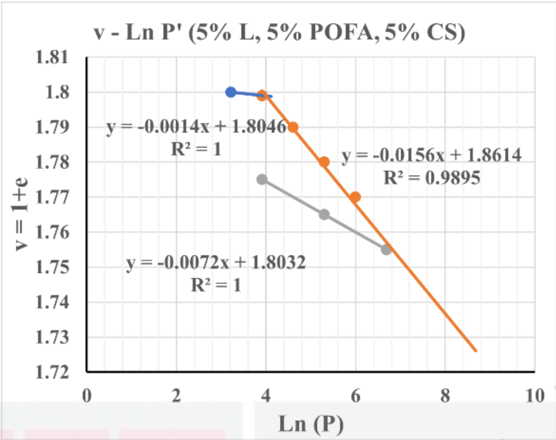

Figure A.25: Preconsolidation stress $P'C$ and specific volume μ relationship for sample SL5P5C5

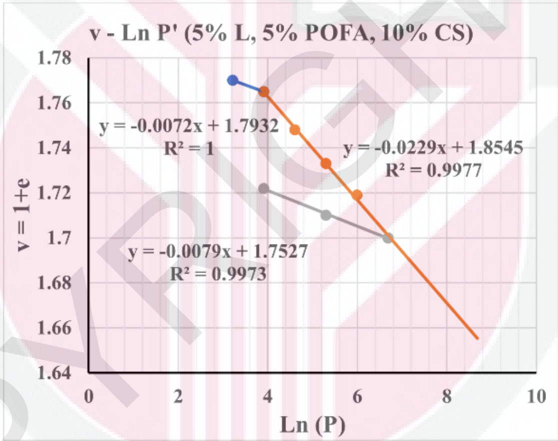

Figure A.26: Preconsolidation stress $P'C$ and specific volume μ relationship for sample SL5P5C10

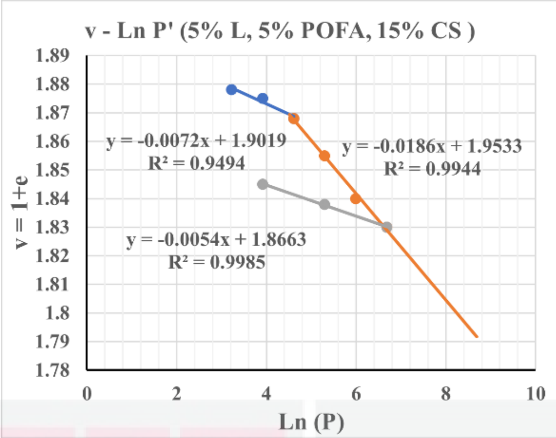

Figure A.27: Preconsolidation stress *P'C* and specific volume *μ* relationship for sample SL5P5C15

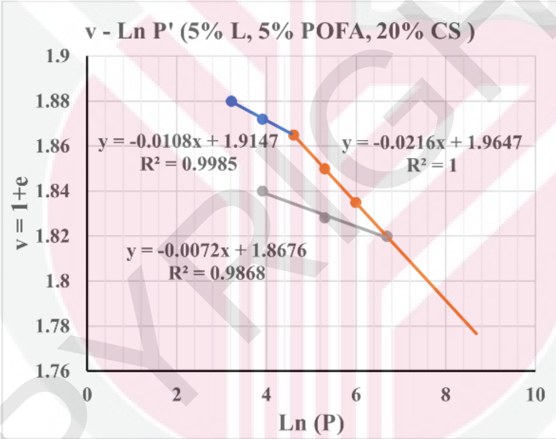

Figure A.28: Preconsolidation stress *P'C* and specific volume *μ* relationship for sample SL5P5C20

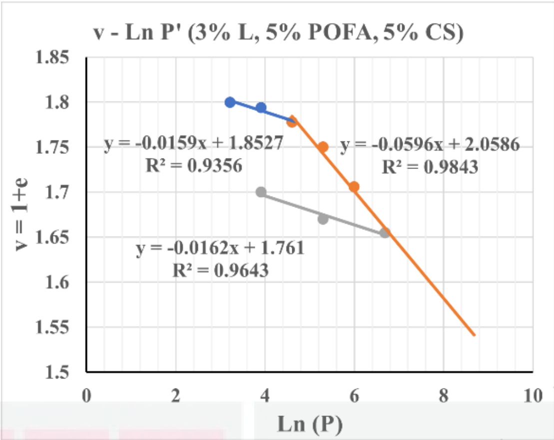

Figure A.29: Preconsolidation stress *P'C* and specific volume *μ* relationship for sample SL3P5C5

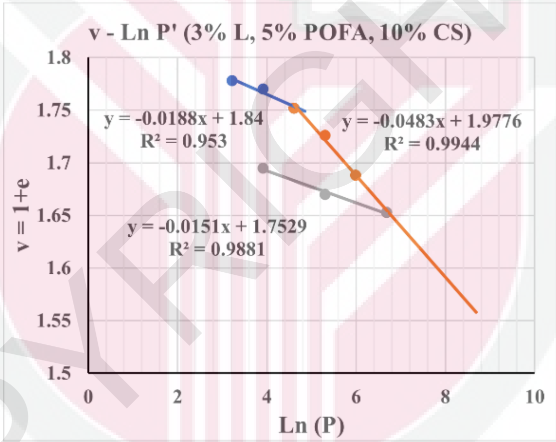

Figure A.30: Preconsolidation stress *P'C* and specific volume *μ* relationship for sample SL3P5C10

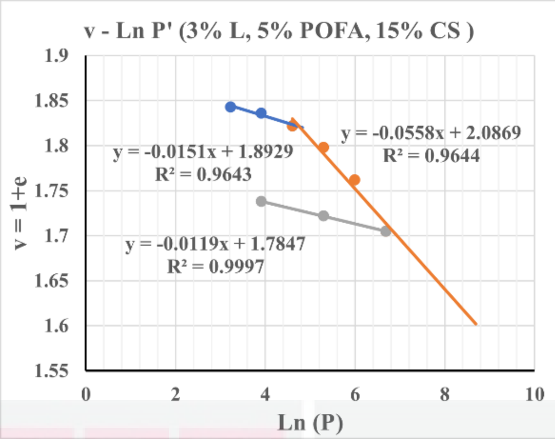

Figure A.31: Preconsolidation stress $P'C$ and specific volume μ relationship for sample SL3P5C15

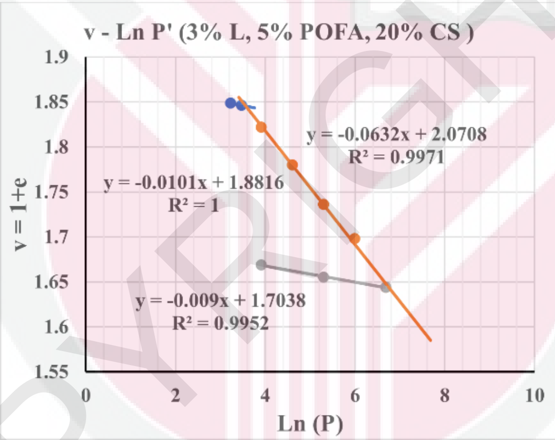

Figure A.32: Preconsolidation stress $P'C$ and specific volume μ relationship for sample SL3P5C20

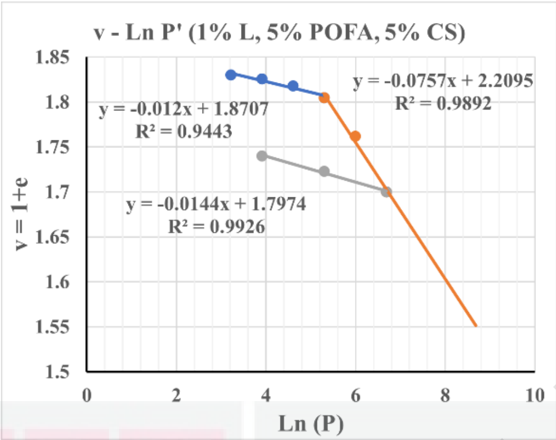

Figure A.33: Preconsolidation stress $P'C$ and specific volume μ relationship for sample SL1P5C5

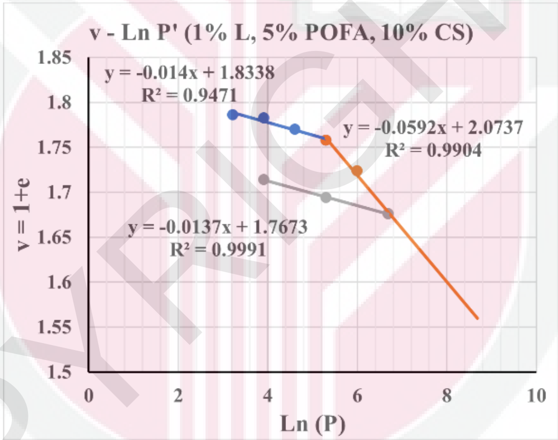

Figure A.34: Preconsolidation stress $P'C$ and specific volume μ relationship for sample SL1P5C10

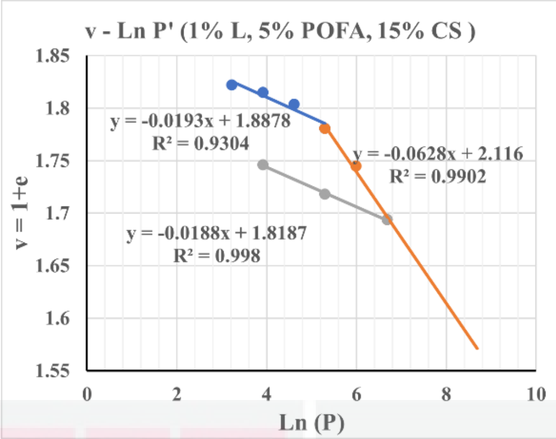

Figure A.35: Preconsolidation stress $P'C$ and specific volume μ relationship for sample SL1P5C15

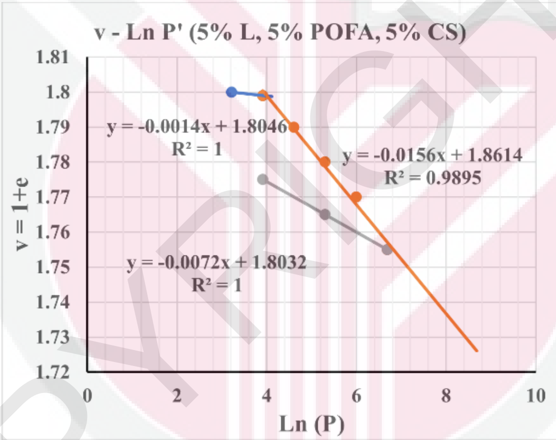

Figure A.36: Preconsolidation stress $P'C$ and specific volume μ relationship for sample SL1P5C20

APPENDIX B

TABLES

Table B.1: Collected data from current and previous research

Code	L	POFA	CS	Soil	Time	UCS	FLX	E	Load
	(%)	(%)	(%)	(%)	(days)	(MPa)	(Mpa)	(Mpa)	(N)
S	0	0	0	100	0	0.362	0.23	1.22	185.47
SL5P0C0–7	5	0	0	95	7	0.89	0.37	1.78	300.56
SL5P1C0–7	5	1	0	94	7	0.923	0.4	2.54	323.88
SL5P5C0–7	5	5	0	90	7	0.937	0.41	2.56	335.39
SL5P10C0–7	5	10	0	85	7	0.727	0.32	2.06	258.87
SL5P15C0–7	5	15	0	80	7	0.594	0.254	1.63	205.4
SL5P20C0–7	5	20	0	75	7	0.56	0.25	1.61	189.3
SL5P5C5–7	5	5	5	85	7	0.986	0.618	4.125	512.94
SL3P5C5–7	3	5	5	87	7	0.962	0.576	3.35	477.75
SL1P5C5–7	1	5	5	89	7	0.8	0.545	2.3	452.35
SL5P5C10–7	5	5	10	80	7	1.08	0.64	4.489	531.2
SL3P5C10–7	3	5	10	82	7	0.978	0.58	4.38	522.9
SL1P5C10–7	1	5	10	84	7	0.817	0.55	2.853	456.5
SL5P5C15–7	5	5	15	75	7	1.034	0.465	3.21	385.95
SL3P5C15–7	3	5	15	77	7	0.64	0.38	2.72	361.05
SL1P5C15–7	1	5	15	79	7	0.497	0.355	1.756	294.65
SL5P5C20–7	5	5	20	70	7	0.745	0.41	2.765	139.44
SL3P5C20–7	3	5	20	72	7	0.416	0.35	2.2	290.5
SL1P5C20–7	1	5	20	74	7	0.414	0.21	1.42	199.2
SL5P5C5–14	5	5	5	85	14	1.067	0.695	4.366	563.44
SL3P5C5–14	3	5	5	87	14	0.994	0.652	4.097	529.42
SL1P5C5–14	1	5	5	89	14	0.824	0.553	3.475	450.51
SL5P5C10–14	5	5	10	80	14	1.259	0.808	5.072	652.55
SL3P5C10–14	3	5	10	82	14	1.103	0.716	4.498	579.88
SL1P5C10–14	1	5	10	84	14	0.842	0.563	3.539	458.22
SL5P5C15–14	5	5	15	75	14	1.106	0.719	4.512	580.93
SL3P5C15–14	3	5	15	77	14	0.654	0.453	2.849	369.75
SL1P5C15–14	1	5	15	79	14	0.502	0.364	2.288	298.72
SL5P5C20–14	5	5	20	70	14	0.853	0.57	3.581	462.15
SL3P5C20–14	3	5	20	72	14	0.475	0.348	2.19	285.5
SL1P5C20–14	1	5	20	74	14	0.422	0.317	1.995	260.97
SL5P5C5–21	5	5	5	85	21	1.151	0.755	4.743	611.29
SL3P5C5–21	3	5	5	87	21	1.024	0.68	4.274	551.91
SL1P5C5–21	1	5	5	89	21	0.833	0.568	3.57	462.65
SL5P5C10–21	5	5	10	80	21	1.456	0.934	5.864	753.31
SL3P5C10–21	3	5	10	82	21	1.235	0.804	5.051	650.16
SL1P5C10–21	1	5	10	84	21	0.867	0.588	3.697	478.31
SL5P5C15–21	5	5	15	75	21	1.195	0.78	4.903	630.58
SL3P5C15–21	3	5	15	77	21	0.697	0.489	3.074	398.34

Table B.1: Continued

Code	L	POFA	CS	Soil	Time	UCS	FLX	E	Load
	(%)	(%)	(%)	(%)	(days)	(MPa)	(Mpa)	(Mpa)	(N)
SL1P5C15–21	1	5	15	79	21	0.512	0.38	2.39	311.69
SL5P5C20–21	5	5	20	70	21	0.918	0.618	3.885	500.74
SL3P5C20–21	3	5	20	72	21	0.51	0.379	2.383	310.01
SL1P5C20–21	1	5	20	74	21	0.435	0.335	2.107	275.17
SL5P5C5–28	5	5	5	85	28	1.239	0.816	5.131	660.64
SL3P5C5–28	3	5	5	87	28	1.053	0.707	4.447	573.88
SL1P5C5–28	1	5	5	89	28	0.841	0.583	3.666	474.83
SL5P5C10–28	5	5	10	80	28	1.545	0.996	6.257	803.16
SL3P5C10–28	3	5	10	82	28	1.263	0.83	5.218	671.4
SL1P5C10–28	1	5	10	84	28	0.884	0.608	3.826	494.71
SL5P5C15–28	5	5	15	75	28	1.219	0.804	5.056	650.04
SL3P5C15–28	3	5	15	77	28	0.716	0.51	3.208	415.45
SL1P5C15–28	1	5	15	79	28	0.517	0.393	2.474	322.37
SL5P5C20–28	5	5	20	70	28	1.017	0.686	4.315	555.4
SL3P5C20–28	3	5	20	72	28	0.562	0.42	2.642	343.02
SL1P5C20–28	1	5	20	74	28	0.448	0.352	2.22	289.55
SL5P5C5–56	5	5	5	85	56	1.243	0.858	5.404	695.28
SL3P5C5–56	3	5	5	87	56	1.093	0.771	4.856	625.82
SL1P5C5–56	1	5	5	89	56	0.841	0.623	3.927	507.99
SL5P5C10–56	5	5	10	80	56	1.663	1.105	6.949	891.13
SL3P5C10–56	3	5	10	82	56	1.309	0.898	5.65	726.21
SL1P5C10–56	1	5	10	84	56	0.893	0.654	4.12	532
SL5P5C15–56	5	5	15	75	56	1.231	0.852	5.361	688.89
SL3P5C15–56	3	5	15	77	56	0.754	0.572	3.607	466.12
SL1P5C15–56	1	5	15	79	56	0.517	0.433	2.735	355.53
SL5P5C20–56	5	5	20	70	56	1.091	0.769	4.846	622.93
SL3P5C20–56	3	5	20	72	56	0.644	0.507	3.202	414.13
SL1P5C20–56	1	5	20	74	56	0.448	0.392	2.481	322.71
SL5P5C5–90	5	5	5	85	90	1.211	0.888	5.605	720.82
SL3P5C5–90	3	5	5	87	90	1.103	0.825	5.207	670.39
SL1P5C5–90	1	5	5	89	90	0.841	0.671	4.244	548.25
SL5P5C10–90	5	5	10	80	90	1.795	1.231	7.751	993.06
SL3P5C10–90	3	5	10	82	90	1.095	0.82	5.178	666.31
SL1P5C10–90	1	5	10	84	90	0.893	0.702	4.437	572.26
SL5P5C15–90	5	5	15	75	90	1.243	0.907	5.724	734.9
SL3P5C15–90	3	5	15	77	90	0.718	0.599	3.792	489.64
SL1P5C15–90	1	5	15	79	90	0.517	0.481	3.052	395.79
SL5P5C20–90	5	5	20	70	90	0.913	0.714	4.51	580.22
SL3P5C20–90	3	5	20	72	90	0.61	0.536	3.395	438.62
SL1P5C20–90	1	5	20	74	90	0.448	0.514	3.258	421.4

Table B.1: Continued

Code	mv	Pc'	Cr	Cc	Cv	K
S	1.29E–04	147.5	0.086	0.086	0.0025	3.25E–08
SL5P0C0–7	1.26E–04	133.67	0.028	0.028	0.0017	2.18E–08
SL5P1C0–7	4.10E–05	87.67	0.0265	0.0265	0.00132	5.20E–09
SL5P5C0–7	4.00E–05	42.09	0.022	0.022	0.00121	5.00E–09
SL5P10C0–7	7.90E–05	147.47	0.0199	0.0199	0.0018	1.40E–08
SL5P15C0–7	9.80E–05	156.71	0.0255	0.0255	0.00321	3.22E–08
SL5P20C0–7	9.60E–05	75.41	0.032	0.032	0.00335	3.23E–08
SL5P5C5–7	7.40E–05	49.4	0.0099	0.0359	0.00121	7.20E–09
SL3P5C5–7	1.23E–04	109.95	0.037	0.1372	0.00128	2.19E–08
SL1P5C5–7	8.15E–05	190.57	0.0304	0.1743	0.0014	9.50E–09
SL5P5C10–7	7.10E–05	44.7	0.0174	0.0527	0.001	6.30E–09
SL3P5C10–7	1.01E–04	90.02	0.039	0.1112	0.00105	1.53E–08
SL1P5C10–7	8.08E–05	210.61	0.0319	0.1363	0.0013	9.20E–09
SL5P5C15–7	6.80E–05	99.48	0.0145	0.0428	0.00212	5.40E–09
SL3P5C15–7	1.30E–04	121.51	0.0311	0.1285	0.0018	2.40E–08
SL1P5C15–7	1.18E–04	134.29	0.0439	0.1446	0.00175	2.04E–08
SL5P5C20–7	8.50E–05	73.7	0.0207	0.0497	0.00225	1.05E–08
SL3P5C20–7	1.20E–04	36.6	0.022	0.1455	0.00249	2.10E–08
SL1P5C20–7	1.04E–04	109.95	0.0319	0.1096	0.0023	1.62E–08
SL5P5C5–14	5.75E–05	49.75	0.0237	0.0858	0.001297	7.20E–09
SL3P5C5–14	1.09E–04	110.49	0.0444	0.1713	0.001284	2.26E–08
SL1P5C5–14	9.19E–05	194.36	0.0375	0.1573	0.001372	1.76E–08
SL5P5C10–14	5.89E–05	47.72	0.0229	0.0827	0.001237	7.70E–09
SL3P5C10–14	1.12E–04	88.87	0.0421	0.1589	0.001309	2.35E–08
SL1P5C10–14	9.66E–05	216.45	0.0395	0.1689	0.001367	1.90E–08
SL5P5C15–14	6.68E–05	98.66	0.028	0.1067	0.001309	1.00E–08
SL3P5C15–14	1.25E–04	108.22	0.0303	0.1166	0.001427	2.75E–08
SL1P5C15–14	1.08E–04	111.44	0.0461	0.1779	0.001474	2.24E–08
SL5P5C20–14	7.65E–05	104.01	0.0293	0.1122	0.001253	1.30E–08
SL3P5C20–14	1.33E–04	33.9	0.0242	0.0859	0.001483	3.00E–08
SL1P5C20–14	1.14E–04	113.12	0.0465	0.1798	0.001499	2.43E–08
SL5P5C5–21	5.55E–05	48.86	0.0234	0.0844	0.001265	6.70E–09
SL3P5C5–21	1.08E–04	111.2	0.0444	0.1713	0.001294	2.23E–08
SL1P5C5–21	9.14E–05	195.06	0.0376	0.1575	0.001364	1.74E–08
SL5P5C10–21	5.49E–05	45.63	0.0221	0.0795	0.00117	6.50E–09
SL3P5C10–21	1.09E–04	86.35	0.0415	0.156	0.001348	2.26E–08
SL1P5C10–21	9.58E–05	217.73	0.0395	0.1692	0.001354	1.87E–08
SL5P5C15–21	6.48E–05	96.79	0.0276	0.1048	0.001337	9.40E–09
SL3P5C15–21	1.24E–04	107.3	0.0301	0.1157	0.001407	2.71E–08
SL1P5C15–21	1.07E–04	111.22	0.046	0.1777	0.001465	2.22E–08
SL5P5C20–21	7.50E–05	102.64	0.029	0.1108	0.00127	1.25E–08

Table B.1: Continued

Code	mv	Pc'	Cr	Cc	Cv	K
S	1.29E–04	147.5	0.086	0.086	0.0025	3.25E–08
SL3P5C20–21	1.32E–04	34.16	0.0241	0.0856	0.001467	2.97E–08
SL1P5C20–21	1.14E–04	112.85	0.0464	0.1795	0.00149	2.42E–08
SL5P5C5–28	5.36E–05	47.93	0.023	0.083	0.001232	6.10E–09
SL3P5C5–28	1.07E–04	111.9	0.0444	0.1714	0.001306	2.20E–08
SL1P5C5–28	9.09E–05	195.75	0.0376	0.1578	0.001356	1.73E–08
SL5P5C10–28	5.29E–05	44.7	0.0217	0.0781	0.001136	5.90E–09
SL3P5C10–28	1.08E–04	85.82	0.0414	0.1554	0.001361	2.24E–08
SL1P5C10–28	9.51E–05	218.77	0.0395	0.1696	0.001343	1.85E–08
SL5P5C15–28	6.40E–05	96.29	0.0274	0.1042	0.001348	9.20E–09
SL3P5C15–28	1.23E–04	106.9	0.03	0.1152	0.001396	2.69E–08
SL1P5C15–28	1.07E–04	111.12	0.046	0.1776	0.001458	2.21E–08
SL5P5C20–28	7.28E–05	100.54	0.0285	0.1086	0.001296	1.18E–08
SL3P5C20–28	1.31E–04	34.51	0.024	0.0852	0.001444	2.93E–08
SL1P5C20–28	1.13E–04	112.58	0.0464	0.1792	0.00148	2.40E–08
SL5P5C5–56	5.22E–05	47.89	0.023	0.0829	0.001209	5.70E–09
SL3P5C5–56	1.05E–04	113.55	0.0444	0.1717	0.001334	2.14E–08
SL1P5C5–56	8.96E–05	197.65	0.0378	0.1588	0.001334	1.69E–08
SL5P5C10–56	4.94E–05	43.46	0.0213	0.0763	0.001077	4.80E–09
SL3P5C10–56	1.06E–04	84.94	0.0411	0.1544	0.001397	2.17E–08
SL1P5C10–56	9.36E–05	221.14	0.0397	0.1707	0.001318	1.81E–08
SL5P5C15–56	6.24E–05	96.03	0.0274	0.104	0.001372	8.70E–09
SL3P5C15–56	1.21E–04	108.48	0.03	0.1155	0.001362	2.63E–08
SL1P5C15–56	1.06E–04	111.12	0.046	0.1776	0.001436	2.17E–08
SL5P5C20–56	7.01E–05	98.99	0.0281	0.107	0.001332	1.10E–08
SL3P5C20–56	1.28E–04	35.03	0.0238	0.0845	0.001397	2.84E–08
SL1P5C20–56	1.12E–04	112.58	0.0464	0.1792	0.001458	2.36E–08
SL5P5C5–90	5.12E–05	48.23	0.0231	0.0835	0.001191	5.40E–09
SL3P5C5–90	1.03E–04	114.97	0.0445	0.1724	0.00136	2.09E–08
SL1P5C5–90	8.80E–05	199.96	0.038	0.16	0.001307	1.64E–08
SL5P5C10–90	4.53E–05	42.06	0.0207	0.0742	0.001009	3.60E–09
SL3P5C10–90	1.08E–04	89.01	0.0422	0.159	0.001358	2.24E–08
SL1P5C10–90	9.20E–05	223.7	0.0399	0.1721	0.001291	1.76E–08
SL5P5C15–90	6.06E–05	95.77	0.0273	0.1037	0.001403	8.20E–09
SL3P5C15–90	1.20E–04	109.22	0.0302	0.1163	0.001346	2.60E–08
SL1P5C15–90	1.04E–04	111.12	0.046	0.1776	0.001409	2.12E–08
SL5P5C20–90	7.18E–05	102.74	0.029	0.1109	0.001309	1.15E–08
SL3P5C20–90	1.27E–04	35.02	0.0239	0.0848	0.00138	2.81E–08
SL1P5C20–90	1.08E–04	112.58	0.0464	0.1792	0.001392	2.24E–08

Table B.1: Continued

Code	av	CR	e	n	MDD	OMC	LL	PL
S	2.50E–04	0.0434	0.98	0.495	14.3	26	75.2	48.95
SL5P0C0–7	2.30E–04	0.0142	0.975	0.494	13.81	32	68	48.67
SL5P1C0–7	7.80E–05	0.0137	0.932	0.482	13.79	32.5	67.3	45.11
SL5P5C0–7	7.50E–05	0.012	0.841	0.457	13.76	33	62	48.24
SL5P10C0–7	1.41E–04	0.0111	0.798	0.444	13.7	34	60.3	47.95
SL5P15C0–7	1.65E–04	0.0148	0.725	0.42	13.6	34.9	61	44.89
SL5P20C0–7	1.62E–04	0.0191	0.675	0.403	13.44	35	65	52.1
SL5P5C5–7	6.00E–05	0.0199	0.805	0.446	14.59	31.5	61.3	48.95
SL3P5C5–7	2.58E–04	0.0758	0.811	0.448	14.74	31	64.55	48.67
SL1P5C5–7	1.50E–04	0.0951	0.832	0.454	14.71	30.5	66.1	45.11
SL5P5C10–7	3.60E–05	0.0297	0.775	0.437	14.6	31.3	59.5	48.24
SL3P5C10–7	1.75E–04	0.0622	0.788	0.441	14.8	30.2	63.4	47.95
SL1P5C10–7	1.45E–04	0.0762	0.79	0.441	14.85	29.77	64.3	44.89
SL5P5C15–7	1.19E–04	0.0228	0.882	0.469	13.78	34	59.2	52.1
SL3P5C15–7	2.41E–04	0.0696	0.845	0.458	13.95	33.2	60.62	48.43
SL1P5C15–7	2.25E–04	0.0786	0.84	0.457	14.8	29.8	62.45	45.95
SL5P5C20–7	1.42E–04	0.0263	0.891	0.471	13.76	35	62.8	53.44
SL3P5C20–7	4.50E–04	0.0774	0.88	0.468	13.81	34.3	63.22	49.85
SL1P5C20–7	1.82E–04	0.0594	0.846	0.458	14.43	30	66.04	47.46
SL5P5C5–14	1.63E–04	0.0477	0.797	0.444	14.73	30.38	55.3	46.7
SL3P5C5–14	1.67E–04	0.095	0.803	0.445	14.67	30.62	64.55	43
SL1P5C5–14	1.76E–04	0.0862	0.824	0.452	14.47	31.42	62.1	42.06
SL5P5C10–14	1.52E–04	0.0468	0.768	0.434	15.03	29.19	59.5	44.45
SL3P5C10–14	1.61E–04	0.0892	0.78	0.438	14.9	29.7	63.4	46.71
SL1P5C10–14	1.75E–04	0.0948	0.782	0.439	14.88	29.77	58.3	44.89
SL5P5C15–14	1.61E–04	0.0569	0.874	0.466	14.01	33.32	53.2	47.46
SL3P5C15–14	1.86E–04	0.0635	0.836	0.455	14.35	31.91	56.62	46.04
SL1P5C15–14	1.94E–04	0.0972	0.831	0.454	14.4	31.71	54.45	41.85
SL5P5C20–14	1.75E–04	0.0596	0.883	0.469	13.92	33.66	52.8	46.48
SL3P5C20–14	1.96E–04	0.0459	0.871	0.466	14.03	33.2	55.22	44.87
SL1P5C20–14	1.98E–04	0.0979	0.837	0.456	14.35	31.93	60.04	41.42
SL5P5C5–21	1.57E–04	0.0472	0.79	0.441	14.8	30.08	50.8	42.36
SL3P5C5–21	1.64E–04	0.0954	0.796	0.443	14.75	30.32	61.55	40.92
SL1P5C5–21	1.75E–04	0.0868	0.816	0.449	14.55	31.11	54.6	40.01
SL5P5C10–21	1.40E–04	0.0452	0.761	0.432	15.1	28.9	56.5	38.67
SL3P5C10–21	1.53E–04	0.088	0.772	0.436	14.98	29.37	61.9	42.22
SL1P5C10–21	1.73E–04	0.0954	0.774	0.436	14.96	29.43	53.8	43.85
SL5P5C15–21	1.55E–04	0.0561	0.866	0.464	14.08	33.02	48.7	35.29
SL3P5C15–21	1.82E–04	0.0633	0.828	0.453	14.43	31.59	50.62	40.65
SL1P5C15–21	1.92E–04	0.0975	0.822	0.451	14.49	31.37	52.95	40.8

Table B.1: Continued

Code	av	CR	e	n	MDD	OMC	LL	PL
SL5P5C20–21	1.70E–04	0.0591	0.876	0.467	13.99	33.38	49.8	41.06
SL3P5C20–21	1.93E–04	0.046	0.862	0.463	14.11	32.88	52.22	39.44
SL1P5C20–21	1.97E–04	0.0982	0.828	0.453	14.43	31.59	57.04	38.25
SL5P5C5–28	1.51E–04	0.0466	0.782	0.439	14.88	29.78	45.47	33.11
SL3P5C5–28	1.62E–04	0.0959	0.788	0.441	14.82	30	61.55	38.84
SL1P5C5–28	1.73E–04	0.0873	0.807	0.447	14.63	30.79	49.27	34.88
SL5P5C10–28	1.35E–04	0.0446	0.754	0.43	15.17	28.61	56.5	38.67
SL3P5C10–28	1.50E–04	0.0881	0.764	0.433	15.06	29.03	56.57	38.09
SL1P5C10–28	1.71E–04	0.096	0.766	0.434	15.05	29.1	49.8	40.74
SL5P5C15–28	1.53E–04	0.0561	0.858	0.462	14.15	32.72	42.03	31.2
SL3P5C15–28	1.80E–04	0.0633	0.82	0.45	14.51	31.26	43.95	30.65
SL1P5C15–28	1.91E–04	0.0979	0.814	0.449	14.57	31.03	52.95	36.67
SL5P5C20–28	1.64E–04	0.0582	0.868	0.465	14.06	33.09	47.13	35.06
SL3P5C20–28	1.89E–04	0.0459	0.854	0.461	14.19	32.56	49.55	39.44
SL1P5C20–28	1.95E–04	0.0985	0.819	0.45	14.52	31.25	54.37	37.2
SL5P5C5–56	1.47E–04	0.0467	0.775	0.437	14.95	29.49	35.47	28.91
SL3P5C5–56	1.55E–04	0.0965	0.78	0.438	14.9	29.68	41.55	35.57
SL1P5C5–56	1.69E–04	0.0883	0.799	0.444	14.71	30.47	41.27	29.53
SL5P5C10–56	1.24E–04	0.0437	0.747	0.428	15.23	28.34	54.5	34.24
SL3P5C10–56	1.44E–04	0.0879	0.755	0.43	15.15	28.68	56.57	37.01
SL1P5C10–56	1.67E–04	0.0971	0.758	0.431	15.13	28.78	49.8	39.67
SL5P5C15–56	1.48E–04	0.0562	0.85	0.459	14.23	32.41	38.03	32.5
SL3P5C15–56	1.74E–04	0.0638	0.811	0.448	14.59	30.94	36.95	30.1
SL1P5C15–56	1.87E–04	0.0984	0.805	0.446	14.65	30.69	40.95	34.46
SL5P5C20–56	1.56E–04	0.0575	0.86	0.462	14.14	32.8	37.13	30.82
SL3P5C20–56	1.80E–04	0.0458	0.845	0.458	14.27	32.24	39.55	31.23
SL1P5C20–56	1.91E–04	0.099	0.81	0.448	14.6	30.9	46.37	32.74
SL5P5C5–90	1.44E–04	0.0472	0.768	0.434	15.02	29.19	33.86	29.73
SL3P5C5–90	1.50E–04	0.0973	0.771	0.435	14.99	29.35	35.12	34.5
SL1P5C5–90	1.65E–04	0.0893	0.792	0.442	14.79	30.16	36.45	24.14
SL5P5C10–90	1.12E–04	0.0426	0.741	0.426	15.3	28.08	34.5	32.01
SL3P5C10–90	1.51E–04	0.091	0.747	0.428	15.23	28.34	43.35	35.19
SL1P5C10–90	1.62E–04	0.0984	0.75	0.429	15.21	28.45	46.59	37.52
SL5P5C15–90	1.43E–04	0.0563	0.841	0.457	14.31	32.1	44.82	31.05
SL3P5C15–90	1.72E–04	0.0645	0.803	0.445	14.67	30.63	39.13	32.24
SL1P5C15–90	1.83E–04	0.0988	0.796	0.443	14.74	30.35	42.91	31.13
SL5P5C20–90	1.61E–04	0.0599	0.852	0.46	14.21	32.5	37.13	30.89
SL3P5C20–90	1.78E–04	0.0462	0.837	0.456	14.35	31.93	34.73	28.23
SL1P5C20–90	1.80E–04	0.0994	0.802	0.445	14.68	30.57	41.55	31.43

Table B.1: Continued

Code	PI	G_S	SL	SiO_2 (%)	Al_2O_3 (%)	Fe_2O_3 (%)	CaO (%)	MgO (%)
S	26.25	2.56	13.71	0	0	0	0	0
SL5P0C0–7	19.33	2.47	10.09	0.49	0.11	0.07	32.73	0.14
SL5P1C0–7	22.2	2.47	11.59	4.34	0.73	0.34	33.16	0.3
SL5P5C0–7	13.76	2.46	7.19	19.75	3.24	1.4	34.91	0.94
SL5P10C0–7	12.35	2.46	6.45	39	6.38	2.74	37.09	1.74
SL5P15C0–7	16.11	2.43	8.41	58.26	9.51	4.07	39.27	2.54
SL5P20C0–7	12.9	2.41	6.74	77.52	12.65	5.4	41.45	3.35
SL5P5C5–7	12.35	2.57	6.43	41.89	12.19	2.93	35.32	1.33
SL3P5C5–7	15.88	2.62	10.71	41.7	12.15	2.9	22.23	1.27
SL1P5C5–7	21	2.69	10	41.5	12.11	2.87	9.14	1.21
SL5P5C10–7	11.26	2.56	5.71	64.04	21.14	4.46	35.74	1.71
SL3P5C10–7	15.45	2.61	10	63.84	21.1	4.43	22.65	1.66
SL1P5C10–7	19.41	2.61	8.57	63.64	21.06	4.4	9.56	1.6
SL5P5C15–7	7.1	2.54	5.36	86.18	30.09	5.98	36.16	2.1
SL3P5C15–7	12.19	2.57	8.57	85.98	30.05	5.95	23.07	2.04
SL1P5C15–7	16.5	2.58	7.86	85.79	30.01	5.93	9.98	1.98
SL5P5C20–7	9.36	2.53	4.29	108.33	39.04	7.51	36.57	2.48
SL3P5C20–7	13.37	2.55	7.86	108.13	39	7.48	23.48	2.43
SL1P5C20–7	18.58	2.51	7.14	107.93	38.96	7.45	10.39	2.37
SL5P5C5–14	8.6	2.62	4.49	83.78	24.38	5.86	70.64	2.65
SL3P5C5–14	21.55	2.62	11.25	83.39	24.3	5.8	44.46	2.54
SL1P5C5–14	20.04	2.61	10.46	83	24.21	5.75	18.28	2.43
SL5P5C10–14	15.05	2.63	7.86	128.07	42.28	8.91	71.48	3.42
SL3P5C10–14	16.69	2.62	8.71	127.68	42.2	8.86	45.3	3.31
SL1P5C10–14	13.41	2.61	7	127.29	42.11	8.8	19.12	3.2
SL5P5C15–14	5.74	2.62	3	172.36	60.18	11.96	72.31	4.19
SL3P5C15–14	10.58	2.6	5.52	171.97	60.1	11.91	46.13	4.08
SL1P5C15–14	12.6	2.6	6.58	171.58	60.01	11.85	19.95	3.97
SL5P5C20–14	6.32	2.62	3.3	216.65	78.08	15.02	73.14	4.96
SL3P5C20–14	10.35	2.6	5.4	216.26	77.99	14.96	46.96	4.85
SL1P5C20–14	18.62	2.6	9.73	215.87	77.91	14.9	20.78	4.74
SL5P5C5–21	8.44	2.63	4.41	125.67	36.57	8.79	105.97	3.98
SL3P5C5–21	20.63	2.62	10.77	125.09	36.45	8.7	66.7	3.81
SL1P5C5–21	14.59	2.61	7.62	124.5	36.32	8.62	27.43	3.64
SL5P5C10–21	17.83	2.64	9.31	192.11	63.42	13.37	107.22	5.13
SL3P5C10–21	19.68	2.62	10.27	191.52	63.29	13.28	67.95	4.97
SL1P5C10–21	9.95	2.61	5.2	190.93	63.17	13.2	28.68	4.8
SL5P5C15–21	13.41	2.62	7	258.54	90.27	17.94	108.47	6.29
SL3P5C15–21	9.97	2.61	5.2	257.95	90.14	17.86	69.2	6.12

Table B.1: Continued

Code	PI	G_S	SL	SiO_2 (%)	Al_2O_3 (%)	Fe_2O_3 (%)	CaO (%)	MgO (%)
SL3P5C20–21	12.78	2.6	6.67	324.39	116.99	22.44	70.44	7.28
SL1P5C20–21	18.79	2.6	9.81	323.8	116.87	22.35	31.17	7.11
SL5P5C5–28	12.35	2.63	6.45	167.57	48.76	11.72	141.29	5.31
SL3P5C5–28	22.71	2.62	11.86	166.78	48.59	11.61	88.93	5.08
SL1P5C5–28	14.39	2.61	7.52	166	48.43	11.49	36.57	4.86
SL5P5C10–28	17.83	2.64	9.31	256.14	84.56	17.82	142.95	6.85
SL3P5C10–28	18.47	2.61	9.65	255.36	84.39	17.71	90.59	6.62
SL1P5C10–28	9.06	2.62	4.73	254.58	84.22	17.6	38.23	6.4
SL5P5C15–28	10.83	2.62	5.66	344.72	120.36	23.93	144.62	8.39
SL3P5C15–28	13.3	2.61	6.95	343.94	120.19	23.81	92.26	8.16
SL1P5C15–28	16.28	2.6	8.5	343.15	120.02	23.7	39.9	7.94
SL5P5C20–28	12.07	2.62	6.3	433.3	156.16	30.03	146.29	9.93
SL3P5C20–28	10.11	2.61	5.28	432.52	155.99	29.92	93.93	9.7
SL1P5C20–28	17.17	2.6	8.97	431.73	155.82	29.81	41.57	9.48
SL5P5C5–56	6.56	2.63	3.43	335.13	97.52	23.44	282.58	10.61
SL3P5C5–56	5.98	2.62	3.12	333.56	97.19	23.21	177.86	10.16
SL1P5C5–56	11.73	2.61	6.13	332	96.85	22.99	73.14	9.72
SL5P5C10–56	20.26	2.65	10.58	512.29	169.12	35.64	285.91	13.69
SL3P5C10–56	19.55	2.61	10.21	510.72	168.78	35.42	181.19	13.24
SL1P5C10–56	10.13	2.62	5.29	509.15	168.45	35.2	76.47	12.8
SL5P5C15–56	5.53	2.61	2.89	689.44	240.72	47.85	289.24	16.77
SL3P5C15–56	6.85	2.61	3.58	687.88	240.38	47.63	184.52	16.32
SL1P5C15–56	6.49	2.6	3.39	686.31	240.04	47.4	79.8	15.88
SL5P5C20–56	6.31	2.62	3.3	866.6	312.31	60.06	292.57	19.85
SL3P5C20–56	8.32	2.61	4.35	865.03	311.98	59.84	187.85	19.4
SL1P5C20–56	13.63	2.6	7.12	863.46	311.64	59.61	83.13	18.96
SL5P5C5–90	4.13	2.63	2.16	538.61	156.74	37.67	454.14	17.06
SL3P5C5–90	0.62	2.61	0.33	536.09	156.2	37.31	285.84	16.34
SL1P5C5–90	12.3	2.62	6.42	533.57	155.66	36.95	117.54	15.62
SL5P5C10–90	2.49	2.66	1.3	823.32	271.8	57.29	459.5	22.01
SL3P5C10–90	8.17	2.61	4.26	820.8	271.26	56.93	291.2	21.29
SL1P5C10–90	9.07	2.62	4.73	818.28	270.72	56.57	122.9	20.57
SL5P5C15–90	13.77	2.61	7.19	1108.04	386.87	76.91	464.85	26.96
SL3P5C15–90	6.89	2.62	3.6	1105.52	386.33	76.55	296.55	26.24
SL1P5C15–90	11.79	2.61	6.16	1103	385.79	76.19	128.25	25.52
SL5P5C20–90	6.24	2.62	3.26	1392.75	501.93	96.53	470.21	31.91
SL3P5C20–90	6.5	2.61	3.4	1390.23	501.39	96.17	301.91	31.19
SL1P5C20–90	10.12	2.61	5.28	1387.71	500.85	95.81	133.61	30.47

Table B.1: Continued

Code	SO_3	Other	LOI
	(%)	(%)	
	0	0	0
S	0.18	1.3	0
SL5P0C0–7	0.25	1.76	1.37
SL5P1C0–7	0.56	3.64	1.99
SL5P5C0–7	0.95	5.99	4.48
SL5P10C0–7	1.34	8.34	7.6
SL5P15C0–7	1.73	10.69	10.72
SL5P20C0–7	0.67	10.68	13.84
SL5P5C5–7	0.6	10.16	4.48
SL3P5C5–7	0.53	9.64	3.94
SL1P5C5–7	0.77	17.71	3.39
SL5P5C10–7	0.7	17.19	4.48
SL3P5C10–7	0.63	16.67	3.94
SL1P5C10–7	0.87	24.74	3.39
SL5P5C15–7	0.8	24.22	4.48
SL3P5C15–7	0.73	23.7	3.94
SL1P5C15–7	0.97	31.77	3.39
SL5P5C20–7	0.9	31.25	4.48
SL3P5C20–7	0.83	30.73	3.94
SL1P5C20–7	1.33	21.35	3.39
SL5P5C5–14	1.19	20.31	8.97
SL3P5C5–14	1.05	19.28	7.88
SL1P5C5–14	1.53	35.41	6.78
SL5P5C10–14	1.39	34.38	8.97
SL3P5C10–14	1.25	33.34	7.88
SL1P5C10–14	1.74	49.48	6.78
SL5P5C15–14	1.6	48.44	8.97
SL3P5C15–14	1.46	47.4	7.88
SL1P5C15–14	1.94	63.54	6.78
SL5P5C20–14	1.8	62.5	8.97
SL3P5C20–14	1.66	61.47	7.88
SL1P5C20–14	2	32.03	6.78
SL5P5C5–21	1.79	30.47	13.45
SL3P5C5–21	1.58	28.92	11.81
SL1P5C5–21	2.3	53.12	10.17
SL5P5C10–21	2.09	51.57	13.45
SL3P5C10–21	1.88	50.01	11.81
SL1P5C10–21	2.6	74.21	10.17
SL5P5C15–21	2.39	72.66	13.45
SL3P5C15–21	2.18	71.11	11.81

Table B.1: Continued

Code	SO_3 (%)	Other (%)	LOI
SL5P5C20–21	2.91	95.31	10.17
SL3P5C20–21	2.7	93.75	13.45
SL1P5C20–21	2.49	92.2	11.81
SL5P5C5–28	2.66	42.7	10.17
SL3P5C5–28	2.38	40.63	17.93
SL1P5C5–28	2.1	38.56	15.75
SL5P5C10–28	3.07	70.83	13.57
SL3P5C10–28	2.79	68.75	17.93
SL1P5C10–28	2.51	66.68	15.75
SL5P5C15–28	3.47	98.95	13.57
SL3P5C15–28	3.19	96.88	17.93
SL1P5C15–28	2.91	94.81	15.75
SL5P5C20–28	3.88	127.08	13.57
SL3P5C20–28	3.6	125.01	17.93
SL1P5C20–28	3.32	122.93	15.75
SL5P5C5–56	5.32	85.4	13.57
SL3P5C5–56	4.76	81.26	35.87
SL1P5C5–56	4.2	77.11	31.5
SL5P5C10–56	6.13	141.65	27.13
SL3P5C10–56	5.57	137.51	35.87
SL1P5C10–56	5.01	133.36	31.5
SL5P5C15–56	6.94	197.9	27.13
SL3P5C15–56	6.38	193.76	35.87
SL1P5C15–56	5.82	189.62	31.5
SL5P5C20–56	7.76	254.16	27.13
SL3P5C20–56	7.2	250.01	35.87
SL1P5C20–56	6.64	245.87	31.5
SL5P5C5–90	8.55	137.25	27.13
SL3P5C5–90	7.65	130.59	57.65
SL1P5C5–90	6.75	123.93	50.63
SL5P5C10–90	9.86	227.66	43.61
SL3P5C10–90	8.96	221	57.65
SL1P5C10–90	8.06	214.34	50.63
SL5P5C15–90	11.16	318.06	43.61
SL3P5C15–90	10.26	311.4	57.65
SL1P5C15–90	9.36	304.74	50.63
SL5P5C20–90	12.47	408.47	43.61
SL3P5C20–90	11.57	401.81	57.65
SL1P5C20–90	10.67	395.15	50.63

Table B.2: Accuracy indicators for algorithms using manual feature selection

Algorithm	Error	Model 1			Model 2			Model 3		
		Test	Train	Validation	Test	Train	Validation	Test	Train	Validation
LR	R^2	0.444	0.573	0.559	0.84	0.858	0.857	0.649	0.813	0.793
	MAE	0.131	0.168	0.16	0.068	0.092	0.087	0.123	0.118	0.119
	MSE	0.034	0.045	0.043	0.01	0.015	0.014	0.022	0.02	0.02
	RMSE	0.185	0.213	0.208	0.099	0.123	0.118	0.147	0.141	0.142
	MSD	0.02	0	0.004	0.007	0	0.001	0.068	0	0.014
	MAPE	0.149	0.209	0.197	0.092	0.127	0.12	0.16	0.146	0.149
	R^2_{adj}	0.444	0.573	0.559	0.84	0.858	0.857	0.649	0.813	0.793
PR	R^2	0.806	0.88	0.871	0.84	0.858	0.857	0.649	0.813	0.793
	MAE	0.085	0.083	0.083	0.068	0.092	0.087	0.123	0.118	0.119
	MSE	0.012	0.013	0.013	0.01	0.015	0.014	0.022	0.02	0.02
	RMSE	0.109	0.113	0.112	0.099	0.123	0.118	0.147	0.141	0.142
	MSD	–0.003	0	–0.001	0.007	0	0.001	0.068	0	0.014
	MAPE	0.12	0.095	0.1	0.092	0.127	0.12	0.16	0.146	0.149
	R^2_{adj}	0.806	0.88	0.871	0.84	0.858	0.857	0.649	0.813	0.793
ANN	R^2	0.994	1	0.999	0.907	0.993	0.981	0.947	0.99	0.984
	MAE	0.012	0.002	0.004	0.032	0.011	0.015	0.033	0.018	0.021
	MSE	0	0	0	0.003	0	0.001	0.002	0.001	0.001
	RMSE	0.015	0.004	0.008	0.056	0.019	0.03	0.042	0.023	0.028
	MSD	0.007	0	0.001	–0.01	0.001	–0.001	–0.002	0	0
	MAPE	0.053	NaN	NaN	0.225	NaN	NaN	0.146	NaN	NaN
	R^2_{adj}	0.994	1	0.999	0.907	0.993	0.981	0.947	0.99	0.984

Table B.2: Continued

Algorithm	Error	Model 1			Model 2			Model 3		
		Test	Train	Validation	Test	Train	Validation	Test	Train	Validation
XGBOOST	R^2	0.912	1	0.979	0.728	1	0.89	0.564	1	0.967
	MAE	0.061	0	0.014	0.115	0	0.031	0.13	0	0.013
	MSE	0.009	0	0.002	0.027	0	0.011	0.043	0	0.003
	RMSE	0.093	0	0.045	0.163	0	0.104	0.207	0	0.057
	MSD	–0.007	0	0.002	–0.023	0	0.007	0.008	0	–0.01
	MAPE	0.076	0	0.014	0.15	0	0.053	0.172	0	0.011
	R^2_{adj}	0.912	1	0.979	0.728	1	0.89	0.564	1	0.967
GBOOST	R^2	0.806	1	0.947	0.865	1	0.963	0.677	1	0.912
	MAE	0.08	0	0.016	0.112	0	0.023	0.151	0	0.031
	MSE	0.026	0	0.005	0.018	0	0.004	0.042	0	0.009
	RMSE	0.16	0	0.072	0.133	0	0.06	0.206	0	0.093
	MSD	–0.014	0	–0.003	0.052	0	0.01	0.078	0	0.016
	MAPE	0.076	0	0.015	0.156	0	0.032	0.21	0	0.043
	R^2_{adj}	0.806	1	0.947	0.865	1	0.963	0.677	1	0.912
RF	R^2	0.833	0.952	0.937	0.804	0.971	0.943	0.812	0.976	0.961
	MAE	0.084	0.044	0.053	0.104	0.039	0.053	0.097	0.036	0.043
	MSE	0.016	0.005	0.006	0.019	0.003	0.006	0.018	0.002	0.004
	RMSE	0.128	0.068	0.079	0.139	0.053	0.075	0.135	0.048	0.062
	MSD	0.004	0.004	0.002	–0.011	–0.002	–0.008	0.01	0.005	0.003
	MAPE	0.11	0.059	0.068	0.135	0.053	0.07	0.126	0.048	0.053
	R^2_{adj}	0.833	0.952	0.937	0.804	0.971	0.943	0.812	0.976	0.961

Table B.3: Accuracy indicators for algorithms using manual feature selection

Algorithm	Error	Model 4			Model 5			Model 6		
		Test	**Train**	**Validation**	**Test**	**Train**	**Validation**	**Test**	**Train**	**Validation**
LR	R^2	–0.005	0.238	0.21	0.098	0.132	0.132	0.107	0.556	0.501
	MAE	0.214	0.24	0.234	0.193	0.259	0.246	0.171	0.181	0.179
	MSE	0.062	0.081	0.077	0.056	0.092	0.085	0.055	0.047	0.049
	RMSE	0.249	0.285	0.278	0.236	0.304	0.291	0.235	0.217	0.221
	MSD	0.038	0	0.008	0.05	0	0.01	0.062	–0.04	–0.019
	MAPE	0.326	0.321	0.322	0.292	0.353	0.341	0.227	0.237	0.235
	R^2_{adj}	–0.005	0.238	0.21	0.098	0.132	0.132	0.107	0.556	0.501
PR	R^2	0.264	0.497	0.47	0.12	0.338	0.313	0.281	0.646	0.601
	MAE	0.181	0.192	0.19	0.192	0.227	0.22	0.169	0.162	0.164
	MSE	0.046	0.053	0.052	0.054	0.07	0.067	0.044	0.038	0.039
	RMSE	0.213	0.231	0.228	0.233	0.265	0.259	0.211	0.194	0.197
	MSD	0.02	0	0.004	0.041	0	0.008	–0.057	–0.055	–0.055
	MAPE	0.248	0.257	0.255	0.294	0.301	0.3	0.212	0.201	0.203
	R^2_{adj}	0.264	0.497	0.47	0.12	0.338	0.313	0.281	0.646	0.601
ANN	R^2	0.462	0.453	0.459	0.714	0.876	0.853	0.977	0.997	0.994
	MAE	0.117	0.14	0.135	0.086	0.061	0.066	0.025	0.008	0.012
	MSE	0.018	0.028	0.026	0.01	0.006	0.007	0.001	0	0
	RMSE	0.135	0.166	0.161	0.098	0.079	0.084	0.028	0.012	0.017
	MSD	0.006	0	0.001	0.04	0.002	0.01	–0.016	0	–0.004
	MAPE	1.007	NaN	NaN	0.482	NaN	NaN	0.173	NaN	NaN
	R^2_{adj}	0.462	0.453	0.459	0.714	0.876	0.853	0.977	0.997	0.994

Table B.3: Continued

Algorithm	Error	Model 4			Model 5			Model 6		
		Test	Train	Validation	Test	Train	Validation	Test	Train	Validation
XGBOOST	R^2	–0.117	1	0.782	–0.079	1	0.738	0.023	1	0.939
	MAE	0.282	0	0.055	0.248	0	0.05	0.255	0	0.019
	MSE	0.109	0	0.021	0.105	0	0.026	0.095	0	0.006
	RMSE	0.331	0	0.146	0.325	0	0.16	0.309	0	0.077
	MSD	–0.009	0	0.01	0.037	0	–0.016	0.049	0	0.006
	MAPE	0.366	0	0.071	0.32	0	0.062	0.333	0	0.028
	R^2_{adj}	–0.117	1	0.782	–0.079	1	0.738	0.023	1	0.939
GBOOST	R^2	0.064	1	0.745	0.182	1	0.777	–0.082	1	0.705
	MAE	0.302	0	0.061	0.272	0	0.055	0.342	0	0.069
	MSE	0.123	0	0.025	0.108	0	0.022	0.142	0	0.029
	RMSE	0.351	0	0.158	0.328	0	0.148	0.377	0	0.17
	MSD	–0.033	0	–0.007	0.161	0	0.033	0.126	0	0.025
	MAPE	0.431	0	0.087	0.361	0	0.073	0.475	0	0.096
	R^2_{adj}	0.064	1	0.745	0.182	1	0.777	–0.082	1	0.705
RF	R^2	–0.02	0.857	0.693	0.425	0.927	0.828	0.4	0.903	0.825
	MAE	0.263	0.096	0.129	0.194	0.069	0.093	0.197	0.077	0.099
	MSE	0.1	0.014	0.03	0.056	0.007	0.017	0.059	0.009	0.017
	RMSE	0.316	0.118	0.173	0.237	0.084	0.13	0.242	0.097	0.131
	MSD	0.005	0.002	0.018	0.009	0.001	0.002	0.016	0.003	0.014
	MAPE	0.359	0.132	0.18	0.258	0.089	0.119	0.274	0.103	0.138
	R^2_{adj}	–0.02	0.857	0.693	0.425	0.927	0.828	0.4	0.903	0.825

Table B.4: Accuracy indicators for algorithms using manual feature selection

Algorithm	Error	Model 7			Model 8		
		Test	**Train**	**Validation**	**Test**	**Train**	**Validation**
LR	R^2	0.953	0.993	0.988	0.116	0.134	0.131
	MAE	0.032	0.02	0.023	98.294	96.589	96.93
	MSE	0.003	0.001	0.001	18727.103	17803.686	17988.369
	RMSE	0.054	0.026	0.034	136.847	133.43	134.121
	MSD	0.01	0.011	0.01	3.524	0	0.705
	MAPE	0.049	0.026	0.031	NaN	NaN	NaN
	R^2_{adj}	0.953	0.993	0.988	0.116	0.134	0.131
PR	R^2	0.953	0.993	0.988	0.563	0.563	0.563
	MAE	0.032	0.02	0.023	71.96	72	71.992
	MSE	0.003	0.001	0.001	9258.802	8986.7	9041.12
	RMSE	0.054	0.026	0.034	96.223	94.798	95.085
	MSD	0.01	0.011	0.01	–22.358	–19.836	–20.34
	MAPE	0.049	0.026	0.031	NaN	NaN	NaN
	R^2_{adj}	0.953	0.993	0.988	0.563	0.563	0.563
ANN	R^2	0.996	1	0.999	0.898	0.912	0.909
	MAE	0.009	0.002	0.003	0.037	0.035	0.035
	MSE	0	0	0	0.002	0.002	0.002
	RMSE	0.011	0.004	0.006	0.05	0.045	0.046
	MSD	0.001	0	0	0.001	0	0
	MAPE	0.056	NaN	NaN	NaN	NaN	NaN
	R^2_{adj}	0.996	1	0.999	0.898	0.912	0.909

Table B.4: Continued

Algorithm	Error	Model 7			Model 8		
		Test	Train	Validation	Test	Train	Validation
XGBOOST	R^2	0.839	1	0.988	0.842	0.952	0.933
	MAE	0.084	0	0.007	44.276	23.31	27.246
	MSE	0.016	0	0.001	3271.48	990.416	1395.484
	RMSE	0.125	0	0.034	57.197	31.471	37.356
	MSD	–0.002	0	–0.001	–0.112	0	–0.086
	MAPE	0.115	0	0.008	NaN	NaN	NaN
	R^2_{adj}	0.839	1	0.988	0.842	0.952	0.933
GBOOST	R^2	0.844	1	0.957	0.824	0.954	0.93
	MAE	0.097	0	0.02	45.465	22.951	27.454
	MSE	0.021	0	0.004	3420.965	963.206	1454.758
	RMSE	0.143	0	0.065	58.489	31.036	38.141
	MSD	–0.018	0	–0.004	–1.17	0	–0.234
	MAPE	0.11	0	0.022	NaN	NaN	NaN
	R^2_{adj}	0.844	1	0.957	0.824	0.954	0.93
RF	R^2	0.864	0.984	0.977	0.859	0.872	0.87
	MAE	0.078	0.028	0.034	41.618	40.087	40.229
	MSE	0.013	0.002	0.002	2196.104	2650.941	2683.314
	RMSE	0.115	0.039	0.047	54.001	51.487	51.801
	MSD	0	0.001	0.001	–0.075	0.09	0.1
	MAPE	0.103	0.039	0.044	NaN	NaN	NaN
	R^2_{adj}	0.864	0.984	0.977	0.859	0.872	0.87

Table B.5: Accuracy indicators for hybrid algorithms using RF in selecting features

Algorithm	Error	Model 9			Model 10			Model 11		
		Test	Train	Validation	Test	Train	Validation	Test	Train	Validation
LR	R^2	0.987	0.982	0.982	0.217	0.746	0.679	0.953	0.993	0.988
	MAE	0.025	0.033	0.031	0.155	0.126	0.132	0.032	0.02	0.023
	MSE	0.001	0.002	0.002	0.048	0.027	0.031	0.003	0.001	0.001
	RMSE	0.028	0.044	0.042	0.22	0.164	0.177	0.054	0.026	0.034
	MSD	0.019	0.019	0.019	0.074	–0.016	0.003	0.01	0.011	0.01
	MAPE	0.034	0.043	0.041	0.202	0.143	0.155	0.049	0.026	0.031
	R^2_{adj}	0.987	0.982	0.982	0.217	0.746	0.679	0.953	0.993	0.988
PR	R^2	0.987	0.982	0.982	0.265	0.689	0.636	0.265	0.689	0.636
	MAE	0.025	0.033	0.031	0.19	0.15	0.158	0.19	0.15	0.158
	MSE	0.001	0.002	0.002	0.045	0.033	0.036	0.045	0.033	0.036
	RMSE	0.028	0.044	0.042	0.213	0.182	0.189	0.213	0.182	0.189
	MSD	0.019	0.019	0.019	0.11	0.112	0.111	0.11	0.112	0.111
	MAPE	0.034	0.043	0.041	0.234	0.209	0.214	0.234	0.209	0.214
	R^2_{adj}	0.987	0.982	0.982	0.265	0.689	0.636	0.265	0.689	0.636
ANN	R^2	0.992	0.999	0.998	0.976	0.999	0.996	1	0.996	0.999
	MAE	0.011	0.004	0.005	0.023	0.004	0.008	0.002	0.009	0.003
	MSE	0	0	0	0.001	0	0	0	0	0
	RMSE	0.016	0.006	0.009	0.029	0.006	0.014	0.004	0.011	0.006
	MSD	–0.008	0	–0.002	–0.003	0	–0.001	0	0.001	0
	MAPE	0.087	NaN	NaN	0.092	NaN	NaN	NaN	0.056	NaN
	R^2_{adj}	0.992	0.999	0.998	0.976	0.999	0.996	1	0.996	0.999

Table B.5: Continued

Algorithm	Error	Model 9			Model 10			Model 11		
		Test	**Train**	**Validation**	**Test**	**Train**	**Validation**	**Test**	**Train**	**Validation**
XGBOOST	R^2	0.875	1	0.981	0.737	1	0.962	0.81	1	0.937
	MAE	0.084	0	0.013	0.104	0	0.016	0.088	0	0.02
	MSE	0.012	0	0.002	0.026	0	0.004	0.019	0	0.006
	RMSE	0.111	0	0.044	0.16	0	0.061	0.136	0	0.078
	MSD	0.014	0	0.002	0.021	0	0.003	0	0	0.001
	MAPE	0.106	0	0.021	0.149	0	0.024	0.11	0	0.021
	R^2_{adj}	0.875	1	0.981	0.737	1	0.962	0.81	1	0.937
GBOOST	R^2	0.872	1	0.965	0.28	1	0.804	0.844	1	0.957
	MAE	0.104	0	0.021	0.189	0	0.038	0.097	0	0.02
	MSE	0.017	0	0.003	0.095	0	0.019	0.021	0	0.004
	RMSE	0.13	0	0.059	0.308	0	0.139	0.143	0	0.065
	MSD	0.009	0	0.002	0.057	0	0.012	–0.018	0	–0.004
	MAPE	0.124	0	0.025	0.26	0	0.053	0.11	0	0.022
	R^2_{adj}	0.872	1	0.965	0.28	1	0.804	0.844	1	0.957
RF	R^2	0.857	0.983	0.973	0.76	0.971	0.951	0.864	0.984	0.977
	MAE	0.084	0.03	0.037	0.109	0.039	0.049	0.078	0.028	0.034
	MSE	0.014	0.002	0.003	0.023	0.003	0.005	0.013	0.002	0.002
	RMSE	0.118	0.04	0.051	0.153	0.053	0.069	0.115	0.039	0.047
	MSD	0.001	0.001	0.002	0.007	0.003	–0.001	0	0.001	0.001
	MAPE	0.11	0.041	0.048	0.145	0.053	0.064	0.103	0.039	0.044
	R^2_{adj}	0.857	0.983	0.973	0.76	0.971	0.951	0.864	0.984	0.977

Table B.6: Accuracy indicators for hybrid algorithms using GBoost in selecting features

Algorithm	Error	Model 12			Model 13			Model 14		
		Test	Train	Validation	Test	Train	Validation	Test	Train	Validation
LR	R^2	0.991	0.986	0.987	0.217	0.746	0.679	0.953	0.993	0.988
	MAE	0.019	0.025	0.024	0.155	0.126	0.132	0.032	0.02	0.023
	MSE	0.001	0.001	0.001	0.048	0.027	0.031	0.003	0.001	0.001
	RMSE	0.023	0.038	0.036	0.22	0.164	0.177	0.054	0.026	0.034
	MSD	0.001	–0.003	–0.002	0.074	–0.016	0.003	0.01	0.011	0.01
	MAPE	0.025	0.032	0.03	0.202	0.143	0.155	0.049	0.026	0.031
	R^2_{adj}	0.991	0.986	0.987	0.217	0.746	0.679	0.953	0.993	0.988
PR	R^2	0.991	0.986	0.987	0.265	0.689	0.636	0.953	0.993	0.988
	MAE	0.019	0.025	0.024	0.19	0.15	0.158	0.032	0.02	0.023
	MSE	0.001	0.001	0.001	0.045	0.033	0.036	0.003	0.001	0.001
	RMSE	0.023	0.038	0.036	0.213	0.182	0.189	0.054	0.026	0.034
	MSD	0.001	–0.003	–0.002	0.11	0.112	0.111	0.01	0.011	0.01
	MAPE	0.025	0.032	0.03	0.234	0.209	0.214	0.049	0.026	0.031
	R^2_{adj}	0.991	0.986	0.987	0.265	0.689	0.636	0.953	0.993	0.988
ANN	R^2	0.994	0.999	0.999	0.976	0.999	0.996	0.996	1	0.999
	MAE	0.011	0.004	0.006	0.023	0.004	0.008	0.009	0.002	0.003
	MSE	0	0	0	0.001	0	0	0	0	0
	RMSE	0.014	0.006	0.008	0.029	0.006	0.014	0.011	0.004	0.006
	MSD	–0.002	0	–0.001	–0.003	0	–0.001	0.001	0	0
	MAPE	0.064	NaN	NaN	0.092	NaN	NaN	0.056	NaN	NaN
	R^2_{adj}	0.994	0.999	0.999	0.976	0.999	0.996	0.996	1	0.999

Table B.6: Continued

Algorithm	Error	Model 12			Model 13			Model 14		
		Test	Train	Validation	Test	Train	Validation	Test	Train	Validation
XGBOOST	R^2	0.677	1	0.958	0.789	1	0.93	0.773	1	0.979
	MAE	0.11	0	0.016	0.098	0	0.024	0.094	0	0.017
	MSE	0.032	0	0.004	0.021	0	0.007	0.022	0	0.002
	RMSE	0.178	0	0.064	0.144	0	0.082	0.149	0	0.045
	MSD	0.014	0	0.01	–0.001	0	–0.003	0.029	0	–0.001
	MAPE	0.161	0	0.024	0.128	0	0.034	0.134	0	0.022
	R^2_{adj}	0.677	1	0.958	0.789	1	0.93	0.773	1	0.979
GBOOST	R^2	0.796	1	0.945	0.28	1	0.804	0.844	1	0.957
	MAE	0.106	0	0.021	0.189	0	0.038	0.097	0	0.02
	MSE	0.027	0	0.005	0.095	0	0.019	0.021	0	0.004
	RMSE	0.164	0	0.074	0.308	0	0.139	0.143	0	0.065
	MSD	0.019	0	0.004	0.057	0	0.012	–0.018	0	–0.004
	MAPE	0.136	0	0.028	0.26	0	0.053	0.11	0	0.022
	R^2_{adj}	0.796	1	0.945	0.28	1	0.804	0.844	1	0.957
RF	R^2	0.846	0.982	0.972	0.76	0.971	0.951	0.864	0.984	0.977
	MAE	0.084	0.03	0.037	0.109	0.039	0.049	0.078	0.028	0.034
	MSE	0.015	0.002	0.003	0.023	0.003	0.005	0.013	0.002	0.002
	RMSE	0.123	0.041	0.052	0.153	0.053	0.069	0.115	0.039	0.047
	MSD	0.003	0.002	0	0.007	0.003	–0.001	0	0.001	0.001
	MAPE	0.113	0.041	0.048	0.145	0.053	0.064	0.103	0.039	0.044
	R^2_{adj}	0.846	0.982	0.972	0.76	0.971	0.951	0.864	0.984	0.977

Table B.7: Accuracy indicators for hybrid algorithms using xGBoost in selecting features

Algorithm	Error	Model 15			Model 16			Model 17		
		Test	Train	Validation	Test	Train	Validation	Test	Train	Validation
LR	R^2	0.982	0.99	0.989	0.669	0.901	0.872	0.948	0.995	0.989
	MAE	0.02	0.023	0.022	0.099	0.086	0.088	0.031	0.017	0.02
	MSE	0.001	0.001	0.001	0.02	0.011	0.013	0.003	0.001	0.001
	RMSE	0.033	0.032	0.032	0.143	0.102	0.112	0.057	0.023	0.033
	MSD	–0.003	–0.006	–0.005	0.071	–0.018	0	0.001	0.004	0.003
	MAPE	0.033	0.03	0.031	0.119	0.1	0.104	0.05	0.023	0.029
	R^2_{adj}	0.982	0.99	0.989	0.669	0.901	0.872	0.948	0.995	0.989
PR	R^2	0.982	0.99	0.989	0.669	0.901	0.872	0.948	0.995	0.989
	MAE	0.02	0.023	0.022	0.099	0.086	0.088	0.031	0.017	0.02
	MSE	0.001	0.001	0.001	0.02	0.011	0.013	0.003	0.001	0.001
	RMSE	0.033	0.032	0.032	0.143	0.102	0.112	0.057	0.023	0.033
	MSD	–0.003	–0.006	–0.005	0.071	–0.018	0	0.001	0.004	0.003
	MAPE	0.033	0.03	0.031	0.119	0.1	0.104	0.05	0.023	0.029
	R^2_{adj}	0.982	0.99	0.989	0.669	0.901	0.872	0.948	0.995	0.989
ANN	R^2	0.988	0.999	0.997	0.989	1	0.998	0.992	1	0.999
	MAE	0.014	0.004	0.006	0.017	0.002	0.005	0.012	0.001	0.003
	MSE	0	0	0	0	0	0	0	0	0
	RMSE	0.02	0.007	0.011	0.019	0.003	0.009	0.016	0.003	0.008
	MSD	0.004	0	0.001	–0.004	0	–0.001	–0.001	0	0
	MAPE	0.082	NaN	NaN	0.068	NaN	NaN	0.065	NaN	NaN
	R^2_{adj}	0.988	0.999	0.997	0.989	1	0.998	0.992	1	0.999

Table B.7: Continued

Algorithm	Error	Model 15			Model 16			Model 17		
		Test	**Train**	**Validation**	**Test**	**Train**	**Validation**	**Test**	**Train**	**Validation**
XGBOOST	R^2	0.742	1	0.971	0.66	1	0.942	0.612	1	0.947
	MAE	0.108	0	0.017	0.103	0	0.017	0.123	0	0.02
	MSE	0.025	0	0.003	0.033	0	0.006	0.038	0	0.005
	RMSE	0.159	0	0.053	0.182	0	0.075	0.195	0	0.072
	MSD	0.004	0	0.008	0.04	0	–0.001	–0.006	0	–0.004
	MAPE	0.15	0	0.026	0.148	0	0.028	0.156	0	0.024
	R^2_{adj}	0.742	1	0.971	0.66	1	0.942	0.612	1	0.947
GBOOST	R^2	0.83	1	0.954	0.569	1	0.883	0.844	1	0.957
	MAE	0.105	0	0.021	0.157	0	0.032	0.098	0	0.02
	MSE	0.022	0	0.005	0.057	0	0.011	0.021	0	0.004
	RMSE	0.15	0	0.067	0.238	0	0.107	0.143	0	0.064
	MSD	0.022	0	0.004	0.045	0	0.009	–0.017	0	–0.003
	MAPE	0.14	0	0.028	0.234	0	0.047	0.111	0	0.022
	R^2_{adj}	0.83	1	0.954	0.569	1	0.883	0.844	1	0.957
RF	R^2	0.853	0.983	0.976	0.805	0.976	0.968	0.866	0.984	0.977
	MAE	0.082	0.029	0.035	0.092	0.034	0.04	0.077	0.028	0.034
	MSE	0.014	0.002	0.002	0.019	0.002	0.003	0.013	0.002	0.002
	RMSE	0.12	0.041	0.049	0.138	0.048	0.056	0.115	0.039	0.047
	MSD	0.001	0.001	0	0.01	0.005	0.003	0	0.001	0
	MAPE	0.11	0.041	0.046	0.127	0.048	0.054	0.102	0.039	0.044
	R^2_{adj}	0.853	0.983	0.976	0.805	0.976	0.968	0.866	0.984	0.977

LIST OF PUBLICATIONS

Saad, A. H., Nahazanan, H., Yusoff, Z. B. M., Mustafa, M., Elseknidy, M. H., & Mohammed, A. A. (2021). Evaluating Biosedimentation for Strength Improvement in Acidic Soil. *Applied Sciences*, 11(22), 10817.

Mohammed, A. A.,Nahazanan, H.,Nasir, N. A. M.,Huseien, G. F., & Saad, A. H. (2023). Calcium–Based Binders in Concrete or Soil Stabilization: Challenges, Problems, and Calcined Clay as Partial Replacement to Produce Low–Carbon Cement. *Materials*, 16(5), 2020.

Saad, A. H., Nahazanan, H., Yusuf, B., Toha, S. F., Alnuaim, A., El–Mouchi, A., … Mohammed, A. A. (2023). A Systematic Review of Machine Learning Techniques and Applications in Soil Improvement Using Green Materials. *Sustainability*, *15*(12), 9738.

Saad, A. H., Nahazanan, H., Yusuf, B. , Toha, S. F. , Elseknidy, M. H., & Mohammed, A. A. (2023). Marine Clay: Properties, Weakness and Challenges of Strengthening – A Review Paper. International Conference and Exhibition for Science (ICES 2023) College of Science, King Saud University, Riyadh, Saudi Arabia. (Accepted).

Saad, A. H., Nahazanan, H., Yusuf, B. , Toha, S. F. , A., Elseknidy, M. H., & Mohammed, A. A. (2023). Long Term Effect of Sustainable L–POFA–CS Improvement Mixture on Mechanical and Geotechnical Properties of Marine Clay. 5th Euro–Mediterranean Conference for Environmental Integration (EMCEI–23), Cosenza, Italy. (Accepted).

Saad, A. H., Nahazanan, H., Yusuf, B. , Toha, S. F. , A., Elseknidy, M. H., & Mohammed, A. A. (2023). Evaluating Long–term Behavior of Eco–Friendly Treated Marine Clay using Finite Element Method. 5th Euro–Mediterranean Conference for Environmental Integration (EMCEI–23), Cosenza, Italy. (Accepted).

Rania , R. M., Elseknidy, M., Saad, A. H., Kineber, A. F. (2023). Mechanical and Microstructural Properties of Concrete Incorporating Nanoparticles from Brine Seawater. 5th Euro–Mediterranean Conference for Environmental Integration (EMCEI–23), Cosenza, Italy. (Accepted).